Development, Testing, and Analysis of a Rotational Friction Connection for Improving the Seismic Performance of Metal Building Systems with Hard Walls

by

Michael J. Langley

A dissertation submitted to the Graduate Faculty of
Auburn University
in partial fulfillment of the
requirements for the Degree of
Doctor of Philosophy in Civil Engineering

Auburn, Alabama
August 4, 2018

Keywords: Earthquake Engineering, Metal Building Systems, Passive Energy Dissipation

Approved by

Justin D. Marshall, Chair, Associate Professor of Civil Engineering
James S. Davidson, Professor of Civil Engineering
J. Michael Stallings, Professor of Civil Engineering
Robert W. Barnes, Associate Professor of Civil Engineering

This dissertation is dedicated to my parents,
Gordon and Jeanne Langley,
for their loving support

Abstract

The use of metal building systems has become commonplace in today's society. For well over two decades, the performance of metal building systems during seismic events has been the subject of intense research. It was revealed that the concrete/masonry hard wall cladding in metal building systems is susceptible to falling away from the structure in major seismic events. The majority of the past research efforts, both experimental and analytical, has been focused on improving the seismic performance of the metal building moment frame. In order to obtain a more complete picture of the seismic performance of metal building systems clad with hard walls, the seismic performance of the longitudinal direction (parallel to the ridge) needed to be investigated. The research presented in this dissertation focused on understanding and improving the longitudinal seismic performance of metal building systems clad with hard walls.

Post-earthquake reconnaissance following the Haiti 2010 earthquake and the Christchurch New Zealand earthquake 2011 highlighted the dangerous effects of connection failures in the hard walls of metal building systems. There exists a large stiffness differential between the hard walls and steel frames, which in turn generates high demands on brittle connections. The problem is exacerbated by little to no coordination between the metal building systems (MBS) engineer and the engineer-of-record who is responsible for the connections, which can result in improper connection design. When these connections fail in a non-ductile manner, the continuous load path is lost and the wall can fall away from the structure. Collapsing wall panels in metal buildings are a life safety issue, as well as an economic concern.

The research presented in this dissertation developed a simple, reliable, friction-based energy dissipating connection, the rotational friction connection (RFC). The energy dissipating mechanism of the connection is geared towards the in-plane horizontal direction, while maintaining out-of-plane strength. To assess the energy dissipating capacity and reliability of the rotational friction connection, experimental tests were performed including monotonic pushover, unidirectional cyclic, bidirectional, out-of-plane, and high cycle testing. Results show that the connection exhibits high ductility and resiliency. Replacement of the connection following a seismic event would not be required. 3-D solid finite element models were developed using Abaqus and validated using the experimental data. A parametric study was performed to expand upon the experimental dataset. A simplified component level RFC model was created in SAP2000 and calibrated using the results from the Abaqus model.

A 3-D global finite element model of a metal building system with hard walls was developed to evaluate the improvement that RFCs have on the structure's seismic performance. Nonlinear dynamic response history analyses were performed using four levels of seismic hazard ranging from a service-level event to a maximum-considered event. A baseline metal building that does not utilize the RFCs served as a comparison with a metal building system that was equipped with RFCs. Results show that there was a reduction in the longitudinal story drifts, significant reductions in the inelastic demands in the longitudinal bracing system, as well as a slight improvement in the moment frame demands.

The results of both the experimental and analytical testing indicate the rotational friction connection shows great potential as a ductile fuse element in metal building system with hard wall cladding.

Table of Contents

List of Tables

List of Figures

Chapter 1 Introduction

1.1 Background and Motivation

Metal Building Systems (MBS) represent a unique structural type. They are optimized from a material standpoint to provide a modular, low-cost, quickly constructed and readily available building. As of 2016, metal building systems accounted for nearly half of non-residential low-rise construction in the United States (MBMA 2016). Reasons for the increase in the use of these systems include their cost-efficiency, durability, modularity, and speed of construction. Typically, these systems are one or two-story structures and have a wide range of applications including use in commercial, industrial, recreational, religious, and educational structures.

Due to their prevalence in today's society and because of life-safety concerns and economic considerations, the performance of metal building systems during earthquake events became a legitimate concern. Metal buildings have been shown to perform well in seismic events, that is, so long as the building cladding is lightweight. This was demonstrated in investigations of past earthquakes including Coalinga, CA (1983), Whittier, CA (1987), Loma Prieta (1989), and Northridge (1994) (Shoemaker 2006). The objective of these investigations was to determine how metal building systems reacted to seismic loads and if any improvements needed to be made to enhance their performance.

The 1994 Northridge earthquake produced very high ground accelerations, however, the metal buildings could be occupied as soon as utility service was restored (Shoemaker 2006). One particular note from the survey team of the Loma Prieta event highlighted a concern that would become a major structural problem for metal buildings. The survey team indicated that based on

their observations, engineers should pay attention to the connection design of metal building components when they are providing support for concrete tilt-up or masonry walls (Shoemaker 2006).

In recent years, it has become a trend to include precast concrete and masonry walls (hard walls) in metal building systems to enhance the architectural aesthetics of the building. It has been shown that when heavy and rigid walls such as concrete masonry units (CMU) or precast concrete panels are used, the performance of the metal building system during seismic events is significantly degraded. While the steel framing of these systems is very resilient, the potential for the failure and collapse of the hard wall is present. The deformation incompatibility between the light, flexible steel framing and the heavy, stiff concrete or masonry wall results in significant force and deformation demands on brittle connections. Post-earthquake reconnaissance missions in Port-au-Prince, Haiti (Baldrige and Marshall 2011) and Christchurch, New Zealand (Marshall and Gould 2012) highlighted the dangerous effect of poor connections between the steel frame and the hard walls. The teams found several instances of collapsed masonry and precast hard walls resulting from excessive connection demands. In metal building systems, it is the nonstructural components, such as precast hard walls and masonry walls, that are likely to suffer damage first in a seismic event.

The poor seismic performance of hard wall metal buildings has been identified through analytical modeling first performed by Hong (2007), experimental shake table tests conducted by Smith (2013d), and post-earthquake reconnaissance. All this research pointed to the same conclusion that metal buildings with hard walls are vulnerable to significant damage and local collapses during earthquake events.

Both the analytical and shake table tests were focused solely on the seismic behavior of metal building systems in the transverse direction (i.e. moment frames). The one-dimensional shake table could only test the structure in the moment frame direction. Therefore, the connections did not experience all the in-plane shear forces that would have been present during an actual earthquake event. Additionally, the connections between the wall panels and the steel frame were much more robust than typical connections. Due to the increased capacity of the connection and decrease in the force demand, the connections did not become damaged and the panels did not disengage as was seen in Christchurch.

Connections between elements with a significant stiffness differential can result in a deformation incompatibility. When this occurs the more rigid element tries to restrain the flexible element which can result in significant force and/or displacement demands at the link between the two. For the structures in Christchurch where panels detached from the structure, this appeared to be the driving force. In the case of the connection of hard walls to steel framing, this is a three-dimensional problem where in-plane and out-of-plane demands must be known in order to provide a reliable, continuous load path and capacity protection for the non-fuse elements.

These connections between the hard walls and the steel frame are failing in a brittle manner during earthquakes. When these failures occur, the continuous load path is lost and the walls can fall away from the structure as occurred in the Christchurch, New Zealand earthquake of 2011. As shown in Figure 1-1, a concrete wall segment has fallen away from a metal building system. In this circumstance, adjacent panels that did not fall away had connections that were so heavily damaged that temporary shoring was required to keep the wall panel in place.

Figure 1-1. Loss of panel and temporary shoring of adjacent panel in Christchurch, New Zealand (Marshall and Gould 2012)

Another example of a non-structural hard wall failure occurred in the Haiti Earthquake of 2010. Figure 1-2 illustrates an out-of-plane failure of a non-structural masonry wall. This wall collapse lead to a roof failure in the adjacent structure. The reconnaissance team found no evidence

of wall ties connecting the masonry wall to the steel frame. Because of the absence of wall ties, it is not surprising that the wall failure occurred. The steel frame that carried the gravity and lateral load appeared undamaged (Eberhard et al. 2010).

Figure 1-2. Infill Masonry Wall Collapse of PEMB in Port-au-Prince, Haiti (Eberhard et al. 2010)

Although such failures in Haiti are not surprising, the fact that wall failures occurred in New Zealand, where the building code is comparable to that in the United States is alarming. Improper connection designs between the hard walls and the steel frame are not satisfying the essential life-safety requirement. Therefore, these wall failures present a significant life-safety hazard to the public. In addition to this, these wall failures result in economic losses due to business interruptions and associated repair costs.

Due to the seriousness of collapsing hard walls of metal buildings during seismic events, attention must be focused on improving the frame-to-wall connections of these nonstructural elements. The solution involves energy dissipating connections between the hard walls and steel framing of the metal buildings to correct the demands due to deformation incompatibility. In order to improve life-safety and provide an enhanced level of performance, a simple, reliable energy

dissipating connection will provide a continuous, resilient load path. The development of the connections included rigorous analytical modeling, experimental testing, and evaluation of system performance.

1.2 Objectives

In order to improve the resilience and safety of hard wall metal building systems during seismic events, it is necessary to develop a new seismic force resisting system with energy dissipating connections. The new system would take advantage of the differential stiffness between the hard walls and steel frames. Energy dissipating will be geared to response in the longitudinal direction (parallel to the ridge) without losing out-of-plane strength for the transverse response, thus avoiding loss of the critical load path. Ideally, the connection will absorb the structure's earthquake energy and avoid excessive force entering the wall system, thus minimizing damage to the wall elements.

In addition to meeting the life-safety requirement, the best outcome would be a connection that would itself incur low damage during a seismic event. A low damage connection would mean that repairs or replacement following an event would be minimal or not required, thus reducing the need for expensive repair costs and business interruptions.

The research presented in this dissertation includes the development of a new rotational friction-based connection that will act as the ductile fuse element between heavy, stiff walls and the flexible steel frame to create a longitudinal lateral force resisting systems capable of enhancing the seismic performance of metal building systems. A new lateral system providing greater resistance to earthquake damage will positively impact life-safety, economic, and environmental concerns. In order to accomplish this objective, the following research tasks were implemented:

1) Assess the feasibility of various energy dissipating connections with considerations including energy dissipation reliability, deformation capacity, constructability, and economy.
2) Develop a simple, reliable energy dissipating connection for use between hard walls and flexible steel framing of metal building systems.
3) Perform experimental component level testing in the laboratory to evaluate the cyclic behavior of the new energy dissipating connection.
2) Develop a 3-D solid finite element model of the rotational friction connection and validate using experimental data collected from component testing.
3) Investigate other geometric parameters that were not included in the testing using the validated numerical model.
4) Develop analytical and simplified numerical models of the energy dissipating connection for implementation in a global metal building system numerical model.
5) Quantify the expected seismic performance of the new structural system and compare with a baseline metal building system.

1.3 Organization

The research presented in this dissertation has been organized into chapters which are summarized below:

Chapter 2 is a literature review focusing on the components of metal building systems with hard walls, failures of connections using current design techniques, and research into advanced energy dissipating connections for hard walls.

Chapter 3 introduces the development of the rotational friction connection (RFC) and the rationale behind its design. Laboratory testing of the RFC is presented. 3-D solid finite element models are developed in Abaqus and verified with theoretical equations and validated with experimental data.

Chapter 4 presents the rationale for the global metal building system numerical model. A simplified model of the rotational friction connection is also developed using SAP2000 and calibrated with the Abaqus model.

Chapter 5 discusses the results of an analytical study of the new seismic force resisting system for metal building systems with hard walls that include the rotational friction connections. A metal building model was created without the new energy dissipating connections to provide a comparison to models the utilize the RFCs. The improvement in structural response of the metal building systems is quantified and presented.

Chapter 6 summarizes the conclusions of this research and provides recommendations for future work.

Chapter 2 Background of Metal Building Systems with Hard Walls

2.1 Introduction

This chapter discusses the current design philosophy for seismic design of building structures. The structural components of metal building systems that are pertinent to seismic events are identified, including the transverse moment frame, longitudinal systems, roof diaphragm, and hard walls. Previous research in the seismic behavior of metal building moment frames involving shake table and cyclic component testing will be discussed. Wall failures that occurred during the Haiti and Christchurch, New Zealand earthquakes involving metal building system cladding connections are highlighted. The chapter concludes with a discussion of current energy dissipating connections for hard wall cladding that have been developed.

2.2 Earthquake Engineering Design Philosophy

Earthquakes represent one of the most destructive hazards on Earth. Over 40 states in the United States are subject to risks from earthquakes, facing potential serious loss of life and injury to citizens, damage to buildings, and economic losses (McCabe 2018). Earthquake intensities vary from small magnitude events that occur more frequently to rare large magnitude events with longer return periods. There is a shift in philosophy that has slowly developed in the United States since the Loma Prieta (1989) and Northridge (1994) earthquakes. Historically, engineering seismic design of building to ensure life safety has been the approach over time (McCabe 2018). In the United States, the prevailing design philosophy for earthquake resistance relies on inelastic behavior and providing sufficient structural ductility so that there is a low probability of collapse

during a Maximum-Considered Earthquake event (AISC 2010a). Designing the structural system to remain elastic and undamaged for very rare earthquake events is not an economically viable solution due to the impractically large structural members that would be required. The prescriptive approach of the US design code is reflected in the following quote, "Most structures are designed only with an expectation of protecting life safety, rather than assuring the feasibility of repair or post-earthquake utility" (AISC 2010a).

The chart in Figure 2-1 illustrates the design objectives of the US seismic design code. The prescriptive approach considers a design-basis event that has a probability of exceedance of approximately 10% in 50 years. For an ordinary structure (Category II) that experiences the design-basis event, there would be considerable damage to structural components. Nonstructural systems may not be operable. The code's objective in the Maximum-Considered Event is to prevent structural collapse allowing for the occupants to escape. However, there is a 10% probability that the structure could collapse and may result in casualties (ASCE/SEI 2016). Also, occupancy and repair may not be possible or feasible, resulting in significant economic disruption. For ordinary structures, the prescriptive approach is only required to provide the life safety objective for a design event.

Seismic Hazard			Tolerable Impact			
			Building Occupancy and Use (Category)			
Event	Occurrence	Probability of Exceedence	Infrequent (I)	Ordinary (II)	Critical (III)	Essential (IV)
Small	Frequent	50% in 30 years (43-year MRI)	Moderate	Mild	Mild	Mild
Medium	Occasional	20% in 50 years (225-year MRI)	High	Moderate	Mild	Mild
Large (DBE)	Rare	10% in 50 years (475-year MRI)	Severe	High	Moderate	Mild
Very Large (MCE)	Very Rare	2% in 50 years (2,475-year MRI)	Severe	Severe	High	Moderate

Mild impact means there is no loss of structural strength and stiffness, and the building is safe to occupy. Nonstructural systems are fully operational, and the overall extent and cost of damage is minimal.

Moderate impact means there is some structural damage, but such damage is limited and repairable. There may be delay in occupancy. Nonstructural systems are operational but may require repair. Emergency systems remain fully operational. The extent and cost of damage is significant in some areas.

High impact means there is significant damage to structural components (but "no large falling debris"). Repair is possible, but significant delays in occupancy are expected. Nonstructural systems are inoperable; emergency systems are significantly damaged, but remain operational.

Severe Impact means there is significant structural damage, but the gravity-load carrying system is still intact. Occupancy and repair may not be possible or feasible. There may be multiple casualties.

Figure 2-1. Performance Objectives of US seismic design code (Judd and Charney 2014)

Recent earthquake events have demonstrated that the prescriptive approach is not achieving the level of performance that society deems acceptable. The economic losses can be devastating and are not necessarily addressed in the prescriptive approach. The Christchurch, New Zealand earthquake in 2011 became a much-examined event. There was extensive damage to buildings even though the life-safety objectives were for the most part met. The life safety objective means the structure will not collapse and the occupants are able to escape (MBIE 2004). As a result of this earthquake, the central business district of Christchurch was 85% destroyed or had to be demolished (Gates 2012). The economic losses and disruption to society was unacceptable. This earthquake highlighted the need for low-damage, earthquake resilient-structures.

Investigations following the 1994 Northridge earthquake led to sweeping changes in seismic design. Perhaps the most significant post-Northridge development in the field of structural engineering was the birth and development of performance-based seismic engineering (PBSE) concepts and methodologies (Naeim 2004). Performance-based engineering is a more comprehensive approach to the seismic design of structures than prescriptive approaches. In performance-based seismic design, structural engineers design structures with the consideration of risk of life, occupancy, and economic loss that may occur as the result of future earthquakes. According to FEMA P58-1 (2012), the first step in performance-based seismic design is the selection of a desired performance level by the building owner or regulator. In the next step, the earthquake hazard level is selected for which this performance is to be achieved. Following this, the designer conducts a nonlinear dynamic analysis to determine if the performance objectives have been met. Performance-based seismic design is probabilistic due to the uncertainty of earthquake intensities and the difficulty in quantifying structural and nonstructural component behavior. However, the extra effort can be offset with an increased reliability of the performance of buildings during seismic events.

Even with the development and implementation of performance-based earthquake engineering, coordination between the performance levels of structural and nonstructural components becomes even more vital. Reduction in performance caused by vulnerability of nonstructural components, which includes hard walls, has been observed during recent earthquakes worldwide (Filiatrault 2014).

This US seismic design code is also applicable to the design of metal building systems. Metal building systems comprised nearly 50% of new low-rise construction in the US (MBMA 2016). Significant research has been underway to understand how these structures perform in

seismic events. The following section describes the components of metal building systems and recent research efforts into improving their performance during earthquakes.

2.3 Metal Building Structural Systems

2.3.1 Typical Components

Metal buildings are typically built from single-story steel moment frames that span the transverse direction. These lightweight structures are built using standardized structural designs which can span long distances, create large column-free spaces, and have dimensions that can be tailored to many different sizes (both clearspan and multi-span configurations). Engineers design the structural members with built-up I-shaped plate sections with tapered webs, as seen in Figure 2-2.

Figure 2-2. Metal Building Frame with tapered webs under construction (Stuart 2013)

These web-tapered members are optimized to provide maximum strength and stiffness by using larger web depths in areas where there is high moment demand, and thicker webs in regions with high shear demand. By optimizing the steel material, significant cost savings can be achieved versus using traditional hot-rolled members (Kaehler et al. 2011).

The metal building system is a collection of several structural systems. The transverse moment frames act as the primary lateral force resisting system and gravity carrying system. Braced frames or shear walls are utilized in the longitudinal direction (parallel to the ridgeline) of the structure. The roofing system, purlins, and cladding act as secondary structural members that transfer load to the primary structural resisting system. The three primary types of cladding elements include lightweight cladding (cold-formed metal buildings, structural insulated panels (SIPS)), concrete masonry unit walls, and precast concrete panels. Figure 2-3 shows a cutaway sketch of a typical metal building showing the primary structure, the secondary members, and the building cladding.

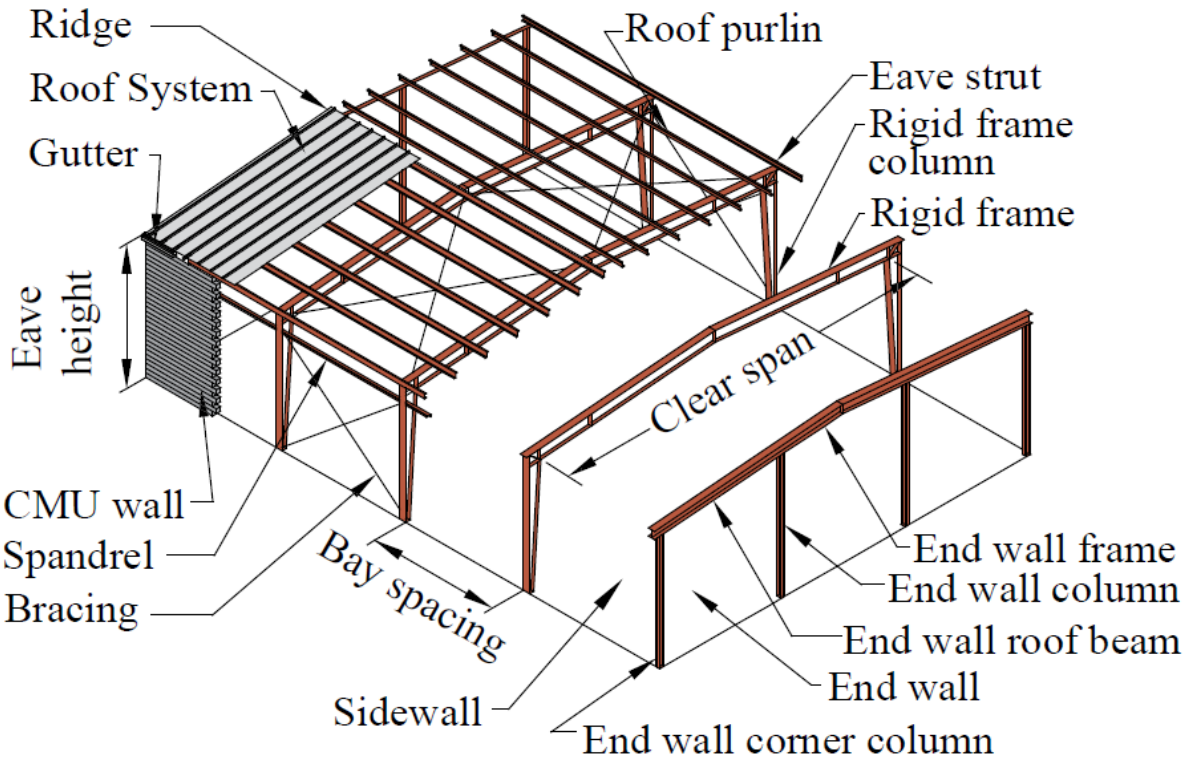

Figure 2-3. Typical Components of a Metal Building System clad with Masonry Wall (NCMA 2011)

2.3.2 Transverse Moment Frame

The primary lateral force resisting system in the transverse direction is a moment frame. It also serves as the primary gravity carrying system. As stated earlier, the metal building moment frames are optimized through the use of web-tapered built-up I-sections to minimize the quantity of steel material. These sections generally are composed of noncompact and slender flanges and webs. This is a significant difference from traditional hot-rolled moment frames whose sections are compact. The controlling structural limit states for metal building frames are stability-induced limit states like lateral-torsional buckling and flange local buckling. It is highly unlikely that a plastic hinge would ever form in a metal building moment frame (Hong 2007).

2.3.3 Longitudinal System

Most seismic research into metal building systems has been focused in the transverse direction, including that performed by Hong (2007) and Smith (2013). As mentioned earlier, the longitudinal system of a metal building system runs parallel to the ridgeline of the structure and includes the roof diaphragm, collector elements, bracing, and wall cladding. Current practice allows for engineers to design metal buildings using 2-D models because the metal roofs are classified as flexible diaphragms (ASCE/SEI 2016). The lateral force resisting systems for each direction are designed independently.

Four practical structural systems are available for design in the longitudinal direction for metal building systems in high seismic zones. They are the steel ordinary concentrically braced frame (OCBF), the ordinary moment frame (OMF), special reinforced masonry shear wall (SRMSW), and the intermediate precast shear wall (IPSW).

The steel ordinary concentrically braced frames are composed of rod-bracing, cables, or steel angles. Figure 2-4 shows an ordinary concentrically braced frame in a metal building system that utilizes rod-bracing as the lateral force resisting system. Rod-bracing and cables are so slender that they can carry tension forces only. The AISC Seismic Specification (2016) allows for the use of tension-only elements if the slenderness ratio is greater than 200. Steel angles are used when the seismic demand exceeds the capacity of rod-bracing. When hard walls are attached to the metal building system, all the connections between the steel frame and hard wall must be designed to allow for differential horizontal displacement to prevent the wall system from resisting the seismic load generated from rest of the structure.

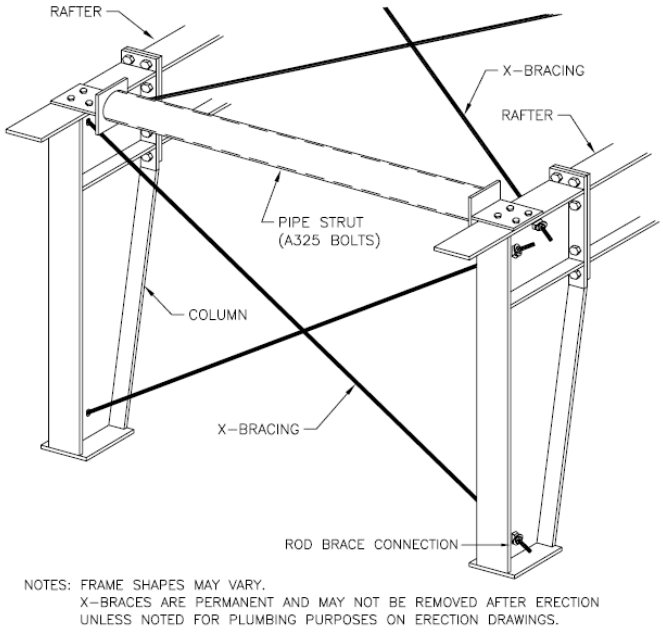

Figure 2-4. Tension-only OCBF for MBS (Nucor 2009)

If a wall has an opening that must not be obstructed, a portal frame such as the one shown in Figure 2-5 can be utilized. These frames are designed as steel ordinary moment frames. Because this seismic force resisting system is flexural based, the longitudinal system becomes much more flexible compared with the braced frame. As with the ordinary concentrically braced

frame, all connections between the steel frame and the wall system must be designed to allow for differential horizontal displacement.

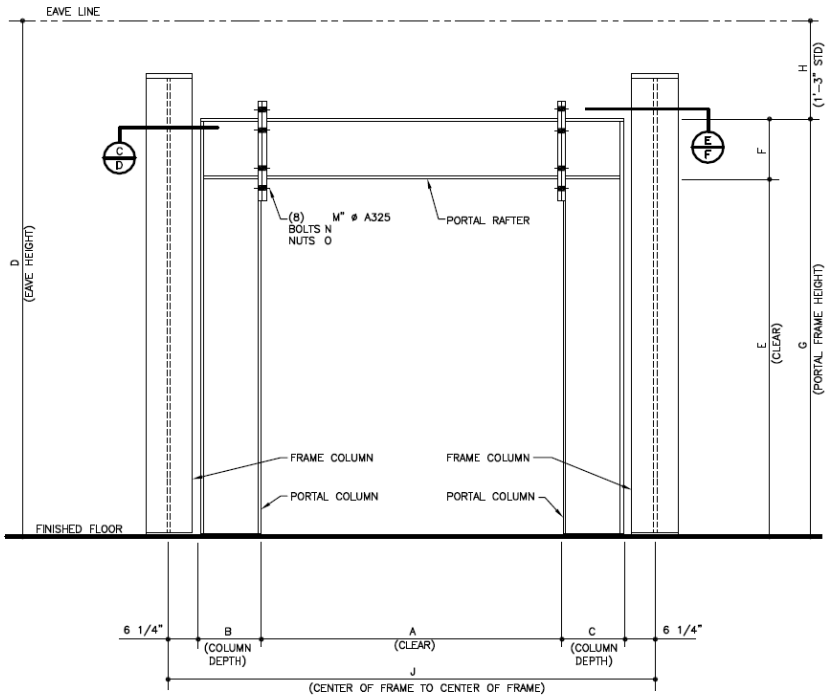

Figure 2-5. Portal Frame in Metal Building System (Nucor 2009)

When hard walls are attached to metal building frames, engineers must decide whether or not to utilize the hard wall as a lateral force resisting element. The connections between the hard walls and steel frames must be designed to be consistent with the intended lateral force resisting system. If there is a mismatch, seismic load will be transferred to elements that were never designed to resist such load. It is left up to the engineer-of-record to design the connections that can maintain an out-of-plane force while allowing for large in-plane horizontal displacement. However, there is no clear guidance on how to achieve this for use in metal building systems. This problem is exacerbated by a lack of communication between the engineer-of-record, who is charged with designing the hard wall connections and the concrete or masonry wall, and the metal building engineer. It is important to properly integrate a structurally sound steel frame and structurally sound hard walls to form a complete building with structural integrity (NCMA 2011).

2.3.4 Roof Diaphragm System

The roof diaphragms in metal buildings are typically light gage sheathing or standing-seam roofs. When designing metal building systems, the roof is assumed to be a flexible diaphragm, which allows for the engineer to utilize 2-D analytical models (ASCE/SEI 2016). Additionally, metal building frames are assumed to have little to no load sharing characteristics between adjacent frame lines. Bajwa (2010) investigated the contributions of lateral stiffness of metal building systems analytically using finite element analysis and full scale experimental tests. A metal building system was laterally tested using the assembly shown in Figure 2-6. The results from the experimental tests and analytical studies showed that the roof sheathing had negligible in-plane stiffness because the frames adjacent to the loaded frame deflected only a small percentage of the loaded frame (Bajwa 2010). The roof diaphragm appears to play a small role in the overall stiffness of metal building systems in the transverse direction.

Figure 2-6. Loading Assembly for Lateral Load Application on MB Frame (Bajwa 2010)

Rogers and Tremblay performed research on flexible diaphragms in low-rise structures in an attempt to provide seismic design strategies that account for the ductility and flexibility of roof diaphragms (2008). They proposed shifting the ductile fuse element from the sidewall braces up into the roof diaphragm as shown in Figure 2-7. Their results showed that including inelastic behavior in the thin metal roof diaphragms could result in an acceptable overall seismic performance. However, allowing inelastic deformation in the diaphragm could result in tearing near the deck fasteners. The deformation capacity is limited, and special measures are required to prevent excessive plastic deformation that could lead to a complete failure of the diaphragm (Rogers and Tremblay 2008).

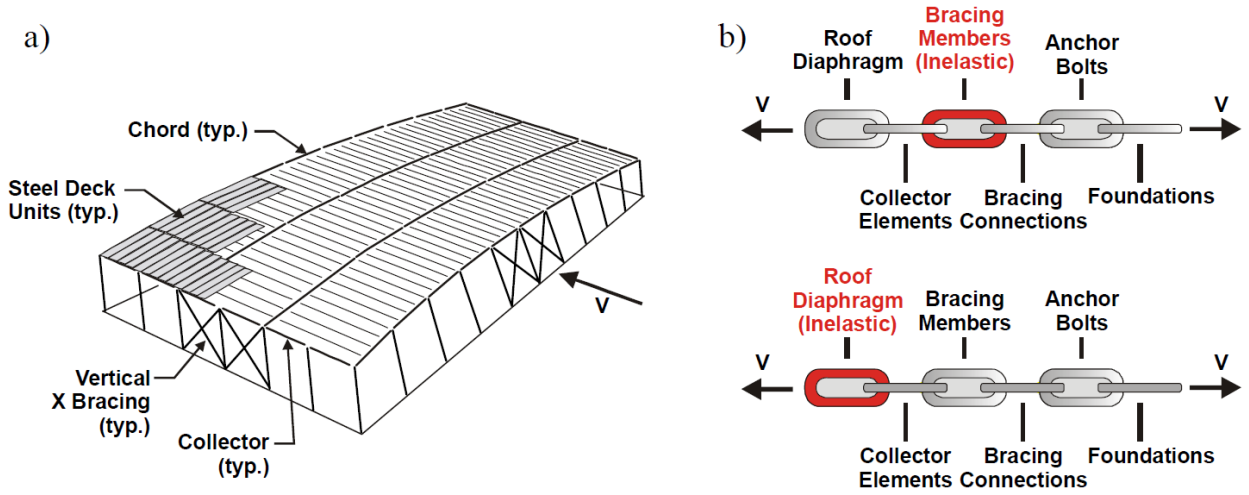

Figure 2-7. Single-story buildings with capacity-based design concepts for seismic load resisting system (Rogers and Tremblay 2008)

2.3.4 Precast Concrete Panels

Metal building systems have wall cladding that is either thin-sheet metal cladding or hard walls to enclose the structure. Architectural precast concrete cladding allows for a wide spectrum of design flexibility such as color, shape, and surface texture. The panels are fabricated in a climate-controlled facility to reduce variability in the products. Finished panels are transported to the construction site and tilted up and installed. The width dimensions of the precast wall panels

are more limited in size due to transportation considerations. Economy is maximized though the use of repetitive sections. Precast concrete walls exhibit superior noise-reduction properties. Rigid insulation sandwiched between two concrete wythes provides excellent thermal performance (PCI 2004).

In high seismic regions, structural engineers can utilize the intermediate precast shear wall as the seismic force resisting system. The seismic energy is dissipated in the shear wall through ductile yielding of the steel reinforcement and cracking of the concrete. Anchor bolts are used to connect the precast shear walls to the metal building system. These connections must be designed with sufficient strength to allow for the ductile yielding mechanism to fully develop.

Architectural precast concrete cladding is generally designed as a nonstructural component. During seismic events, the panel's inertial loads are passed through the steel connections to the seismic force resisting system. The wall connections are designed to resist the out-of-plane inertial load while accommodating structural displacement in the in-plane horizontal direction. Panels are connected at the bottom with bearing type connections and at the top with tieback connections that utilize slotted-holes or flexural rods (Pantoli 2015).

It is typical for the seismic force resisting systems designed in the United States to assume that the structure-cladding interaction is negligible. Recent research into the dynamics of precast panels has called this assumption into question. The natural frequency of these panels depends on the panel's mass and stiffness, as well as the connections' stiffnesses. Through resonant testing, it was determined that the natural frequency of the wall cladding is much lower than 20 Hz and as low as 5.4 Hz. This is well within the frequency content of earthquakes, which means the walls could play a significant role in the overall response of the structure (Pantoli 2015).

Through experimental resonance testing and analytical studies, it was revealed that three modes of vibration dominate the dynamic behavior of architectural precast concrete panels. These include a warping mode (a and b), rocking mode (c), and vertical translational mode (d) as shown in Figure 2-8. The warping mode has the lowest frequency and has the greatest possibility to be activated during a seismic event. The out-of-plane stiffness and location of the tieback connections has the most effect on the natural frequency of the warping mode. Stiffer tieback rods can increase the natural frequency. Additional, connections that are spaced closer together will stiffen the panel (Pantoli 2015).

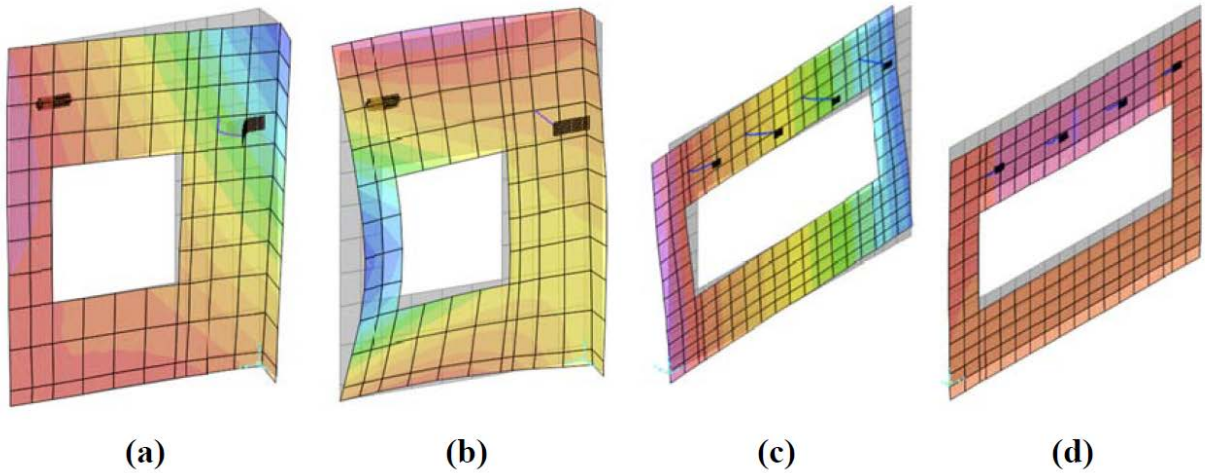

Figure 2-8. Modes of Vibration of various architectural precast cladding units (a) first and (b) second warping mode, and (c) rocking and (d) vertical translation mode [The contour shows the out-of-plane displacement in (a) and (b), the in-plane horizontal displacement in (c) and the in-plane vertical displacement in (d)] (Pantoli 2015)

2.3.5 Reinforced Masonry Walls

Reinforced masonry walls are popular enclosure systems for metal buildings due to their aesthetics, design flexibility, low cost, and ease of construction. In addition, masonry walls provide impact resistance, strength, energy efficiency, improved noise reduction, and fire

resistance. Choices for design using concrete masonry walls include exterior full-height walls, either with or without a parapet, as well as exterior partial-height or wainscot walls. Concrete masonry walls are most commonly designed to span vertically, supported by a steel spandrel beam at the top, and the foundation at the bottom as shown in Figure 2-9.

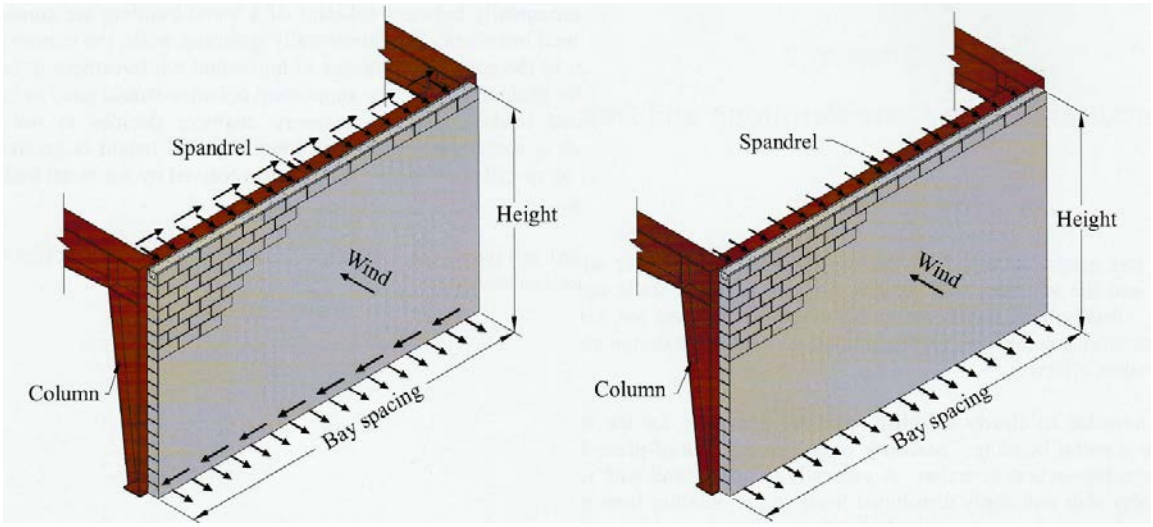

Figure 2-9. Vertically Spanning Masonry with In-Plane Shear Resistance (Left Diagram) or without In-Plane Shear Resistance (Right Diagram) (NCMA 2011)

Structural engineers have the choice of whether or not to use concrete masonry walls as the seismic force resisting system. In high seismic regions, the only seismic force resisting system allowed for masonry walls is the special reinforced masonry shear wall (SRMSW). Energy is dissipated in these walls through ductile yielding of the steel reinforcement and cracking of the masonry wall.

In order for these shear walls to develop their inelastic mechanisms, the wall connections between the spandrel beam and the wall must have sufficient in-plane shear strength. Typically, masonry wall anchors rigidly attach the spandrel beam to the masonry wall (Figure 2-10). If the masonry wall is not to be relied on as the seismic force resisting system, then the wall connections must be designed to prevent in-plane shear force from passing between the metal building system and the wall.

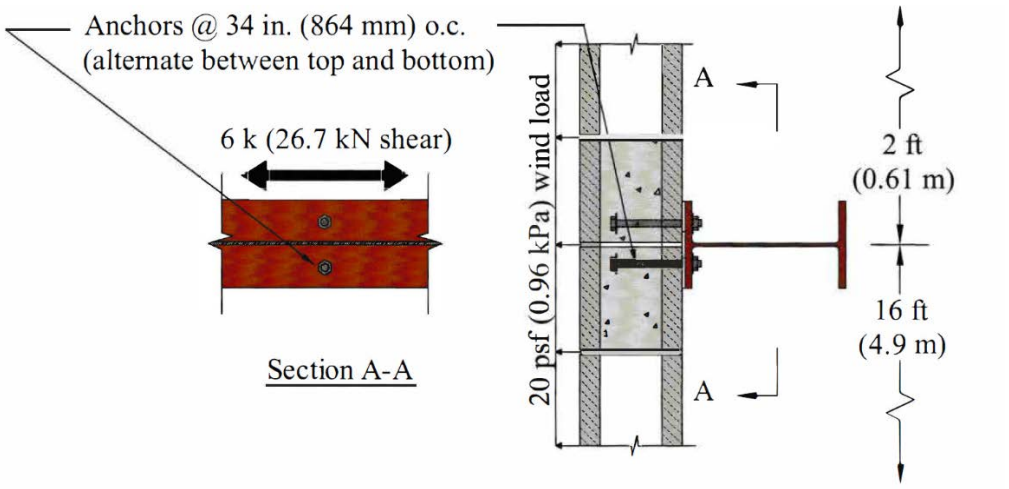

Figure 2-10. Anchor Bolt Design for Concrete Masonry Shear Wall (NCMA 2011)

2.4 Metal Building Moment Frame Seismic Research

Over the past decade, the metal building system industry has shown a desire to understand and improve the reliability of their systems during earthquakes. After the Northridge Earthquake of 1994, the metal building industry was caught up in the numerous building code changes that affected conventional steel moment frames. Hong (2007) states that the Northridge failures were primarily associated with the brittle fracture of welded joints at beam-to-column moment connections in multi-story steel buildings. According to Hong, the new stringent requirements in the seismic design provisions were adopted for use in metal building frames partly due to lack of research. It has been shown that the metal building frames performed well during the Northridge event as well as previous seismic events (Shoemaker 2006). Because metal building frames are completely different building systems from conventional steel moment frames, and because metal building systems performed well in earthquakes, it was unreasonable to adopt the same seismic requirements for both systems. Some of these changes unfairly impacted the metal building industry, which made it more difficult for this industry to remain competitive as an option for building construction. The Metal Building Manufactures Association (MBMA) represents the

interests of this industry and has provided funding for recent research projects for improving metal building systems. The ultimate goal of these research tasks is to develop seismic-force resisting systems tailored specifically for metal building frames. The systems currently being developed are the Metal Building Ordinary Moment Frame (MBOMF) for lightweight wall cladding, and the Metal Building Intermediate Moment Frame (MBIMF) for hard wall systems.

2.4.1 Cyclic and Analytical Testing of Metal Building Moment Frames

Hong (2007) at the University of California San Diego undertook the task to develop a seismic design procedure for metal building systems. It should be noted that at the beginning of his research, there existed very limited metal building test data, and even less for seismic applications. Experimental and analytical studies on metal building frames were required before a new seismic design procedure could be developed.

Hong performed cyclic tests on a full-scale metal building system. Cyclic behavior of metal building frames had not been investigated prior to this. The current seismic design procedure for metal building frames uses the ordinary moment frame (OMF). Because web-tapered members are often composed of non-compact and slender elements, stability limit states control the capacity rather than the formation of a plastic hinge. Figure 2-11 shows the test setup used by the researchers. The testing focused primarily on the performance of the web-tapered steel frame.

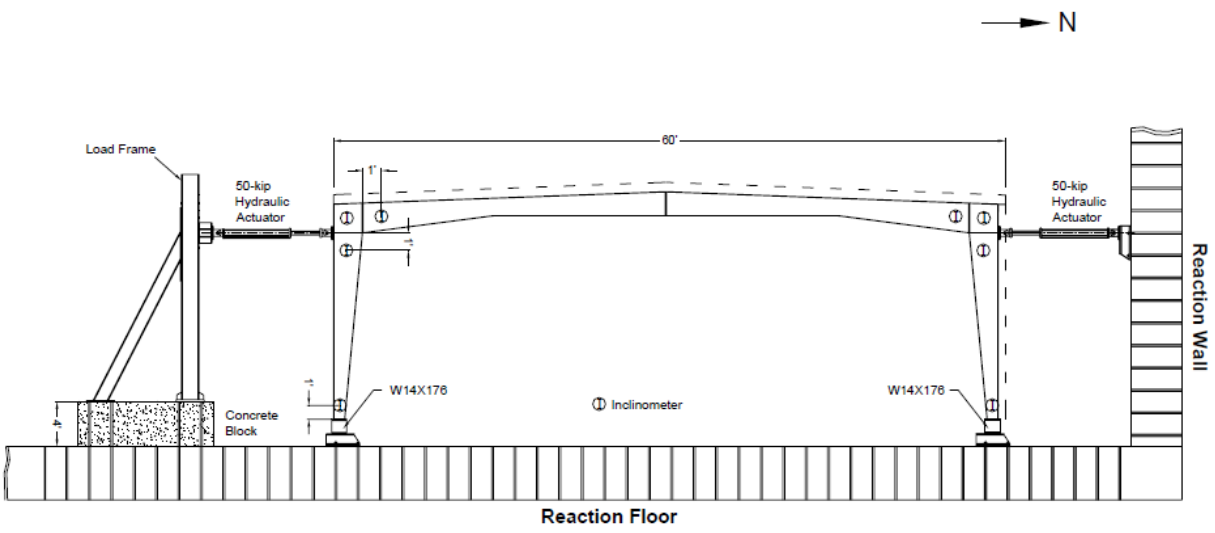

Figure 2-11. Cyclic Testing for Metal Building Frame (Hong 2007)

Several significant findings resulted from the experimental tests. It was shown that the metal building frames exhibited high deformability, but limited ductility. When compared to conventional moment resisting frames, the elastic drift range was significantly larger. The results showed that there was significant strength degradation following lateral buckling. It was also shown that the overstrength of this system was high because non-seismic load combinations controlled the frame design. This inherent reserve strength along with the light-weight characteristic of these systems explained why metal buildings with light-weight cladding performed well in past earthquake events.

Nonlinear finite element analysis models were developed using Abaqus (Simulia 2016) to predict global and local behaviors of the frames. A correlation study was performed to compare the experimental test results with computer analyses. This was done to specifically provide additional insight into the behavior of the metal building frame.

According to Hong's research, predicting the ultimate capacity of metal building frames can be achieved through nonlinear finite element analysis. To accomplish this, the following procedures were implemented. The Modified-Riks algorithm was used to capture the post-

buckling behavior of the frame. A geometric imperfection was introduced into the models using the first buckling mode shape from a linearized eigenvalue buckling analysis. Without this imperfection, the predicted failure mode would be incorrect (flange local buckling instead of lateral-torsional buckling) and the ultimate load would be much higher. A parametric study was conducted to determine the appropriate amplitude of geometric imperfection to apply. The most accurate prediction was obtained when an amplitude of $L_b/1000$ was used, where L_b is the length of the unbraced segment. The correct failure modes from one of the analyses are shown in Figure 2-12.

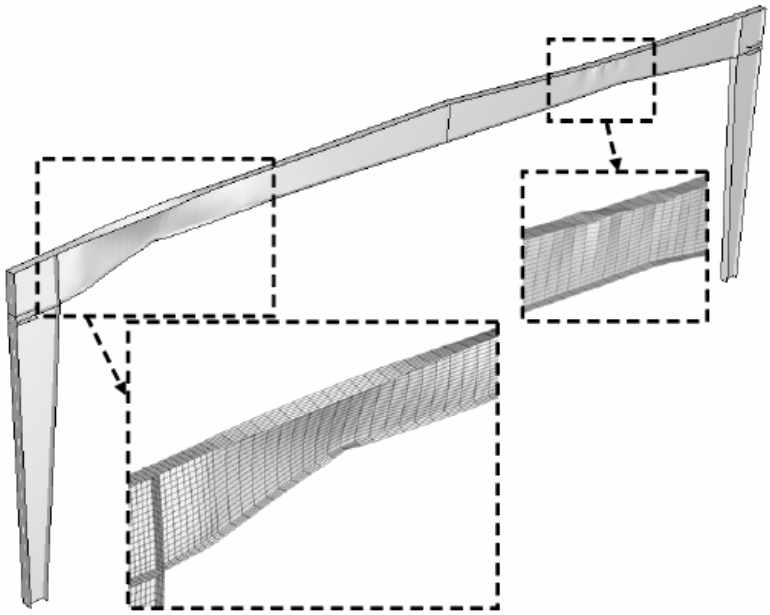

Figure 2-12. LTB Failure and Flange Local Buckling of Metal Building Frame (Hong 2007)

Using the results for the experimental and analytical tests, Hong developed a new drift-based seismic design procedure for metal building frames. This research demonstrated that the new design procedure worked well for metal building systems with light-weight cladding. However, one important finding from the case study was that metal buildings with heavy sidewalls

designed in accordance with current design provisions are vulnerable to collapse under major earthquakes.

2.4.2 Shake Table Testing of Metal Building Moment Frames

Continuing the goal to develop a new seismic force resisting system specific to metal building frames, Smith (2013a and 2013b) first performed full-scale shake table tests to provide experimental data concerning the seismic performance of metal buildings (Figure 2-13).

Figure 2-13. Metal Building with Concrete Walls on Shake Table (Smith 2013b)

The results of the shake table tests revealed several important aspects about the dynamic response of metal buildings during earthquake excitations. One of the test specimens was a metal building system with metal sidewall panels. Another specimen was clad with precast concrete panels. Both specimens exhibited lateral buckling in the rafters near pinch points, as seen in Figure

2-14. The term pinch point refers to a location in the frame where the angle of taper changes from one segment to the other.

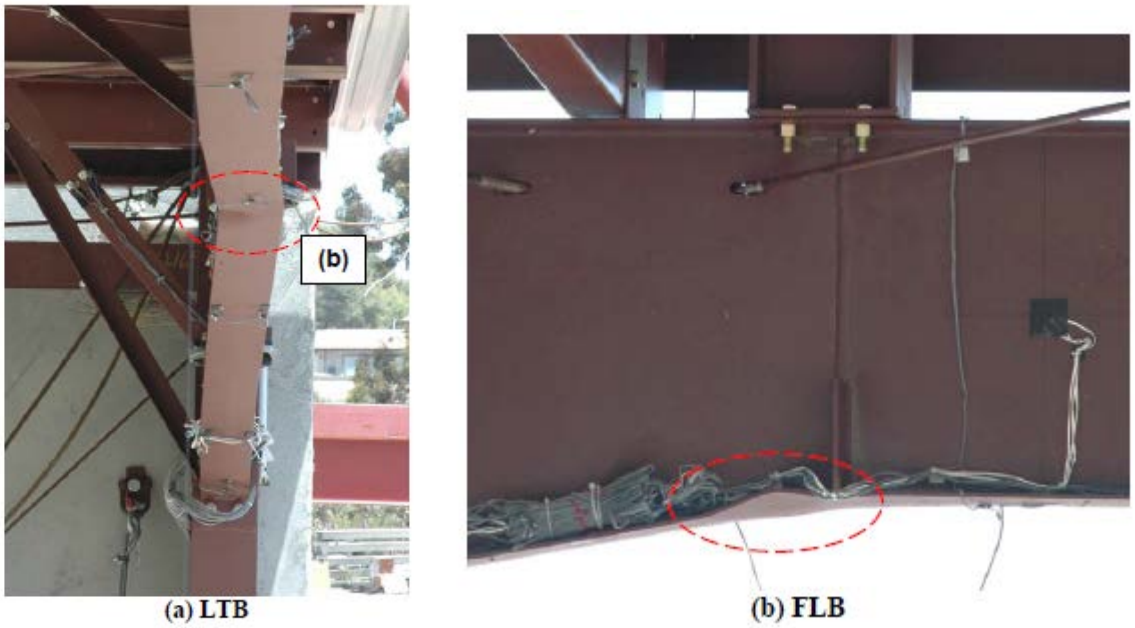

Figure 2-14. Buckling around the Pinch Point (Smith 2013b)

It was discovered that the behavior of the buckled segment was very similar to the behavior of steel Special Concentrically Braced Frames (SCBF). In SCBFs, the buckled segments alternate between buckling and straightening as the loading changes direction (Figure 2-15).

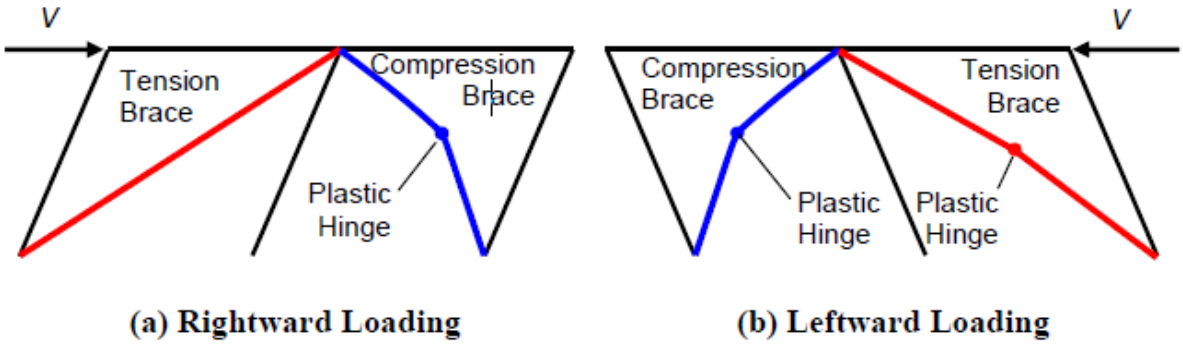

Figure 2-15. SCBF Cyclic Behavior (Smith 2013d)

During the tests, the inner flange of the buckled segment cycled between compression and tension. More than one buckle could not form simultaneously in the frame. None of the test

specimens collapsed on the shake table even though they were subjected to very intense accelerations. This can be explained by the fact that only one segment in the frame was buckling at a given time (Figure 2-16). The unbraced segment that undergoes cyclic LTB is referred to as the controlling segment. The post-buckled frame was still statically determinate. The second hinge did not form for two reasons. First, the outer flange is braced more frequently than the inner flange, which increases its resistance to LTB. Second, the post-buckled stiffness reduction requires increasingly large displacements to increase internal force demand in the rafters.

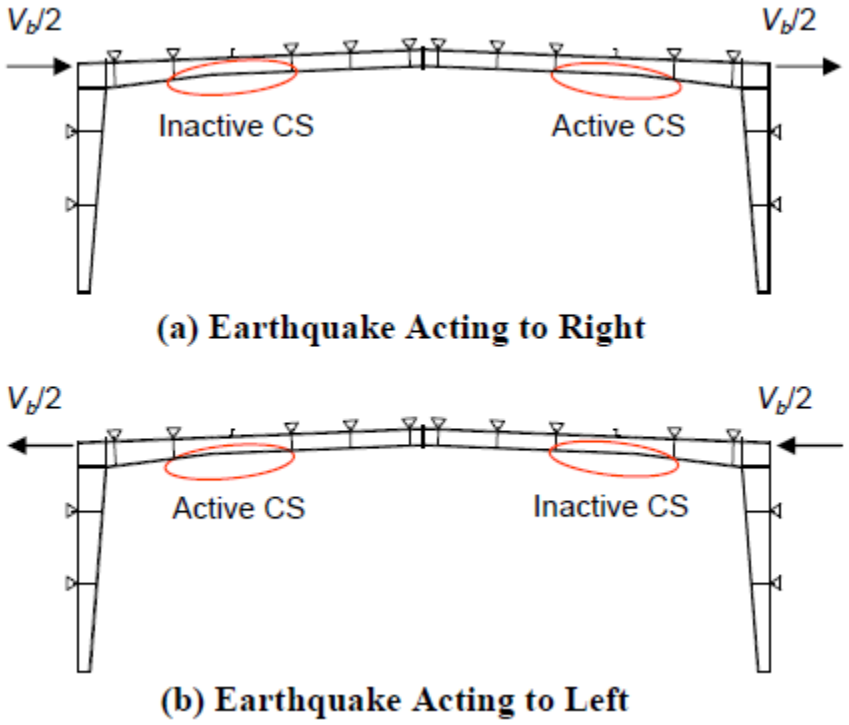

Figure 2-16. Active and Inactive Controlling Segments (Smith 2013d)

The shake table tests agreed with the findings of Hong (2007) regarding the overstrength of metal building frames. For the lightweight specimen, there was a high level of overstrength, suggesting that these types of systems would survive a Design Basis Earthquake (DBE) or Maximum Considered Earthquake (MCE) event and remain elastic. The overstrength for the hard-

wall metal building system was lower. The hard-wall metal building system did not remain elastic and undamaged at the DBE level. Smith's research revealed that the safety factor at design level is less than one for metal buildings with concrete walls. This finding was in agreement with the case study performed by Hong (2007).

Smith's research identified that lateral-torsional buckling could act as an inelastic mechanism for a new seismic force resisting system for metal buildings with hard walls. This was a significant step toward the development of what will become the Metal Building Intermediate Moment Frame (MBIMF), which is still in development. For a new structural system to be approved for inclusion in the building code, a rigorous validation process by means of a FEMA P695 (FEMA 2009) study is required. Component level behavior must be known before any attempt can be made to develop analytical models that simulate the complete behavior of metal building frames during an earthquake.

2.4.3 Cyclic Lateral Torsional Buckling Tests

In order to provide experimental data for the development of the new seismic force resisting system (SFRS), Smith (2013c) conducted a study to investigate the cyclic lateral-torsional buckling behavior of built-up, web-tapered I-section rafters. As shown in Figure 2-17, the testing setup was comprised of a metal building moment frame subassembly with both a column and rafter segment. A hydraulic actuator loaded the specimens under displacement control. Since the column acted as a moment arm, it was designed to exceed the capacity of all the rafters and remain elastic. Each rafter was braced in order to achieve the desired buckling mode. A total of ten rafters were cyclically tested.

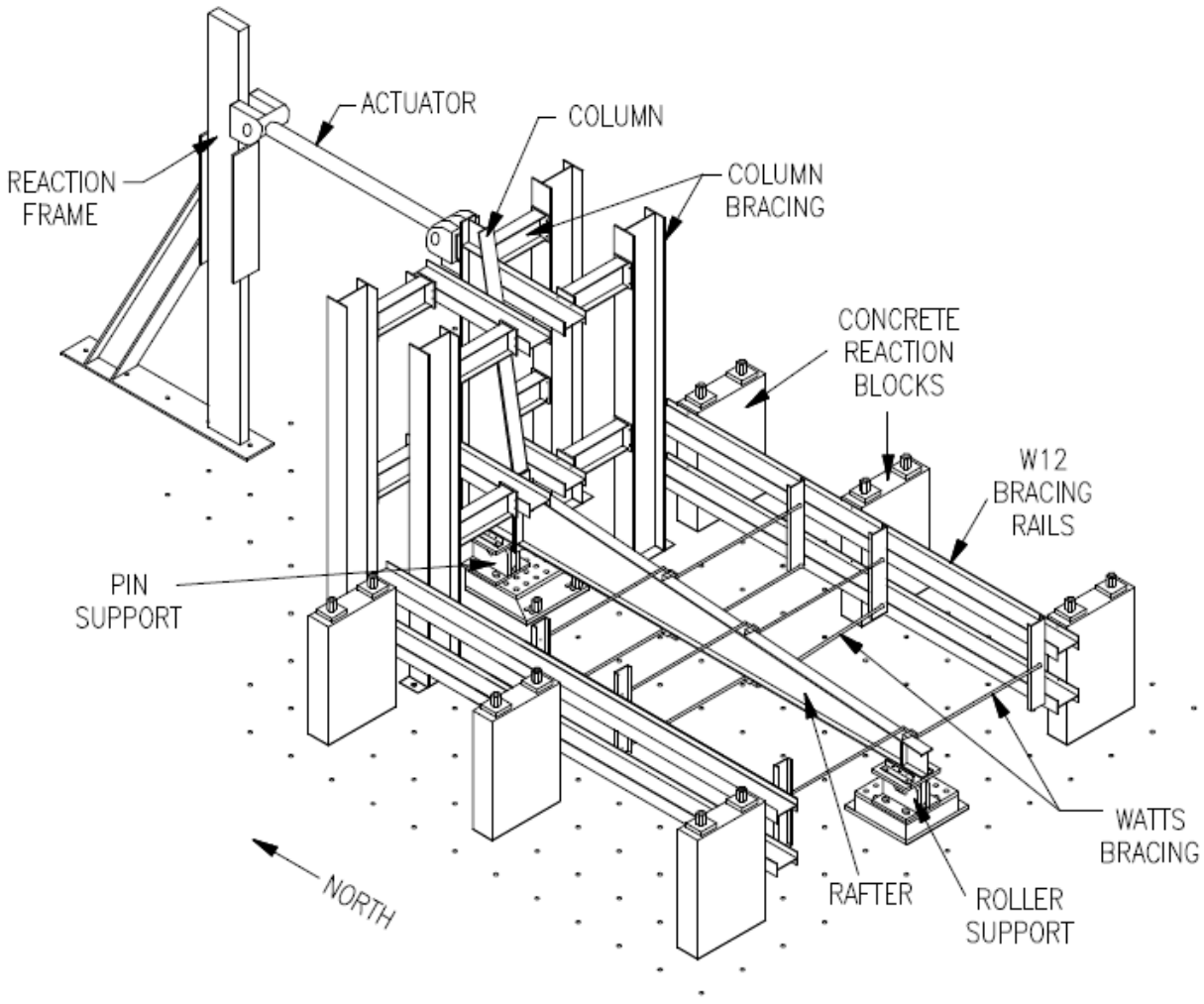

Figure 2-17. Cyclic Test Setup (Smith 2013c)

"Frame Design Using Web-Tapered Members" (Kaehler et al. 2011), herein referred to as Design Guide 25, is the most complete informational guide concerning the analysis and design of web-tapered members. It provides equations for determining member strengths for axial, flexural, and shear limit states. The LTB strength for nonprismatic I-beams is very challenging. An accurate prediction of the LTB capacity is imperative for seismic design, as underestimating the true strength could undersize members around the controlling segment and an undesirable failure could occur.

It was recognized from previous research that adjacent unbraced segments significantly influence the LTB capacity. Smith expanded the LTB equations in Design Guide 25 to include the effects of adjacent unbraced segments as well as plate size changes within the unbraced length, which is not uncommon in metal building practice. The torsional stiffness of an I-beam is much higher when the effects of warping torsion are included, thereby increasing its LTB resistance. When performing an eigenvalue buckling analysis, the elastic lateral torsional buckling load is much more accurate when the analysis model uses a 14 degree of freedom beam-column element which includes a warping degree of freedom. The improved elastic lateral torsional buckling value can be used in the LTB calculations in Design Guide 25.

The results from the cyclic tests provided insight into the critical flexural capacities, load-displacement paths, lateral brace forces, and failure modes. Every rafter specimen developed lateral buckling within the critical segment. The LTB capacities predicted from Design Guide 25 were in agreement with the test results when the effect of the adjacent segments were included. Just as in the shake table tests, the LTB response in the cyclic tests exhibited many characteristics similar to a compression brace of a steel Special Concentrically Brace Frame (SCBF). After LTB, compression flanges formed local buckles at two to three locations within the critical segment. With every positive cycle, the controlling segment buckled in compression at a lower load each time (Figure 2-18). For the negative cycle, the controlling segment flange straightened, while gaining stiffness, until it carried tension. The load-deformation plots showed a significant strength loss after buckling. The rate of strength loss appeared to decrease at an exponential rate with each cycle.

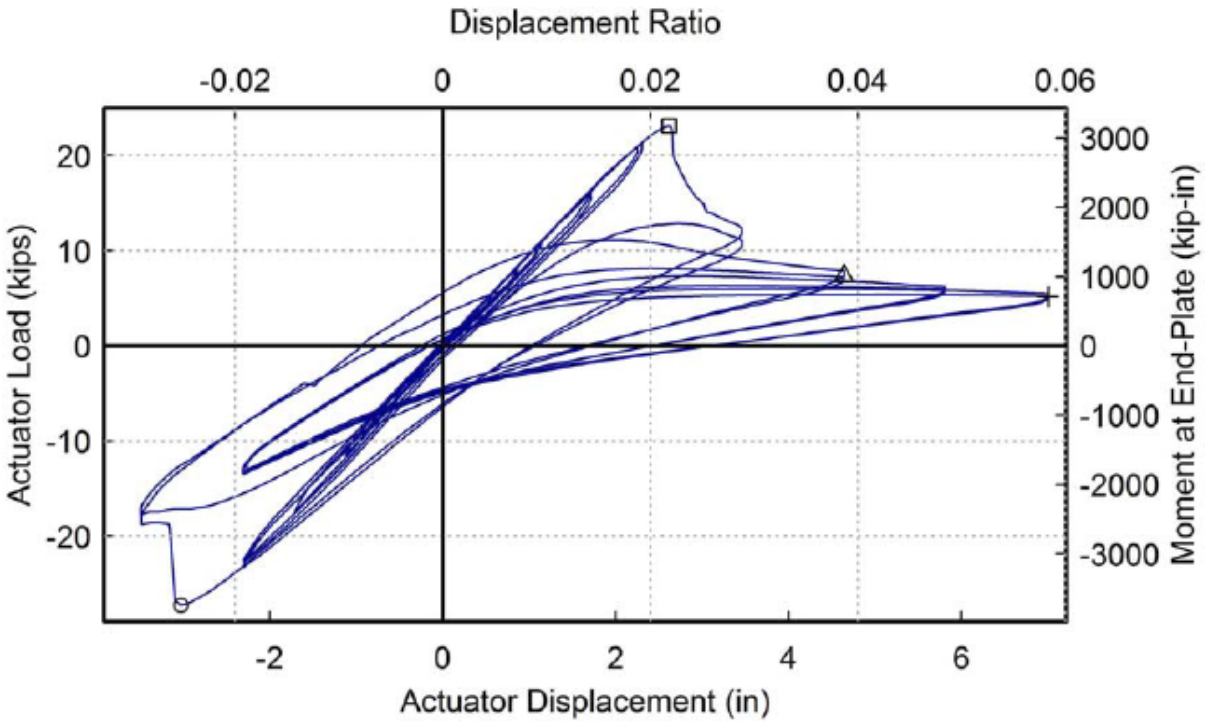

Figure 2-18. Global Response of Rafter undergoing Cyclic LTB (Smith 2013c)

These results help establish the fundamental component frame behavior after the critical segment has buckled. Research for this thesis uses these post-buckling characteristics described above to develop a custom LTB hinge that can be used in nonlinear dynamic analyses.

2.4.4 Approximate Fundamental Period Study for Metal Building Systems

Metal building engineers use the Equivalent Lateral Force (ELF) Procedure outlined in the *Minimum Design Loads for Buildings and Other Structures: ASCE/SEI 7-10* (ASCE/SEI 2010) for seismic design of metal building frames. One aspect of this procedure involves calculating the fundamental period of vibration, *T*, for initial design. The period equation in ASCE 7-10 uses a sample of multistory steel moment frame buildings. It is obvious that these structures are not comparable to low-rise metal building moment frames. New approximate period equations were

needed for metal building systems to improve the significant conservativism that comes with using the ASCE-7 period equations.

In order to develop new period equations, a sample of 192 metal building frames were generated by engineers at Metal Building Software, Inc. These frames were designed under a wide variety of geometric configurations, such as clear span length, eave height, and roof slope. Two levels for seismic hazard, snow load, and wind hazard were selected. Half of the models were designed with metal wall cladding (3psf) and the other half were designed with hard walls (75 psf). Also, half of the models were clear span metal building frames and the rest of the models had interior columns, or modular frames. A story drift of 2% was imposed for metal buildings with hard walls at the DBE level, per ASCE-7.

Smith (2013d) investigated the effect different panel zone models had on the fundamental period and lateral stiffness of metal building frames. Panel zones are composed of a web plate, column cap plate, column outer flange, and horizontal stiffeners. This element transfers moment and shear from the rafter into the column. It is recognized that the panel zone is not a rigid element in metal building frames. The accuracy of analytical models can be improved when this flexibility is taken into consideration. Figure 2.19 displays three panel zone modeling techniques. Any frame with a rigid panel zone model (Figure 2-19.c) overestimates the lateral stiffness of the frame and should be avoided. Metal building engineers often model panel zones using a centroidal extension method. Two elements with the cross-sectional properties of the ends of the columns and rafters are extended into the panel zone and connected at an intersection point (Figure 2-19b). This model does not capture the true kinematics of a panel zone. A proposed panel zone model (Figure 2-19a), similar to the “Revised Krawinkler Model” described by Charney and Marshall (2006), uses

two rigid links connected to a rotational spring at the corner of the panel zone. This modeling scheme captures the kinematics of a panel zone accurately.

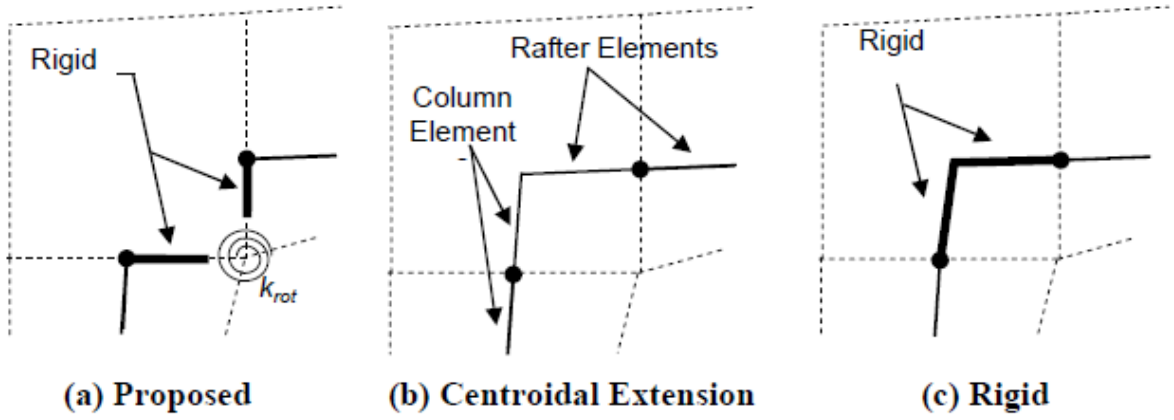

Figure 2-19. Panel Zone Modeling Schemes (Smith 2013d)

Smith calculated the rotational spring stiffness from a shell finite element model using Abaqus (Simulia 2016). Each model was composed of a prismatic column, prismatic rafter and panel zone plates (Figure 2-20). The length of the column and rafter had a length of three times the depth to mitigate stress concentrations from geometric and loading discontinuities. The flanges were discretized into 8 elements and the web into 20 elements. Nominal thicknesses were applied to the plates. Geometric and material nonlinearities were not considered in these models. The relative displacements at nodes A, B, and C were used to calculate the change in angle ABC, θ. The linear rotational spring stiffness was calculated by dividing the applied moment by the angle θ.

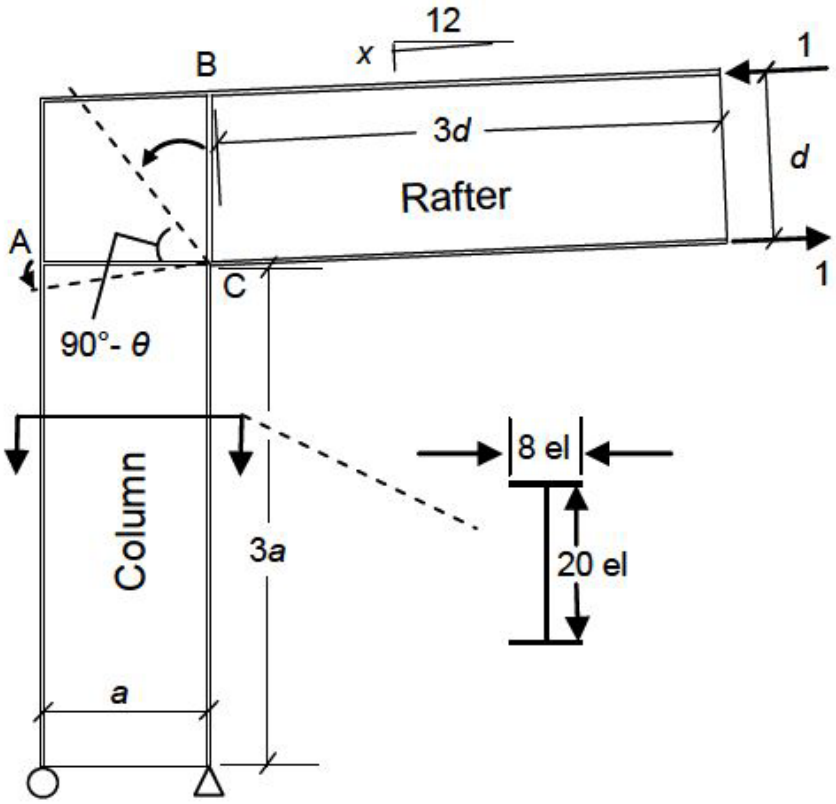

Figure 2-20. Panel Shell Element Model (Smith 2013d)

2.4.5 Conceptual Development of Metal Building Intermediate Moment Frame

Combining the findings from the cyclic tests by Hong with the shake table tests and the cyclic LTB tests by Smith lead to a conceptual development for the Metal Building Intermediate Moment Frame. The new seismic force resisting system for metal buildings with hard walls relies on LTB as the inelastic hinge. An unbraced length in the rafter, called the Controlling Segment, can be used as the structural fuse that will dissipate energy and protect the frame from excessive forces. The system will remain stable after the formation of one hinge because initially the system was indeterminate to the first degree. If a second hinge is allowed to form, a collapse mechanism will develop. To prevent this, a Capacity Design approach must be used for the frame outside of the controlling segment. Smith (2013d) proposed a displacement-based design procedure

requiring that the post-buckled frame not exceed any strength limit states at the MCE displacement demands. The life-safety at MCE intent of the seismic codes is to be satisfied by restricting the collapse mechanism from forming at the MCE, beyond DBE.

Research is currently underway to develop a new seismic force resisting system specific to metal building frames. One of the tasks in developing a new structural system involves a FEMA P695 study. A FEMA P695 study is a rigorous analytical study that is used to determine the collapse margin of a structural system (2009). In order to predict the actual collapse of a metal building, it became apparent that more sophisticated computer models would be needed. The finite element models would capture the inelastic behavior, residual stress, geometric imperfections, and nonlinear behavior beyond the first buckle. Figure 2-21 demonstrates how the cyclic lateral torsional buckling tests performed by Smith (2013) are being used to validate the computer models. The finite element model accurately predicted the location of the failure in the test rafter. The finite element models will not simulate collapse of the buildings, but closely match the exact behavior of the metal buildings on the shake table, up through the maximum considered earthquake (Shoemaker 2015).

Test of rafter showing the formation of lateral torsional buckle.

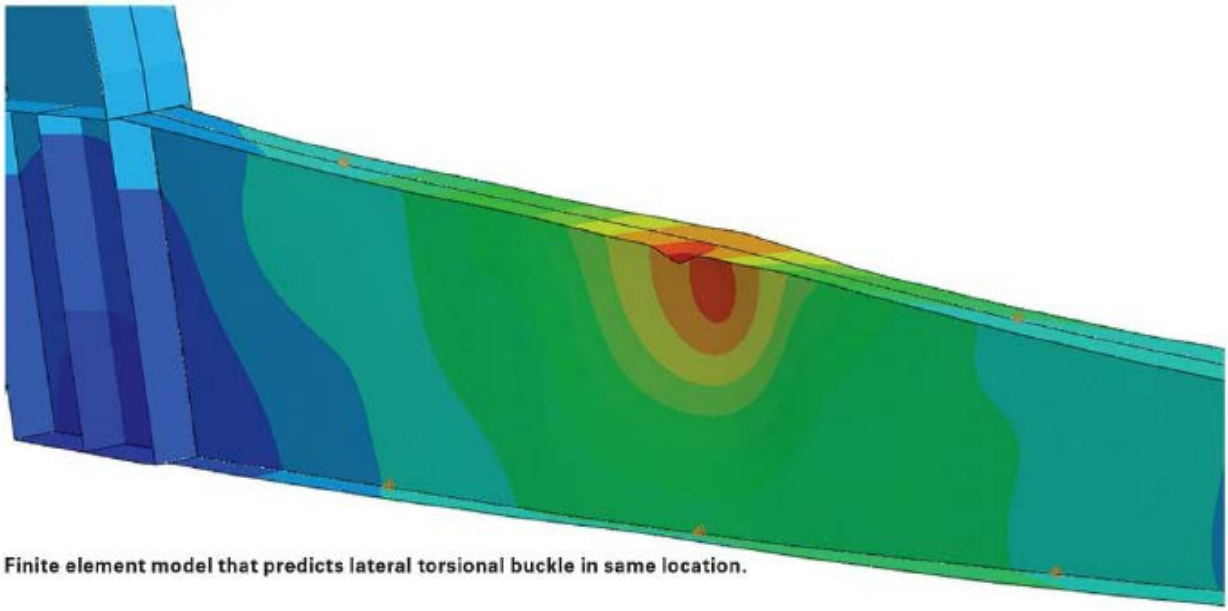

Finite element model that predicts lateral torsional buckle in same location.

Figure 2-21. Comparison of Cyclic Lateral Torsional Buckling Experiment and Finite Element Model (Shoemaker 2015)

All the research presented in this section was focused in the transverse moment frame direction. The shake table experiments were unidirectional, and because the shaking was in the moment frame direction, wall connections did not experience the loads in the in-plane horizontal direction they would have during a real seismic event.

2.5 Wall Connection Failures observed after Haiti and New Zealand Earthquakes

Post-earthquake reconnaissance has exposed a significant problem in the performance of metal building systems with hard walls. There exists a stiffness incompatibility between the stiff hard walls and the flexible steel frame. Brittle connections between these two elements can experience large force demands and can fail in a non-ductile manner.

Specifically, the reconnaissance of recent earthquakes in Port-au-Prince, Haiti in 2010 and Christchurch, New Zealand in 2011 highlighted the dangerous effect of poor connections between the steel frames and hard walls in metal building systems (Marshall and Gould 2012).

One prevalent type of failure that occurred with metal building systems in the 2010 Haiti earthquake was the detachment of non-structural masonry. Figure 2-22 shows an out-of-plane failure of a non-structural masonry wall. This wall collapse lead to a roof failure in the adjacent structure. The reconnaissance team found no evidence of wall ties connecting to the steel frame. Because of the absence of wall ties, it is not surprising that the wall failure occurred. The steel frame that carried the gravity and lateral load appeared undamaged (Eberhard et al. 2010).

Figure 2-22. Infill Masonry Wall Collapse of PEMB in Port-au-Prince (Eberhard et al. 2010)

The reconnaissance following the 2011 Christchurch earthquake identified that metal buildings systems with precast tilt-up wall panels had connections that were insufficient, causing the wall panels to fall away from the building. As seen in Figure 2-23, a wall segment has fallen away from a metal building system. For wall panels that did not collapse, the connections were so damaged that temporary shoring was required. As mentioned before, the fact that building codes for New Zealand and the United States are similar should be cause for alarm.

Figure 2-23. Loss of panel and temporary shoring of adjacent panel (Marshall and Gould 2012)

The research presented up to this point was focused primarily on the seismic behavior of the metal building moment frame. The one-dimensional shake table could only test the structure in the transverse moment frame direction. Therefore, the connections did not experience in-plane shear forces that would have been present during an actual earthquake event. Additionally, the connections between the wall panels and the steel frame were much more robust than typical connections. Due to the increased capacity of the connection and decrease in the force demand, the connections did not become damaged. The panels did not disengage as was seen in Christchurch, New Zealand.

2.6 Energy Dissipating Connections

The goal of the research presented in this dissertation is to allow the connections to be the primary energy dissipating elements in the longitudinal seismic force resisting system of metal buildings. Therefore, a background on energy dissipating connections is necessary.

2.6.1 Slotted-Bolted Friction Connections

A common energy dissipating connection is the slotted-bolted friction connection due to their simplicity and reliability. These connections consist of a plate with a long-slotted hole that is sandwiched between friction pads and the outer connecting members as seen in Figure 2-24.

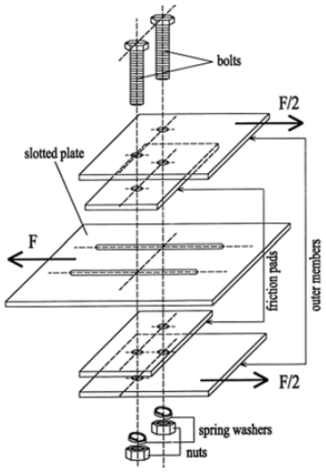

Figure 2-24. Typical Slotted-Bolted Friction Connection (Balendra et al. 2001)

High strength bolts are pretensioned to apply pressure to the contacting surfaces. When the force overcomes the static friction force developed in the connection, the plates slide relative to each other in a unidirectional fashion. The peak force necessary to induce motion is derived from coulomb friction and is shown in Equation 2-1, where Fs is the frictional force, Ntf is the bolt pretension, n is the number of bolts, μ is the coefficient of friction, and η is the number of slip planes (MacRae et.al. 2010). As the connection slides, seismic energy is dissipated in the form of heat. The hysteresis loops are generally rectangular in shape, which allows for large amounts of energy dissipation.

$$Fs = n \times \mu \times \eta \times Ntf \qquad \textbf{Equation 2-1}$$

Several disadvantages are present in these types of friction connections. The slotted-bolt must have a sufficient length so that the connection could not lock-up as shown in Figure 2-25. The additional forces due to bearing could overload the surrounding elements and lead to a brittle

failure. High contact pressures at the edge of the bolt holes can lead to significant thinning of the shims, which in turn reduce the tension in the bolt. Additionally, residual drifts could be significant following a seismic event.

Figure 2-25. Slotted-Bolted Friction Connection and Lock-up (Baird 2014)

2.6.2 Asymmetrical Friction Connections

Asymmetrical Friction Connections are a variation of the slotted bolted friction connection first proposed by Clifton (2005) that has been implemented in New Zealand. This connection gets its name from the eccentricity that exists between the slotted plate and the main connecting member. Figure 2-26 shows two possible configurations for steel brace utilizing an AFC.

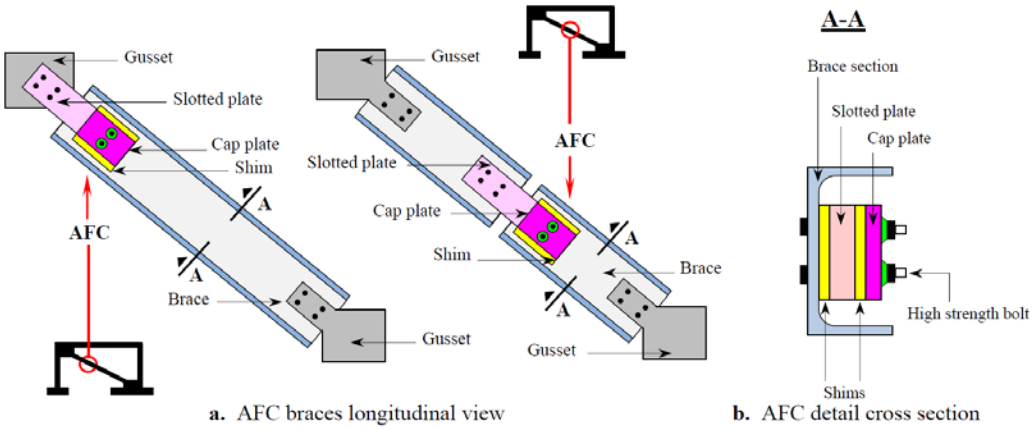

Figure 2-26. Braces with Asymmetrical Friction Connections (Golondrino 2014)

Several research tasks have been undertaken to optimize the performance of these connections. Steel shims that have a much higher hardness than the surrounding contacting elements yield a more reliable and consistent sliding force (Golondrino 2012). Maintaining the bolt pretension is imperative to prevent significant degradation in the stiffness of the connection (Ramhormozian 2014). Belleville spring washers help maintain the bolt pretension throughout the duration of sliding (Ramhormozian 2015).

2.6.3 Tapered Yielding Connections

Another means of dissipating earthquake energy is through inelastic deformation, or yielding, of flexural elements. Pinelli (1996) developed such a connection for precast concrete cladding panels. A flexible tapered tube element attaches the wall cladding to a stiff square tube as shown in Figure 2-27.

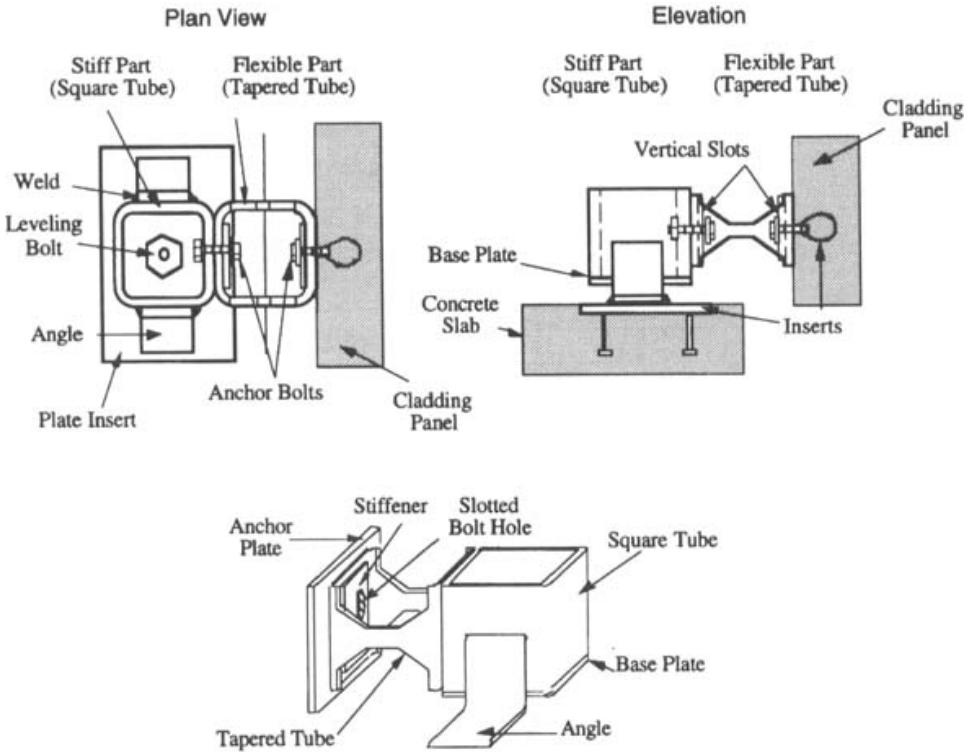

Figure 2-27. Tapered Yielding Connection (Pinelli 1996)

As the connection moves laterally, the tapered elements bend in double curvature. The shape is optimized to allow plastification to occur along all the cross sections of the tube. Stiffeners are added to the two ends to achieve a fixed rotational support. Pseudo-static cyclic component testing demonstrated that the hysteresis loops were large and stable with no apparent stiffness or degradation or strength loss behavior (Goodno 1998).

The experimental results were used to develop and calibrate analytical models of the connection in order to test the improvement in seismic performance. Nonlinear dynamic analyses were performed on a six-story moment frame structure with three bays clad with two heavy cladding panels per bay. Each panel was configured with two advanced tapered connections at the top and two bearing connections at the bottom. An energy-based design procedure was proposed to determine an appropriate yield strength and size of the connections. The results showed that the structure clad with the advanced tapered connections dissipated up to 70% of the input energy. For some earthquakes, the stiffening effect along with the added energy dissipation reduced story drifts up to 58% versus the bare clad structure (Pinelli 1995).

2.6.4 U-shaped Flexural Plates

The Christchurch, New Zealand earthquakes in 2010 highlighted the need for improved connections with precast panel cladding. Baird (2014) developed and tested a new U-shaped flexural plate connection to add energy dissipation capabilities to precast cladding, shown in Figure 2-28. Earthquake energy is dissipated through ductile yielding of the steel plate as the interior of the structure moves relative to the wall cladding. An HSS housing confines the movement of the flexural plate, which enhances the hysteretic behavior of the connection.

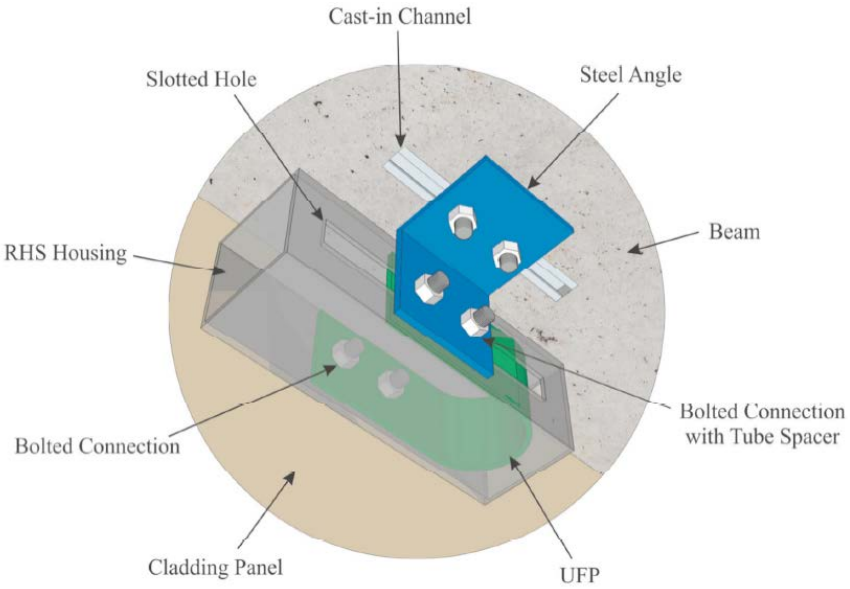

Figure 2-28. U-Shaped Flexural Plate Dissipator (Baird 2014)

A full-scale, one-bay, one-story system was tested in a pseudo-static fashion to assess the performance of the proposed connection. It was shown that the frame with the UFPs increases the lateral stiffness of the system while increasing the energy dissipation capacity, as shown in Figure 2-29. The connection showed no signs of fatigue, even after being tested to large drifts.

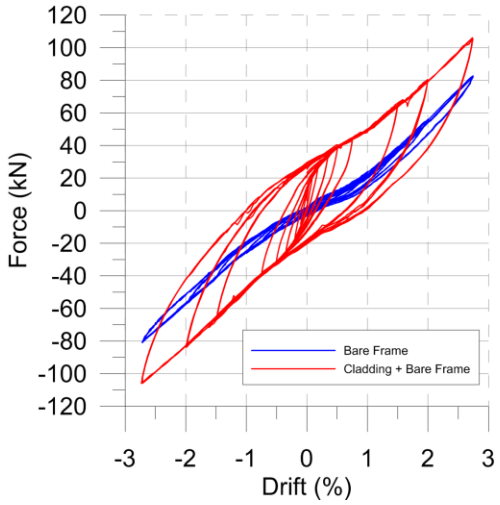

Figure 2-29. Force displacement behavior of test frame with and without cladding using UFP connections (Baird 2013)

Analytical models were developed for the UFP and validated with the experimental data. A 2-D numerical frame model of a 10-story concrete moment frame was tested using nonlinear dynamic earthquake analyses to investigate the seismic response of the structure utilizing the UFP connections. The results showed that the mean interstory drift was reduced by 25% compared with the bare frame model. The hysteretic energy of the structure was reduced and instead consumed by the UFP connections. The new system exhibited great potential by limiting maximum displacements in the structure and reducing potential damage to non-structural components (Baird 2013).

2.6.5 Rotational Friction Damper

A recent development in energy dissipating dampers has been the rotational friction damper. Unlike slotted-bolted friction connections, the rotational friction damper dissipates energy through contact surfaces that rotate about an axis, as opposed to surfaces the translate through unidirectional motion. This damper consists of a high strength bolt that pretensions a rotating central plate sandwiched between two friction pads and two side plates as shown in Figure 2-30.

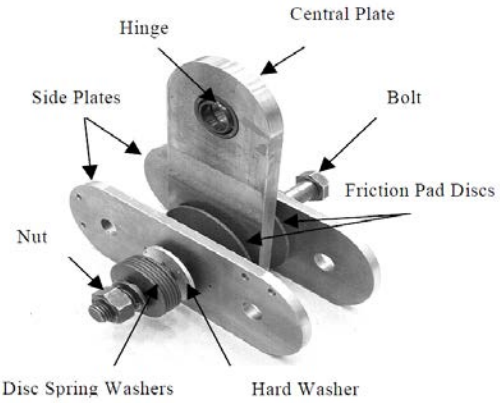

Figure 2-30. Rotational Friction Damper Details (Mualla 2000)

Dynamic tests on a scale model have shown that the hysteresis loops are stable without any degradation in the friction force (Mualla 2000). A 3-story steel frame was constructed and tested on a shake table shown in Figure 2-31. The frame was tested with the rotational friction damper and compared with the bare structural frame. Several scaled earthquake records with peak ground accelerations up to 0.3g were utilized. The results showed that the test frame with these dampers showed a 70% decrease in the peak story drifts vs a frame without the damper (Mualla 2002). This reduction is significant considering that most nonstructural damage is drift sensitive. Damage and business interruption following a major earthquake can be greatly reduced for structures utilizing rotational friction dampers.

Figure 2-31. Three-story steel structure equipped with Rotational Friction Dampers (Mualla 2002)

2.7 Conclusions

As a result of the recent earthquakes in Haiti and New Zealand, it has been shown that metal building systems clad in hard walls are not satisfying the "life-safety" requirement of the modern seismic codes. The post-earthquake reconnaissance was conclusive that the connections between hard walls and the steel frame are susceptible to brittle failure. Most seismic research for metal building systems has been focused on the development of a new structural system in the transverse moment frame direction, while the longitudinal direction of metal building systems has received little to no attention. There is a need to investigate the longitudinal seismic performance of metal building systems clad with hard walls.

The components of a typical metal building system were described and illustrated, which included a background into transverse moment frame, hard wall cladding, connections, and connection failures. Several energy dissipating connections for other structures were discussed, but these connections have yet to be incorporated in metal building systems. The research presented in this dissertation seeks to provide insight into the seismic performance of metal building systems, and develop energy dissipating connections for metal building systems clad in hard walls.

Chapter 3 Conceptual Development of the Rotational Friction Connection and Finite Element Model Development

3.1 Introduction

This chapter introduces the rationale for a new low-damage friction connection for use as a ductile fuse element between hard walls and steel frames in metal building systems. The essential requirements for the connection are detailed. Various energy dissipating connections were considered and evaluated for their suitability in metal building systems. A rotational friction connection was developed and experimentally tested. Fundamental mechanics of the rotational friction connection are derived through equilibrium and mechanics of materials. 3-D solid finite element models are developed and validated with experimental data. A parametric study was performed using the validated model to investigate the effects of various geometric parameters on the force-displacement behavior of the connection.

3.2 Essential Requirements for Connections

According to ASCE 7 (ASCE/SEI 2016), metal building systems that incorporate hard walls in Seismic Design Category D currently have two types of seismic force resisting systems that can be utilized in the longitudinal direction. They are the systems that utilize the hard wall as the ductile fuse element, and systems that do not use the hard wall as the primary lateral force resisting system. The selection of the seismic force resisting system determines whether the wall is designed as a structural element or a nonstructural element. The differential stiffness between the flexible metal building system and the stiff hard walls creates a stiffness incompatibility.

Careful attention must be paid to the connections between these two elements. They must be designed in a manner that is consistent with the function of the chosen seismic force resisting system.

When a precast concrete panel or a masonry wall is being used as the seismic force resisting system, the wall must satisfy the design and detailing requirements of an intermediate precast shear wall or a special reinforced masonry shear wall. For the wall system to act as the ductile fuse element, the connections between the metal building frame and the wall system must be designed with overstrength to satisfy capacity design requirements. As a result, the wall system absorbs the seismic input energy through significant cracking of the concrete and yielding of the steel reinforcement. Costly repairs or replacement of the wall would be necessary after such a seismic event.

The other option would be to isolate the wall system from the metal building frame. An example of this seismic force resisting system would be an ordinary steel concentrically braced frame or an ordinary steel moment frame. All wall connections must allow for sufficient in-plane displacement capacity to prevent the wall from resisting the seismic load from the rest of the structure. Otherwise, the wall system could experience much larger forces than it could handle, resulting in significant damage to the wall.

Instead of rigid connections or isolating connection, a new seismic force resisting system can take advantage of the differential stiffness between the hard walls and steel frames by forcing the ductile fuse element to be the connections themselves. In addition to being the ductile fuse element, a suitable resilient connection is one that is low-damage, meaning that repairs or replacement following an earthquake would not be required. The new structural system is aimed at introducing energy dissipating characteristics in the in-plane horizontal direction of the wall.

One of the challenges of these connections is the ability to maintain out-of-plane strength, to avoid losing a critical load path for wall stability.

The next task was to investigate currently available energy dissipating connection that could possibly satisfy these requirements.

3.3 Selection of an Energy Dissipation Mechanism

Simple, economic energy dissipating connections are of two primary types: steel yielding and sliding friction. Both have their advantages and can be constructed economically, and thus were considered as candidates for the ductile fuse element between the steel frame and hard wall. However, the frame-to-wall connection demands in hard wall metal building systems present unique challenges to these energy dissipating connections.

3.3.1 Yielding Tapered Connections

Yielding taper connections were shown to provide significant reductions in peak displacement demand (Pinelli 1995). Figure 3-1 displays a prototype of such a connection in metal building systems. These connections were used in single-story precast concrete cladding panels that are typically 10-12 feet in height. But, concrete panel heights used in metal building systems can be up to 35 feet in high seismic zones (ASCE/SEI 2016). The deformation demand on the connections of the taller wall panels is higher for a given percent story drift. A tapered yielding connection used in metal building systems might not have the required deformation capacity necessary to achieve this story drift limit.

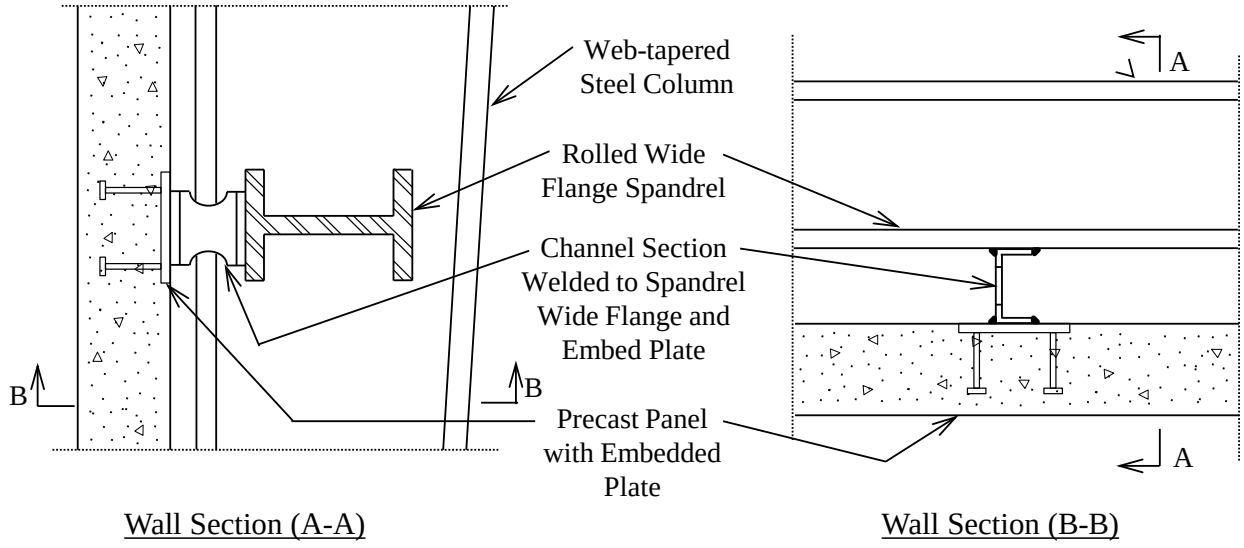

Figure 3-1. Prototype Tapered Yielding Connection in Metal Building System Hard Walls

Another challenge for the frame-to-wall connections is the presence of simultaneous out-of-plane forces and deformation demands during seismic events. The yielding connections are typically designed with a unidirectional displacement demand. The out-of-plane forces from the hard wall panels would most likely cause excessive strain in the steel material of the tapered plates. This could result in a premature fracture of the connection. Additionally, all the yielded tapered tube sections would have to be replaced following a seismic event.

Also, the required tolerances for this type of connection make their use unfeasible in metal building systems. The fabrication of the tapered steel element was expected to be challenging and costly for that type of an element. For these reasons, the use of yielding tapered connections in metal building systems with hard walls was discarded for use in this research.

3.3.2 Tie-back rods

Tie-back rods are another example of a yielding connection. As the structure displaces, the energy is dissipated a through the development of plastic hinges at the two ends of the rod as

seen in Figure 3-2. Tie-back rods have several drawbacks including that any yielded rod will require replacement following a seismic event. These rods are also susceptible to low-cycle fatigue (Rihal 1989). During Baird's (2014) cyclic testing, the threaded rods developed cracks, as seen in Figure 3-3. This lead to a reduction in its tensile capacity and ruptured the rod. The simultaneous out-of-plane forces and in-plane horizontal displacements that exist in the metal building system wall connections could potentially exceed the fracture strain in the plastic hinges and lead to rupture of the rod. For these reasons, tieback rods were discarded as a viable option for a hard wall connection in metal building system.

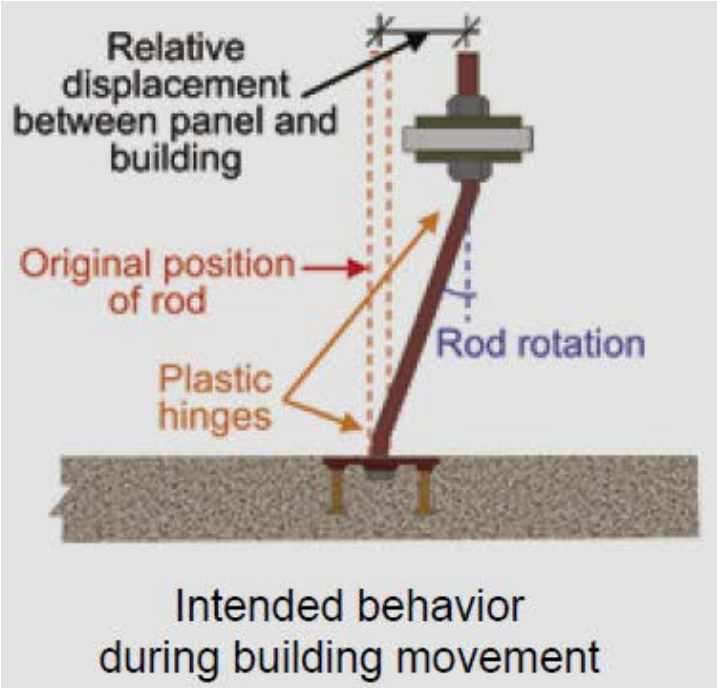

Figure 3-2. Tie-Back Rod Yielding Connection (Pantoli 2016)

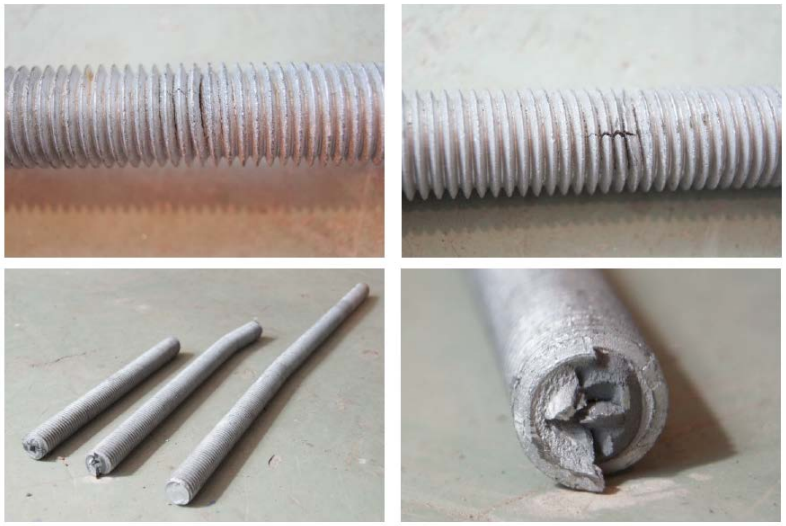

Figure 3-3. Parallel cracks (top left), perpendicular cracks (top right) and rupture (bottom left and bottom right) of long threaded rods (Baird 2014)

3.3.3 Slotted-bolted Friction Connection

A third consideration was the slotted-bolted friction connection. As mentioned in the Literature Review, these relatively simple connections can dissipate large amounts of seismic energy through heat generated by the sliding of steel plates. Slotted-bolted friction connections are designed and perform optimally when subjected to a unidirectional force condition. The predictability and reliability of the slip force depends on the applied bolt tension and coefficient of friction.

High contact pressure can cause galling in and around the slotted-hole and reduce the effectiveness of the connection (Baird 2014). Additionally, slotted-bolted friction connections are susceptible to lock-up when the bolt encounters the end of the slotted hole as shown in Figure 3-4.

Figure 3-4. Slotted-Bolted Friction Connection and Lock-up (Baird 2014)

One possible configuration for slotted-bolted friction connections for use in metal building systems between the frame-to-wall connections is shown in Figure 3-5. In this configuration, the anchor bolt serves two functions: to develop a clamping force for the slotted-bolted friction connection and to transfer the out-of-plane force from the wall to the metal building frame. During a seismic event, the out-of-plane force would be dynamic, which in turn changes the slip force required for the connection to slide in the in-plane horizontal direction. The combination of out-of-plane force and in-plane horizontal shear force acting on the anchor bolt could potentially exceed the capacity of the anchor system.

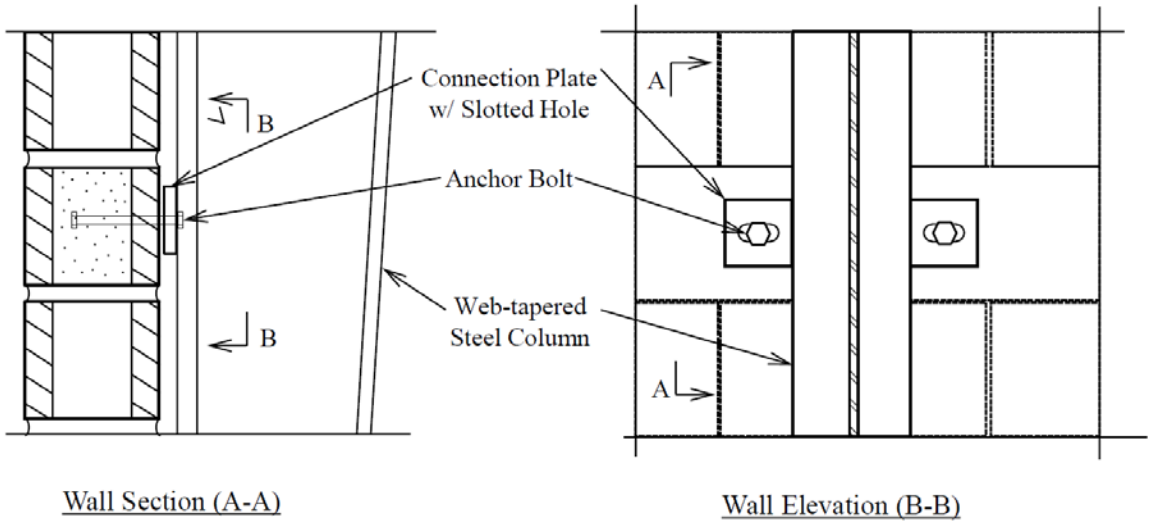

Figure 3-5. Steel Column to Masonry Wall Connection with Long Slotted Holes

The frame-to-wall connections in metal building systems must be able to slip predictably and reliably. The bidirectional demands on slotted-bolted connections reduces the essential predictability and reliability of the slip force. For this reason, the slotted-bolted connection was discarded as a viable option as the ductile fuse element between hard walls and steel frames.

After review of the connections that have already been developed, it was evident that they would not solve the stiffness incompatibility that exists between the flexible steel frame of the metal building system and the hard walls. A new energy dissipating connection needed to be developed that would be ductile in the in-plane horizontal direction, while maintaining out-of-plane capacity.

3.4 Development of a Rotational Friction Connection

The rotational friction connection (RFC) developed in this research is a new approach for connecting the incompatible hard walls and metal building systems and aims to provide the capability for increased energy dissipating and allowing for large displacements between these two elements. The initial inspiration for the new connection began with the investigation of a successful damper developed by Mualla (2000), as shown in Figure 3-6. Mualla's device consisted of three steel plates rotating against each other in opposite directions. Between the steel plates were two circular nonasbestos organic friction pads that provide enhanced performance through a stable friction force and non-degrading hysteretic behavior. Experimental full-scale shake table testing of a steel frame using this damper showed a remarkable reduction of peak interstory drifts by 70-80% (Mualla 2002). This successful application of rotational friction as a means of energy

dissipation and improved seismic performance were attractive characteristics that could be used in metal building systems with hard walls.

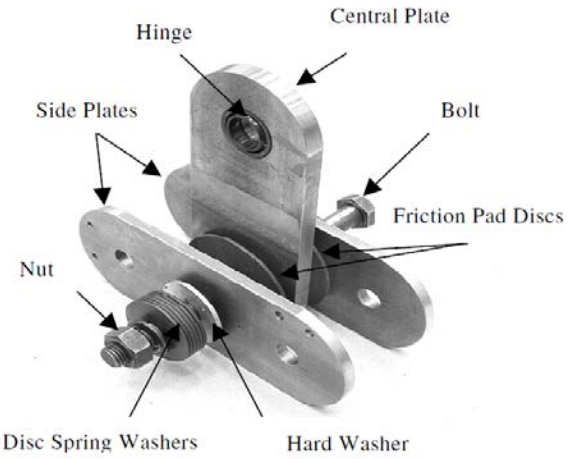

Figure 3-6. Details of the Friction Damper Device (Mualla 2000)

Additionally, research into improving the sliding performance of slotted-bolted friction connections played a role in the development of the new rotational friction connection. Golondrino (2012) showed that the stability of hysteresis loops of slotted-bolted friction connections can be improved by using steel shims with a high Brinell hardness. The use of hardened structural washers can reduce the complexity of the connection, thus the cost of the new connection can be reduced without sacrificing structural performance.

The connection developed in this research relies on rotational friction as the energy dissipating mechanism. The RFC is composed of standard steel components that allow for an economical option for connecting hard walls to metal building frames. A prototype of the rotational friction connection is shown in Figure 3-7. The connection consists of two steel angle sections. A steel strut connects the spandrel beam with the angle sections and acts as the moment arm. The use of nonasbestos organic circular pads, as in Mualla (2002) damper would significantly increase the cost of this connection. As a substitute for the friction pads, two standard hardened structural washers sit between the angle sections and strut. The washers provide a high differential

material hardness, which has been shown to enhance the hysteretic stability of friction surfaces (Golondrino 2012). According to the ASTM F3125 (2015) which governs structural washers, the Brinell hardness must be between 358 and 635. The angle sections and strut are composed of A572 Grade 50 steel, which has an approximate Brinell hardness of 131 (PGI 2016). The difference in hardness is a lower bound value of 227 and an upper bound value of 504.

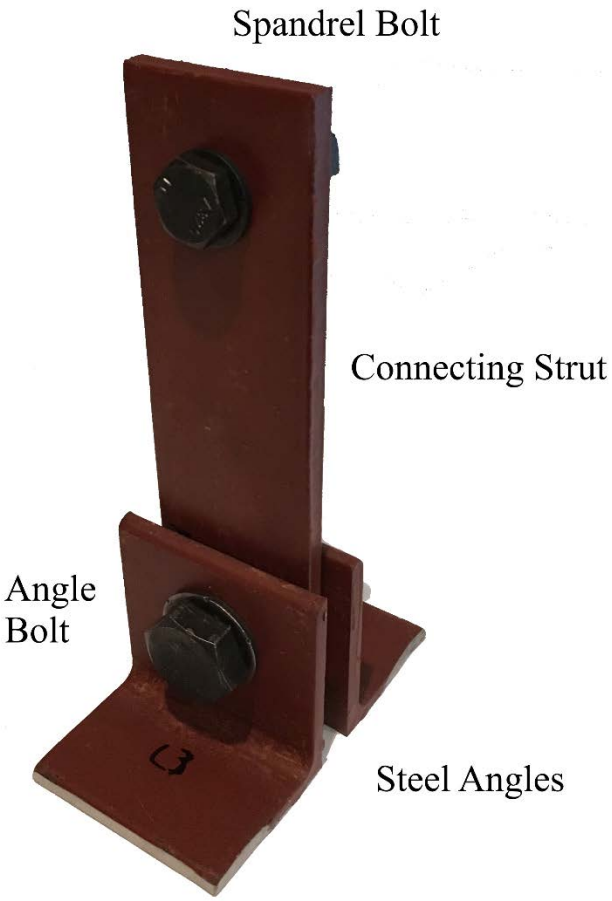

Figure 3-7. Prototype of Rotational Friction Connection

The reliability and the predictability of the slip force of the rotational friction connection can be improved by having a well-defined contact surface. There would be uncertainty in the total area in contact if the steel strut could press up against the steel angles. The addition of the washers provides a well-defined annular contact surface that can be calculated using the geometry. Figure 3-8 shows the hardened washers installed between the steel strut and angle sections.

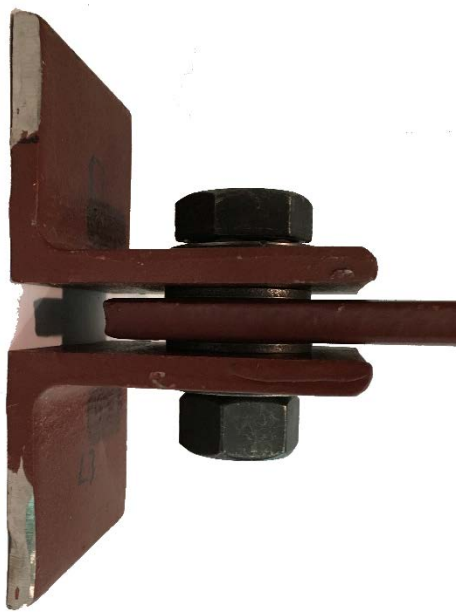

Figure 3-8. Hardened Structural Washers sandwiched between Steel Angles and Strut

Standard A325 structural bolts are used to apply contact pressure on the rotating surfaces. During the bolt installation process, the tension in the bolts can be controlled by using direct-tension indicator washers. The contact surfaces develop circumferential shear stresses around the bolt holes. One advantage of the RFC is that the contact pressure due to the bolt load is lower versus the slotted-bolted friction connection. A higher pressure can cause galling in around the slotted-hole and reduce the effectiveness of the connection (Baird 2014). Additionally, slotted-bolted friction connections are susceptible to lock-up when the bolt encounters and end of the slotted hole as shown in Figure 3-3. The RFC has a high displacement/rotational capacity that can be increased by adjusting the length of the steel strut. In the event of an earthquake, the RFC will slip at a prescribed force that depends on the bolt tension, friction coefficient, and strut length. Once that force is reach, the steel strut can rotate about the angle bolt and dissipate seismic energy. Unlike slotted-bolted friction connections, a primary characteristic of the RFC is that the energy dissipating mechanism is decoupled from the presence of out-of-plane forces. For a given displacement cycle, the same amount of frictional energy is dissipated no matter if there is an out-

of-plane force present. This is a significant advantage over slotted-bolted friction connections, which does not have this feature.

This connection is located between the external concrete cladding panel and the spandrel beam of the metal building frame. The steel angles are welded directly to an embed plate. Figure 3-8 shows a typical metal building frame with an external hard wall and highlights the location of the connections which is typically near the top of the wall along the eave for a full height wall. Figure 3-9 shows a profile and plan view of the rotational friction connection as it would be installed in a metal building system. By utilizing this new connection as the ductile fuse element in the longitudinal direction of metal building systems, the connections will slip during an earthquake event and damage to the wall elements can be precluded.

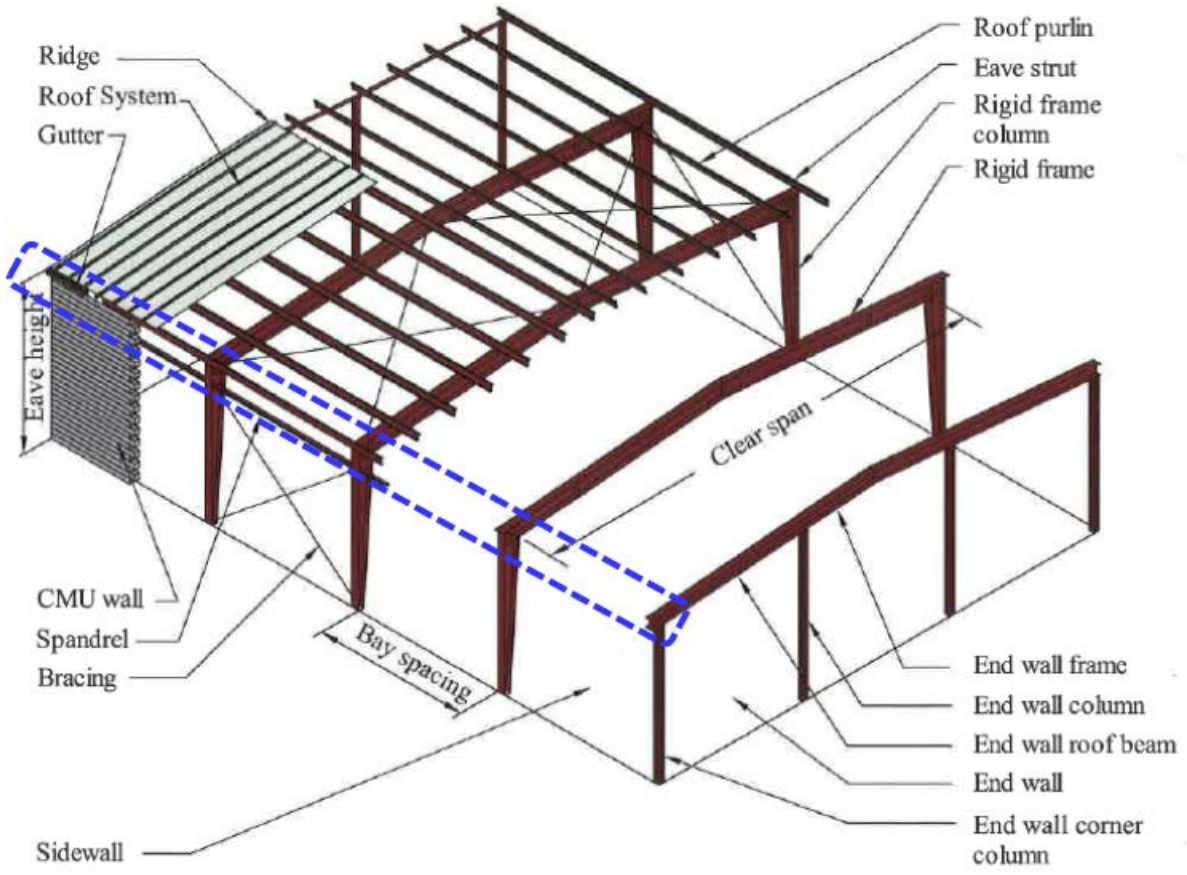

Figure 3-9. Typical Metal Building Frame with Hard Wall

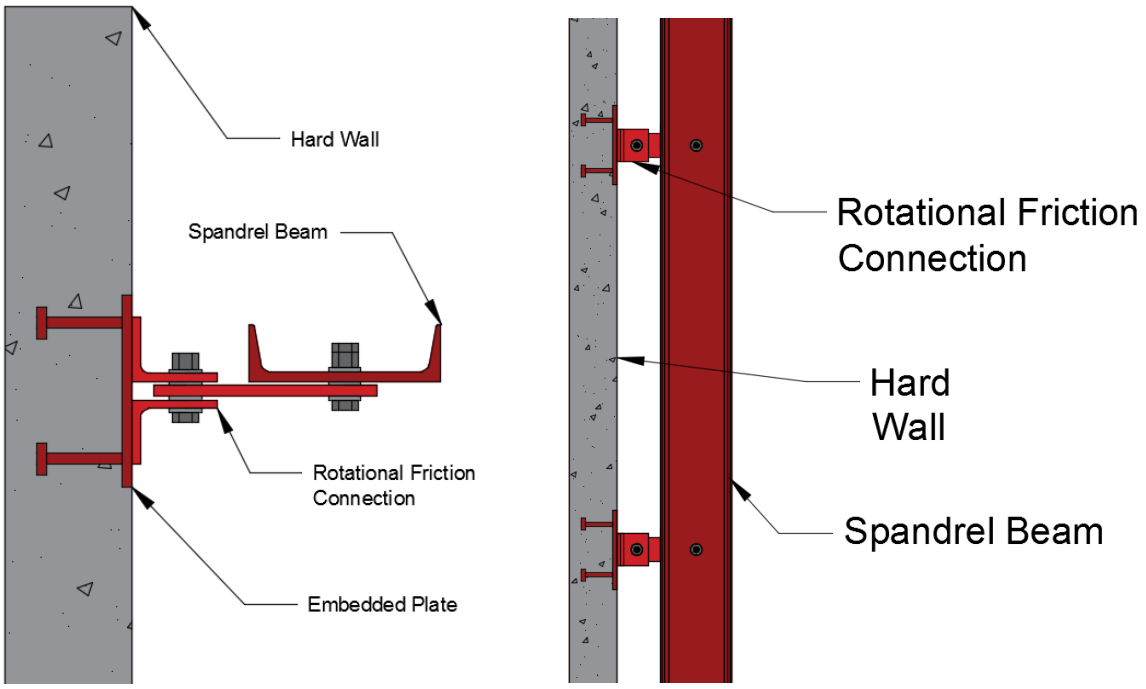

Figure 3-10. Profile (left) View and Plan (right) View of Rotational Friction Connection Assembly

3.5 Theoretical Equations

3.5.1 Derivation of Free Rotation Moment and Free Rotation Force

By using mechanics of materials, a theoretical equation for the initial slip moment or free rotation moment can be derived. These theoretical equations were used to verify the accuracy of the numerical models. The contact surface between the steel and the hardened structural washer is an annulus with an inner radius of r_i and an outer radius of r_o. The bolt applies a normal stress that varies with the radial distance as shown in Figure 3-10. The normal stress is highest at the inner radius and decreases toward the outer radius.

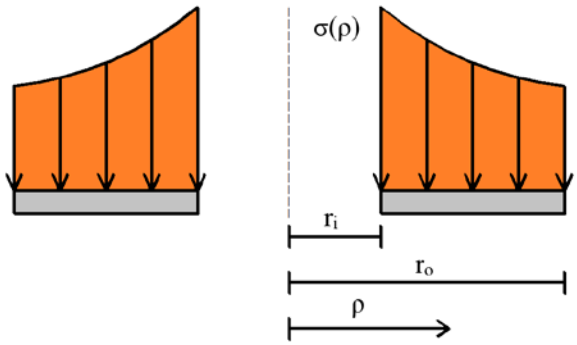

Figure 3-11. Normal Stress Distribution Applied to Washer

According to Coulomb friction, the shear stress that the surface can develop prior to slip is equal to the product of the normal stress and the coefficient of static friction.

$$\tau(\rho) = \mu\, \sigma(\rho) \qquad \textbf{Equation 3-1}$$

Where,

τ = Shear stress

ρ = Radial distance

μ = Coefficient of static friction

The free-rotation moment can be calculated by summing the differential circumferential area that the shear stress acts from the inner radius to the outer radius as shown in Figure 3-11 below. The sequence of equations is shown below.

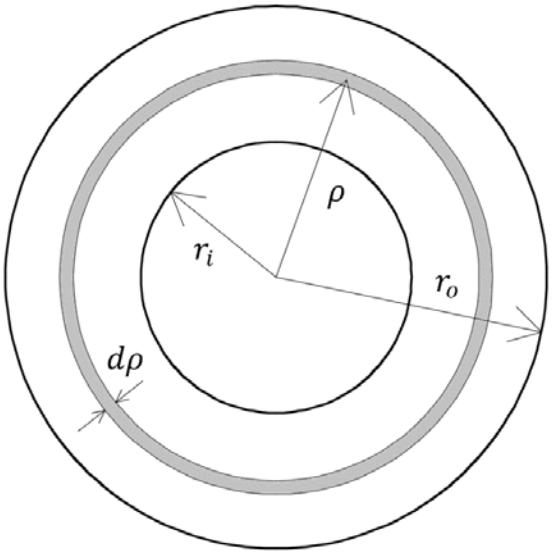

Figure 3-12. Differential Circumference

$$M_{FR} = \int \rho\, \tau(\rho)\, dA \qquad \textbf{Equation 3-2.}$$

Where

M_{FR} = Free-rotation moment

ρ = Radial distance

τ = Shear stress

dA = Differential area

By substituting the differential area with the circumference,

$$M_{FR} = 2\pi \int_{r_i}^{r_o} \rho^2\, \tau(\rho)\; d\rho \qquad \textbf{Equation 3-3.}$$

By substituting equation 3-1 into equation 3-2,

$$M_{FR} = 2\pi\mu \int_{r_i}^{r_o} \rho^2\, \sigma(\rho)\; d\rho \qquad \textbf{Equation 3-4.}$$

It is recognized that the normal stress is highest at the inner radius and decreases toward the outer radius. By not knowing the true distribution of the normal stress, the normal stress equation is simplified by assuming that the normal stress distribution is uniform across the entire contacting surfaces. This assumption is verified later in this chapter. By evaluating the integral

from the inside radius to the outside radius, the moment capacity of the RFC becomes Equation 3-5.

$$M_{FR} = \frac{2\mu n N(r_o^3 - r_i^3)}{3(r_o^2 - r_i^2)}$$ **Equation 3-5.**

where

M_{FR} = Free-rotation moment

μ = Effective coefficient of friction

n = Number of shear planes

N = Mean bolt pretension

r_o = Outer radius of washer

r_i = Inner radius of washer

By substituting the moment equilibrium equation, force times the moment arm length, the free-rotation force of the connection becomes Equation 3-6.

$$F_{FR} = \frac{2\mu n N(r_o^3 - r_i^3)}{3L(r_o^2 - r_i^2)}$$ **Equation 3-6.**

where

F_{FR} = Free-rotation force

L = Center-to-center distance between the bolts

3.5.2 Force-Rotation Curves for RFC

The connection will not slip until the free-rotation moment is reached. Once that occurs, the connection begins to rotate about the angle bolt axis while maintaining the free-rotation moment. The sliding friction coefficient is assumed to be the same as the static friction coefficient. The validity of the assumption will be investigated in the experimental phase. This behavior is

commonly referred to as elastic-perfectly-plastic behavior. The force-displacement curves can be computed analytically by applying equilibrium principles to the rigid body assembly shown in Figure 3-12.

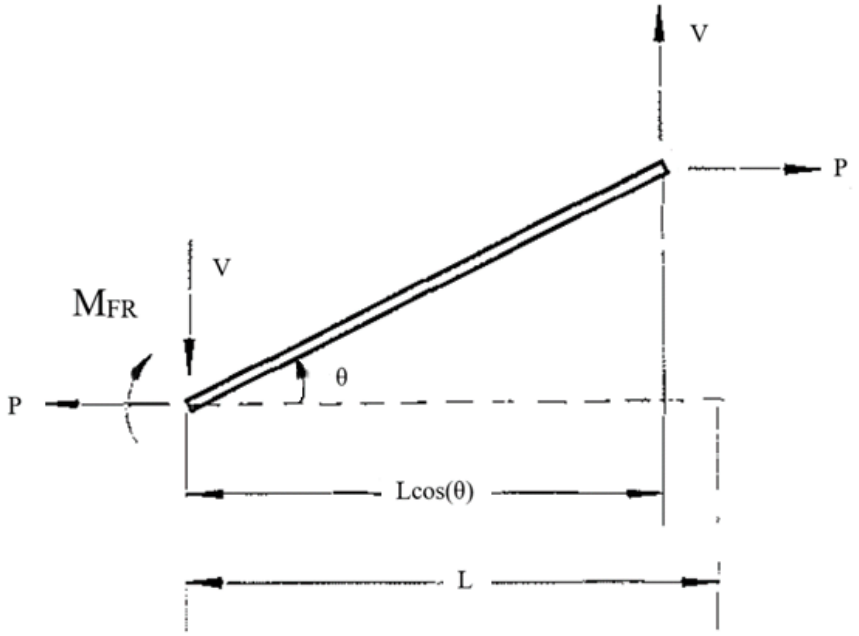

Figure 3-13. Large-Displacement Rigid Body Assembly for RFC rotating Clockwise

The contact surface near the angle bolt is represented with a rigid-perfectly plastic rotational spring with a capacity M_{FR}. An idealized hinge condition is assumed at the location of the spandrel bolt. The rigid bar represents the steel strut that has a length L equal to the center-to-center distance between the bolts. It is imperative to consider the presence of an out-of-plane load for any connection between the hard wall and steel frame of a metal building system. During an earthquake, the connections will inevitably be subjected to simultaneous horizontal force demands and out-of-plane force demands. Two forces are applied at the tip of the rigid bar. The out-of-plane load is P, with tension being positive, and the in-plane shear load is V. In this system, the counterclockwise direction is assigned as positive rotation. In order to calculate the force-rotation curves, a governing equation can be derived by using moment equilibrium in the deformed

configuration. Solving for V, the in-plane shear force equation for the system rotating clockwise is shown in Equation 3-7. The counterclockwise rotating in-plane shear force is shown in Equation 3-8.

$$V^{CW} = \frac{-M_{FR}+PLsin(\theta)}{Lcos(\theta)}$$ **Equation 3-7**

$$V^{CCW} = \frac{M_{FR}+PLsin(\theta)}{Lcos(\theta)}$$ **Equation 3-8**

Figure 3-13 shows normalized force-rotation curves for a range of rotations theta = -0.5 radians to 0.5 radians. The three magnitudes of out-of-plane force are zero, 10, and -10. There are two sets of curves that represent the connection rotating in a clockwise and a counterclockwise manner as well as both a positive and negative axial force.

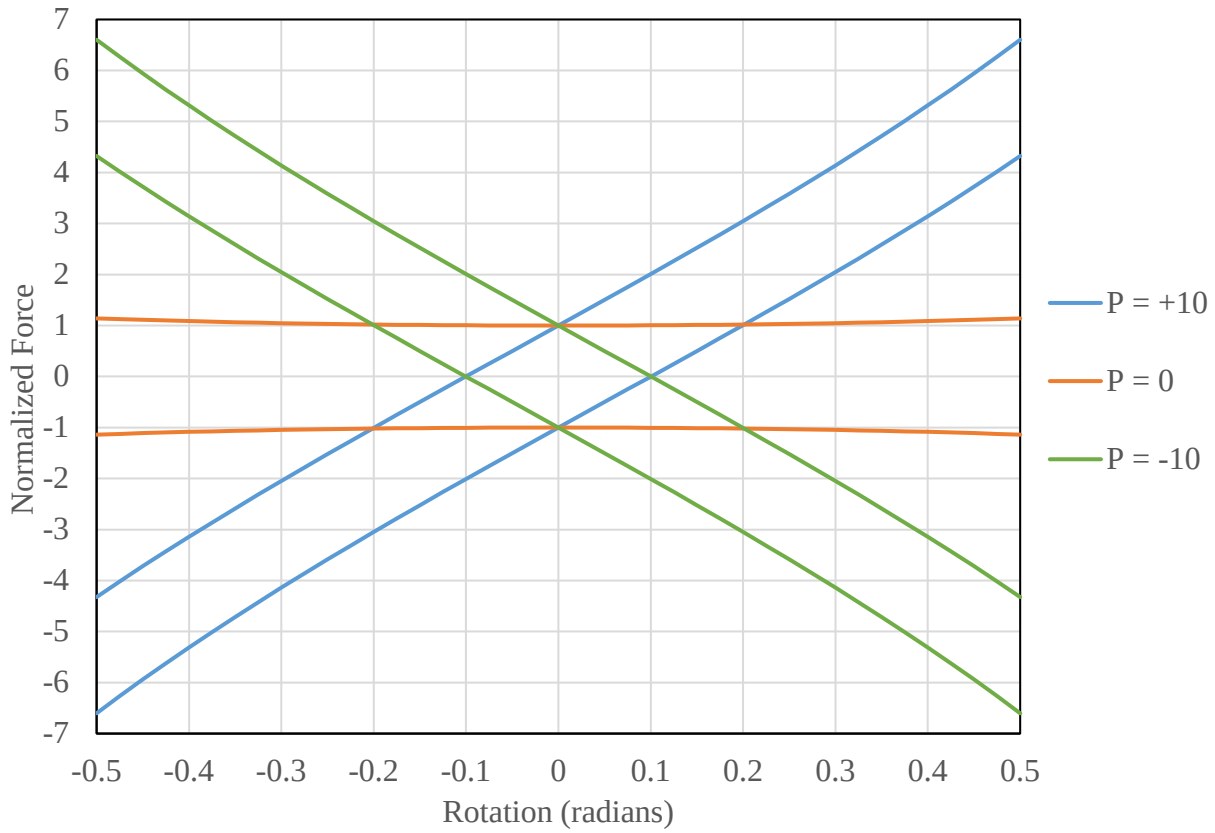

Figure 3-14. RFC Force-Displacement Envelopes considering P-Delta Effects

The force-rotation envelopes show that the P-Delta effects are significant and cannot be ignored. The out-of-plane force generates a geometric stiffness in the connection that is positive under a tensile out-of-plane load and negative under a compressive out-of-plane load. Within the range of -0.5 to 0.5 radians, the geometric stiffness is nearly linear with a slope of P/L. A maximum rotation of ±0.5 radians has been set as peak rotation performance goal for the rotational friction connection.

It is apparent that the horizontal shear force demand on the anchorage system is coupled with the out-of-plane force. During a seismic event, the rotational friction connection will be subjected to simultaneous in-plane and out-of-plane loads. The P-Delta effects will generate additional loads that must be resisted by the anchorage system.

One important feature of the rotational friction connection is that the energy dissipating capabilities are uncoupled with the out-of-plane forces. No matter the magnitude of the out-of-plane force, the same amount of energy will be dissipated for a given displacement cycle. This is a significant advantage over other energy dissipating connections like tie-back rod connections that rely on the formation of plastic hinges to dissipate energy. The axial-moment interaction in tie-back rods causes additional strain demands that could compromise the ductility of the connection. Additionally, if the strain at the extreme fiber reaches the rupture strain, the wall panel would lose a crucial load path. Because the RFC relies on friction to dissipate energy, lack of ductility should not be an issue.

3.6 Experimental Component Level Testing of RFC

Prototypes of the rotational friction connection were tested in Auburn University's Structural Research Laboratory. The objectives of the experiment were to determine the

connection stiffness, reliability of the elastic limit, and the ability to deform in a ductile fashion. The test data collected was used to validate finite element models of the connection. One of the challenges with rotational friction connection is the reliability of the friction connection and maintaining the bolt tension. In addition to the in-plane performance, out-of-plane strength was tested to ensure that the capacity is not significantly degraded by the large in-plane ductility demands. The data from these tests were used to calibrate the solid finite element models in Abaqus (Simulia 2016). The solid models were then used to generate component models for use in SAP2000. A summary of the testing and results is presented here. For more details about the experimental procedure, see "Experimental Testing of a Rotational Friction Connection for Use with Precast Concrete Cladding Panels in Metal Building Systems" (Sellers 2017).

3.6.1 Experimental Setup

The rotational friction connections tested using two identical precast concrete panels with a 28-day compressive strength of 5000 psi. Each panel was 90 in. x 42 in. x 6 in. and was post-tensioned to the strong floor. The panels were designed with three A36 steel embed plates measuring 10 in. x 12 in. x 5/8 in. The steel angles of the rotational friction connection were welded to each of the panels. The experimental setup is shown in Figure 3-16. The center (B and C) and right (D and E) embed plates had two connections installed to allow for additional test specimens as seen in Figure 3-14.

Figure 3-15. Experimental Setup for RFC Component Testing

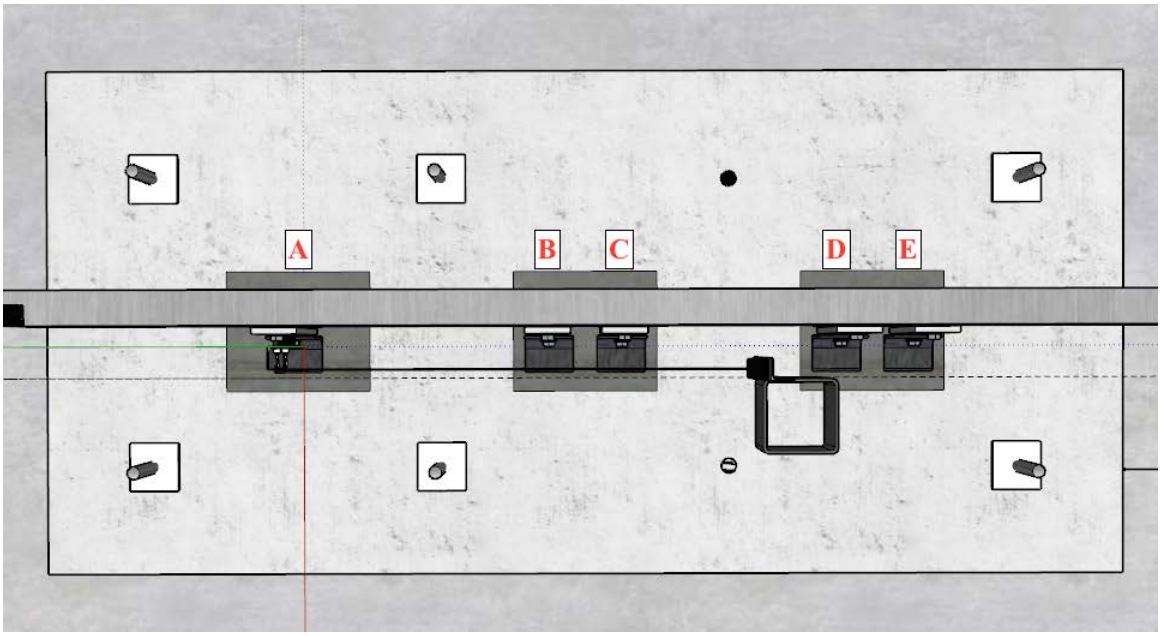

Figure 3-16. Plan View of Test Panel with Locations of Connections Tested (Sellers 2017)

Two hydraulic actuators were used in testing, one for applying in-plane horizontal direction and one for the out-of-plane direction. The horizontal actuator was attached to a reaction block which was post-tensioned to the strong floor. The vertical actuator was connected to an overhead steel frame to apply out-of-plane force to the connection at Location A. The C9x20 steel spandrel

beam was connected to the end of the horizontal actuator and bolted to the strut of the rotational friction connections.

3.6.2 Surface Preparation

The steel angles and struts of the RFC needed to have the paint removed prior to installation. The Society on Protective Coatings (2016) defines Surface Preparation 3 as a power tool cleaning. The tools that can be used are power sanders, wire brushes, power chipping hammers, abrasive grinding wheels, or needle guns. AISC Steel Specification (2016a) defines a Class A surface as an unpainted clean mill scale steel surface or surfaces. The faying surfaces would be expected to achieve a friction coefficient of 0.30. However, the Class A surface detail is for steel-on-steel contact. For the RFC, rotating plies are steel-on-washers. Performing a surface preparation on new washers was unnecessary. Therefore, steel angles and struts were cleaned using a power wire brush to remove any mill scale and paint.

3.6.3 Bolt Calibration

The structural bolts used in this testing were a 3/4 in. diameter and a 5/8 in. diameter A325 steel bolt. A 2 mm diameter hole was drilled through the center of each bolt and a strain gauge was installed inside and epoxied. A bolt calibration process was performed to determine the relationship between the applied tension and the strain.

3.6.4 Connection Detailing

The components of the rotational friction connection consist of two steel angles that are welded to an embedded plate, a steel strut with two interior structural washers, a bolt (angle bolt)

that attaches the strut to the steel angles, and a bolt (spandrel bolt) that connects the strut the spandrel beam of the metal building system. A disassembled rotational friction connection and its components are shown in Figure 3-17. The connection shown in Figure 3-18 is representative of the orientation used in experimental testing, however the connection will be installed into a real structure as seen in Figure 3-10.

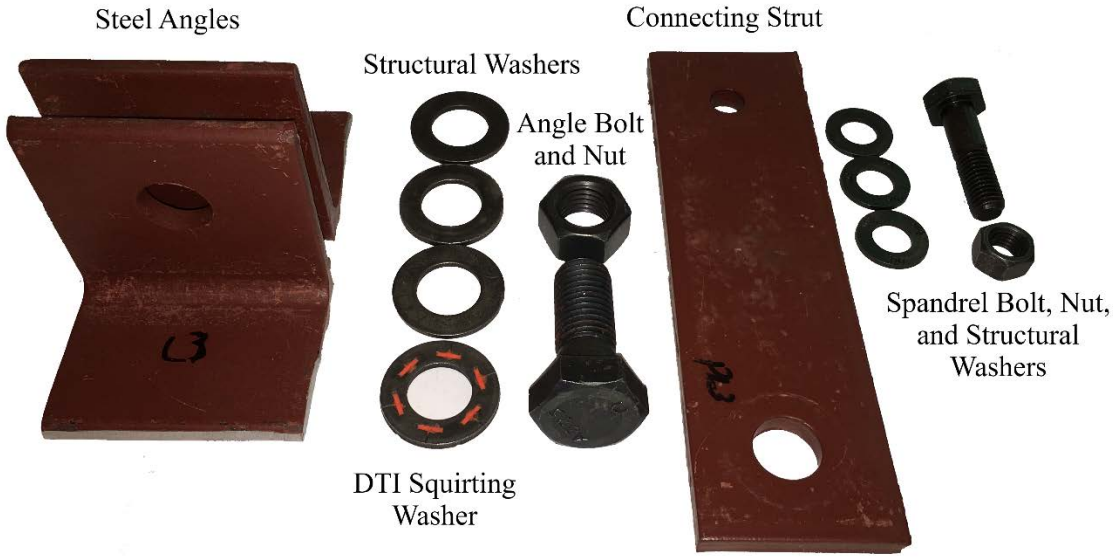

Figure 3-17. Disassembled Rotational Friction Connection and Components

The list of structural elements used for testing are as follows:

- *L4"x3"x0.375", 4 inches in length, A572 Gr. 50 Steel*
- *PL12"x10"x5/8" A36 Embedded Plate (Not shown)*
- *C9x20, 9'2" in length, A572 Gr. 50 Steel*
- *A325 Bolts, 5/8" and 3/4" diameter*
- *A563 Structural Nuts*
- *F436 Circular Washers*
- *PL10.5"x3.5"x0.5" A572 Gr. 50 Steel*
- *Jamb Nuts, Grade 8*

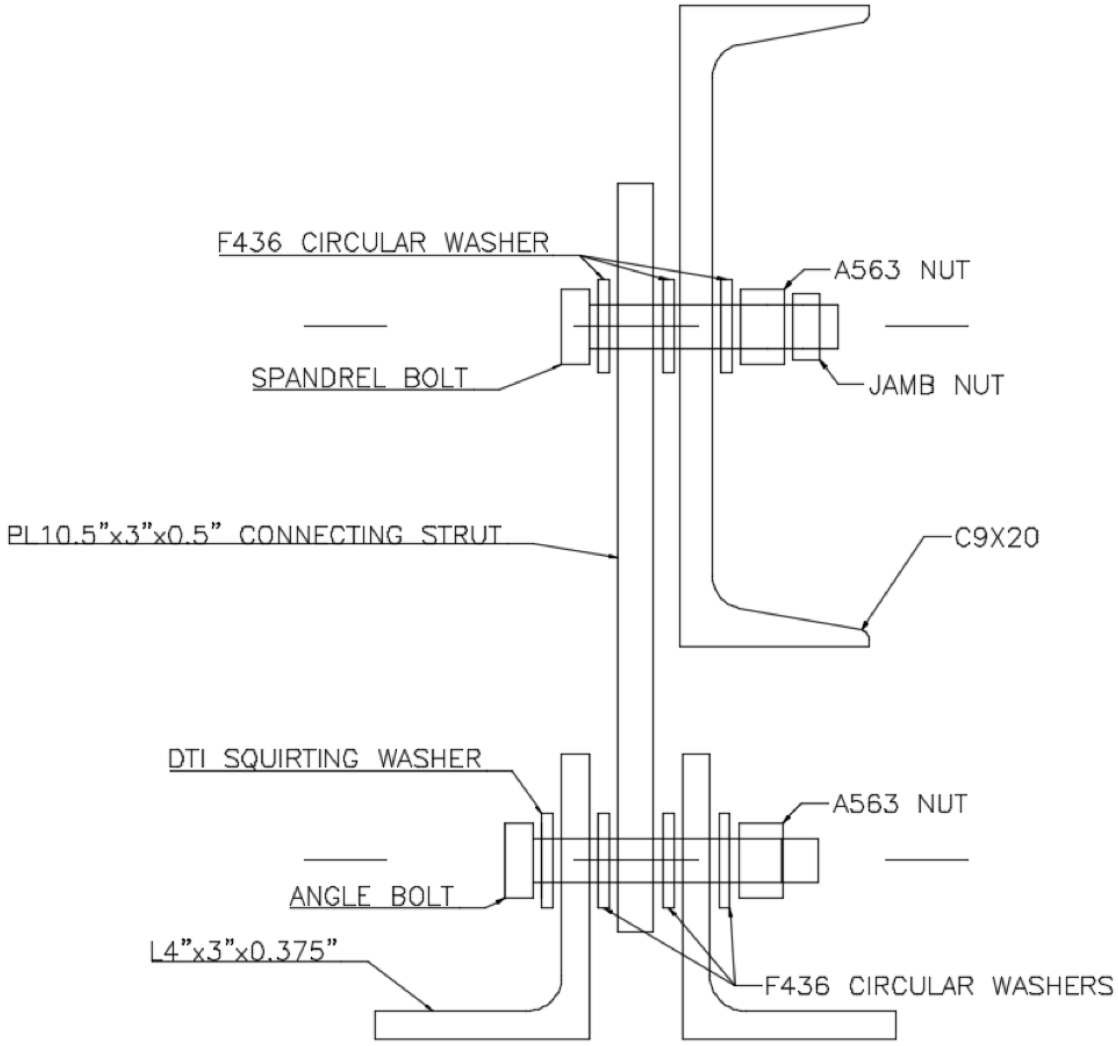

Figure 3-18. Assembly Drawing of Rotational Friction Connection (Sellers 2017)

The connection strength limit states for the out-of-plane direction are displayed in Table 3-1. The out-of-plane capacity of the connection is controlled by concrete breakout. The steel components of rotational friction connection did not control the strength in the out-of-plane direction. The calculations of the strength limit states are detailed in Appendix A.

Table 3-1. Strength Limit States and Capacities of Experimentally Tested RFC

Component	Limit State	Capacity (kips)
Embed Plate	Concrete Breakout	21.3 kips (controls)
	Steel Anchor	52.0 kips
	Headed Stud Weld	57.2 kips
	Plate Flexure	N.A.
Steel Angle	Angle Weld	41.8 kips
	Shear Yielding	84.6 kips
	Shear Rupture	82.2 kips
	Angle Bolt Bearing	53.2 kips
Angle Bolt	Bolt Shear	80.1 kips
Steel Strut	Angle Bolt Bearing	35.4 kips
	Tensile Yielding	67.5 kips
	Tensile Rupture	47.2 kips
	Spandrel Bolt Bearing	40.0 kips
Spandrel Bolt	Bolt Shear	22.5 kips
Spandrel Beam	Spandrel Bolt Bearing	54.8 kips

3.7 Experimental Results

The laboratory testing of the rotational friction connection included monotonic pushover, unidirectional cyclic, bidirectional, out-of-plane, and 100-cycle testing. The following section includes the description of each test and the results.

3.7.1 Monotonic Testing

The monotonic pushover testing revealed two damage limit states for the rotational friction connection. The first damage limit state (DL1) is defined as the transition from the operational to the immediate occupancy performance level. This state occurs at the instant at which the connection begins to slip. As the actuator continues to displace the connection, the force resisted by the connection is nearly constant. The difference in the sliding friction coefficient and the static coefficient of friction appears to be negligible. This continues until the spandrel beam begins to

bear on the steel angles of the RFC and the second damage limit state is reached. The second damage limit state (DL2) is defined as the transition from immediate occupancy to the life safety performance level. The force-displacement curve for the rotational friction connection is shown in Figure 3-19. This curve illustrates the large ductility capacity of the RFC.

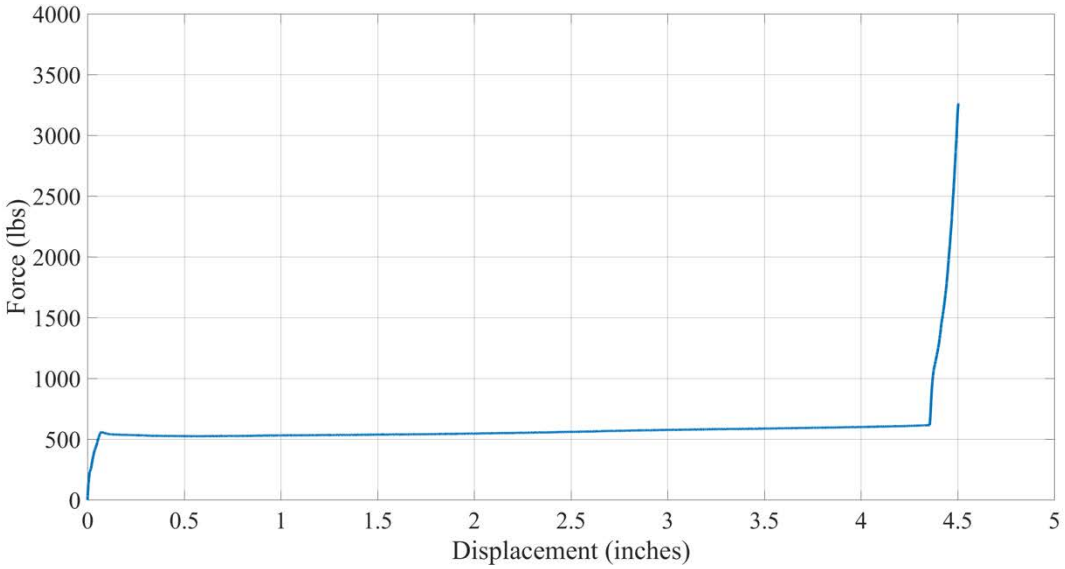

Figure 3-19. Monotonic Pushover Curve for RFC0750_A

3.7.2 Unidirectional Testing

The unidirectional cyclic testing was performed to identify the cyclic response of the rotational friction connection. The FEMA 461 (Applied Technical Council 2007) interim displacement-based protocol I was used to perform this test, as seen in Figure 3-20. The smallest deformation amplitude of the loading history, Δ_0, was 0.05 in. After two cycles, the amplitude increases by 40% until the final target deformation amplitude, Δ_m, of 3.00 in. is reached.

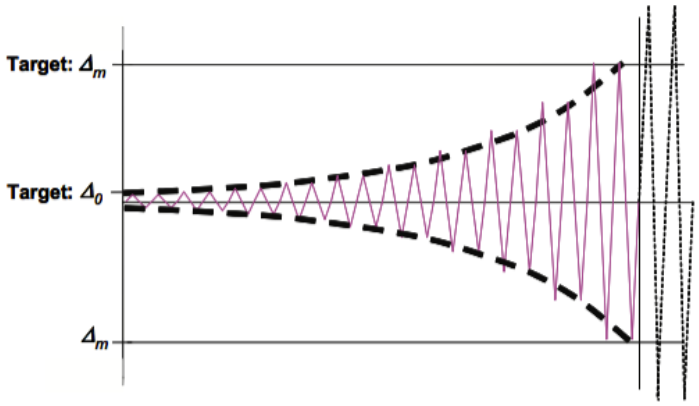

Figure 3-20. FEMA 461 Displacement Protocol (Applied Technology Council 2007)

The unidirectional cyclic tests revealed that the hysteresis loops of the rotational friction connection are nearly rectangular in shape, which is expected behavior for friction-based energy dissipating mechanisms. The force resisted by the connection gradually increased as the testing progressed. This effect was clearly visible in the comparison of the first run and second run of RFC0750 as shown in the hysteresis loops in Figure 3-21. The initial forces are shown in Table 3-2. The average free rotation force for the first run was 576 lbs and 649 lbs for the second run. There was a reduction in the angle bolt tension throughout testing as shown in Table 3-3. The percentage drop in bolt tension decreased in the second run over the first run. However, it is believed that surface roughening effects are compensating for the bolt tension loss and providing an overall growth in the hysteresis loops.

The free-rotation force in all the test specimens was much lower than anticipated. It was determined that the initial coefficient of friction had a mean of 0.13, which is much lower than the anticipated 0.30 for a steel-on-steel surface. The initial coefficient of friction of the tests specimens varied from 0.12 to 0.15.

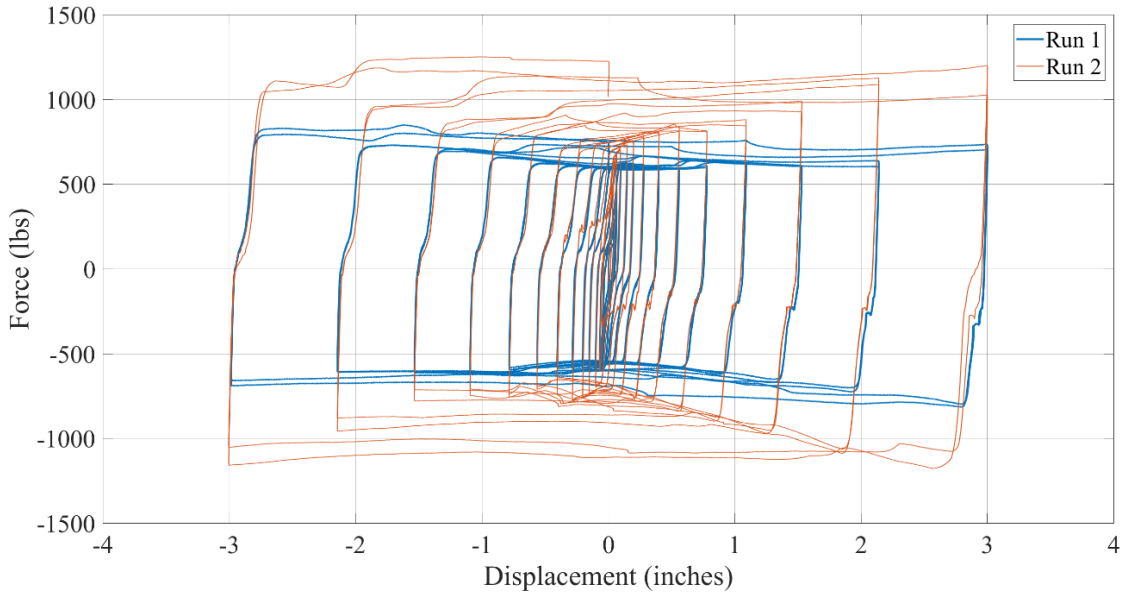

Figure 3-21. Hysteresis Loops for RFC0750_A

Table 3-2. In-Plane Horizontal Forces for RFC0750.

RFC0750	In-Plane Horizontal Force (lbs)	
	Run 1	Run 2
Specimen 1	626	671
Specimen 2	554	555
Specimen 3	561	580
Specimen 4	584	665
Specimen 5	554	775

Table 3-3. Angle Bolt Tension Loss for RFC0750.

RFC0750		Initial Angle Bolt Tension (lbs)	Final Angle Bolt Tension (lbs)	Percentage Change (%)
Run 1	Specimen 1	30,975	26,824	-13.4
	Specimen 2	29,893	22,490	-24.8
	Specimen 3	30,705	25,126	-18.2
	Specimen 4	30,058	22,465	-25.3
	Specimen 5	29,203	22,436	-23.2
Run 2	Specimen 1	25,554	24,741	-3.2
	Specimen 2	22,472	18,841	-16.2
	Specimen 3	25,028	24,261	-3.1
	Specimen 4	22,396	19,944	-10.9
	Specimen 5	22,302	19,483	-12.6

3.7.3 Bidirectional Testing

The bidirectional testing was performed on the connection at Location A of the experimental setup. The steel strut and washers were replaced prior to the test. The bidirectional testing results confirm the P-Delta effects that occur on for RFCs. Figure 3-22 shows the hysteresis loops from the bidirectional test. The P-Delta effect increases the in-plane horizontal force that is experienced in the rotational friction connection as the deformation increases. Under a tensile load, the post-slip stiffness is positive while under a compressive load, the post-slip stiffness is negative. Table 3-4 summarizes the results of biaxial testing. The larger angle bolt for RFC0750 resulted in a higher initial stiffness, post-slip stiffness. in-plane horizontal force, and total energy dissipated over RFC0625.

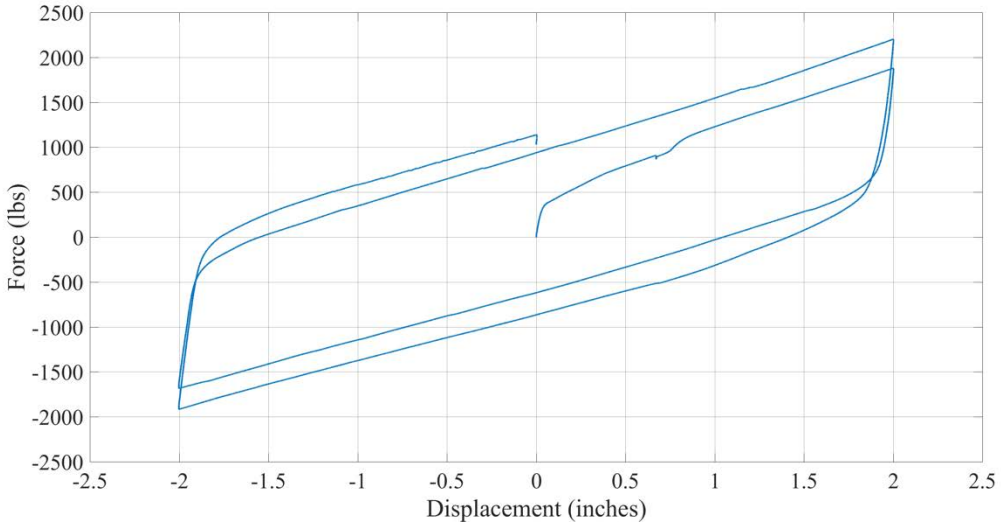

Figure 3-22. Bidirectional Hysteresis Loops of RFC0750.

Table 3-4. Results of Bidirectional Testing

	Initial Stiffness (k/in)	Secondary Stiffness (k/in)	Free Rotation Force (lbs)	Energy Dissipated (k-in)	Maximum Force (lbs)	Minimum Force (lbs)
RFC0625	8.27	0.76	380	12.4	2228	-1892
RFC0750	16.47	0.79	543	15.1	2430	-2040

3.7.4 Out-of-Plane Testing

An out-of-plane load was applied using the vertical actuator and wire ropes on the rotational friction connection as seen in Figure 3-23. Testing was terminated when the force reached 16.0 kips which was the safe working load for the wire ropes. The peak out-of-plane force applied to the rotational friction connection was 16 kips. The calculated out-of-plane stiffness is approximately 63 k/in and 67 k/in for RFC0625 and RFC0750, respectively. The out-of-plane stiffness is generally linear throughout the test, with an R^2 value of 0.97 for RFC625 and RFC750. After the test, there was no observable damage to the connection in the steel or concrete.

Figure 3-23. Out-of-Plane Testing Setup of RFC.

3.7.5 100-Cycle Testing

Due to the hardening behavior that was observed in the unidirectional testing, additional cyclic testing was performed to determine the causes of this hardening behavior. One hundred cycles with an amplitude of 1.10 in. were applied on RFC0750. Ten cycles at 2.20 in. were added after the initial 100 cycles to observe the behavior at larger displacements. Figure 3-24 shows the hysteresis loops of the high amplitude 100-cycle test. The rotational friction connection initially slips at an in-plane horizontal force of approximately 600 lbs. As the test progresses, the slip-force gradually increases and by the end of the test, the resisting force has more than doubled.

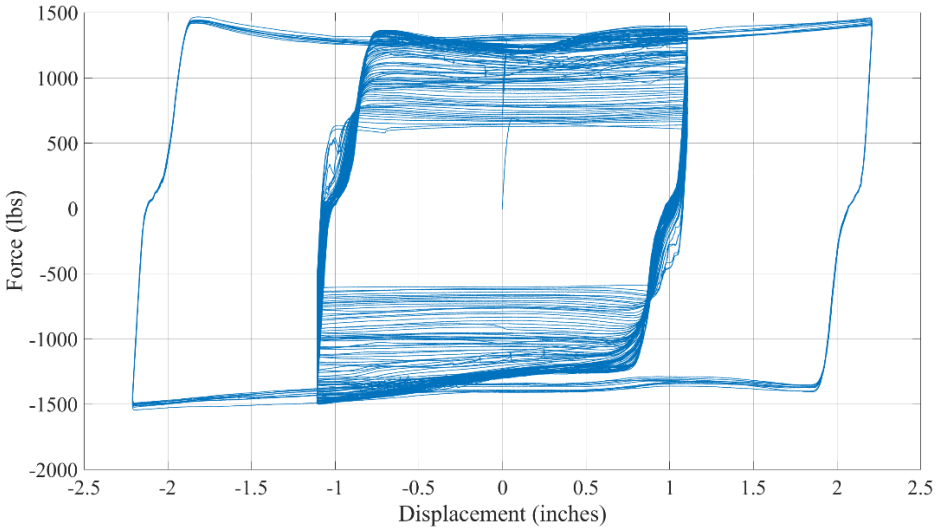

Figure 3-24. Hysteresis for 100-Cycle High Displacement Testing Protocol.

After testing was complete, the contact surfaces were examined. It was found that there was a noticeable roughening of the structural washers and strut as seen in Figure 3-25. The surfaces were also coated in very fine steel particles. It is evident that the hardening behavior is due to the roughening of the contact surfaces, which causes an increase in the coefficient of friction. The roughening effect more than compensates for the nearly 50% drop in initial bolt tension.

Figure 3-25. Wearing of Connection Before (Left) and After (Right) 100-Cycle Testing

3.7.6 Major Findings from the Experimental Testing

The laboratory testing demonstrated that the rotational friction connection exhibits many positive structural properties that make it suitable for use as a ductile fuse element between steel frame and hard walls in metal building systems. These properties include significant ductility in the in-plane horizontal direction. This energy dissipating capacity is not hindered by the presence of an out-of-plane force. Damage to the surrounding elements and wall panel was minimal. The only damage present was roughening of the contacting surfaces including the washers. The testing shows that the rotational friction connection should not require replacement following a seismic event. With testing complete, the next step was to develop computer models that capture the behavior of the rotational friction connection.

3.8 3-D Solid Finite Element Modeling

The software program Abaqus 2016 (Simulia 2016) was used to perform the 3-D solid finite element analyses of the rotational friction connection (Figure 3-26). The modeling procedure is detailed in this section along with the verification and validation process using theoretical calculations and experimental data.

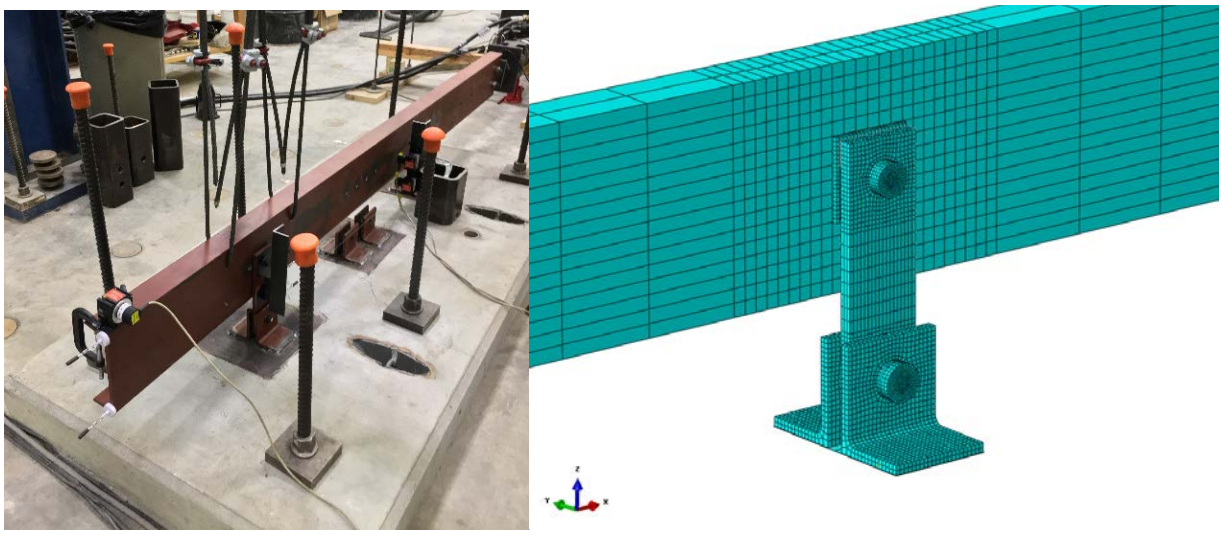

Figure 3-26. Experimental Setup and Finite Element Analysis Model

3.8.1 Material Mechanical Properties

Yielding of the steel material is not expected in the model due to the primary energy dissipation mechanism being friction. When the connection is subjected to an in-plane shear force, yielding would be limited to regions near the weld connecting the steel angle legs to the embed plate. The steel components were modeled with an elastic modulus of 29,000 ksi and a Poisson's ratio of 0.30. Table 3-5 displays the steel grade that was assigned to each component of the friction connection and the corresponding yield stress and ultimate stress. These yield stress and ultimate stress values were selected from the corresponding ASTM specifications (2015 and 2016).

Table 3-5. Material Properties of RFC Components

Component	Steel Type	Yield Stress (ksi)	Ultimate Stress (ksi)
Structural Bolts	A325	110	130
Washers	F436	110	130
Spandrel Beam C9x20	A572Gr50	50	65
L4x3x0.375	A572Gr50	50	65
Strut	A572Gr50	50	65

The inelastic behavior of the steel in the rotational friction connection was not of concern in this research because the primary inelastic mechanism of the connection is friction, not yielding of the steel material. No tensile coupons were created to obtain this information. For simplicity, a bilinear stress-strain curve was assigned for the various steel types based on their minimum yield stress and ultimate stress. The stress-strain curves are displayed in Figure 3-27. The ultimate strain values do not have much effect because the peak strain values are so low. After each analysis was performed, it was found that the bolts and washers never yielded. The highest strain achieved was 0.007 in/in within the A572Gr50 steel angles in the elements nearest the location of the fixed boundary support.

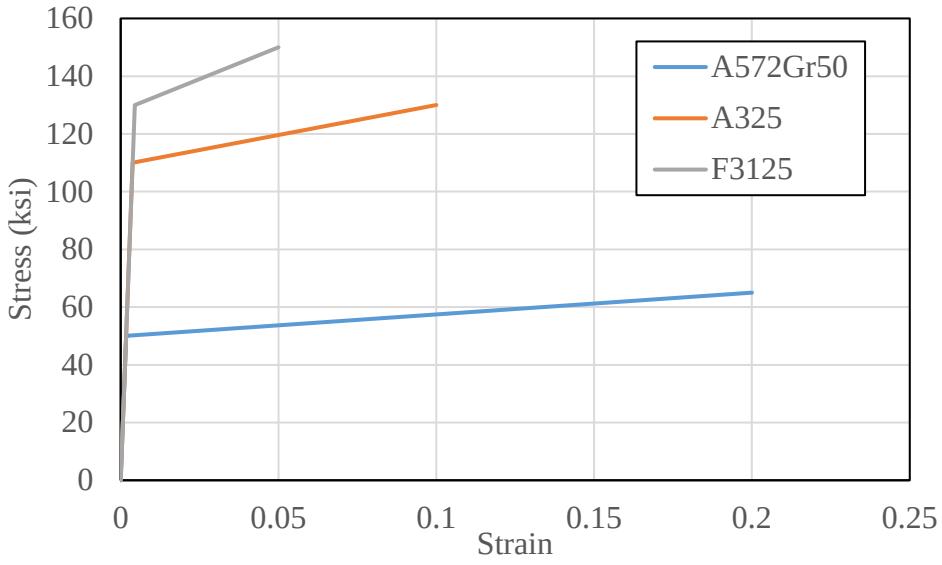

Figure 3-27. Stress-Strain Curve for Steel

3.8.2 Element Type and Mesh Density

A concerted effort was made to find an optimum mesh density for the model. The region around the bolt holes was the most important because it experiences the highest stress gradients and it is where the contact surfaces are located. The parts were strategically partitioned to allow for the mesh algorithm to generate a structured uniform mesh.

The 3-D model utilized the solid hexahedral element (C3D8R). This element is an isoparametric element that is suitable for general stress analyses. These elements have a total of 8 nodes each with 3 translational degrees of freedom. The stress in each element is evaluated using one gauss integration point, or reduced integration, which significantly improves the computational efficiency (Simulia 2016).

After a convergence study was performed, it was found that using a maximum element size of 0.167 inch provided sufficient accuracy for the force-displacement behavior. Three elements were used in the thickness of the steel strut. Two elements comprise the thickness of the steel angles. Figure 3-28 shows the partitions and refined mesh around the bolt holes. Thirty-two elements were used around the perimeter of all bolt holes. Five layers of elements were utilized between the inner and outer radii of the washers.

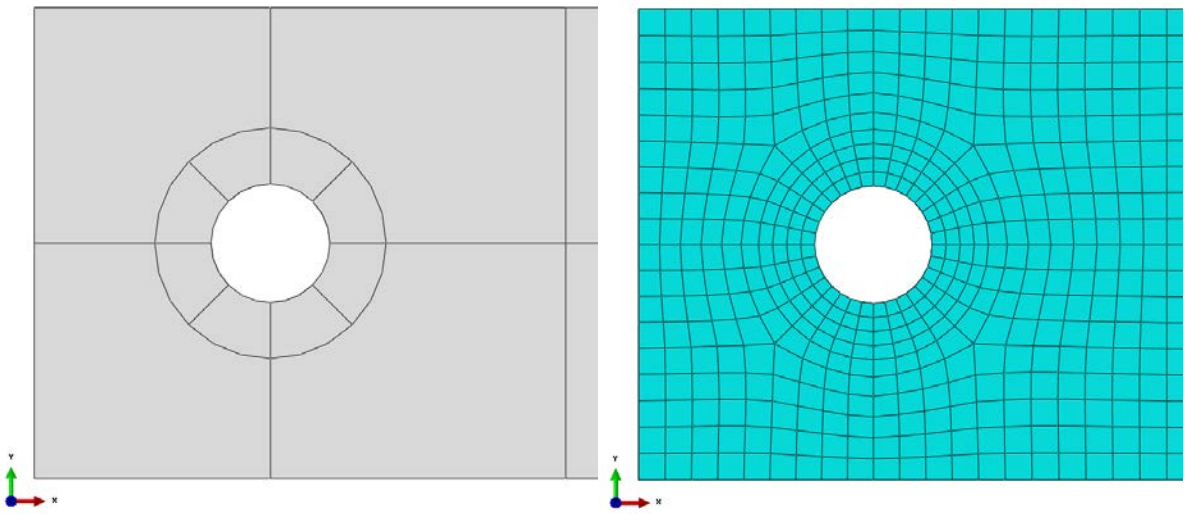

Figure 3-28. Partitions and Mesh Around the Bolt Holes

3.8.3 Contact Behavior

Abaqus allows the user to assign manually the contact pairs as master and slave surfaces. However, the general contact procedures were used due to the complex contact within the region of the bolt. It is possible that the nodes around the perimeter of the bolt hole could encounter two contact surfaces simultaneously. Using the master to slave surface constraints would make these nodes overly constrained and possibly lead to numerical convergence issues (Simulia 2016).

For simplicity, the coulomb friction model was used for the frictional behavior. In the coulomb friction model, the slip force is proportional to the normal force applied times a coefficient of friction (Chopra 2009). The normal behavior was assigned a hard contact that implemented the penalty method formulation. Using the experimental results, a calibration process was performed to determine the friction coefficient to be 0.13. This coefficient of friction was assigned to the tangential behavior for all numerical analyses.

3.8.4 Bolt Geometry Simplification

The RFC utilizes two standard A325 structural bolts with standard hardened nongalvanized structural washers that conform to the ASTM F3125 specification. These bolts have hexagonal bolt heads and nuts, but for the model, the geometry was simplified into a circular bolt head and nut. In the actual connection, the washers are free separate components that can move independently of the bolt. In order to reduce the number of contact planes, the washers were fused with the bolt and nut to create one part, as seen in Figure 3-29.

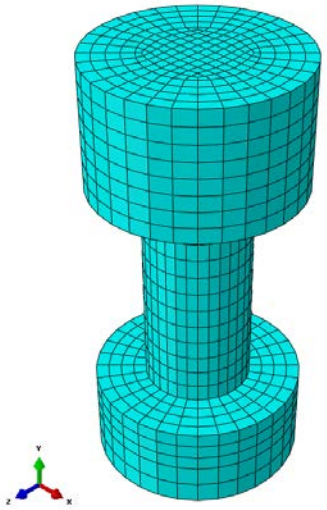

Figure 3-29. Mesh for Three-Fourths Inch Diameter Angle Bolt

During the experiment, the bolts lost some of its initial pretension. The inclusion of bolt threads could capture the loosening of bolt that was experienced during the experiment. However, this would significantly increase the complexity of the model with the addition of thousands of degrees of freedom and numerous contact surfaces. The RFC finite element model was focused on capturing the global behavior force-displacement behavior of the connection. Because local bolt stresses are not the focus of this simulation, it is reasonable to exclude the threads (Montgomery 2008).

3.8.5 Bolt Pretension

Abaqus has a built-in function for applying bolt load directly. Figure 3-30 shows the bolt load application. For the validation analysis runs, an identical bolt load that was measured at the start of each trial run for the experiment was used to pretension each bolt. After the pretensioning step, the length of the bolt was locked in to allow the bolt tension to vary during the simulation.

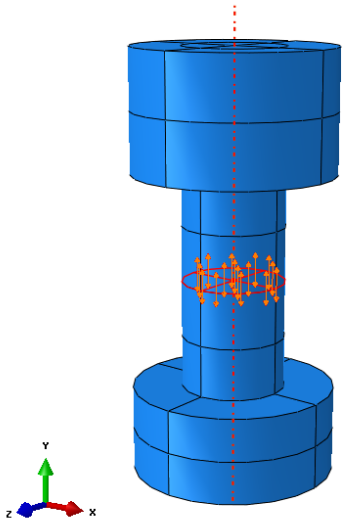

Figure 3-30. Bolt Pretension Load Application

3.8.6 Analysis Procedure

Due to the pseudo-static nature of which the experiment was performed, performing dynamic analyses was not required. The numerical analyses were divided into two static load steps. The first load step applied the same bolt tension recorded in the experiment to the angle bolt and spandrel bolt. During that same analysis step, the self-weight of all components was applied. The second analysis step simulated the horizontal motion of the hydraulic actuator. The second analysis step imposed a displacement boundary condition at the far end of the spandrel beam. The initial step size was 0.01 in, and the maximum step size allowed was 0.05 in.

3.9 Validation of Finite Element Model

The experiment performed in the laboratory included monotonic, cyclic, out-of-plane, and biaxial testing on the rotational friction connection. There were two angle bolt sizes that were tested: five-eighths inch diameter bolt and three-fourths inch diameter bolt. The center-to-center distance between the center of the angle bolt and the spandrel bolt was 7.5 inches for all tests. Complete details about the experimental procedure are described in Sellers (2017).

3.9.1 Cyclic Test Validation

The results from the cyclic tests were used to validate the finite element model. A calibration process determined the coefficient of friction to be 0.13. The theoretical free-rotation moment and free-rotation force was calculated for the nine cyclic tests. Table 3-6 displays the bolt pretension measured during each test, the nominal radii of the washers, and the calculated theoretical free rotation moment and free rotation force.

Table 3-6. Theoretical Free Rotation Moment and Free Rotation Force

RFC Specimen	Bolt Pretension (kips)	Inner Radius (in)	Outer Radius (in)	Theoretical M_{FR} (lb-in)	Theoretical F_{FR} (lbs)
RFC0750_A	31.0	0.406	0.734	4730	630
RFC0750_B	29.9	0.406	0.734	4550	607
RFC0750_C	30.7	0.406	0.734	4680	624
RFC0750_D	30.1	0.406	0.734	4590	612
RFC0750_E	29.2	0.406	0.734	4450	593
RFC0625_A	21.2	0.344	0.656	2840	379
RFC0625_B	23.1	0.344	0.656	3100	413
RFC0625_D	24.1	0.344	0.656	3230	431
RFC0625_E	23.1	0.344	0.656	3100	413

Table 3-7 displays the free-rotation force from the numerical analysis for the nine cyclic tests and is compared with the theoretical and experimental force. The percent error was calculated by comparing the numerical results with the theoretical results. The numerically determined free-rotation force appears to be in good agreement with the highest error being just -4.8%. Part of this error can be attributed to the assumption regarding the uniform normal stress distribution used in the development of the theoretical equations. The Abaqus model revealed that the normal stress was highest at the inner radius and decreased toward the outer radius. However, the variation in magnitude was minimal.

The percent difference was calculated between the numerical and the experimental free-rotation force. The largest percent difference of 15.6% of RFC0625_A can be attributed to the variability in the coefficient of friction between the contacting surfaces. All the numerical analysis used a friction of coefficient of 0.13, while the experimental value suggests that 0.15 would provide a better match for that specimen.

Table 3-7. Comparison of Free Rotation Forces

RFC Specimen	Numerical F_{FR}	Theoretical F_{FR}		Experimental F_{FR}	
	(lbs)	(lbs)	Percent Error (%)	(lbs)	Percent Difference (%)
RFC0750_A	600	630	-4.8	626	4.2
RFC0750_B	585	607	-3.6	554	5.4
RFC0750_C	595	624	-4.6	561	5.9
RFC0750_D	602	612	-1.6	584	3.0
RFC0750_E	619	593	4.4	554	11.1
RFC0625_A	366	379	-3.4	428	15.6
RFC0625_B	410	413	-0.7	414	1.0
RFC0625_D	420	431	-2.6	390	7.4
RFC0625_E	411	413	-0.5	368	11.0

3.9.2 Limitations of the Numerical Models

The hysteresis loops were generated from the RFC at Location A and Location B. The hysteresis loops from the numerical models were compared with the experimental results, shown in Figures 3-30 and 3-31. Other than the location, the RFCs were identical in geometry to one other with a ¾" diameter A325 angle bolt tensioned to the full minimum pretension. During the cyclic tests, the bolts did lose some of the initial pretension, but the size of the hysteresis loops continued to grow. Surface roughening caused the effective coefficient of friction to increase over the duration of the testing. According to the theoretical equations, the effective coefficient of friction began at 0.13 and grew to around 0.35. The roughening effect made up for the loss of bolt tension. Even though the Abaqus model does not capture the drop in bolt tension or surface roughening effects, the hysteresis loops are in reasonably good agreement.

For the RFC at Location A, the hysteresis loops from the numerical analysis underpredicts the force resisted by the connection as the analysis progresses (Figure 3-31). As a result, the total energy dissipated through friction is underpredicted in the numerical model. For the RFC at

Location B, the forces from the experiment and the numerical analysis were in better agreement (Figure 3-32). The numerical analysis did predict slightly higher energy dissipation.

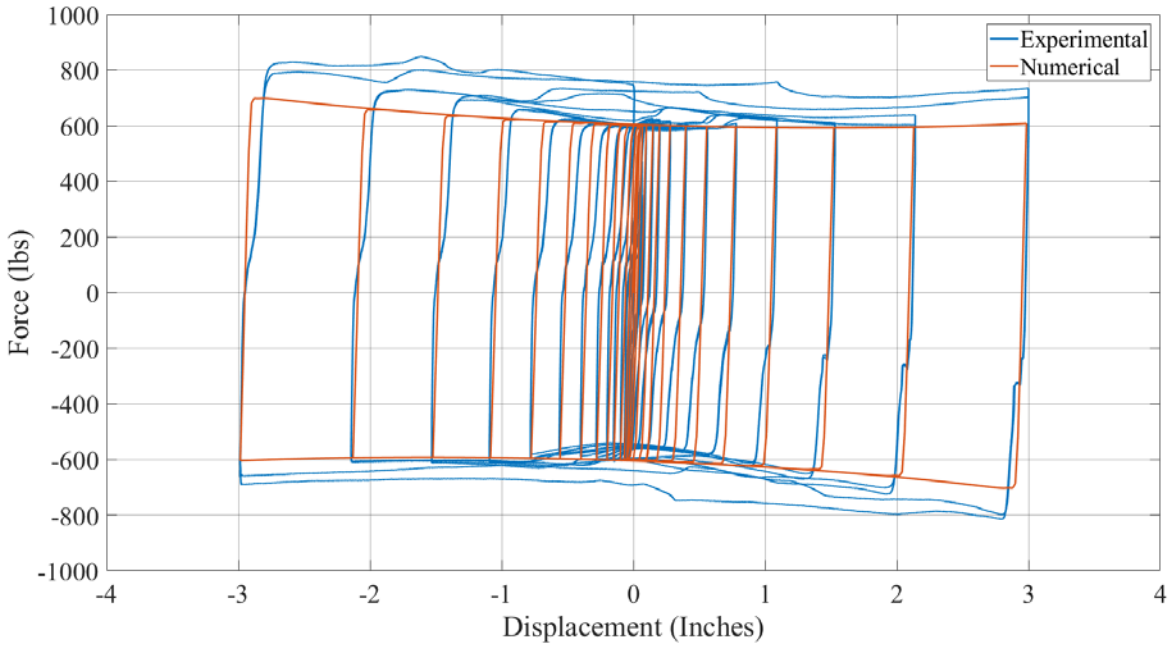

Figure 3-31. Hysteresis Comparison of RFC0750_A

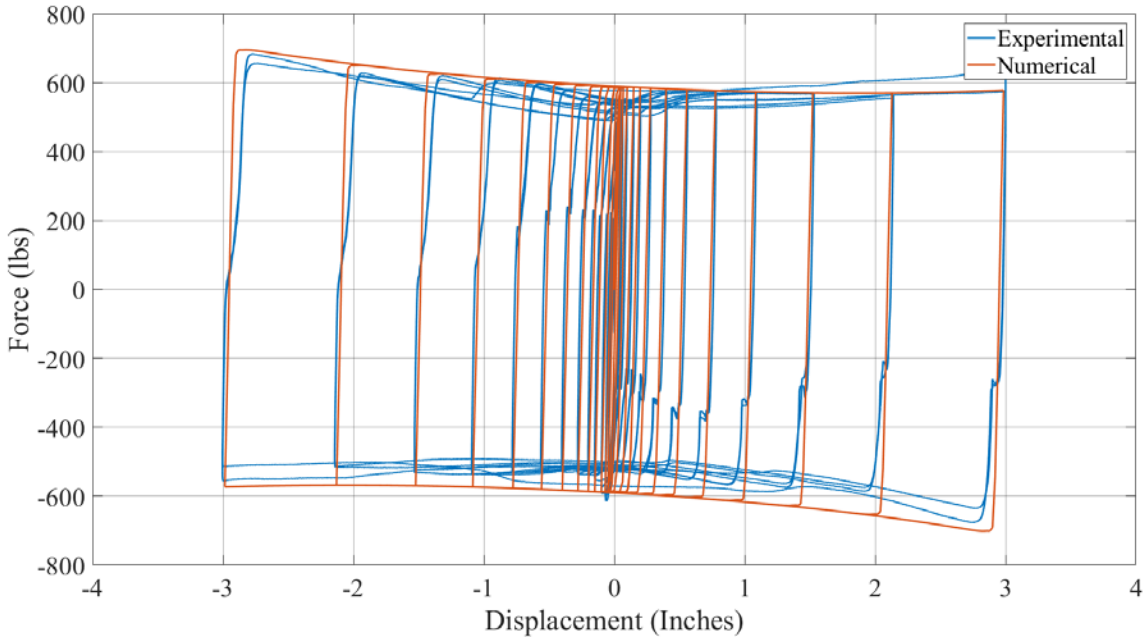

Figure 3-32. Hysteresis Comparison of RFC0750_B

3.10 Parametric Investigation

Once the 3-D solid finite element model was validated, a parametric study was performed for RFCs with geometries not tested in the laboratory. The force-displacement behavior the connection is governed by the applied bolt tension, the coefficient of friction, and the moment-arm length. Therefore, different standard bolt sizes were selected along with different moment arm lengths as the parameters that were considered in this parametric investigation. The objective of this study is to determine the free-rotation force and corresponding initial stiffness of the connection.

The most important geometric parameters that impact the behavior of this connection are the bolt diameter and strut length. The naming scheme of each numerical model uses the following scheme: RFC0625_SL07.5 where the first four digits represent the bolt diameter in one-thousandths of an inch, and the second set of digits equal the center-to-center distance between the angle bolt and spandrel bolt. The pretension applied to the angle bolt used the mean bolt pretension specified in AISC 360 (2016). The four monotonic pushover curves for the RFC with 7.5" center-to-center distance are shown in Figure 3-33. As expected, the free rotation force was highest for the one-inch diameter bolt and lowest for the five-eighths diameter bolt. Once the connection began to slip, the secondary stiffness was nearly zero and increased as the connection rotated farther.

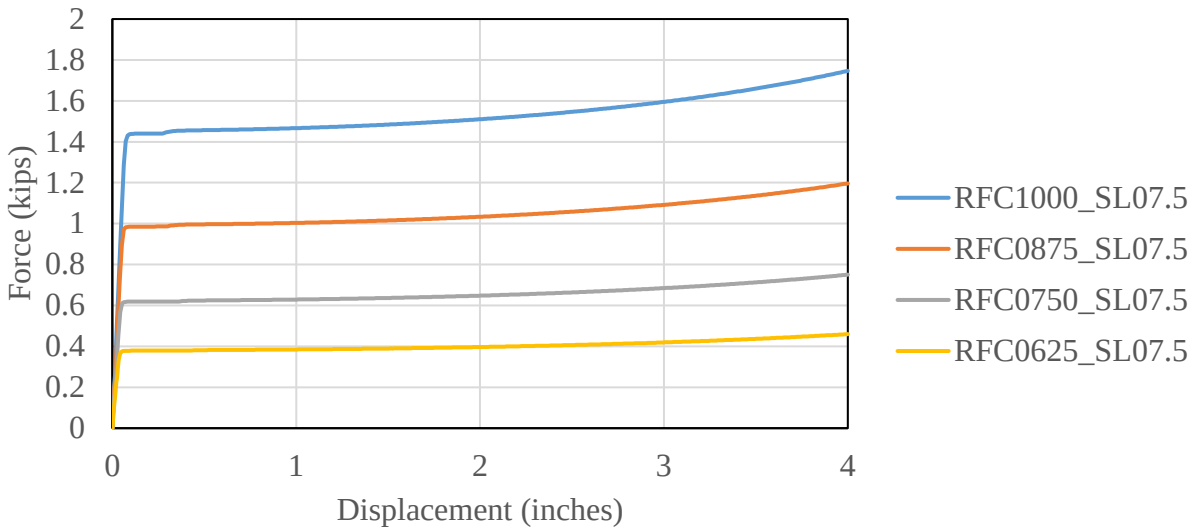

Figure 3-33. Monotonic Pushover Curves for RFCs with 7.5 in. Strut Length

The analyses were performed for a connection with a bolt center-to-center distance of 14.5 in. The monotonic pushover curves are shown in Figure 3-34. The force-displacement behavior is very similar to the previous moment arm length. The initial free rotation forces are smaller due to the longer moment arm length.

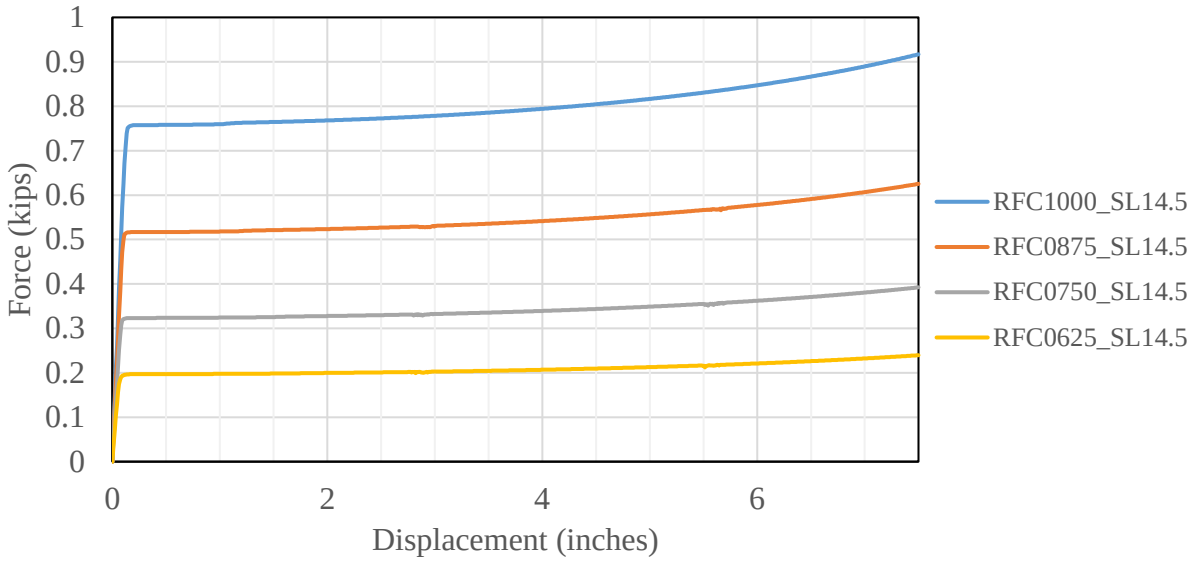

Figure 3-34. Monotonic Pushover Curves for RFCs with 14.5 in. Strut Length

During the experiment, the initial stiffness of the connection was difficult to capture due to the fact that the actual bolt hole diameter is 1/16 in. larger than the nominal bolt diameter. As the connection rotated, this small gap would have to close before the connection could provide resistance. The initial stiffness was calculated for each model and are shown in Table 3-8. As the bolt size increased, the initial stiffness increased. A longer moment arm length decreased the initial stiffness as expected. These values will be used in the SAP2000 RFC link element calibration process.

Table 3-8. Initial In-Plane Horizontal Stiffness for RFC's

	Initial In-Plane Shear Stiffness (kip/in)
RFC1000_SL07.5	20.7
RFC0875_SL07.5	17.4
RFC0750_SL07.5	13.6
RFC0625_SL07.5	9.4
RFC1000_SL14.5	6.21
RFC0875_SL14.5	5.29
RFC0750_SL14.5	4.12
RFC0625_SL14.5	2.94

The parametric study included an investigation into the force-displacement behavior of the RFC under a simultaneous out-of-plane load. The connection was subjected to either a tensile or compressive out-of-plane force of 5.0 kips and then displaced in the in-plane horizontal direction to four inches. Force-displacement curves are those two cases are shown in Figures 3-35 and 3-36. The post-slip behaviors are nearly linear and are parallel, which is characteristic of geometric nonlinearity.

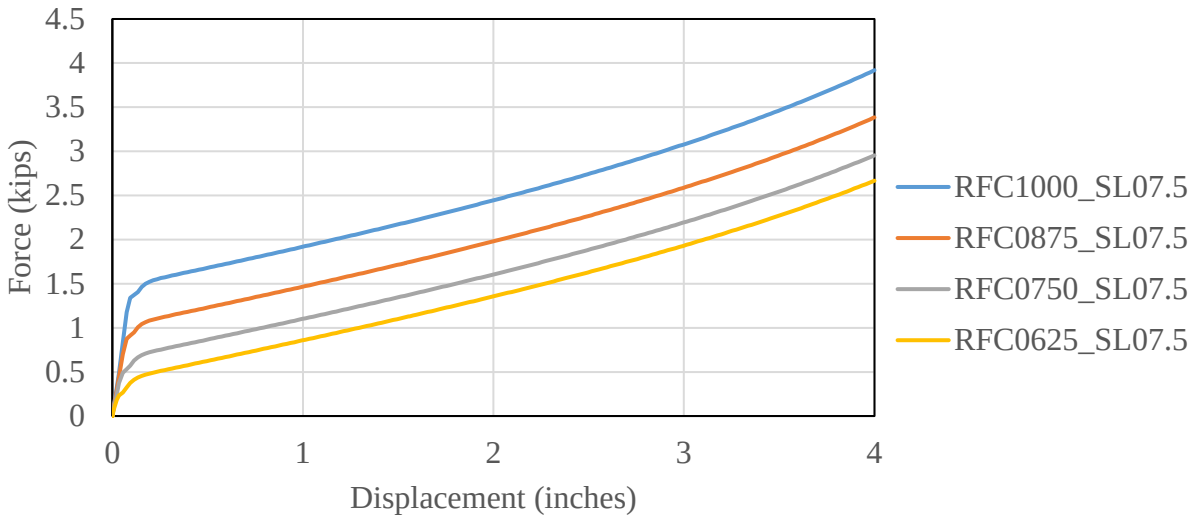

Figure 3-35. Tensile Biaxial Curves for RFCs with 7.5 in. Strut Length

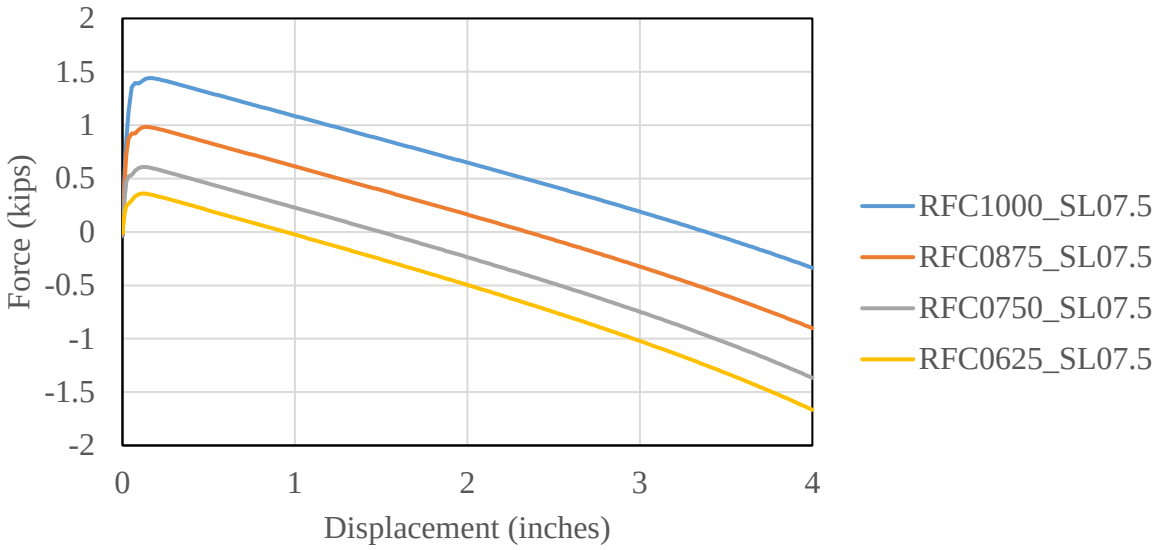

Figure 3-36. Compressive Biaxial Curves for RFCs with 7.5 in. Strut Length

The results for the RFC with a bolt center-to-center distance of 14.5 in. are shown in Figures 3-37 and 3-38. Again, the post-slip regions of the force-displacement curves nearly parallel one another. They are linear at first, and then begin to have a slight curvature as the rotation increases.

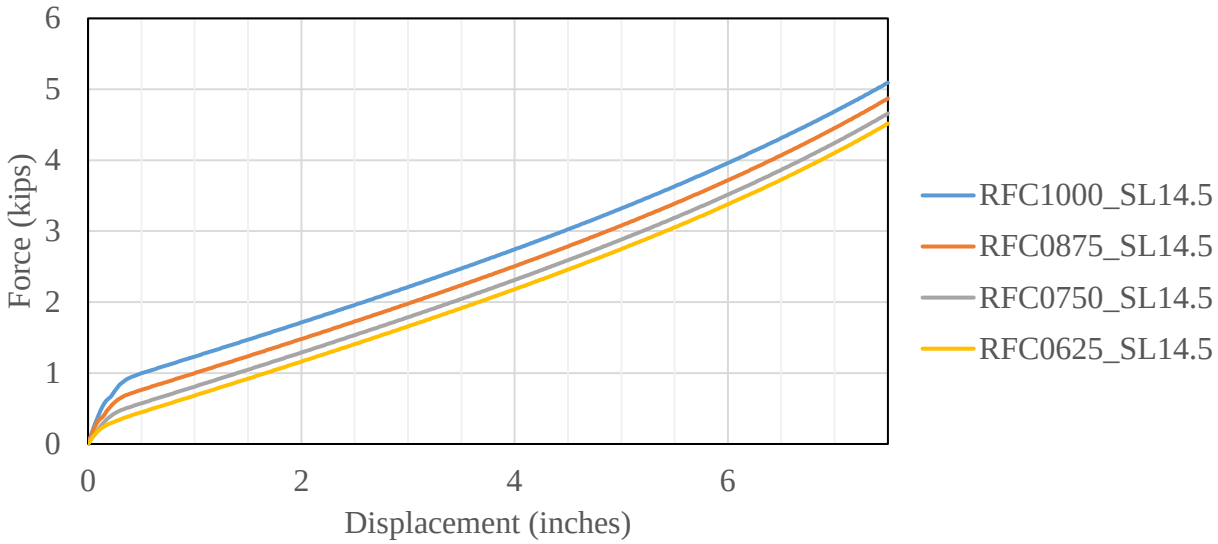

Figure 3-37. Tensile Biaxial Curves for RFC with 14.5 in. Strut Length

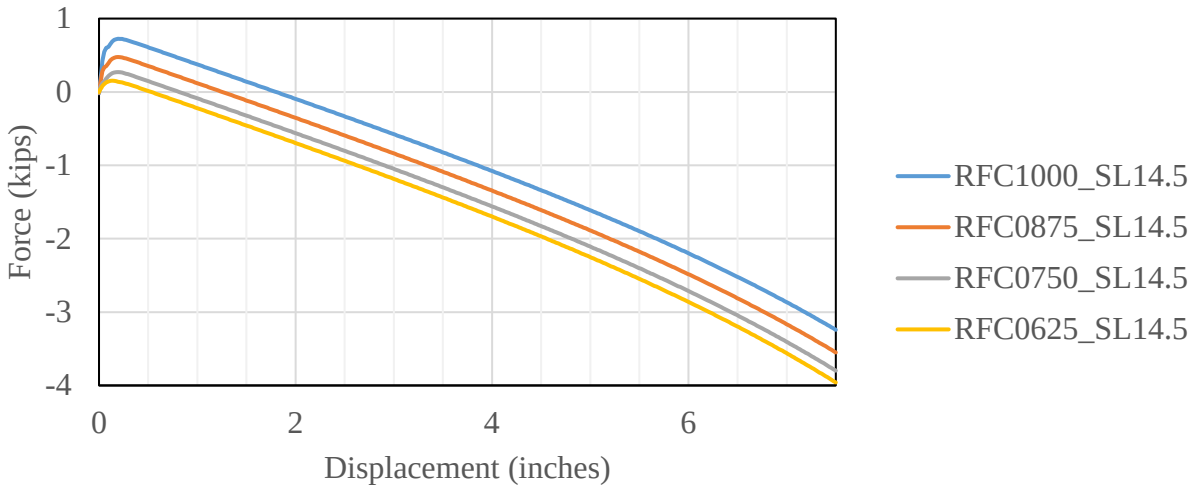

Figure 3-38. Compressive Biaxial Curves for RFCs with 14.5 in. Strut Length

The initial in-plane stiffness for the biaxial tests were computed and compared with the analyses with zero out-of-plane force (Table 3-9). According to the results, the in-plane horizontal stiffness decreased in all cases when the connection was subjected to a tensile load and increased when subjected to a compressive load. This contradicts the expected behavior due to P-Delta effects. However, this unexpected behavior can be explained by considering the stiffness contribution of the angle legs. When the connection was loaded in tension, the angle legs are

pulled away from the embed plate, and the legs experience flexural stress. When a compressive load is applied, the angle legs go into bearing with the embed plate, and no flexural stress is developed. Under the compressive force, the load path changes and the force travels straight down to the embed plate. Another source of the increased lateral stiffness due to compression could be the Poisson's effect on the strut. The compressive load would increase the width and thickness of the strut and increase the bolt tension applied on the contact surfaces. This did not seem to be the case because the monitored bolt tension increased very little and did not have a substantial impact.

Table 3-9. Initial In-Plane Horizontal Stiffness considering P-Delta Effects

	Initial In-Plane Stiffness (kip/in)		
	Zero Out-of-Plane Force	Tensile Biaxial	Compressive Biaxial
RFC1000_SL07.5	20.7	14.8	40.8
RFC0875_SL07.5	17.4	12.2	33.5
RFC0750_SL07.5	13.6	9.7	21.9
RFC0625_SL07.5	9.4	7.3	14.0
RFC1000_SL14.5	6.21	4.3	11.85
RFC0875_SL14.5	5.29	3.77	9.30
RFC0750_SL14.5	4.12	2.72	4.56
RFC0625_SL14.5	2.94	2.09	2.36

Lastly, the secondary in-plane horizontal stiffness was calculated for each analysis. The results for the secondary in-plane horizontal stiffness are shown in Table 3-10. The bolt diameter size appears to have little to no influence on the post-slip stiffness. The calculated theoretical geometric stiffness of the connection is 0.5 kips/in, which is in close agreement with the values predicted from the Abaqus model.

Table 3-10. Secondary In-Plane Horizontal Stiffness

	Secondary In-Plane Stiffness (kip/in)		
	No Axial Force	Tensile Biaxial	Compressive Biaxial
RFC1000_SL07.5	0	0.51	-0.44
RFC0875_SL07.5	0	0.50	-0.45
RFC0750_SL07.5	0	0.49	-0.46
RFC0625_SL07.5	0	0.49	-0.46
RFC1000_SL14.5	0	0.48	-0.47
RFC0875_SL14.5	0	0.48	-0.47
RFC0750_SL14.5	0	0.48	-0.47
RFC0625_SL14.5	0	0.48	-0.47

3.11 Conclusions

This chapter described the development of a new rotational friction connection for use between hard walls and steel frames in metal building systems. Theoretical equations describing the free-rotation force and force-displacement curves were developed using engineering mechanics and equilibrium. In laboratory tests, this connection was shown to exhibit stable and predictable hysteretic behavior. 3-D finite element models were verified with theoretical equations. The models were shown to provide reasonable agreement with experimental data in terms of the free-rotation force.

The most important parameters in the RFC are the bolt pretension, coefficient of friction, and distance between the angle bolt and spandrel bolt. A parametric study expanded upon the geometries tested in the lab to determine the free-rotation force, initial stiffness, and force-displacement behavior. These values can be used to calibrate a simplified rotational link element that represents the RFC for global frame analyses.

Chapter 4 Analytical Model Development of New Seismic Force Resisting System for Metal Building Systems with Hard Walls

4.1 Introduction

A 3-D analytical model using SAP2000 was developed that can quantify the seismic performance of metal building systems. The major structural components of a metal building system were identified and modeled: which include the metal building moment frame, secondary framing system, longitudinal bracing system, hard walls, and the rotational friction connection. Each of these components underwent a validation process to determine the acceptability of the modeling procedure. The Abaqus model results of the RFC from Chapter 3 were used to develop and calibrate an idealized finite element model of the RFC for use in nonlinear dynamic analyses. With all the modeling components combined, the SAP2000 model was used to assess the global system's performance during seismic excitations.

4.2 Selection of Computer Analysis Program

In order to predict the structural behavior and performance of metal building systems with hard walls during seismic events, it was necessary to develop 3-D analytical models for use in nonlinear dynamic analyses. Prior to this research, principally 2-D models have been used for earthquake analyses. The use of a 3-D model is significant because it is necessary to capture the in-plane and out-of-plane connection demands between the steel frame and the hard walls.

Three software programs were considered in the development of these 3-D models: SAP2000 Version 19.2.2 (CSI 2017), Perform 3D V5 (CSI 2011), and OpenSEES (Mazzoni et al.

2007). Each has advantages and disadvantages. The solution algorithms that Perform 3D and OpenSEES employ trump SAP2000 in nonlinear dynamic analyses in speed and robustness. Developing a 3-D OpenSEES model would have required an exorbitant amount of time to code. OpenSEES has no graphical user interface, which means finding any errors in the model geometry and section assignments would be very difficult. Also, OpenSEES currently lacks a nonprismatic frame element. For these reasons OpenSEES was eliminated.

Perform 3D is well suited for conventional steel and reinforced concrete structures. However, metal building frames are inherently very different from conventional steel moment frames. Metal building frames do not utilize hot rolled sections. Instead, the column and rafter cross-sections are composed of built-up plate sections that are often web-tapered and singly symmetric. Perform 3D does not contain nonprismatic frame elements and the I-beam shapes can only be doubly-symmetric. For this reason, Perform 3D was eliminated.

SAP2000 has a very user-friendly graphical interface which makes spotting errors much easier than a program with purely code-based input. It also has nonprismatic frame elements that can be made up of any custom cross-section. Nonprismatic elements eliminate the need to use a series of prismatic elements. This, in turn, reduces the number of degrees of freedom in the model, and can greatly increase the speed of analyses.

Unfortunately, all three programs lacked a beam-column element that includes the warping degree of freedom. Warping plays a crucial role in the torsional behavior of non-circular cross-sections. Without the warping degree of freedom, the St. Venant torsion is the only component used for calculating the torsional stiffness of all the frame elements. All torsional stiffness in the frames will be underestimated. Because of this, any chance of simulating LTB with kinematic accuracy is nearly impossible. Therefore, a clever use of a custom flexural hinge is necessary to

approximate post-buckling behavior of metal building frames, which can be accomplished in SAP2000. Ultimately, after all these considerations, SAP2000 was used in the development of the 3-D models of metal building systems with hard walls for nonlinear dynamic earthquake analyses. The remainder of this chapter will discuss the development of the SAP2000 model (Figure 4-1).

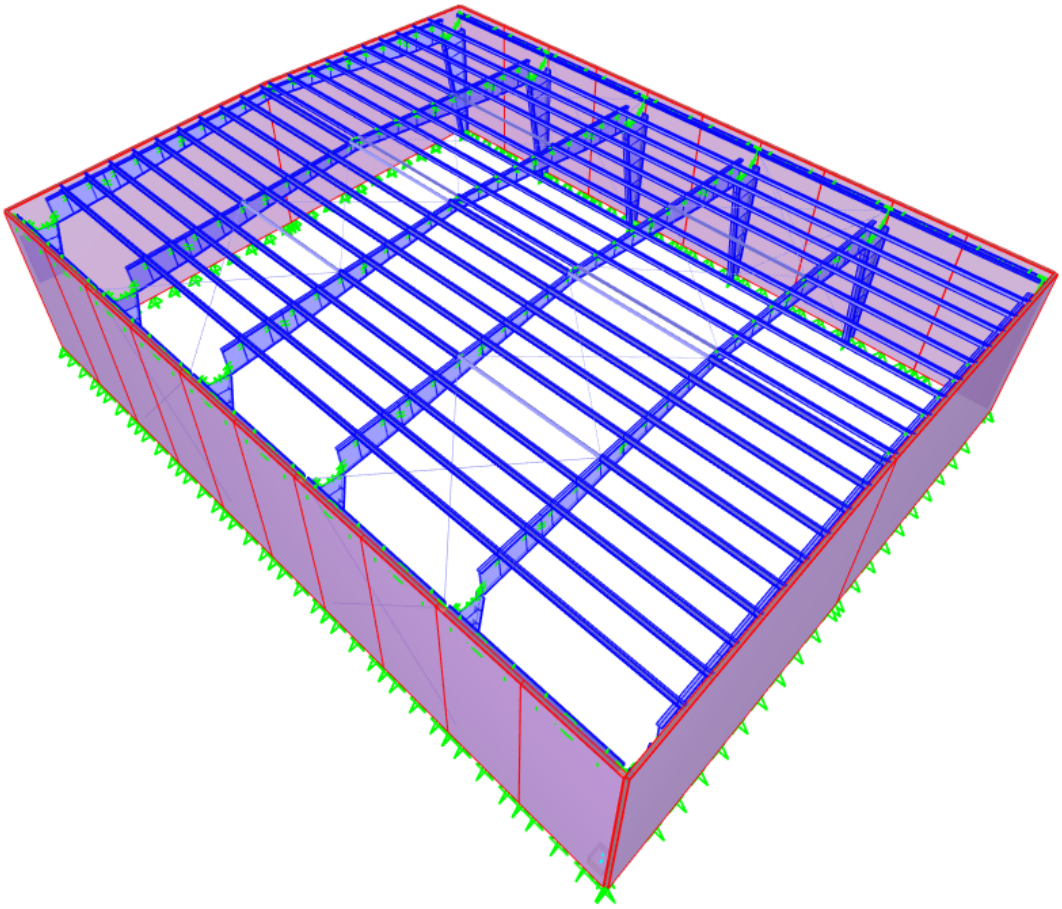

Figure 4-1. Extruded View of SAP2000 Model

4.3 Metal Building Frame Selection

As mentioned in the literature review, 192 metal building frame designs were available from the Approximate Fundamental Period Study for Metal Building Frames (Smith 2013d). The objective was to select frames designed with hard walls that would produce a sample with wide

variety in both building geometry and load conditions. Five frames were selected that, when combined, represent a wide spectrum of the metal building system population. The geometry and design parameters of each frame are listed in Table 4-1. For consistency, the frame numbers for this research will utilize the same model numbers as in the Approximate Fundamental Period Study (Smith 2013d).

Table 4-1. Metal Building Design Parameters

Model Number	Building Type	Eave Height (ft)	Transverse Length (ft)	Snow Load (psf)	Wind Speed ASCE 7-05 (mph)
16	Clear Span Symmetrical Gable	30	40	0	120
41	Clear Span Symmetrical Gable	30	100	0	85
42	Clear Span Monoslope	30	160	42	85
85	Clear Span Symmetrical Gable	15	40	0	120
138	Modular Symmetrical Gable	30	120	0	85

The selection process only considered frames designed with a high seismic risk. All the frames used in this research have a roof slope of 0.5:12, as it was believed that any variation in the slope would not impact connection demands. In Metal Building Systems, both clear span frames and modular frames are used. Clear span frames are used when the enclosed space requires that there be no interior obstructions, such as a sports facility. Modular frames can be used for storage facilities where an isolated column is not an issue. Four clear span building frames and one modular building frame were selected to represent these two building uses. One frame, Model 42, included a high snow load for buildings built in Alaska. This will help determine if a higher roof mass affects the connection demands. Model 42 has a monoslope roof as opposed to a symmetrical gable roof. This results in one side wall being taller than the other one. This model was included to see if the geometry of the system would cause differences in the connection demands in the walls on opposing sides of the building due to the differing flexibilities.

All previous seismic metal building research has been geared towards the development of new seismic force resisting systems specifically for the metal building moment frames. It is unknown what the wall weight height limitations for the future metal building ordinary moment frame (MBOMF) and metal building intermediate moment frame (MBIMF) will be, as that research is currently ongoing. For this particular research, it was decided to maintain the wall weight height limitations required for an OMF in Seismic Design Category D, in accordance with ASCE 7 (2016). In the future, these modeling procedures can be used to determine the connection demands on metal building frames with wall heights of 45, and possibly 60, feet.

4.4 Metal Building Frame Elastic Modeling

Metal building moment frames have characteristics that are very different from conventional steel moment frames. Conventional moment frames are constructed using prismatic hot-rolled I shaped members. Metal building frames are constructed of built-up I shapes that have been optimized to reduce material weight (Newman 2004). Web-tapered sections are used to increase the flexural capacities where the moment demand is greater. The highest moment demand is located at the top of the columns and at the ends of the rafters.

4.4.1 Nonprismatic Element

For this research, the frame components will utilize the nonprismatic beam-column element that is proprietary to SAP2000. Another option would have been to use a series of prismatic elements. But, in order to reduce the total number of degrees of freedom while maintaining accuracy, the nonprismatic beam-column element was used in modeling the columns and rafters of the frames. Smith (2013d) has already shown that the nonprismatic beam-column

element in SAP2000 provides sufficiently accurate results when the column or rafter segment is discretized into four elements. This was verified using the benchmark problems in AISC Design Guide 25 (Kaehler et al. 2011). The nonprismatic frame element's formulation has not changed from Version 15.0.0 to Version 19.2.2. Figure 4-2 shows a single frame for Model 85.

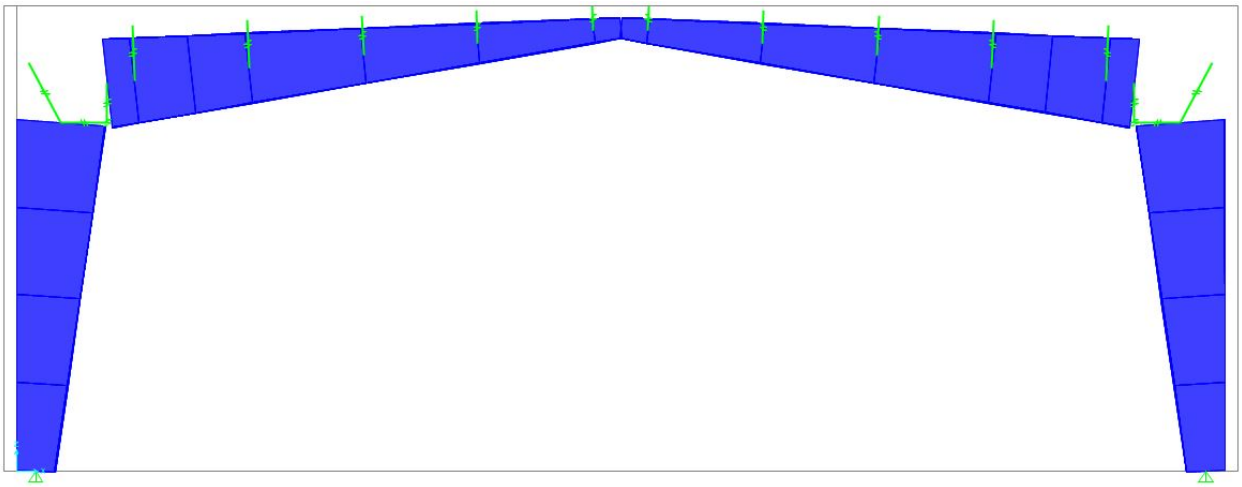

Figure 4-2. Extruded View of Discretization of Frame 85 into Nonprismatic Elements

To build the nonprismatic element, the two end cross-sections were generated. SAP2000 allows the user to set the variation in flexural stiffness for major axis bending and minor axis bending. The formula used in the moment of inertia variation for the nonprismatic element is shown in Figure 4-3. For linear web-tapered members, the variation in the major axis moment of inertia is predominantly a parabolic function. The axial, shear, torsional, mass, and weight properties all vary linearly over each segment (CSI 2017). The variation in the major axis was set to parabolic and for minor axis, a linear variation was set.

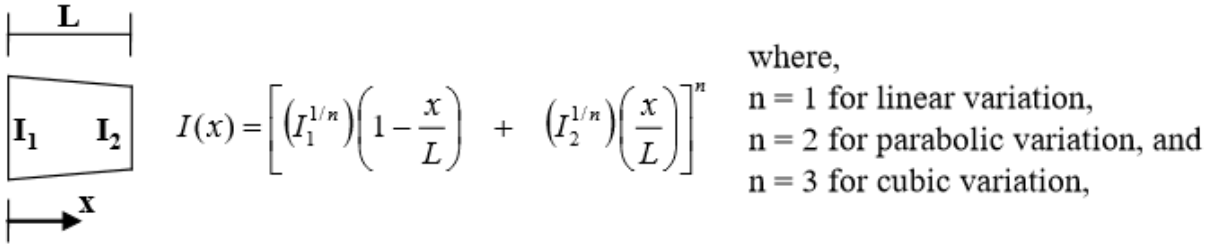

Figure 4-3. SAP2000 Nonprismatic Moment of Inertia Variation (CSI 2017)

One fundamental characteristic of singly symmetric cross-sections that are web-tapered is that the centroidal axis is curved (Figure 4-4). When an axial load is present, this out-of-straightness results in a second order P-δ effect in that segment. For this research, the nodal locations were computed as the centroidal locations. Thus, curvature in the centroidal axis is accounted for in all models.

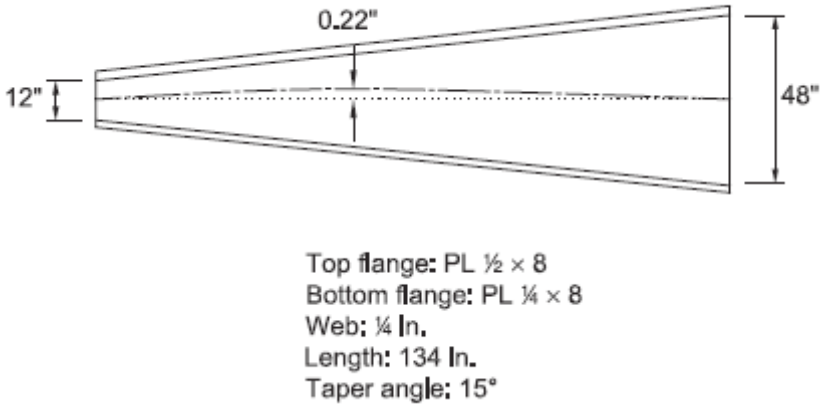

Figure 4-4. Curved Centroidal Axis of Singly Symmetric Tapered Member (Kaehler et al. 2011)

At the location of segment transitions, the use of different flange sizes is common. When this occurs, there exists a discontinuity in the theoretical centroidal axes (Figure 4-5). In some instances, this separation can be as high as a several inches (Kaehler et al. 2011). The SAP2000 frames in this research use a rigid link to connect the two nodes whenever this situation is encountered (Figure 4-6).

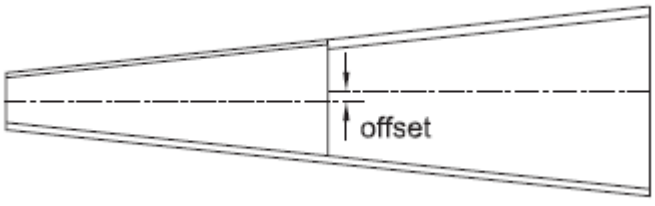

Figure 4-5. Centroidal axis offset at a plate change (Kaehler et al. 2011)

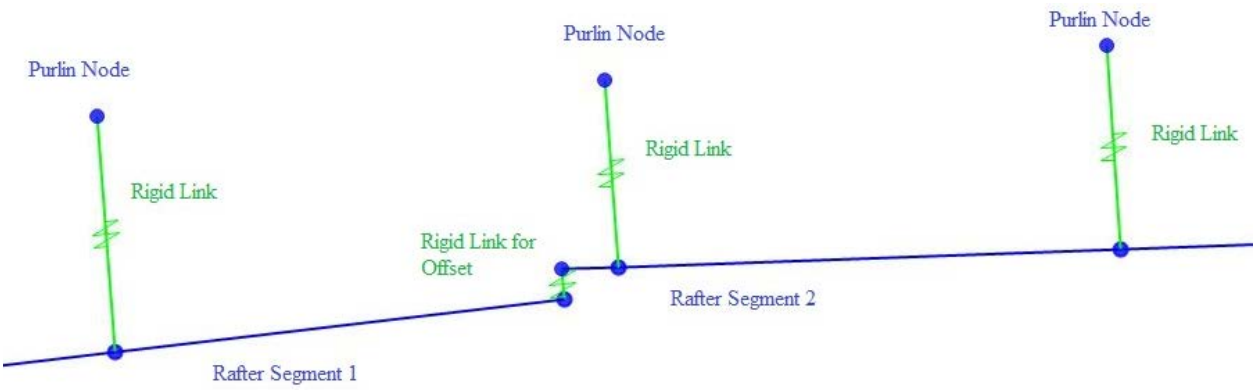

Figure 4-6. Rigid Link connecting two nodes with Different Centroidal Locations

4.4.2. Panel Zone Modeling

As stated in the literature review, it has been recognized that the panel zone is not a rigid element in metal building systems. Ignoring the flexibility of the panel zone would cause the structural model to be too stiff and underpredict lateral deflections. There exist several methods for modeling panel zones that have been used in the metal building industry and other that have been proposed in recent research. This research uses the same modeling technique presented by Smith (2013d). His proposed panel zone modeling was superior to the others due to its kinematic accuracy. Figure 4-7 shows the panel zone region as it was modeled in SAP2000. A double node was placed at the location of the interior bottom corner of the panel zone. A zero-length rotational link element connects the double nodes together. A rigid link element connects the top of the column centerline node to one side of the panel zone spring element. A second link element connects the other end of the panel zone element to the centerline node of the rafter. A rigid link was extended to the location of the spandrel beam near the backside of the panel zone.

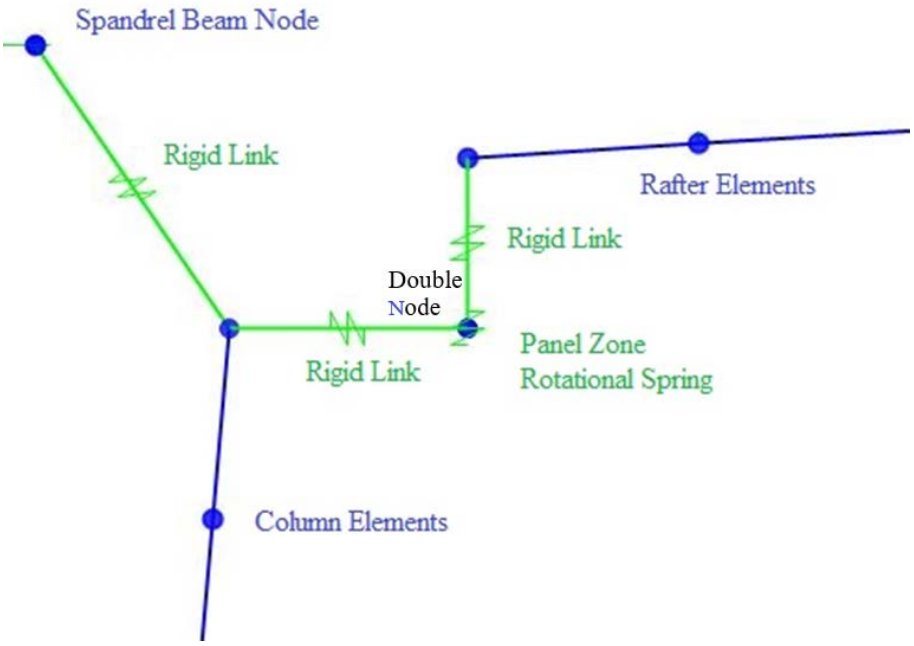

Figure 4-7. Panel Zone Modeling Scheme

The rotational spring stiffness was derived using the same procedure in Abaqus (Simulia 2016) described by Smith (2013d). The spring stiffness values calculated in each model are displayed in the table below. Because Frame 42 has a monoslope roof, the panel zones for the right side and the left side were different.

Table 4-2. Rotational Stiffness for Panel Zone Spring

Model Number	Rotational Stiffness (kip-inches/radian)
16	2790000
41	6120000
42 Left	4464000
42 Right	6197000
85	1060000
138	4700000

The panel zone modeling scheme was originally developed for use in a 2-D planar frame analysis. For this research, it was assumed that the panel zone flexibility in the out-of-plane

direction would not be considered. With this rigidity, the torsional rotation at the top of the column well be equal to the minor axis bending rotation in the rafter. Torsional rotation in the rafter will equal the column minor axis rotation.

4.4.3 Column-to-Base Connections

As mentioned in the literature review regarding Bajwa's (2010) research, the true column-base connection is partially rigid. The connection rotational stiffness can be determined through a detailed finite element model of the column-to-base connection. For a static analysis, all the factors identified by Bajwa that affect the rotational stiffness remain constant. A discrete rotational stiffness can be extracted for such static load situations. However, due to the change in axial load in the column during a dynamic analysis, the rotational stiffness of the connection changes during the analysis. It is unlikely that a discrete rotational spring model, or any of the simplified model configurations that were proposed by Bajwa (2010), could be used to capture the changing rotational stiffness due to the changing axial load that exists during a dynamic earthquake analysis. A refined finite element model of the connection would handle this complex behavior, but it was decided not to include it in the SAP2000 models as it would have significantly increased the complexity of the model. Therefore, the columns in this research utilized an ideal pin condition.

4.5 Metal Building Frame Inelastic Behavior

One very crucial and challenging aspect about modeling the full behavior of metal building frames was how to include inelastic behavior in the SAP2000 model. Because metal building frames are composed of noncompact flanges and slender webs, flexural capacities are controlled by stability limit states such as lateral-torsional buckling (LTB). The formation of a plastic hinge,

like those in conventional steel moment frames, simply cannot happen. Therefore, the use of a traditional plastic hinge is not appropriate for modeling inelastic behavior of metal building frames. A modeling procedure that captures the post-buckling response of a metal building frame during an earthquake excitation using only frame elements does not currently exist. The use of shell elements has the capability of capturing this post-buckling behavior, but for this research, the exorbitant time required to run numerous nonlinear response history analyses would be prohibitive. This research relies on the fundamental characteristics of LTB to develop a custom frame hinge in SAP2000 that approximates the post-buckling response.

4.5.1 Metal Building Moment Frame Shell Finite Element Model

In a conventional steel moment frame, the location of the plastic hinges is well known. For metal building frames, the location of the critical segment is not as straightforward because the nonprismatic frame has been optimized for the capacity to meet the demand along the entire frame. In order to determine the capacity of the metal building frame, nonlinear static pushover analyses were performed in Abaqus.

As stated in the literature review, Hong (2007) developed a finite element analysis procedure for determining the capacity of metal building frames. In order to verify the finite element analysis procedure used in this research, the Hong test frame was recreated in Abaqus and the analysis results were compared with experimental results.

The metal building columns and rafters were modeled using a reduced integration shell element with 4 nodes (SR4). Twenty shell elements were used along the depth of the web, and the flanges were discretized into 12 elements (Figure 4-8).

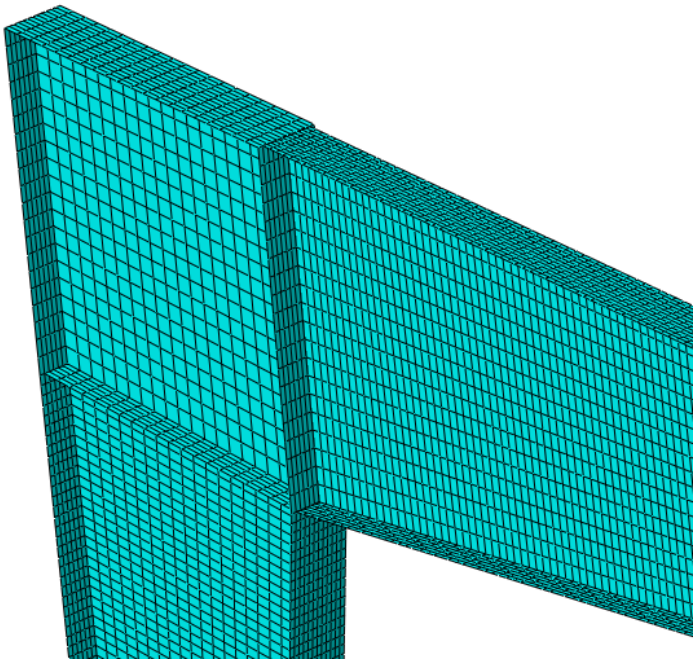

Figure 4-8. Mesh Refinement for Flanges and Webs

The stress-strain diagram used for the steel material is shown in Figure 4-9. The true stress strain curve was used because the SR4 element is formulated for large displacements.

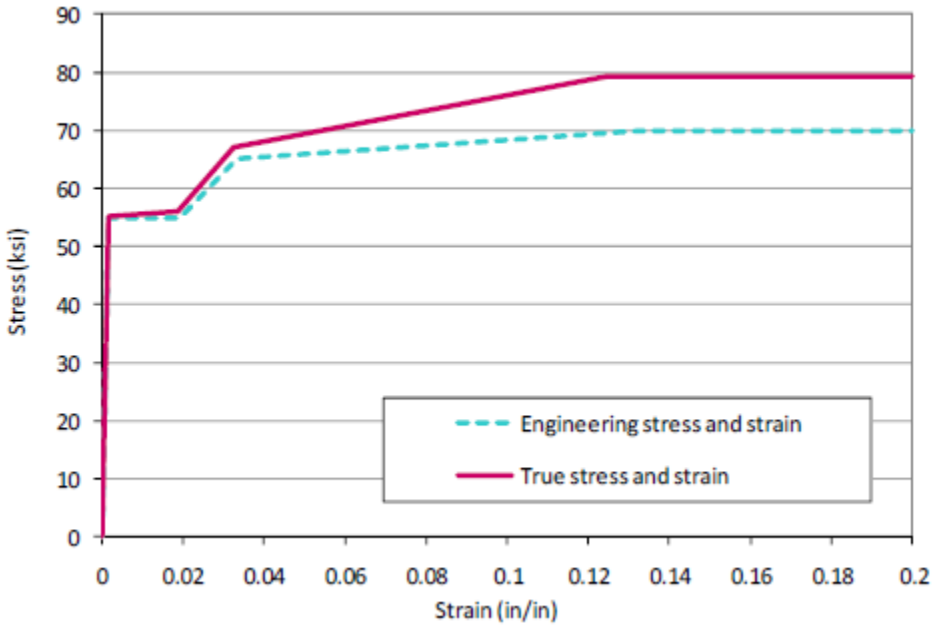

Figure 4-9. Typical Stress-Strain Curve (F_y = 55 ksi) (Kim 2010)

Hong (2007) showed that the inclusion of a rotational spring at the base of the column improved the accuracy of the finite element model. However, the rotational spring stiffness was derived from the experimental results. Because such data does not exist for the frames used in this research, the base of the columns assume an ideal pin condition. The out-of-plane displacement was restrained at locations where a purlin with a flange brace exists. Wherever there was a purlin, the out-of-plane displacement at the centroid of the purlin (four inches above the flange) was restrained. The rafter was constrained to rotate about the centroid of the purlin (Figure 4-10).

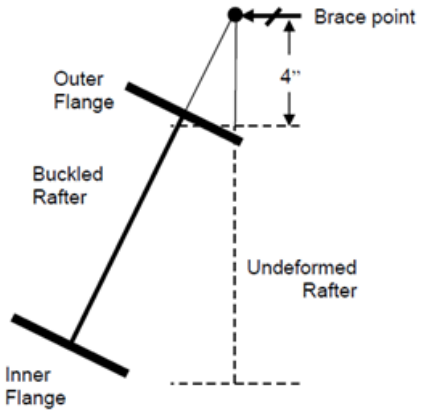

Figure 4-10. Constraint Condition for Outer Flange (Smith 2013c)

One of the models was a modular frame in which interior columns were present. The interior columns were not modeled using shell elements. Instead, the interior column was discretized into 10 frame elements. Because the interior column is a leaner column, the base and the connection with the rafter were modeled as pinned connections.

To accurately simulate a physical system like a metal building frame, it is imperative to include appropriate imperfections. Without such imperfections the failure mechanism would be incorrect. An eigenvalue buckling analysis was performed using the equivalent lateral force load, dead load, collateral load, and snow load. The buckling mode shapes exhibited web buckling. The

first positive buckling mode shapes were imposed as an initial geometric imperfection with the magnitude set to L/1000, with L being the length of the unbraced segment (Hong 2007).

The inclusion of residual stresses and an additional compression flange sweep was investigated to see if it had a significant impact in the frame's capacity. A residual stress pattern for welded I-shaped members was imposed in the Abaqus model (Figure 4-11). When the web residual compressive stress exceeded the critical plate buckling load of the web, the residual stress values were scaled back to just below the critical buckling stress. To generate this sweep, a distributed out-of-plane load was applied to the nodes along the compression flange. The maximum displacement of the compression flange sweep was set to a magnitude of L/1000 (Kim 2010).

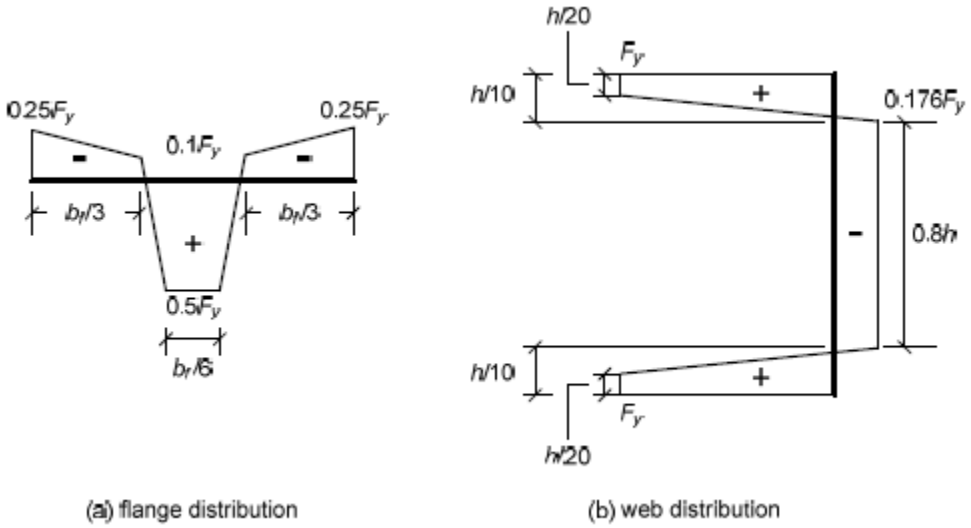

Figure 4-11. Residual Stress Pattern for Flanges and Webs (Kim 2010)

Before the pushover analyses were performed, the dead, collateral, and 20% of the full snow load were applied to the imperfect frame. The pushover analysis was performed using the Modified-Riks Algorithm. The only load pattern that the solution algorithm adjusted was the lateral load.

4.5.2 Shell Model Verification

Figure 4-12 shows the comparison of the two modeling procedures of the Hong test frame with the experimental results. The first modeling procedure includes the eigenvalue buckling mode imperfection and the second modeling procedure includes the addition of a residual stress pattern and a compression flange sweep. Both modeling procedures underestimate the lateral stiffness of the frame because a column base was idealized as a pin-connection. Hong (2007) asserts that models with ideal hinges at the column bases underestimate the lateral stiffness, but are acceptable. The first modeling procedure underestimated the frame's peak capacity by 15% while the second underestimated the strength by 40%. It is likely that the residual stress pattern was too severe. The compression flange sweep imperfection was set to the maximum tolerance allowed for in-field construction. Based on these results, the first modeling procedure was deemed acceptable and was used for all remaining pushover analyses.

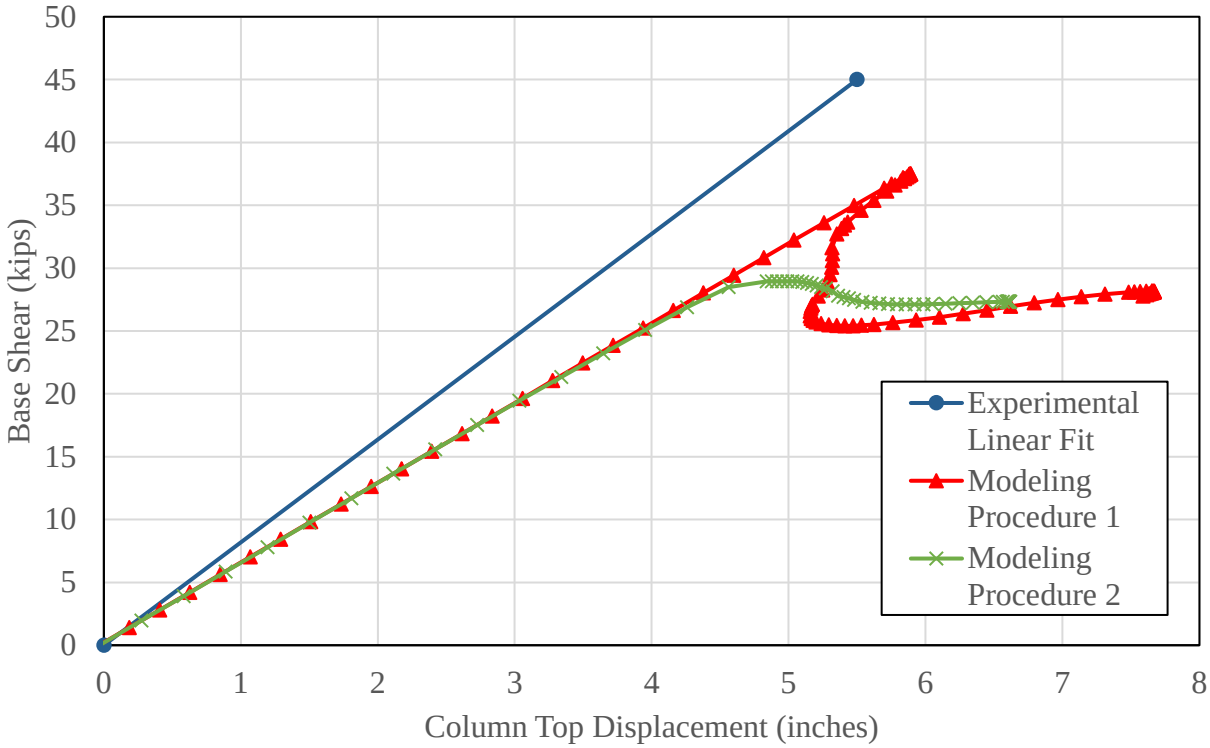

Figure 4-12. Comparison of Finite Element Analysis Modeling Procedures

4.6 Metal Building Frame Capacities

The pushover analysis results and failure mechanisms for each frame are discussed in the following section.

4.6.1 Frame 16 Pushover Results

This model is a clear span symmetrical gable frame with a span of 40 feet and eave height of 30 feet (Figure 4-13). The post-buckled shape at the end of the analysis is shown in Figure 4-14. The pushover curve for Frame 16 is displayed in Figure 4-15. The elastic behavior ends at roughly 2.8 inches of displacement or 0.8% story drift. When the base shear reached 35 kips, inelastic lateral torsional buckling occurred in segment S4 in the unbraced segment closest to the column. The von Mises stress contours and equivalent plastic strain contours for the buckled segment are shown in Figures 4-16 and 4-17. According to Smith (2013c), LTB of a rafter segment was accompanied by flange local buckling at the middle of the segment and at the flange brace points. This characteristic can be seen in Figure 4-16. After LTB, the frame lost 23% of its peak strength. At 4.0 inches of displacement or 1.1% story drift, flange local buckling occurs at the top flange in segment S3 in the unbraced segment closest to the column. The von Mises stress contours and equivalent plastic strain contours for this buckled segment are shown in Figures 4-18 and 4-19. At this point in the analysis, the frame has formed a collapse mechanism.

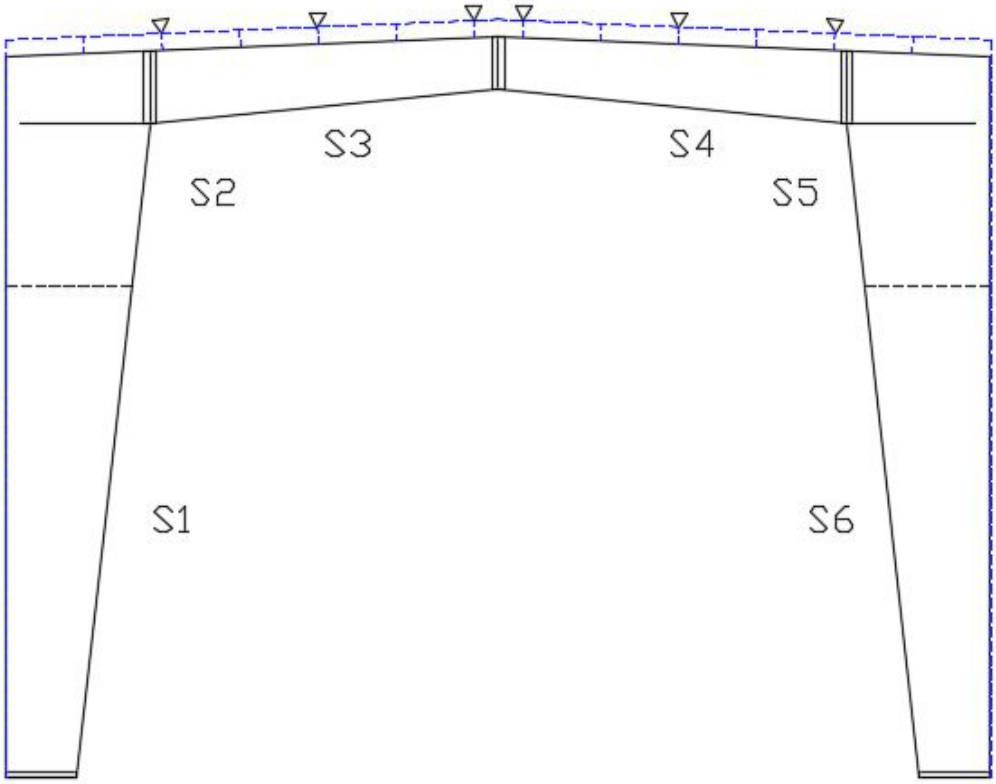

Figure 4-13. Segment Identification for Frame 16

Figure 4-14. Post-Buckled Frame at the End of Analysis (Deformation Scale Factor = 3)

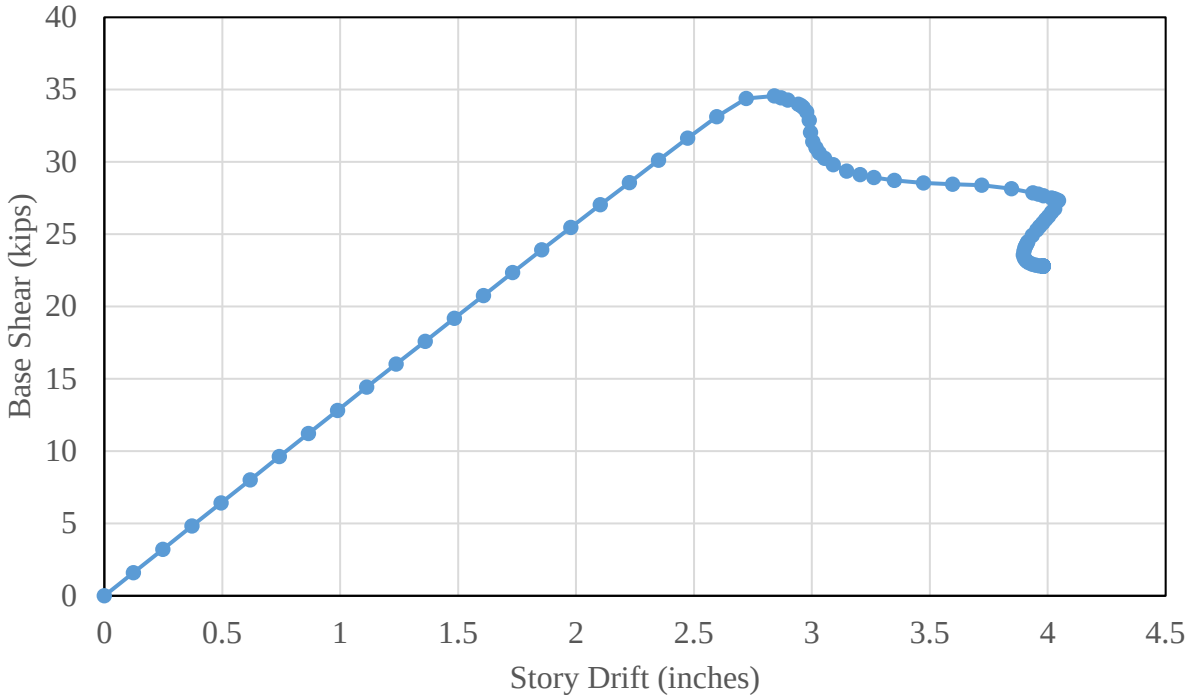

Figure 4-15. Pushover Curve for Frame 16

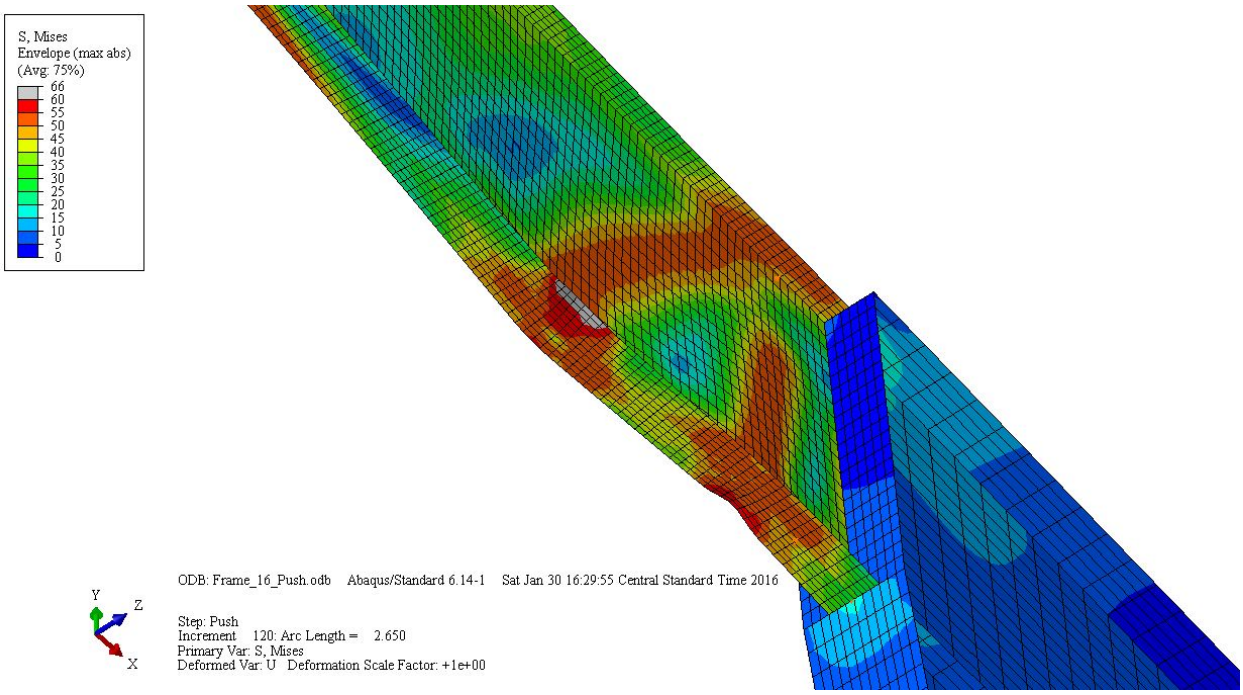

Figure 4-16. Von Mises Stress Contours for LTB Segment in Frame 16

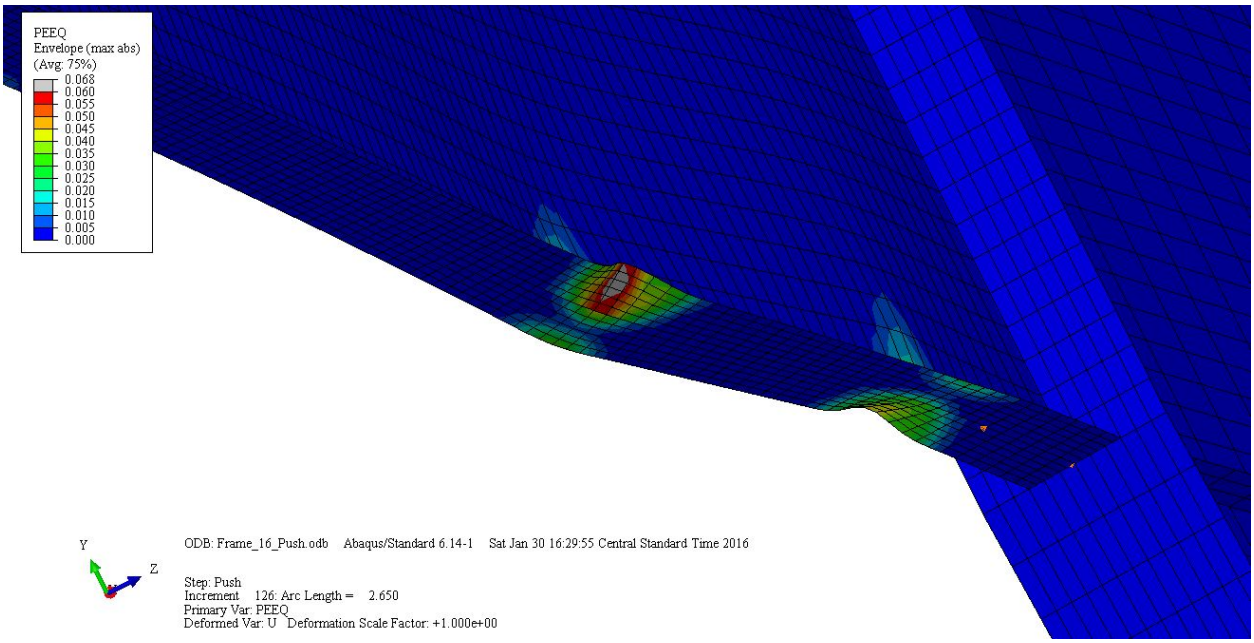

Figure 4-17. Equivalent Plastic Strain Contours for LTB Segment in Frame 16

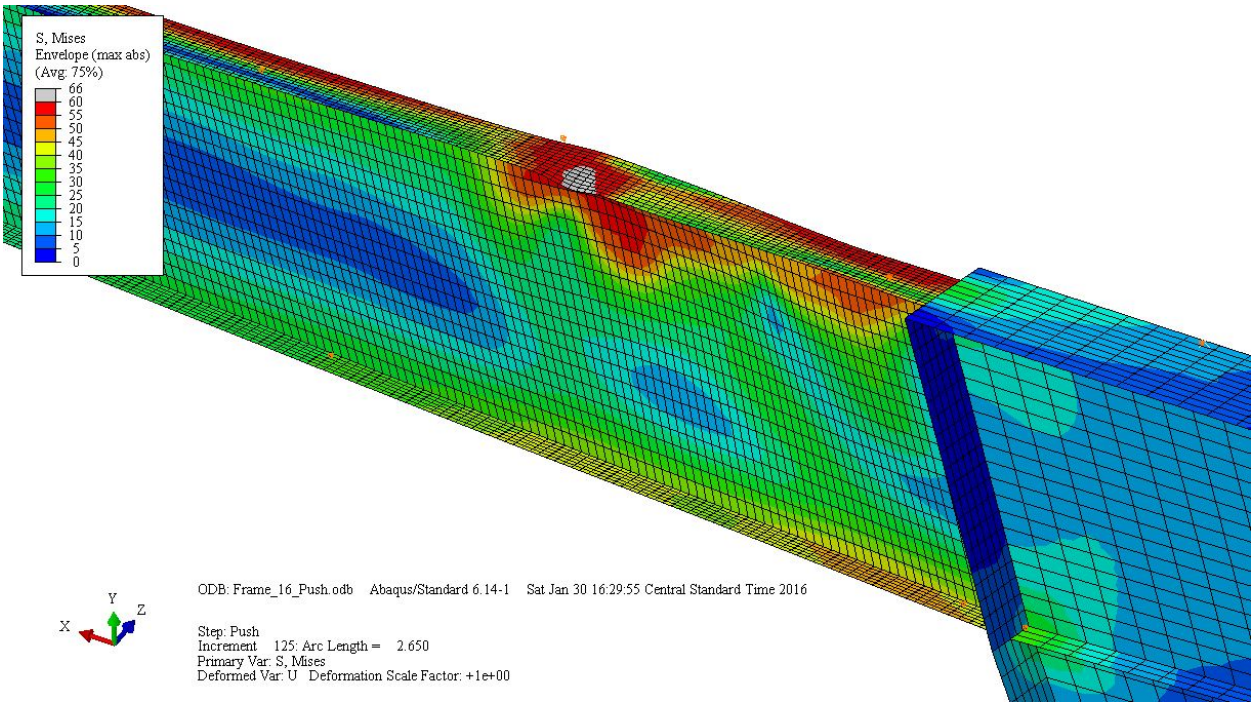

Figure 4-18. Von Mises Stress Contours for FLB Segment in Frame 16

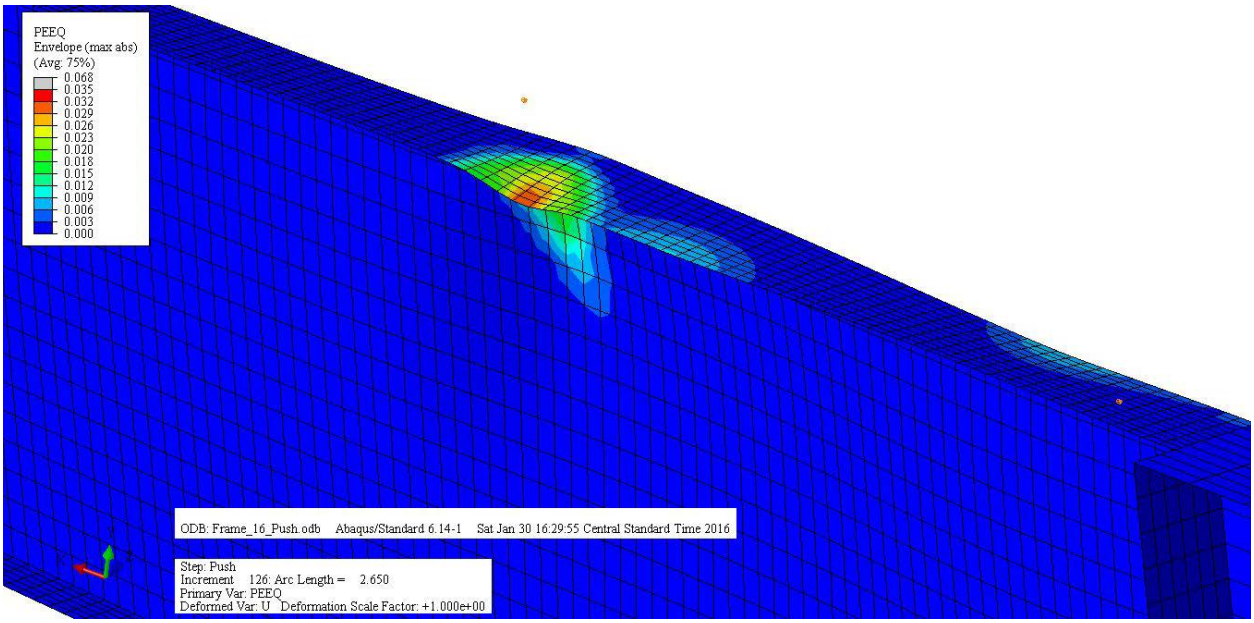

Figure 4-19. Plastic Equivalent Strain Contours for FLB Segment in Frame 16

4.6.2 Frame 41 Pushover Analysis

This model is a clear span symmetrical gable frame with a span of 100 feet and eave height of 30 feet (Figure 4-20). The post-buckled shape at the end of the analysis is shown in Figure 4-21. The pushover curve for Frame 41 is displayed in Figure 4-22. The elastic behavior ends at roughly 5.4 inches of displacement or 1.5% story drift. When the base shear reached 69 kips, inelastic lateral torsional buckling occurred at the pinch point between segments S6 and S7. The von Mises stress contours and equivalent plastic strain contours for the buckled segment are shown in Figures 4-23 and 4-24. Unlike Frame 16, the pushover analysis failed to converge soon after LTB occurred. This frame exhibited the most severe post buckling path of all the frames analyzed.

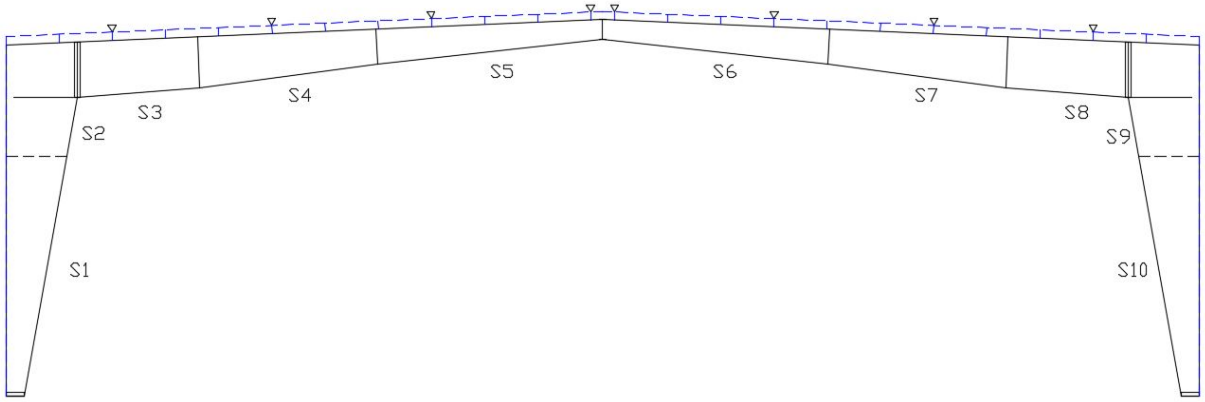

Figure 4-20. Segment Identification for Frame 41

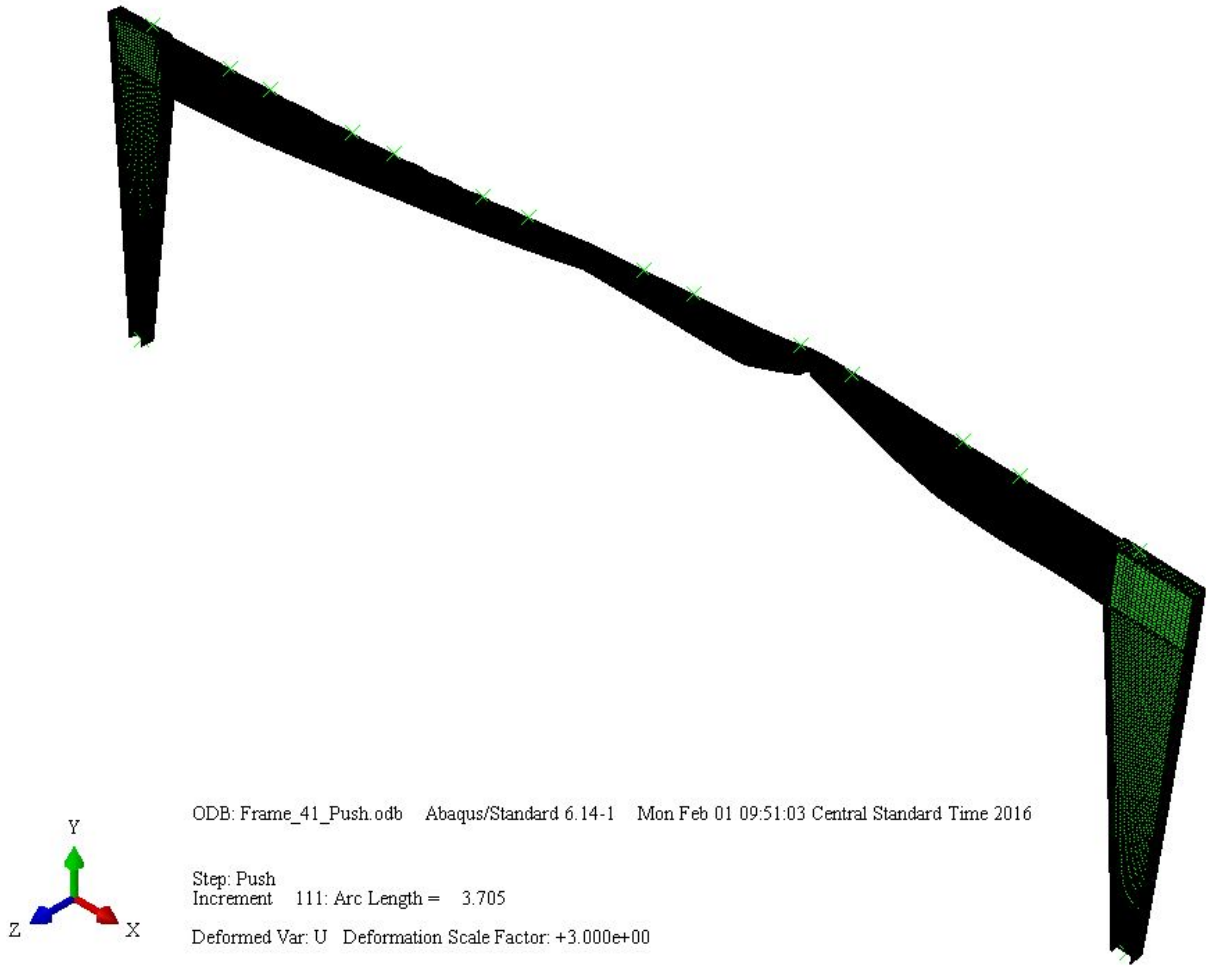

Figure 4-21. Post-Buckled Frame at the End of Analysis (Deformation Scale Factor = 3)

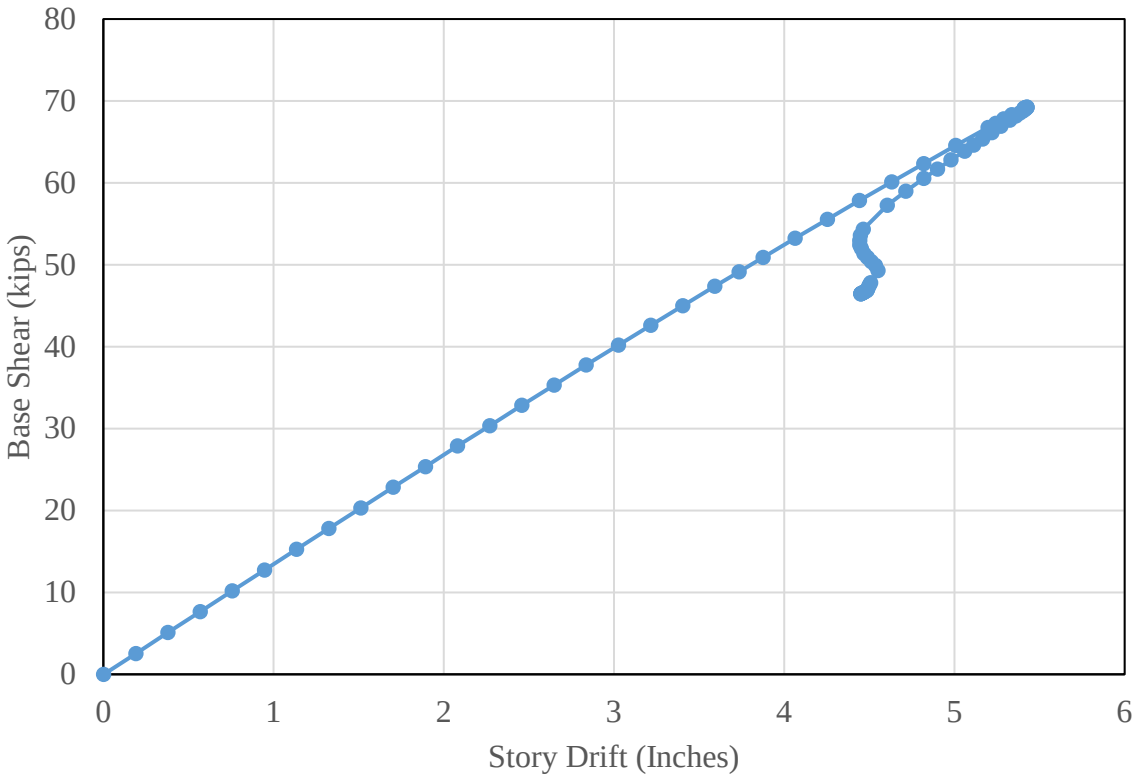

Figure 4-22. Pushover Curve for Frame 41

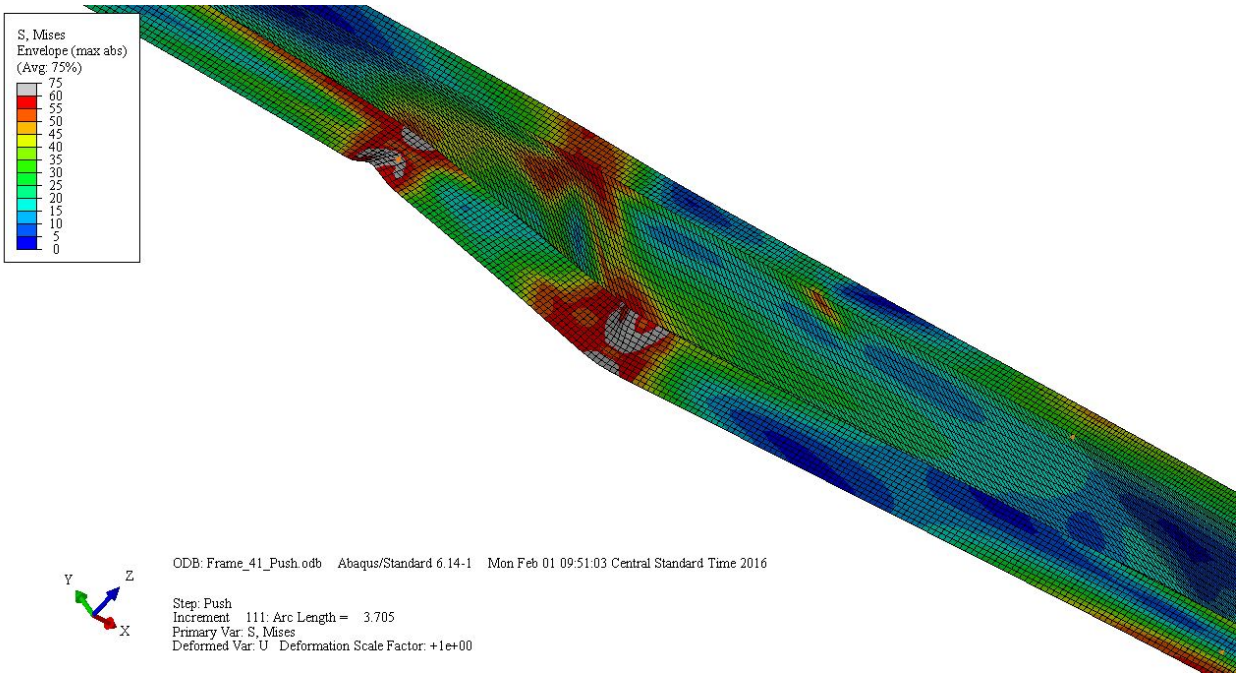

Figure 4-23. Von Mises Stress Contours for LTB Segment for Frame 41

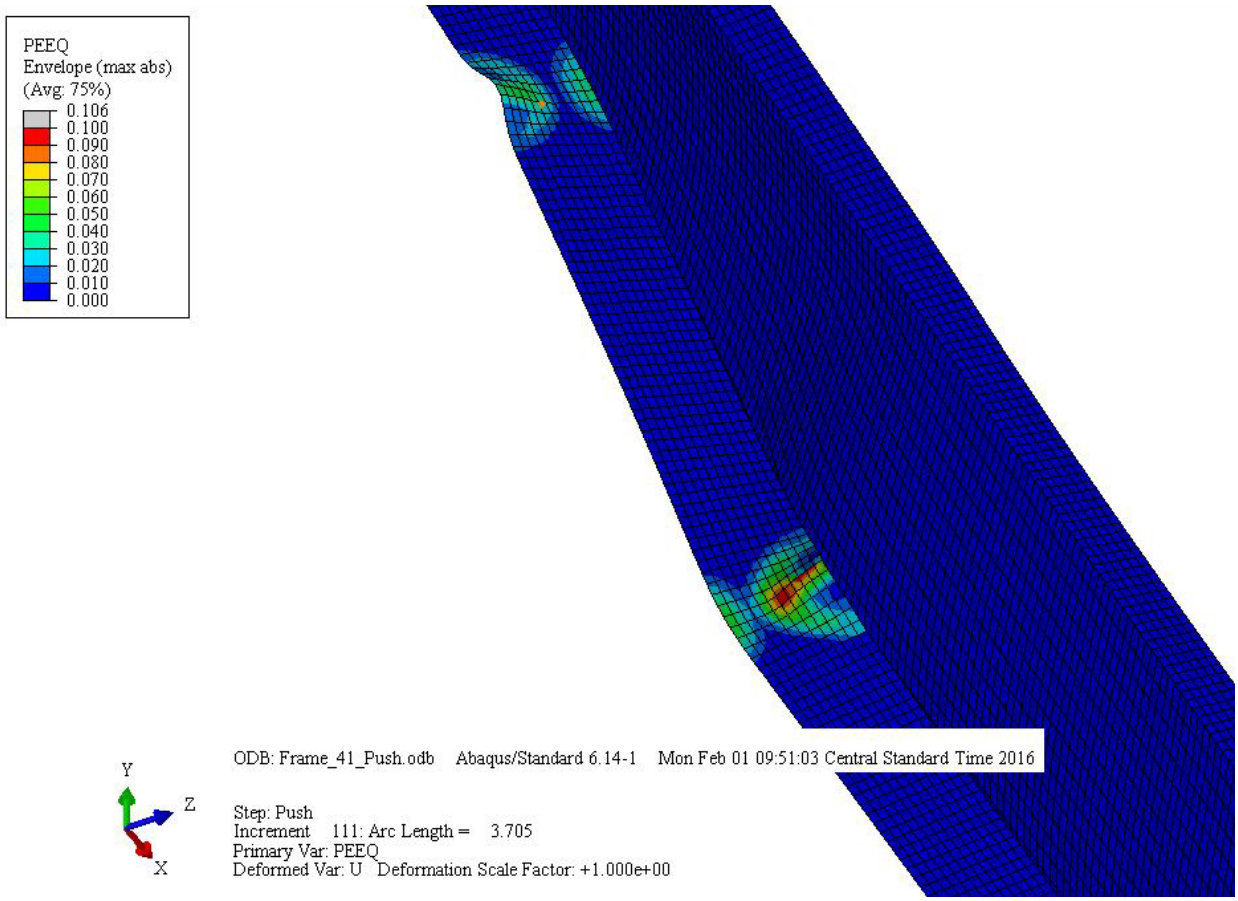

Figure 4-24. Equivalent Plastic Strain Contours for LTB Segment for Frame 41

4.6.3 Frame 42 (Push East) Pushover Results

The same frame was analyzed with the lateral load application to the right (Figure 4-25). The post-buckled frame is displayed in Figure 4-26. The pushover curve for this frame is shown in Figure 4-27. The elastic behavior ends at roughly 8.7 inches of displacement or 2.4% story drift, which is quite considerable. When the base shear reached 184 kips, LTB occurred at the pinch point between segments S9 and S10. The von Mises stress contours and equivalent plastic strain contours for the buckled segment are shown in Figures 4-28 and 4-29. By the end of the analysis, the frame experienced a strength loss of 23% and a lateral displacement of 10.2 inches.

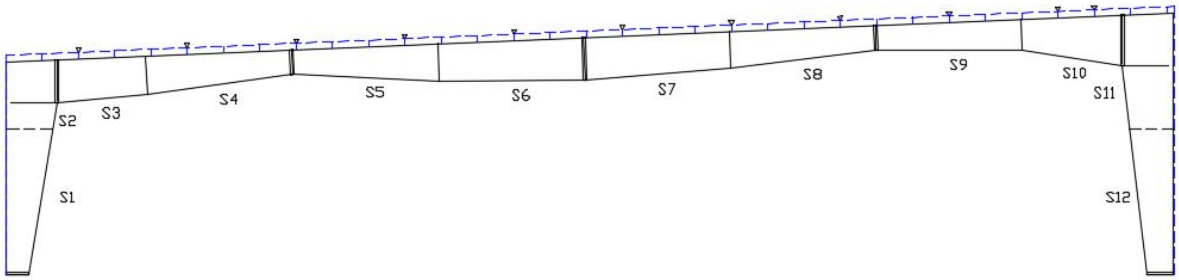

Figure 4-25. Segment Identification for Frame 42

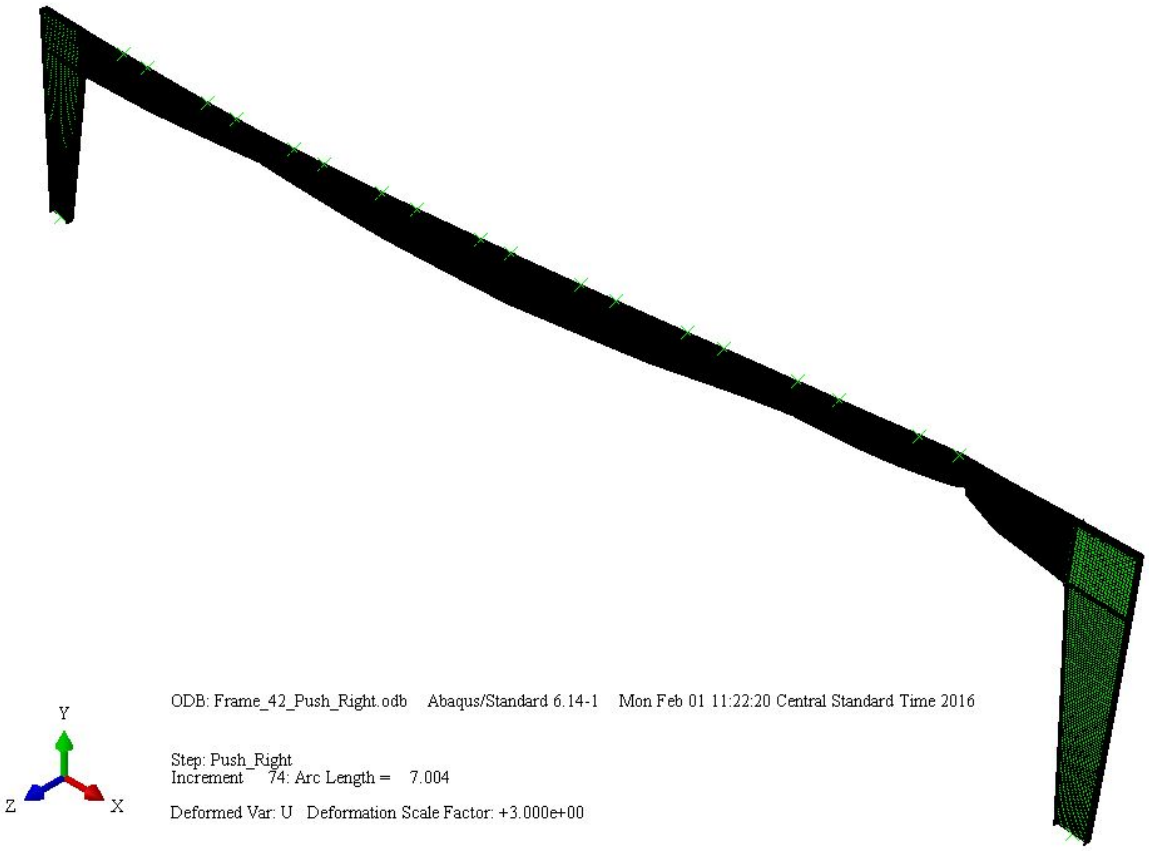

Figure 4-26. Post-Buckled Frame at the End of Analysis (Deformation Scale Factor = 3)

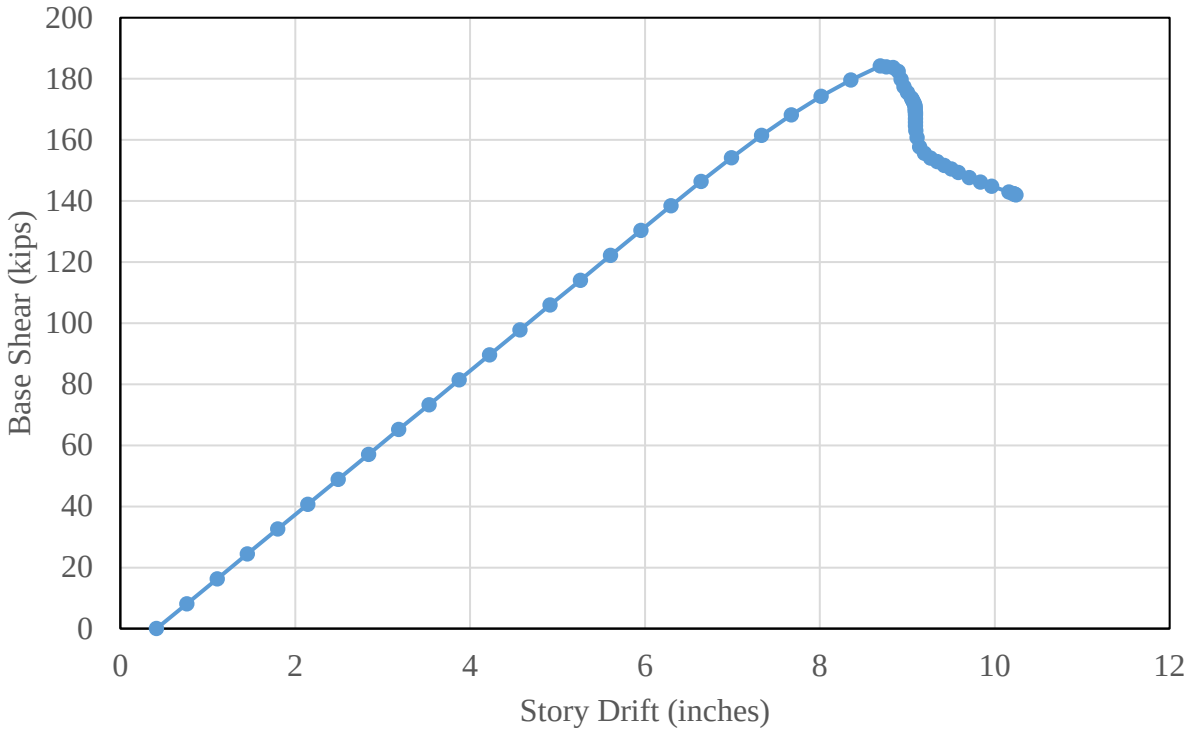

Figure 4-27. Pushover Curve for Frame 42 (East)

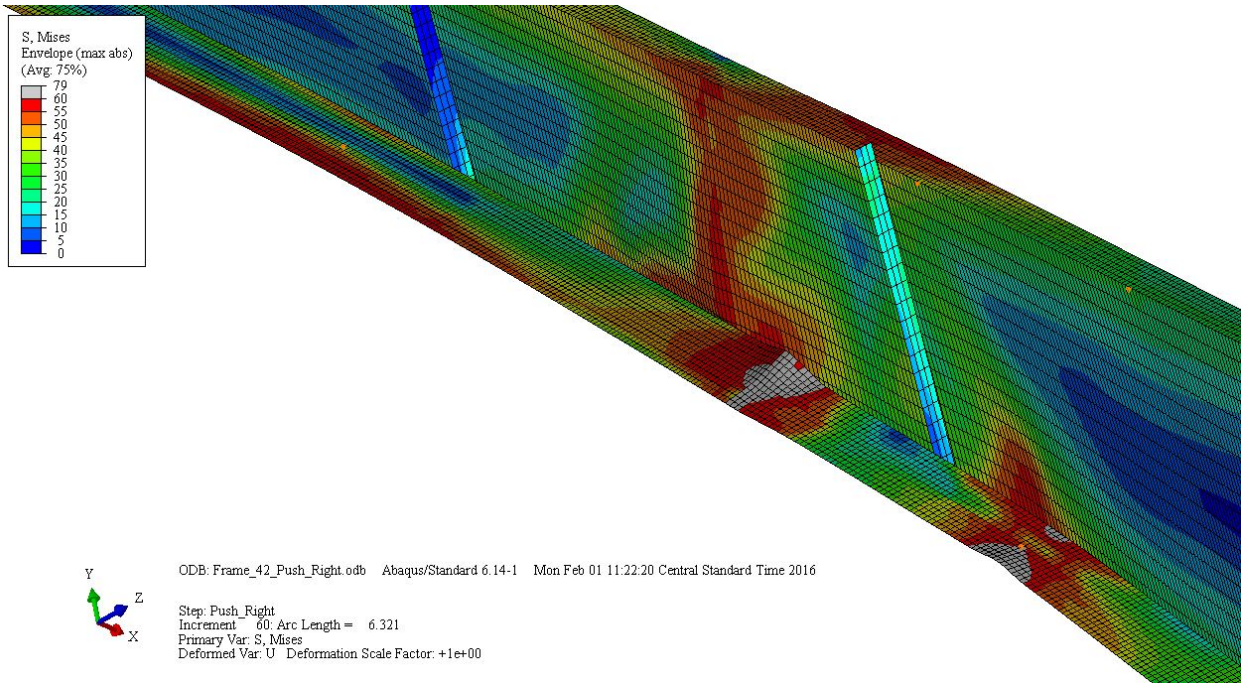

Figure 4-28. Von Mises Stress Contours for LTB Segment for Frame 42 (East)

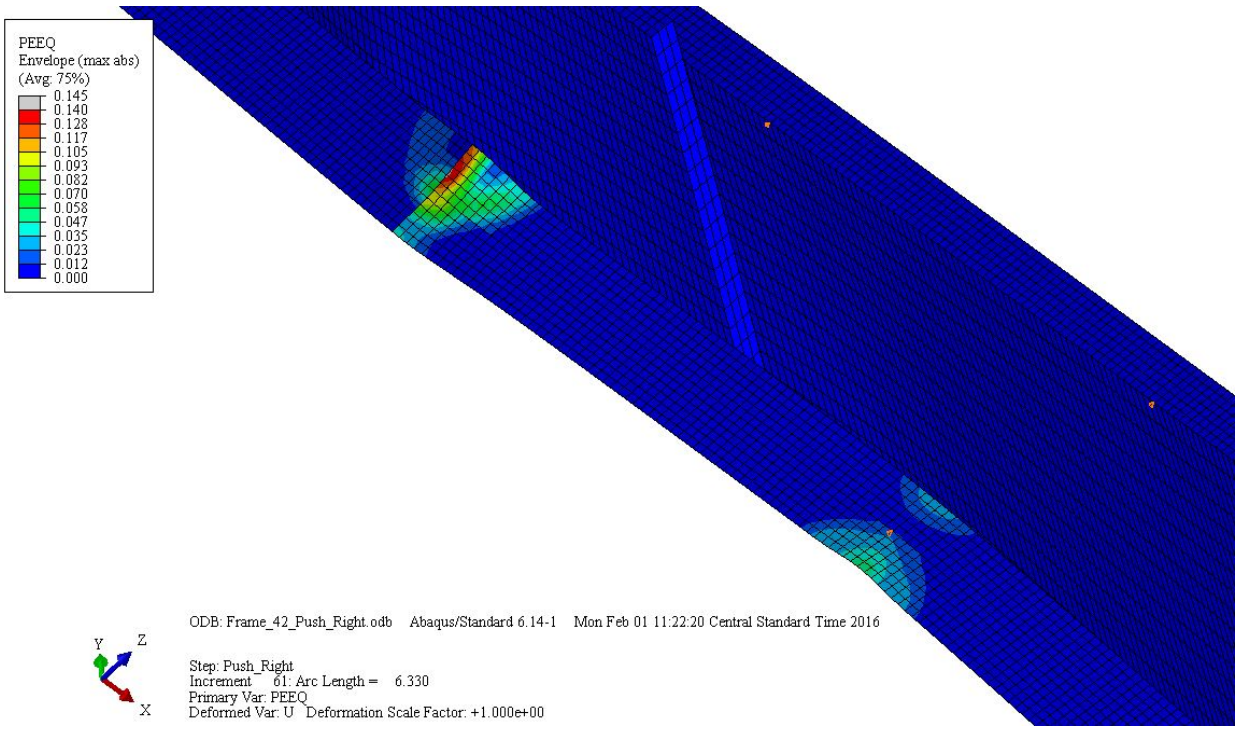

Figure 4-29. Equivalent Plastic Strain Contours for LTB Segment for Frame 42 (East)

4.6.4 Frame 42 (Push West) Pushover Results

This model is a clear span monoslope frame with a span of 160 feet and left eave height of 30 feet (Figure 4-30). Because this is an unsymmetrical frame, two pushover analyses were necessary to determine the failure progression for each direction. The pushover curve for this frame is shown in Figure 4-31. Because the frame is unsymmetrical, the application of the dead, collateral, and snow loads caused the frame to displace to the right. Due to this initial sway, the pushover curve does not begin at a lateral displacement of zero. The elastic behavior ends at roughly 6 inches of displacement or 1.7% story drift. When the base shear reached 147 kips, flange local buckling occurred in segment S5 in the region closest to segment S4. The post-buckled path showed a load reversal followed by a reduced positive frame stiffness. The analysis terminated at a story drift of 7.5 inches.

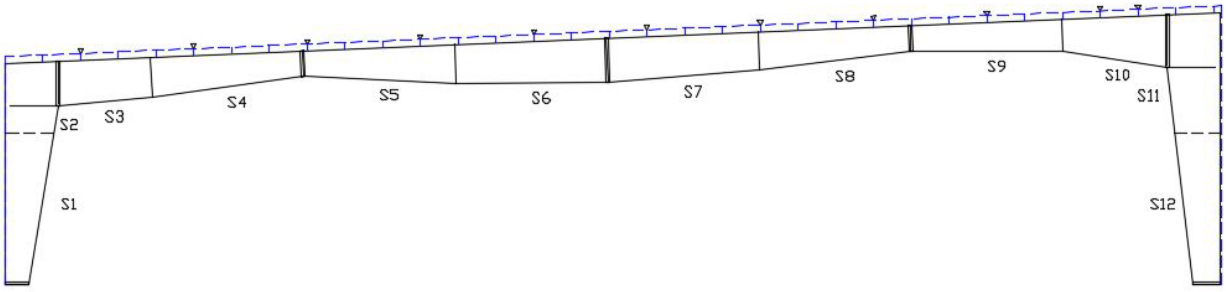

Figure 4-30. Segment Identification for Frame 42

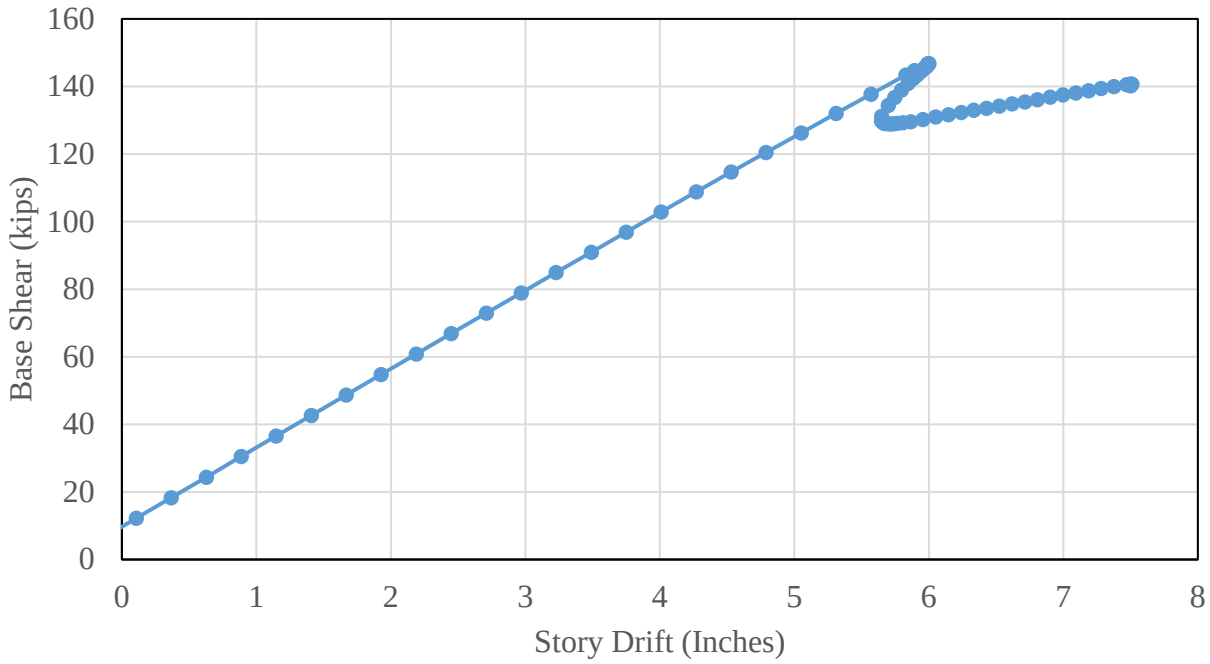

Figure 4-31. Pushover Curve for Frame 42 (West)

4.6.5 Frame 85 Pushover Results

This model is a clear span symmetrical gable frame with a span of 40 feet and an eave height of 15 feet (Figure 4-32). An analysis was performed using the flange web thickness for the column that was specified for the design. The first significant inelastic behavior occurred in the column in the form of FLB and LTB. Because the gravity load is supported by the column, any

stability failure of the column could compromise the integrity of the entire structure. This was deemed unsuitable for a seismic design. In order to move LTB into the rafter segment, a complete frame redesign that is highly optimized would have been necessary. As this is outside to scope of this research, the column flange thickness was increased from 0.188 inches to 0.25 inches so that LTB first occurred in the rafter segment.

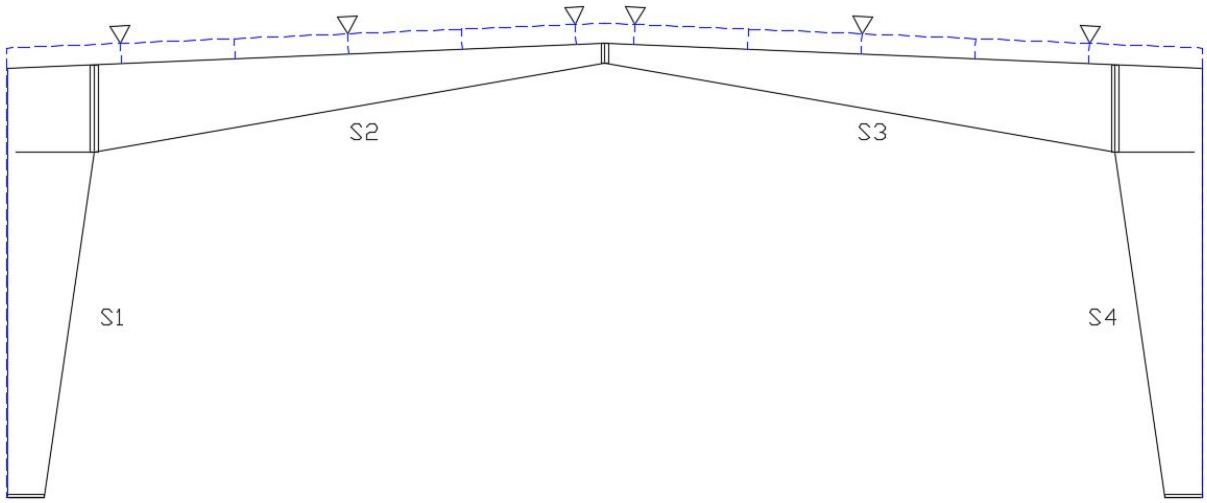

Figure 4-32. Segment Identification for Frame 85

The modified post-buckled frame at the end of the analysis is displayed in Figure 4-33. The pushover curve for this frame is displayed in Figure 4-34. Elastic behavior ends at a lateral displacement of 2.5 inches or 1.4% story drift. When the base shear reached 40 kips, distortional buckling occurred in segment S3 in the unbraced length closest to the column. The von Mises stress contours and equivalent plastic strain contours for the buckled segment are shown in Figures 4-35 and 4-36. This distortion lead to LTB in the rafter segment. The frame never achieved a positive stiffness following buckling. The second inelastic event was flange local buckling in the top flange near the ridgeline (Figures 4-37 and 4-38). The analysis terminated in a convergence

failure at a story drift of 4.8 inches. However, at this point in the analysis, a collapse mechanism in the frame has formed.

Figure 4-33. Post-Buckled Frame at the End of Analysis (Deformation Scale Factor = 3)

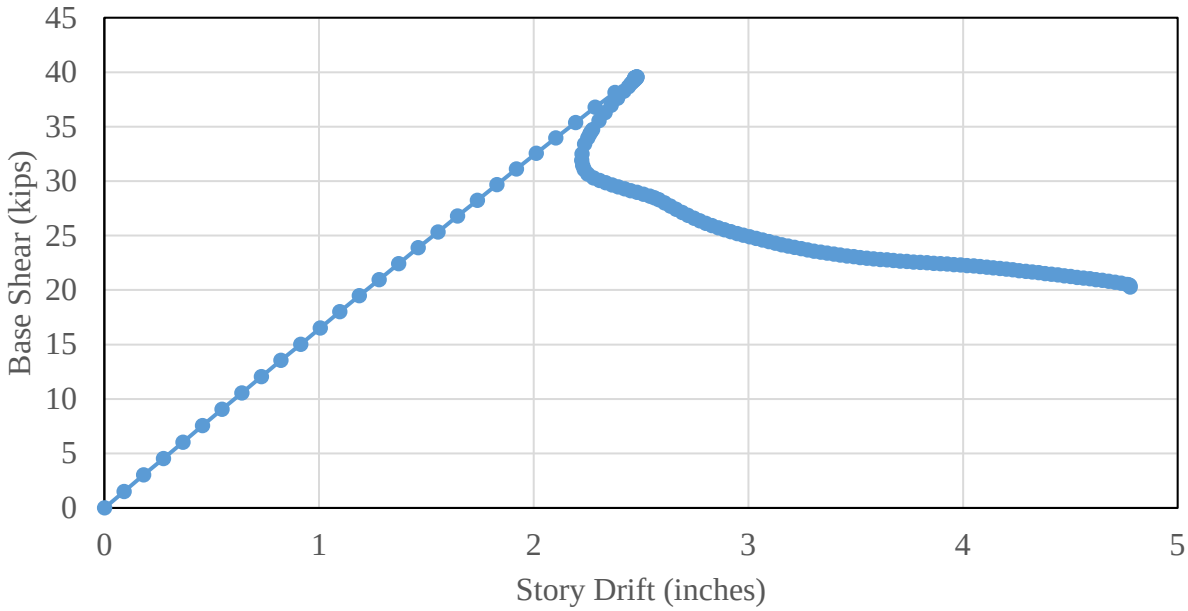

Figure 4-34. Pushover Curve for Frame 85

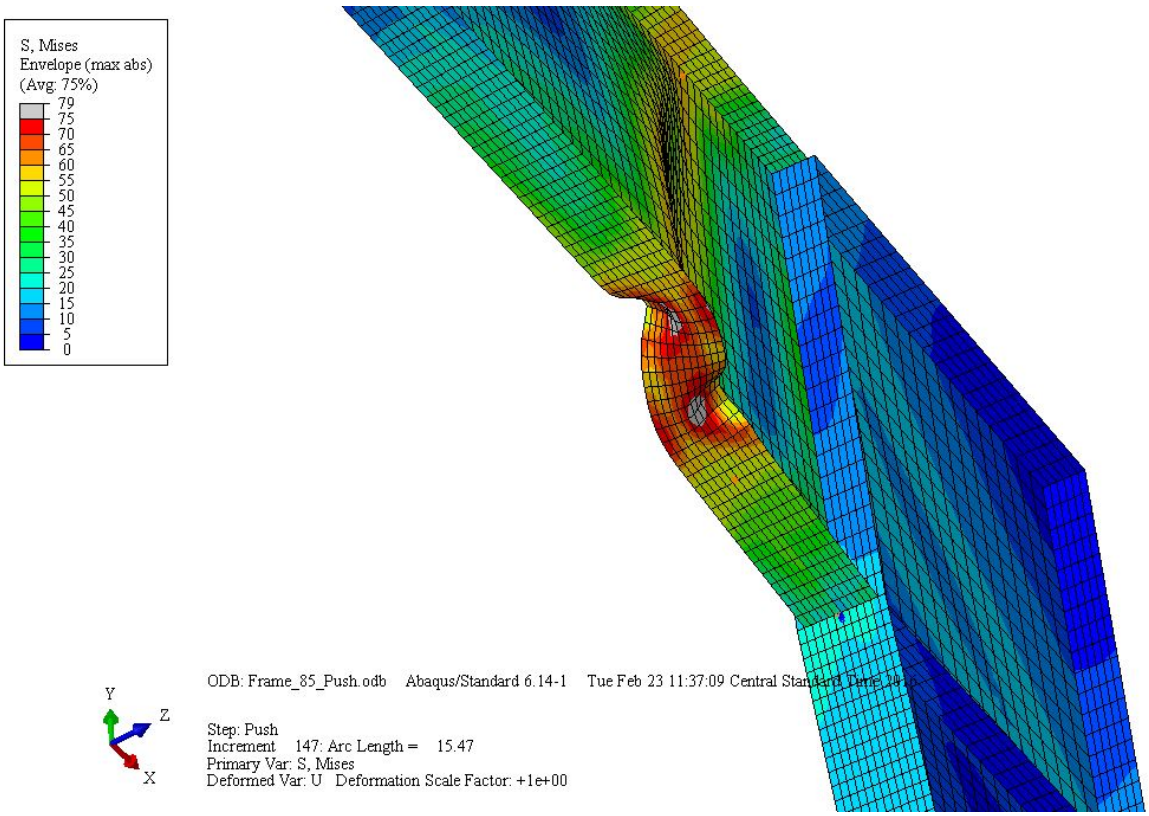

Figure 4-35. Von Mises Stress Contours for Buckled Segment in Frame 85

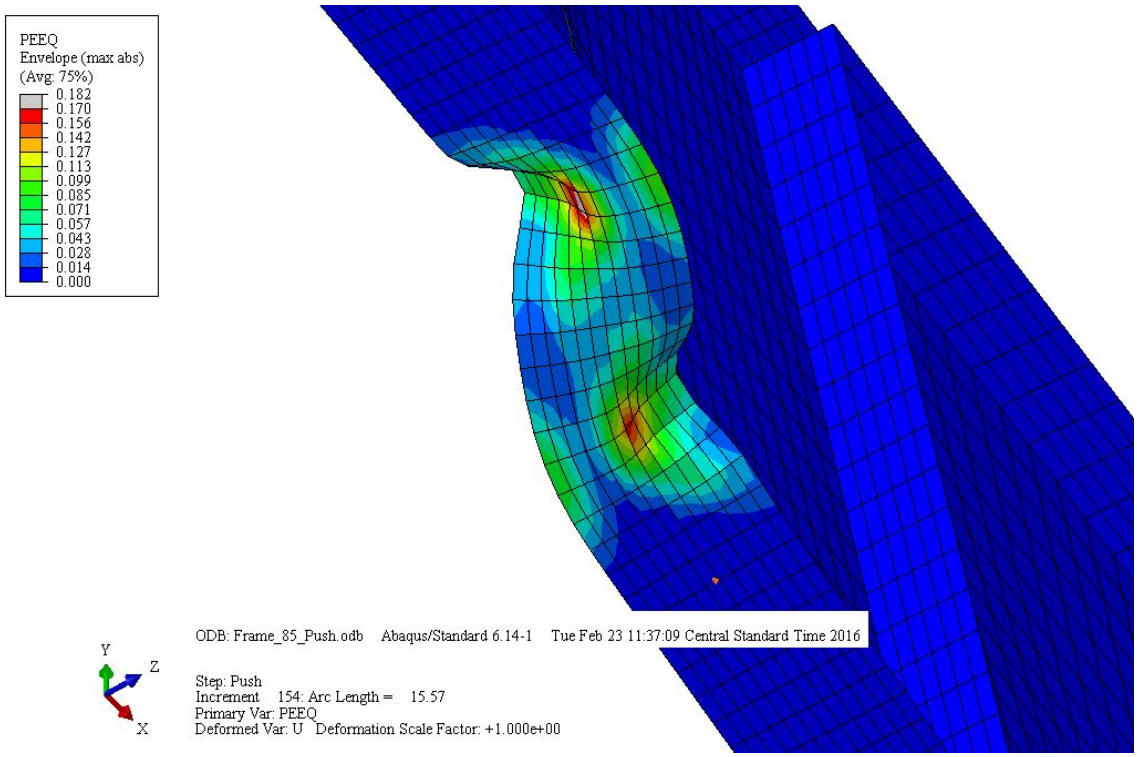

Figure 4-36. Equivalent Plastic Strain Contours for Buckled Segment in Frame 85

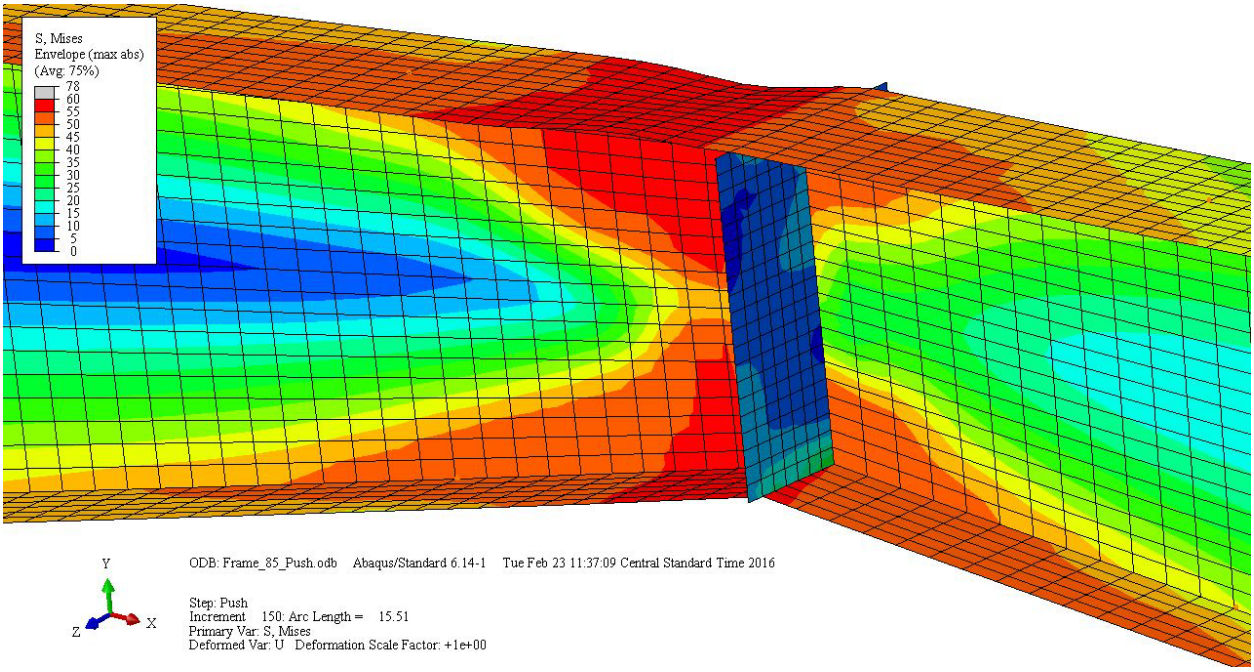

Figure 4-37. Von Mises Stress Contours for FLB in Frame 85

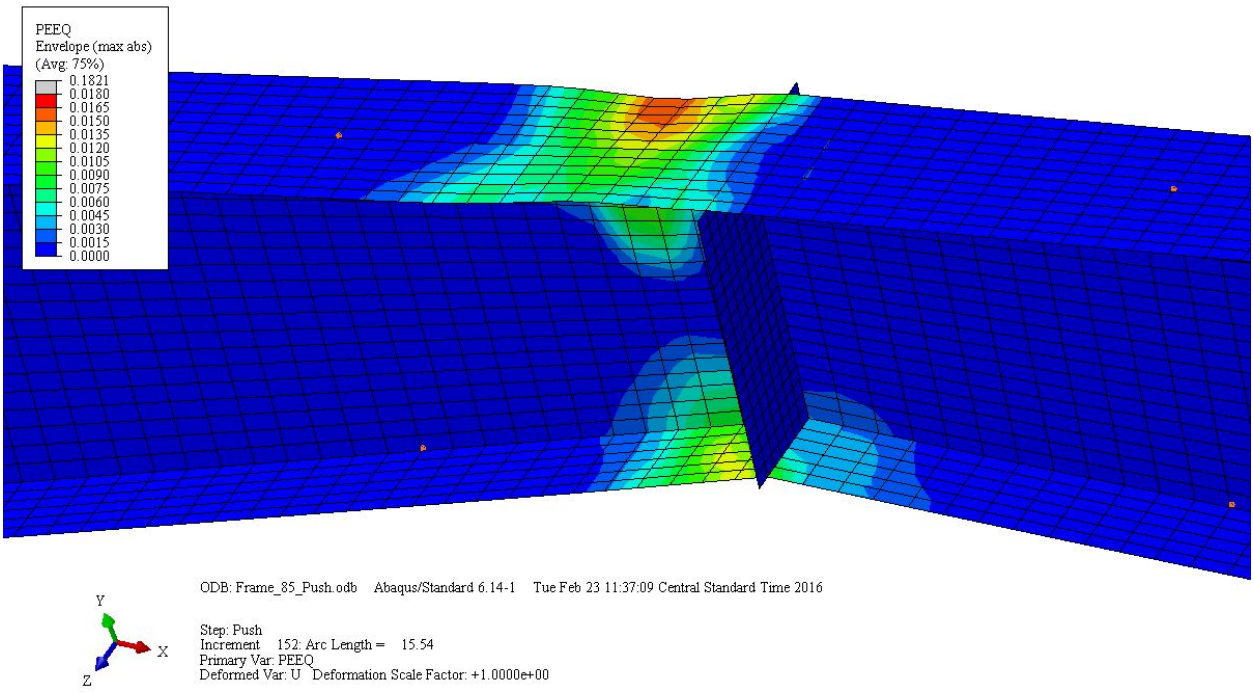

Figure 4-38. Equivalent Plastic Strain Contours for Buckled Segment in Frame 85

4.6.6 Frame 138 Pushover Results

This model is a modular symmetrical gable frame with one interior column. The frame has a total span of 120 feet and an eave height of 30 feet (Figure 4-39). The post buckled frame is shown in Figure 4-40. The pushover curve for this frame is displayed in Figure 4-41. The elastic portion ends at 5 inches of displacement or 2.4% story drift. When the base shear reached 58 kips, yielding of the column flanges near the base occurred first, followed by lateral torsional buckling of the column segment. When the frame was designed, the column base was fixed in order to meet the 2% seismic drift requirement. This consequently caused yielding in the columns flanges to occur first in the frame, which led to the column stability failure. It was desired to move the LTB critical segment into the rafter. After several attempts at increasing the plate thicknesses of the column, it became clear that an entire frame redesign would be necessary to force the critical segment to be located in the rafter. Since this was outside of the scope of this research, the

nonlinear dynamic analyses in SAP2000 will be run assuming the entire frame remains elastic. The maximum story drifts will be investigated to see if this assumption is reasonable.

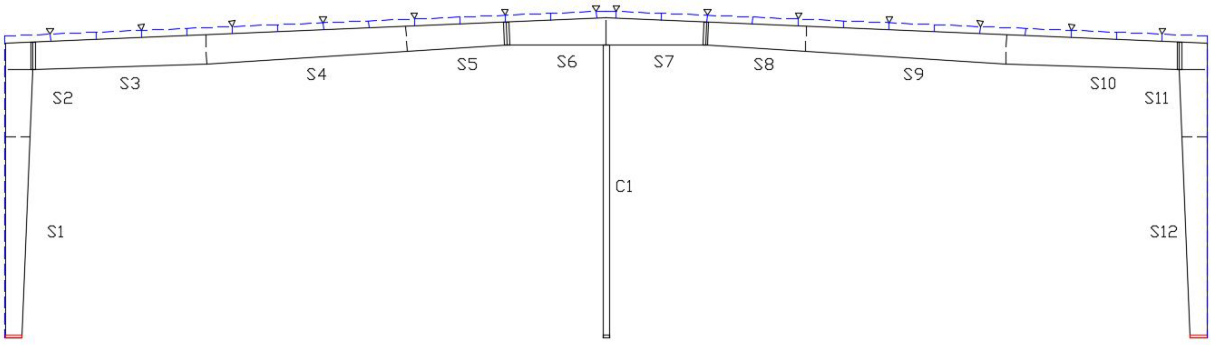

Figure 4-39. Segment Identification for Frame 138

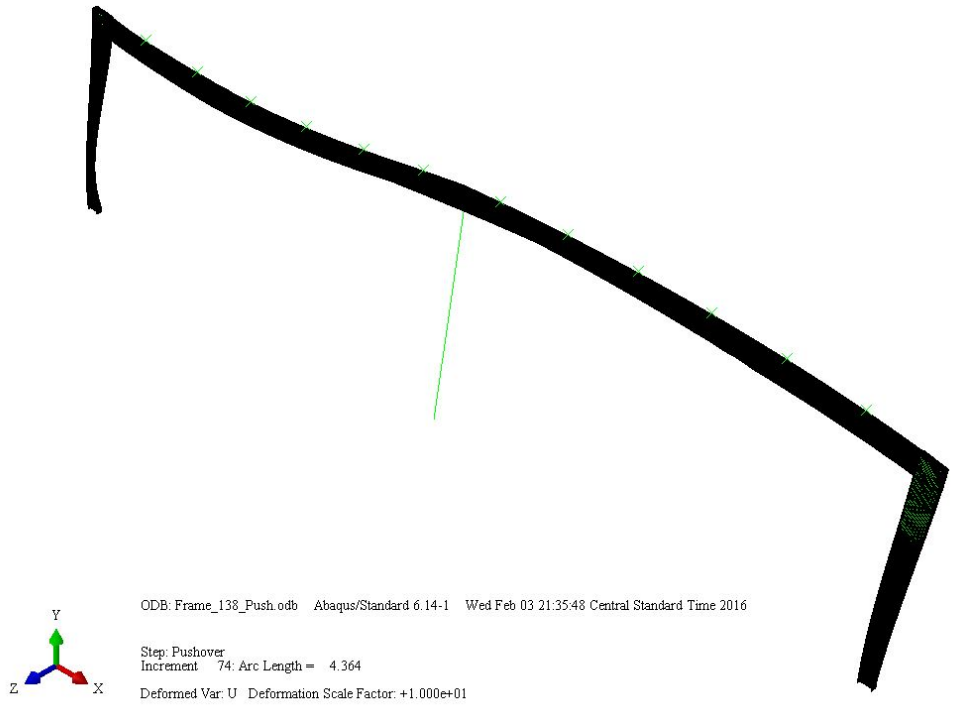

Figure 4-40. Post-Buckled Frame at the End of Analysis (Deformation Scale Factor = 10)

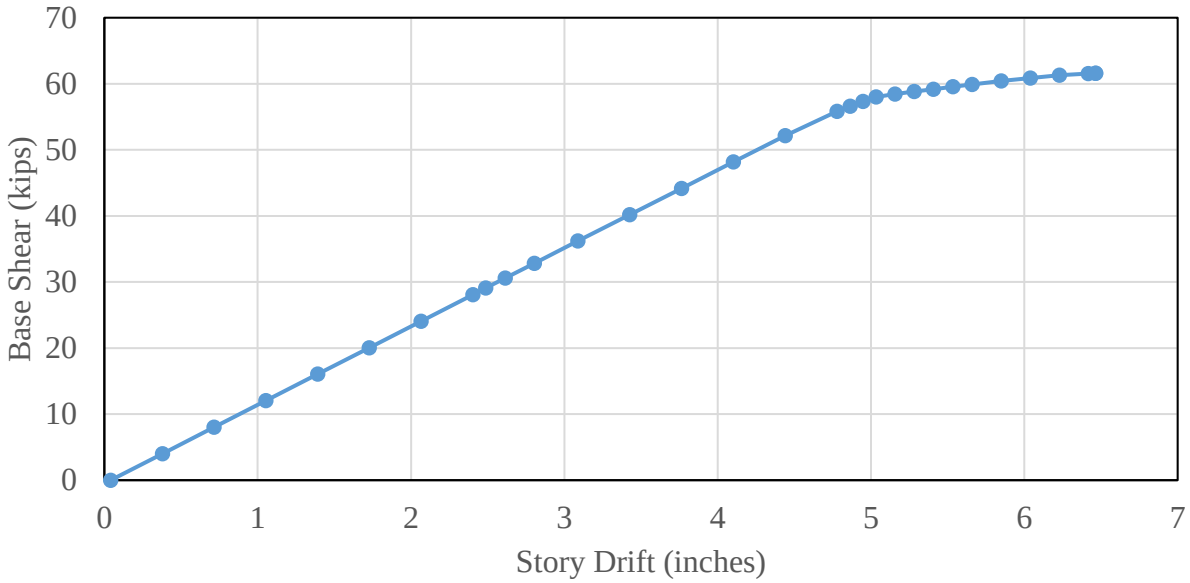

Figure 4-41. Pushover Curve for Frame 138

These analyses show the demarcation between elastic and inelastic frame behavior. The location of the critical segments and the inelastic mechanisms were identified. These pushover analysis results were used to calibrate the SAP2000 custom hinge.

4.7 LTB Hinge in SAP2000

This research approximates the post-buckling behavior of the frame using a custom flexural frame hinge in SAP2000. An analysis that assumes that the frame will remain elastic and undamaged will likely result in unrealistic connection demands. However, with the inclusion of a LTB hinge, frame damage can be accounted for in the analysis, making the results more realistic. As stated earlier, there does not exist a modeling technique using frame elements that captures the behavior following lateral-torsional buckling during earthquake excitations. In SAP2000, the user can define a custom backbone curve for the plastic response. The type of hysteresis behavior can also be assigned. Through clever manipulation of the available hinge parameters that can be

adjusted in SAP2000's interface, post-buckling behavior can be approximated. The proposed hinge was developed to include several critical characteristics of post-buckling.

1. There is a significant reduction in strength following the critical buckling load.
2. There is a significant reduction in global lateral stiffness following buckling.
3. During an unloading cycle following buckling, the buckled compression flange straightens out and can carry tension (Smith 2013d).

One important aspect to note about this flexural hinge is that the true kinematics of LTB will not be captured. The model developed for the critical segment will not be physically buckling out-of-plane and twisting. Rather, the hinge will undergo large plastic rotations about the major axis of bending while remaining in-line with the frame. A similar modeling technique is applied for modeling concentrically braced frames in compression. The out-of-plane buckling of the brace is mimicked through axial deformation alone.

4.7.1 SAP2000 Pushover Procedure

The first step of the LTB hinge is to define a backbone curve such that the pushover curves from the Abaqus models match, as closely as possible, the SAP2000 pushover curve. A single frame line from the 3-D SAP2000 model was isolated to be used for a planar frame analysis (Figure 4-42). The wall elements were changed from shell elements to a series of 6 frame elements with cross-sectional properties based on a tributary width of 25 feet. A rod constraint was used to connect the side wall to the metal building frame. The unbraced length typically spans two to three nonprismatic frame elements in the SAP2000 model. The element closest to the inelastic mechanism of the unbraced length was subdivided into two equal length elements. A major axis flexural hinge was assigned to one of the newly created subdivided elements. Traditional plastic

hinges for wide flange sections assign a frame hinge length of two times the depth of the cross-section. Because the backbone curve is being calibrated, the choice of hinge length is arbitrary. This research assigns a hinge length equal to the entire length of the newly subdivided element for all models (Figure 4-43).

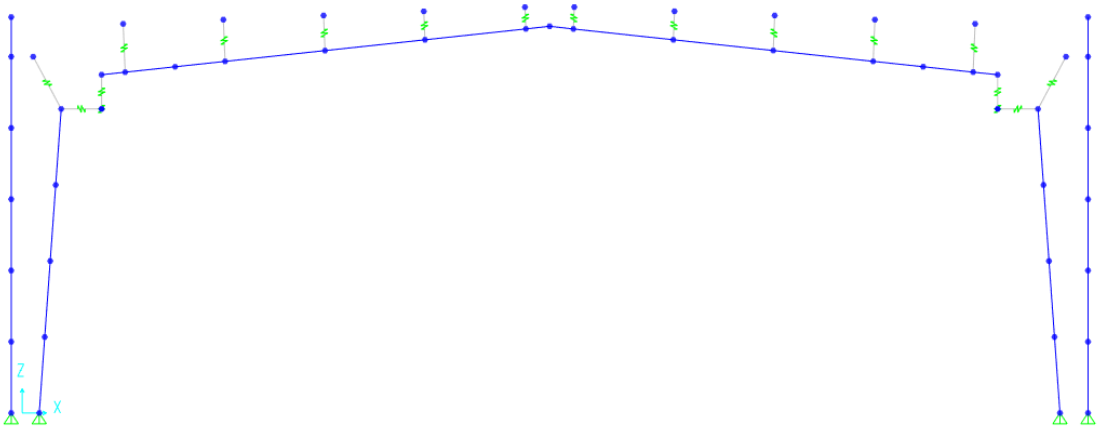

Figure 4-42. Planar Analysis of Frame 85

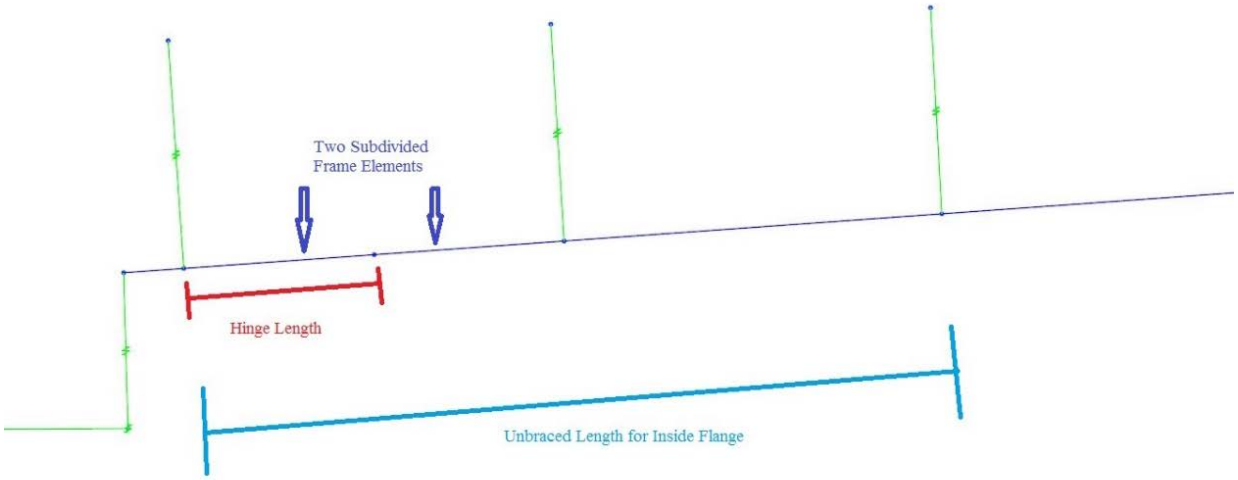

Figure 4-43. LTB Hinge Length Definition

A nonlinear static analysis with P-Δ geometric nonlinearity was performed with the applied dead load, collateral load, and 20% of the full snow load. In SAP2000, there are two nonlinear static procedures that can be utilized in an analysis: force-controlled method and displacement-controlled method. The force-controlled method incrementally increases the force from zero to the specified full load. When loss of load-carrying capacity is expected in a pushover analysis, the displacement-controlled method is the better option (CSI 2017).

A calibration process was performed to determine the points of the custom backbone curve for the LTB hinge using the pushover curves from the Abaqus models. For convenience, the moments were normalized using the plastic moment of the cross-section at the hinge location, and the plastic rotations were normalized with the yield curvature. The general shape of the negative moment side of the backbone curve includes either a small yield plateau at the critical LTB load or a slight positive slope up to the critical LTB load, a significant decrease in flexural strength with increasing curvature, and finally a constant residual strength (Refer to Figure 4-44). Because large rotations can be expected due to LTB, the hinge allowed the backbone curve to be extrapolated beyond the last point and never drop load to zero. For the positive moment side of the backbone curve, all but Frame 16 used the plastic moment as the ultimate strength. It is not expected for the positive moment strength to reach this level during the dynamic analyses.

The following figures, 4-44 through 4-51, show the assigned backbone curve for the LTB hinge and the resulting pushover curves from both the Abaqus analysis and SAP2000 analysis. For each of the frames, the pushover curves from the Abaqus analysis reasonably matches with that of the SAP2000 analysis. Based on these results, the SAP2000 model successfully approximates the monotonic post-buckling path of the metal building frame.

4.7.2 Frame 16 LTB Calibration

As stated earlier, Frame 16 experiences LTB first, and then is followed by FLB when the story drift reaches 4 inches. According to Smith's (2013d) recommendations for the development of the Metal Building Intermediate Moment Frame (MBIMF), the frame should be able to undergo large displacements after LTB of the first segment without forming a second inelastic hinge elsewhere in the frame. When the second hinge activates, a collapse mechanism is formed, and should be avoided. There was no attempt to match the Abaqus pushover curve after a second inelastic event occurred. In lieu of this, the positive moment backbone points maintain a constant value of 0.75 times the plastic moment instead of losing strength. That is why a divergent behavior is visible in the two pushover curves for Frame 16 after 4 inches of displacement.

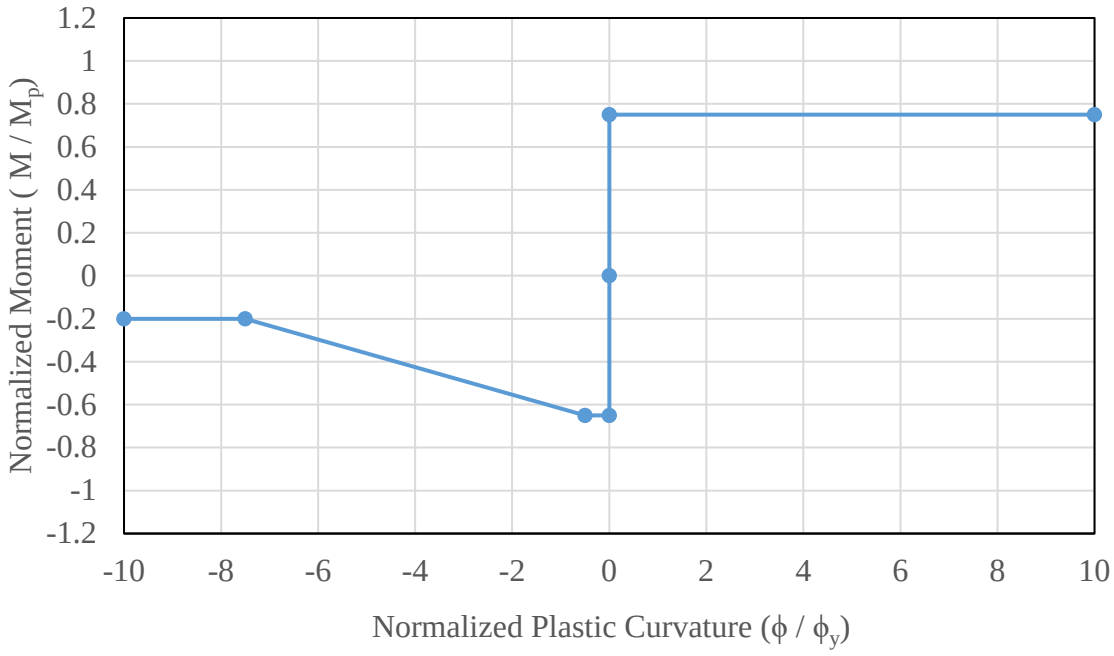

Figure 4-44. Backbone Curve for LTB Hinge in Frame 16

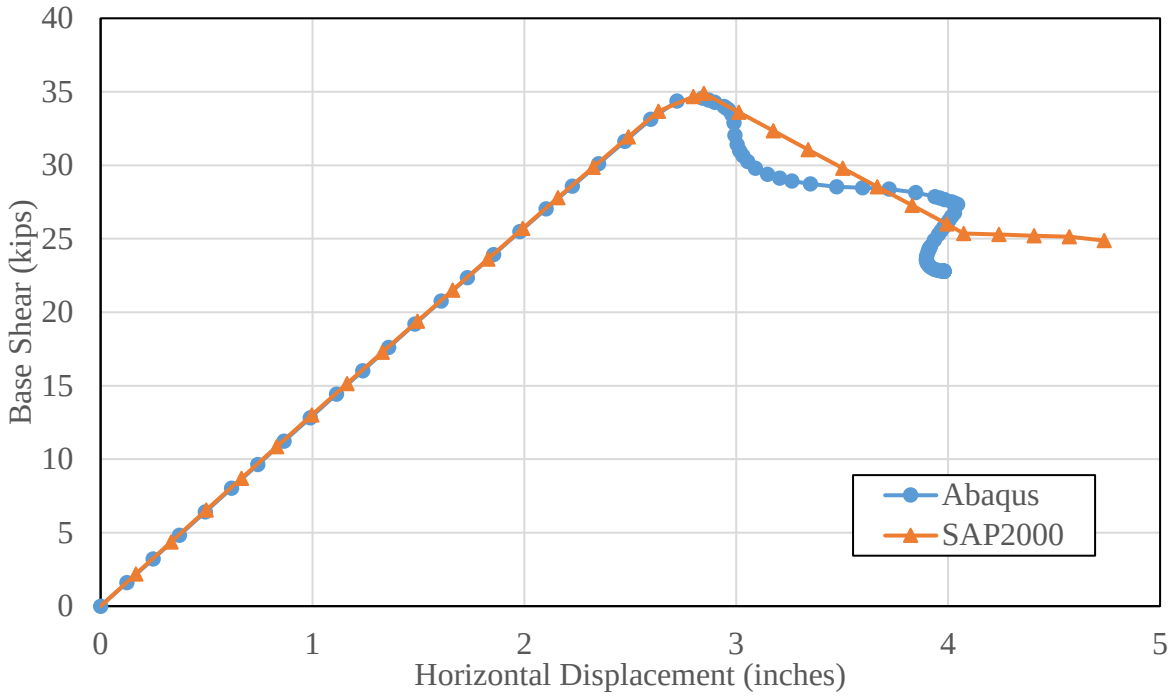

Figure 4-45. Comparison of Pushover Analyses for Frame 16

4.7.3 Frame 41 LTB Calibration

The post-buckled path for Frame 41 was the most severe of all the frames analyzed. The LTB hinge procedure developed in this research is not applicable for such a severe post-buckling path. All earthquake analyses for this frame will assume the frame remains elastic because this post-buckling path cannot be captured.

4.7.4 Frame 42 LTB Calibration

The pushover curves for Frame 42 (Figures 4-47 and 4-49) match each other the best of all the frames. These results best illustrate that SAP2000 can be used to model inelastic behavior of metal building frames. Though flange local buckling was the first inelastic mechanism when the frame was pushed to the left, the same procedure developed for the LTB hinge appears to work for flange local buckling as well.

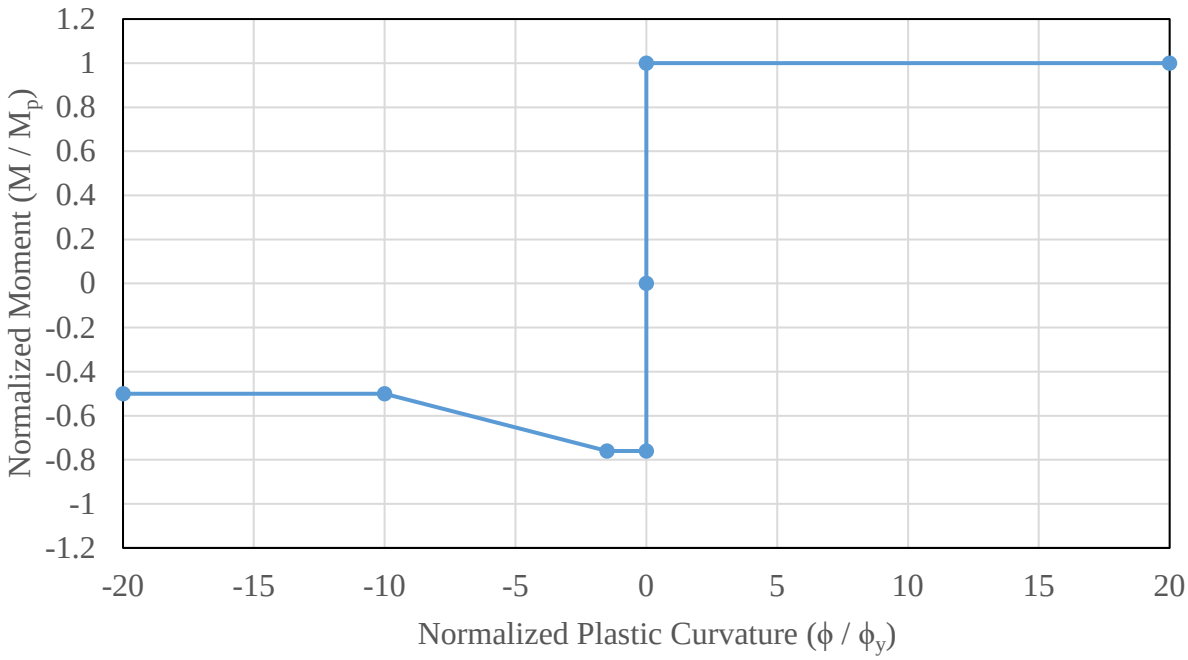

Figure 4-46. Backbone Curve for LTB Hinge in Frame 42

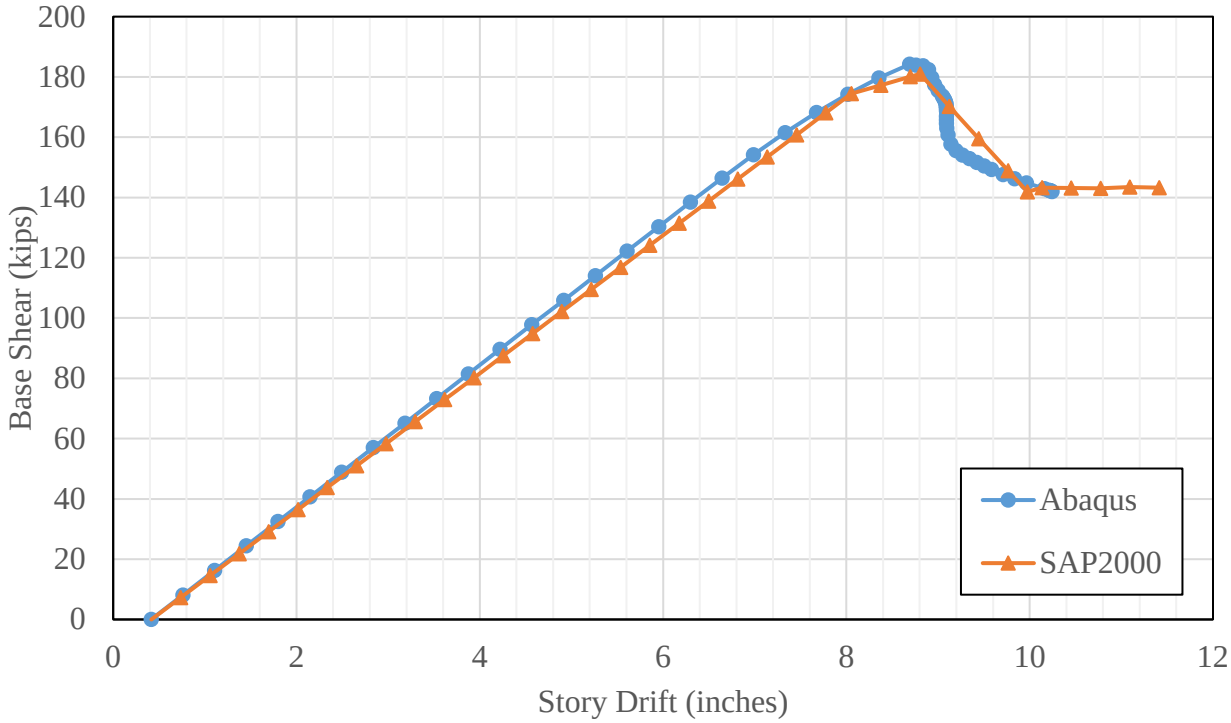

Figure 4-47. Comparison of Pushover Curves for Frame 42 (Right)

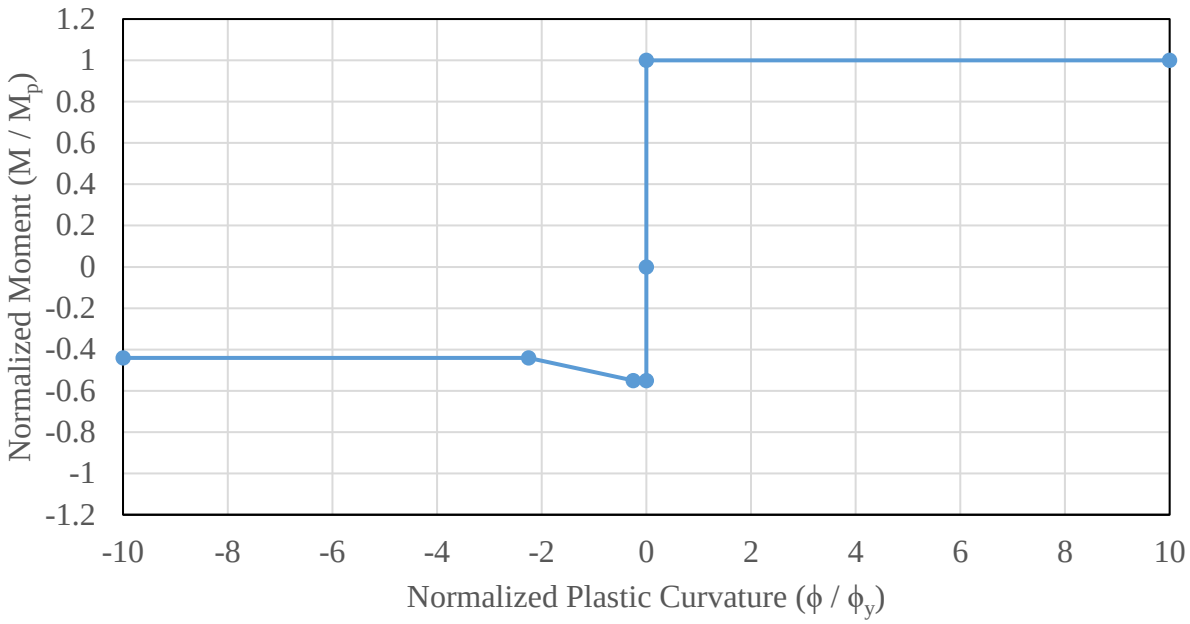

Figure 4-48. Backbone Curve for FLB Hinge in Frame 42

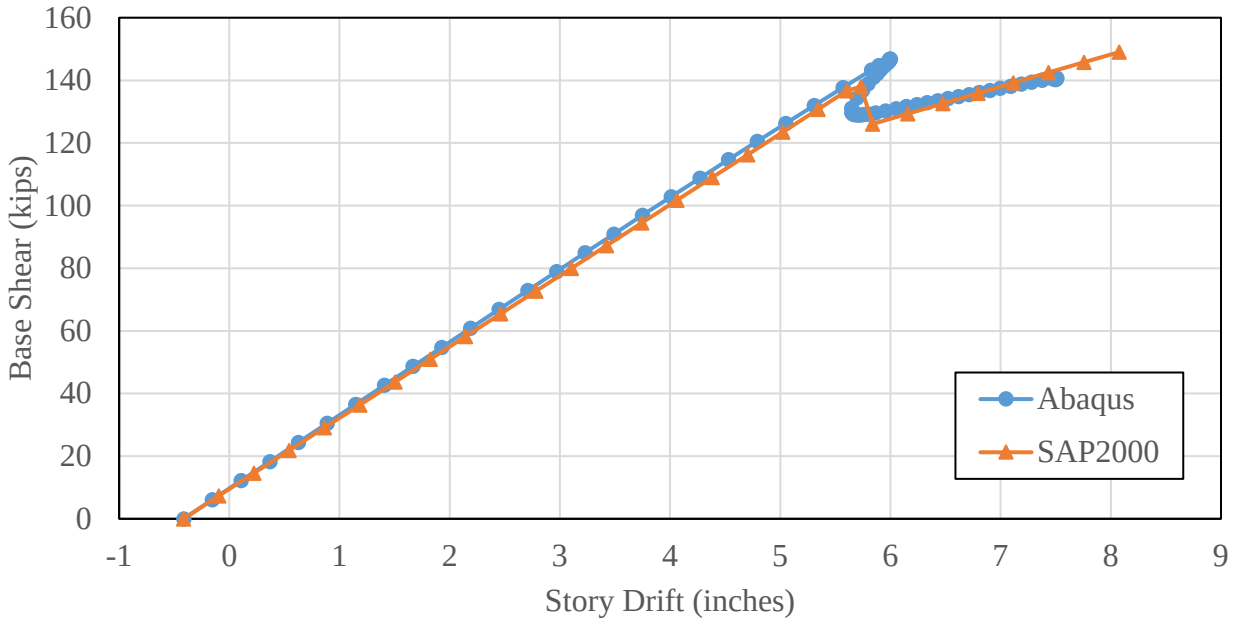

Figure 4-49. Comparison of Pushover Curves for Frame 42

4.7.5. Frame 85 LTB Calibration

Frame 85 exhibits a significant drop in strength after LTB (Figure 4-51). It was challenging to match the Abaqus and the SAP2000 curves. The Abaqus analysis showed that the post-buckling path never achieved a positive stiffness. A SAP2000 hinge backbone curve would not allow for such a post-buckling curve due to the limited number of points that can be defined in the frame hinge. Instead, the post-buckling path for the SAP2000 model assumes a significant drop in strength with a positive post-buckling stiffness. From the Abaqus results, the second inelastic mechanism was flange local buckling in the top flange near the ridgeline. The SAP2000 model does not consider the second inelastic event due to previously stated reasons concerning the MBIMF.

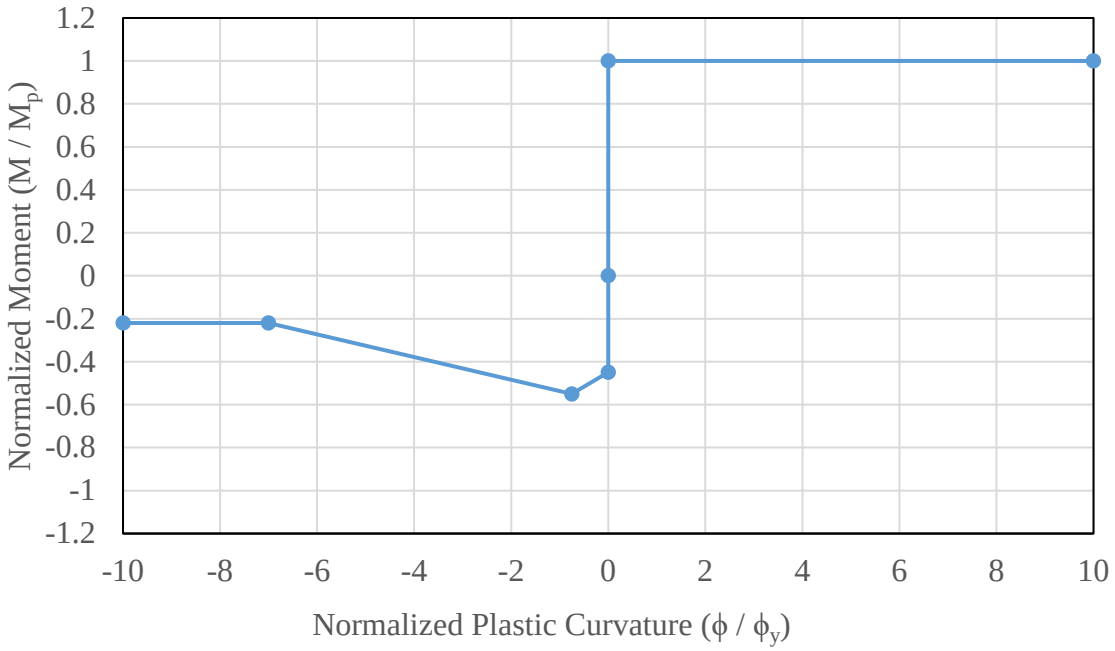

Figure 4-50. Backbone Curve for LTB Hinge in Frame 85

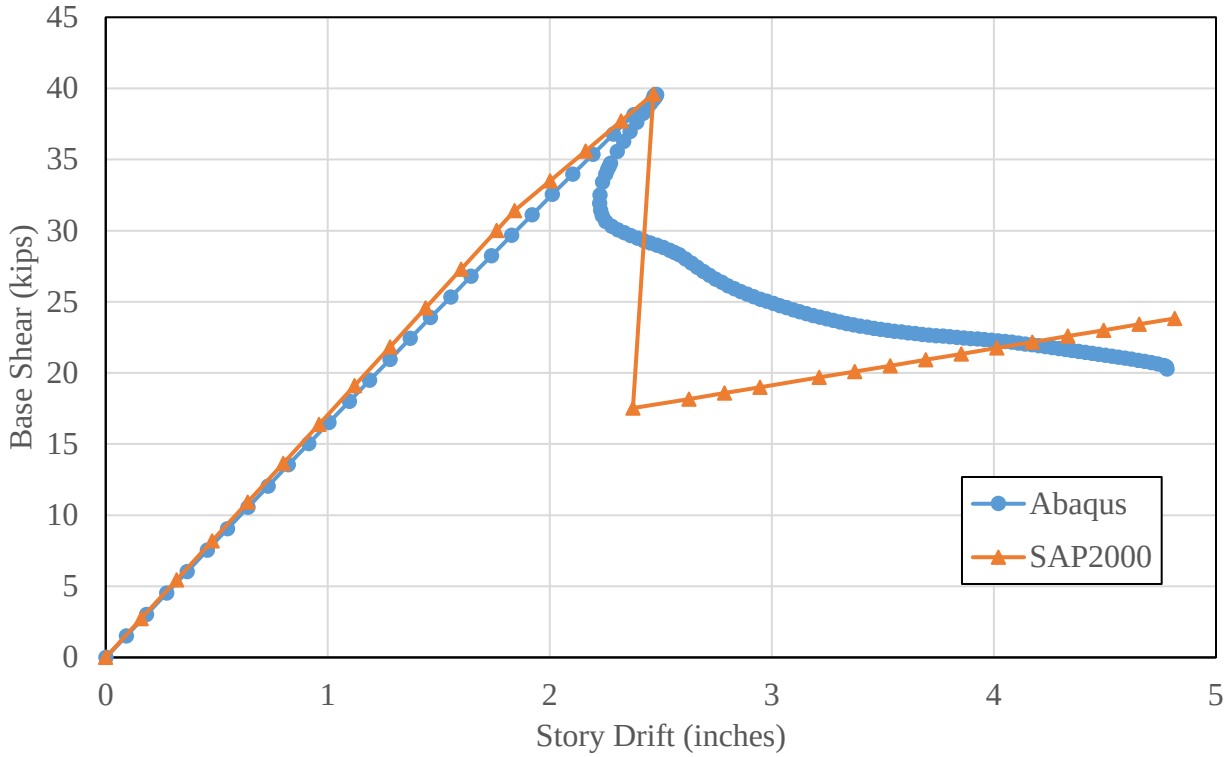

Figure 4-51. Comparison of Pushover Curves for Frame 85

4.7.6. Hysteretic Behavior for LTB Hinge

To this point, the static behavior of the LTB hinge has been examined and defined. It was then necessary define how cyclic behavior can be modeled with the custom hinge.

One major characteristic of cyclic behavior as noted by Smith was that the compression flange in the buckled segment straightens out and gains stiffness until the flange carries tension again (Smith 2013d). This behavior was the primary consideration in the selection of an appropriate hysteresis method for the LTB hinge.

The available hysteresis behaviors available for SAP2000 frame hinges are multi-linear isotropic plasticity, multi-linear kinematic plasticity, multi-linear Takeda Plasticity, and multi-linear pivot hysteretic plasticity. Isotropic plasticity and Kinematic plasticity have been used successfully to model metallic yielding for traditional plastic hinges. The Takeda method was developed for reinforced concrete members and exhibits a degraded hysteresis loop. This method

dissipates less energy than the Kinematic hysteresis method. The Pivot method is similar to the Takeda method, but additional parameters are available for controlling the shape of the degrading hysteresis loop. This method was developed for reinforced concrete members after noticing that unloading and reloading tends to be directed towards specific points, also called pivot points.

The hysteresis method chosen for the LTB buckling hinge was the pivot method. The pivot points can be chosen by modifying the α_1, α_2, β_1, and β_2 scaling parameters, as shown in Figure 4-52. The α_1 value identifies the scaling pivot point for unloading to zero from positive force. α_2 locates the point for unloading to zero from a negative force. β_1 locates the pivot point for unloading to zero from positive force. β_2 locates the pivot point for reverse loading from zero towards negative force (Dowell 1998). The following values were assigned in order to minimize the energy dissipation the hinge would provide for a given cycle. All alpha values selected were 3.0. A β_2 value of 0.5 was assigned. The most important value was the β_1 term as it represents the rate at which the compression flange straightens out after buckling and begins to carry tension upon load reversal. The initial β_1 values assigned correspond to one-half the peak LTB capacity. If convergence was difficult, the β_1 value was increased to allow for more energy dissipation. The final values selected for β_1 are shown in Table 4-3.

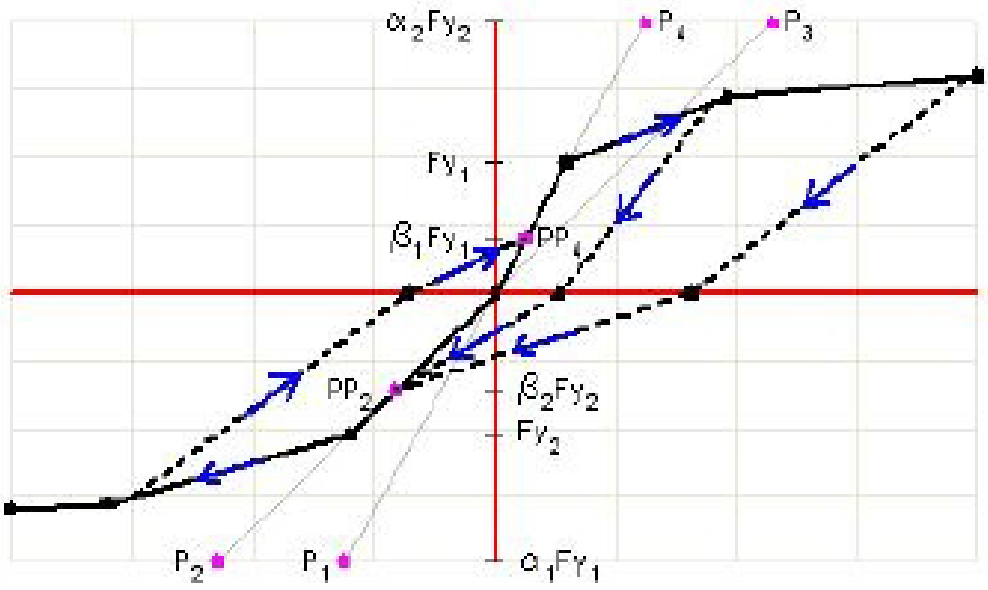

Figure 4-52. Pivot Hysteresis Method (CSI 2017)

Table 4-3. Assigned β1 Values

Model Number	β_1
16	0.4
41	0.2
42 LTB	0.38
42 FLB	0.25
85	0.275

4.7.8 The Resulting LTB Hinge

The results from the Abaqus nonlinear static pushover analyses were used to generate a backbone curve for the LTB hinge to approximate the post-buckling behavior in SAP2000. The goal for this hinge was to include the reduction in strength and stiffness of the frame. Fundamental characteristics of the LTB cyclic behavior were modeled using the pivot hysteresis method. By matching the Abaqus results to the simplified SAP2000 model, post-buckling behavior was captured in a dynamic analysis using SAP2000. As a result, the time required to run dynamic

analyses is reduced by orders of magnitude when comparing a dynamic frame element model versus a dynamic shell element model. It was then necessary to examine the newly developed LTB hinge to determine if this modeling technique successfully captures appropriate post-buckling behavior during a dynamic analysis.

Nonlinear pushover analyses and cyclic tests were performed to test the proposed LTB hinge. The frame capacity, up to the initiation of buckling, was validated. A modeling procedure was proposed for the cyclic behavior of the LTB hinge. The focus of this research is the seismic behavior in the longitudinal direction of metal building systems. The incorporation of this hinge in the metal building frame allows inelastic behavior to occur. Peak accelerations in the structure are decreased and thus reduce the peak out-of-plane force demands in the wall connections.

4.8 Secondary Framing Systems

The metal building moment frame is the primary lateral resisting system in the frame direction. Purlins are used as a secondary system to transfer the loading from the roof, along the purlin, into the primary frame. The purlins are generally cold-formed steel Z-shaped members that run continuously in the longitudinal direction of the building. For this research, a standard Z-section was used in all the models with a material assignment of a cold-formed steel. The nodal locations were set to the true location of the purlin in relation to the primary frame. A rigid link was used to connect the purlin node to the moment frame node (Figure 4-53).

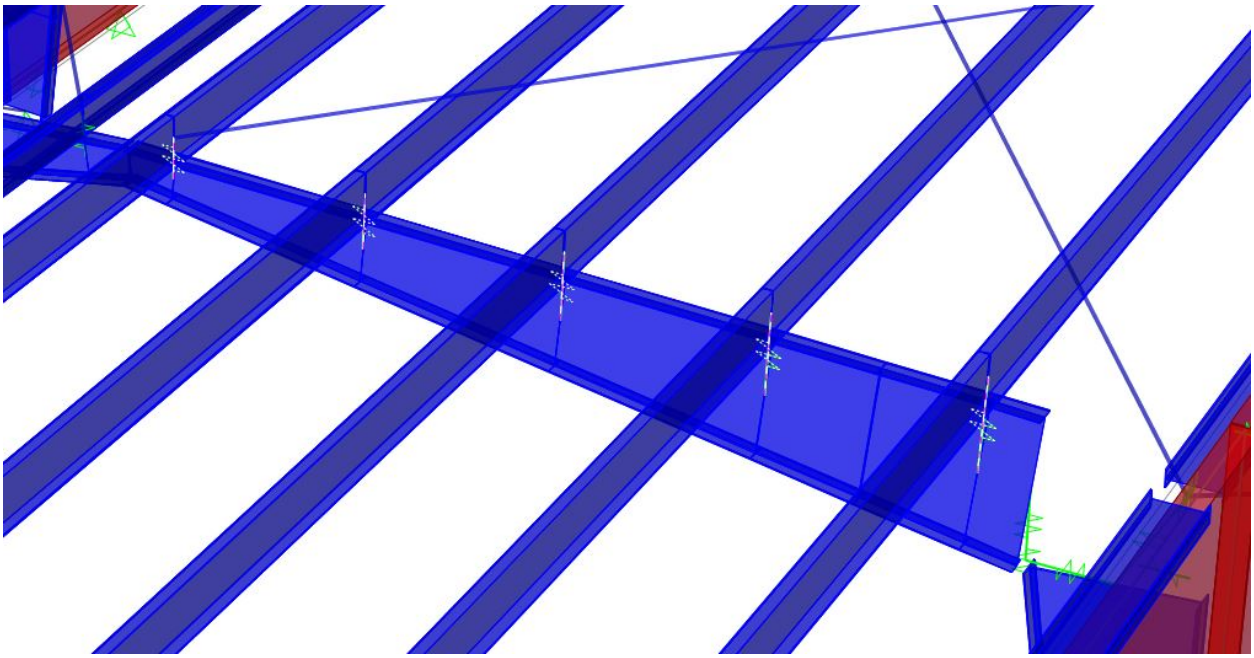

Figure 4-53. Rigid Links connecting Metal Building Frame nodes to Purlin Nodes

For this research, the diaphragm was not explicitly modeled. Bajwa (2010) at Virginia Tech experimentally and analytically showed that the moment frames in metal building systems act independently from one another. "The roof sheeting appears to provide negligible in-plane shear stiffness" (Bajwa 2010). This is true for any system that has a flexible diaphragm. The research conducted at Virginia Tech only investigated the flexible diaphragm assumptions for a metal building system with light weight metal cladding.

Because the roof diaphragm is not explicitly modeled in SAP2000, careful consideration had to be made in the members connecting the primary frames. The purlins were modeled as a frame element spanning between each moment frame line. A verification model was generated by using three identical frame lines of the metal building system. The wall elements were removed along with the diaphragm bracing. Figure 4-54 shows the verification model using Frame 41. A total lateral load of 20 kips was applied to the top of the columns in the central frame. The results showed that nearly 8% of the total load, or 1.6 kips, was resisted by two adjacent frames. The

purlins will inherently provide some resistance and 8% is sufficiently low and acceptable for the purposes of this research.

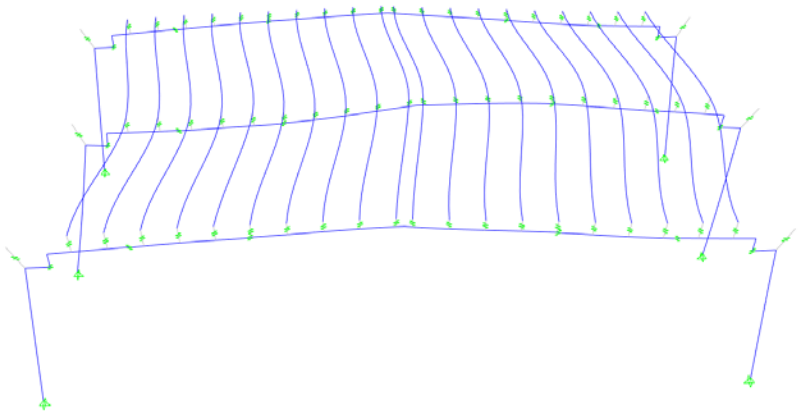

Figure 4-54. Verification of Diaphragm Model

There were no shell elements to brace and restrain motion in the purlin along the length. It is apparent that the mass distribution of the roof diaphragm could not be lumped along the length of the purlin, as this would generate superfluous modes of vibration in the purlins. Therefore, the mass of the roof is lumped at the nodes on the frame line based on the tributary area (Figure 4-55). The mass was assigned in all three spatial directions because horizontal ground excitation can induce vertical vibrations in the rafter segments. Twenty percent of the snow load was included in the mass calculations only if the ground snow load exceeded 30 psf per ASCE 7 (2016).

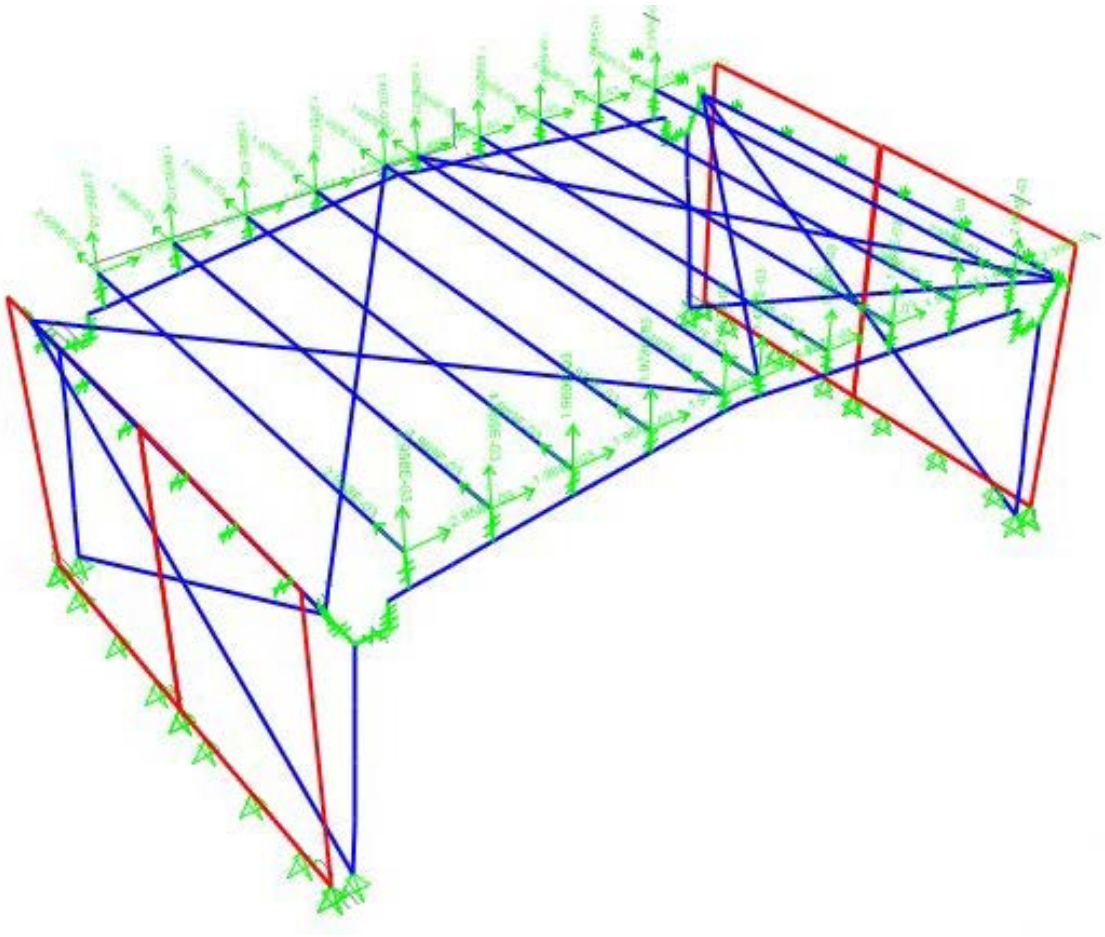

Figure 4-55. Partial SAP2000 Model showing nodal mass at Purlin Nodes

The superimposed dead load, collateral load, live load, and snow load were also applied at the purlin nodes along the primary frame based on tributary area. The self-weight and self-mass of the nonprismatic elements were calculated and included in the models using SAP2000's automatic features. The self-weight and self-mass property modifiers for the purlins was set to zero as the superimposed dead load already included the weight of the purlins.

4.9 Hard Wall Modeling

In the development of the SAP2000 models, two hard wall types were considered. The first was precast tilt-up wall panels and the other was a continuous masonry wall. The wall

elements were modeled using four-node thin shell elements with an assigned thickness equal to the nominal wall thickness. One important aspect in the finite element analysis is determining the mesh density needed for the results to converge. The shell elements in these models make up the vast majority of the total degrees of freedom in the model. A fine mesh density would increase the time required for a dynamic analysis. Also, one of the performance goals of the new seismic force resisting system is to move the inelastic behavior away from the wall elements and into the resilient connections. A convergence test was performed to find the minimum mesh density required. This study used a maximum element size of 90 in. x 90 in for the sidewall elements (Figure 4-56).

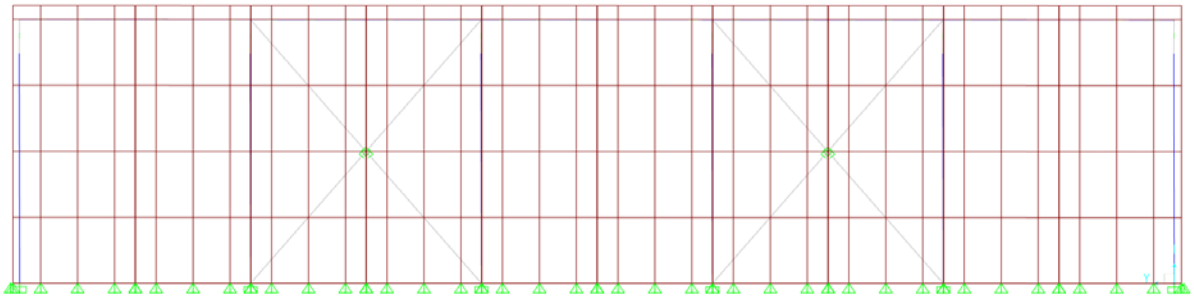

Figure 4-56. Mesh Refinement of Tilt-up Wall Panels

The design of precast tilt-up wall panels is often controlled by the stripping process, transportation, and construction load. The thickness of the panel is sized so that during the removal of the panel from the mold, the wall segment does not crack. The wall elements were modeled using an elastic concrete material with 5,000 psi concrete. For the nonlinear dynamic analyses, it is assumed that the panels will remain uncracked during the earthquake for the lowest intensity service level event and cracked for the more intense levels. Precast tilt-up wall panels that are built at a fabrication plant and have to be transported to a work site, must be dimensioned in a manner that is transportable. The distance between frame lines is 25 feet in all the models. For

the sidewalls, two discrete tilt-up panels are used in each bay. The panels are not connected to each other and a gap of 0.5 inch separates them. The segmented wall panels are modeled so that they will not interact with each other in any way during the dynamic analysis.

One important consideration about the wall panels is the interaction effect at the corner of the building. For simplicity, the wall panels were modeled with no connection at the intersection. as shown in Figure 4-57. An out-of-plane detail of the rotational friction connection will be outlined in Chapter 5 so that the load path is continuous at this critical junction

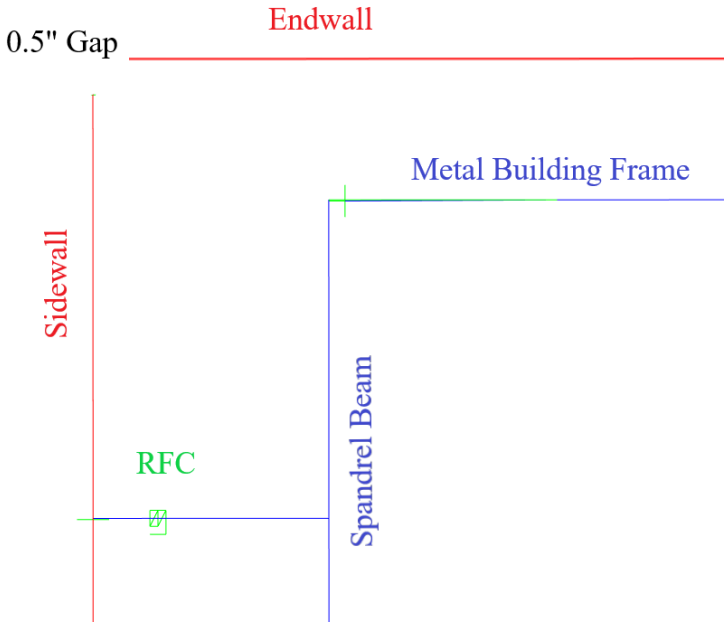

Figure 4-57. Plan View of Precast Walls structurally separated at Corner of Building

Openings in the end wall segments were not explicitly modeled. To account for openings, the endwall shell element mass and weight properties were reduced by 20%.

4.9 Longitudinal Bracing and Diaphragm Bracing

For metal building systems, it is typical for the lateral force resisting system in the longitudinal direction of the building to be composed of diagonal, tension-only rod braces. Table 4-4 displays the longitudinal dimension of each metal building frame, as well as the number of bays that contain the bracing system. It is not common to place rod bracing in adjacent bays due to constructability issues.

Table 4-4. Longitudinal Geometry of Metal Building Sample

Model Number	Transverse Dimension (ft)	Longitudinal Dimension (ft)	Number of Bays	No. of Bays with Rod Bracing
16	40	75	3	1
41	100	125	5	2
42	160	175	7	3
85	40	75	3	1
138	120	125	5	3

The sidewall bracing for this research was designed as a tension-only ordinary concentrically braced frame (AISC 2010b). The equivalent lateral force method was used to size the bracing. Due to the large mass of the end walls, the seismic load combinations controlled the design. The roof diaphragm bracing was designed using the overstrength factor, Ω_o, to ensure the braces remain elastic for the full strength of the energy dissipating fuse elements. The 3-D SAP2000 models were used to perform the structural analysis of the bracing system. This is a departure from common practice, as these systems are designed using 2-D models of the longitudinal frame and roof diaphragm. This was done here for convenience since the 3-D models had already been generated.

The location of the braces in the SAP2000 model were carefully considered. Figure 4-58 shows the details of a typical panel zone in a metal building frame. The spandrel beam's location was assumed to be 18 inches below the eave height. Due to the proximity of the braces near the

spandrel beam, the rod brace connection points for the side wall and roof diaphragm, highlighted in red in Figure 4-58, were made at the node where the panel zone intersects the spandrel beam. Every brace was modeled using a one-dimensional link element with axial stiffness based on the brace's cross-sectional area, length, and modulus of elasticity. The compression limit was set to zero as the slenderness ratio of each rod brace is very high. Self-weight and mass property modifiers were set to zero for the braces to simplify the nonlinear dynamic analyses.

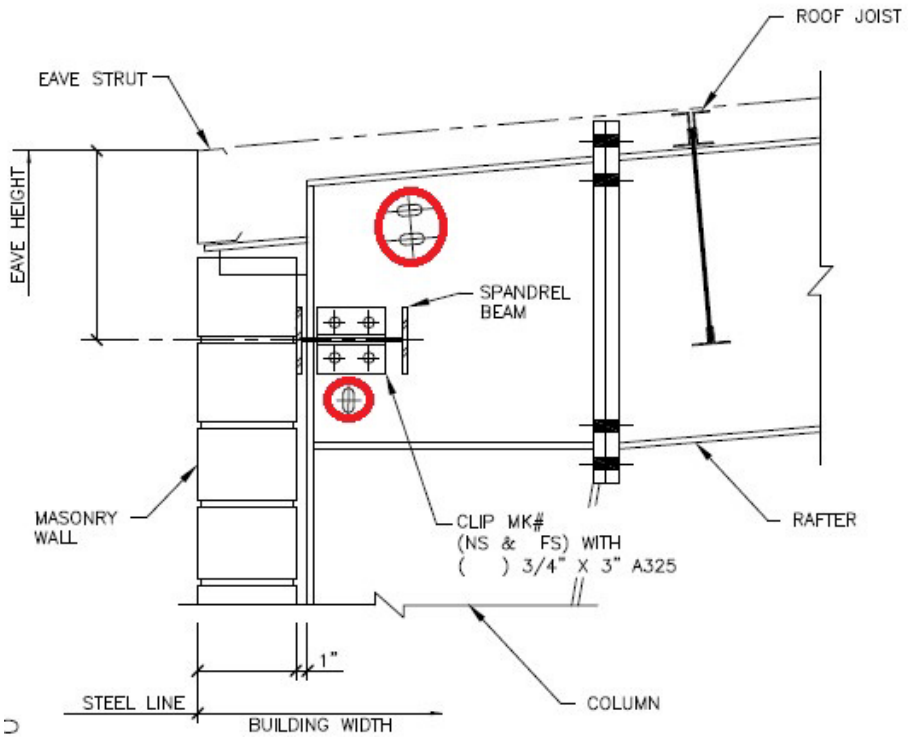

Figure 4-58. Panel Zone Detail (Nucor 2009)

The roof diaphragm bracing was located at purlin nodes. Diagonal braces are most effective when they are oriented at 45 degrees, and an effort was made to maintain an aspect ratio close to 1:1 for the x-bracing. The purlins act in compression as struts in the roof diaphragm. If a purlin was found to have inadequate axial capacity, an adequate pipe strut was used to replace the purlin (Figure 4-59).

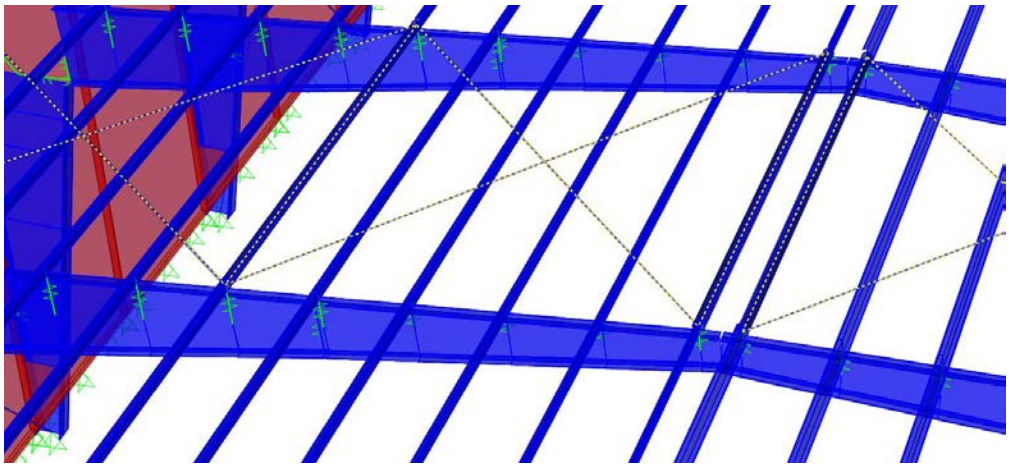

Figure 4-59. Roof Bracing and Pipe Struts in the Diaphragm

To model the nonlinear brace behavior, a one-dimensional multilinear plastic link element was utilized. The backbone curve assigned to the braces was based on the ASCE-41 hinge definitions for a brace in tension (ASCE 2013). Figure 4-60 displays the generalized shape for the backbone curve for tension-only rod braces and angle braces, where Δ_t is the tensile yield displacement. The three acceptance categories are the immediate occupancy, life-safety, and collapse prevention. According to ASCE-41, whenever braces act in a tension-only configuration, the acceptance criteria is reduced by one-half. All the link element parameters used in the models are listed in Appendix B.

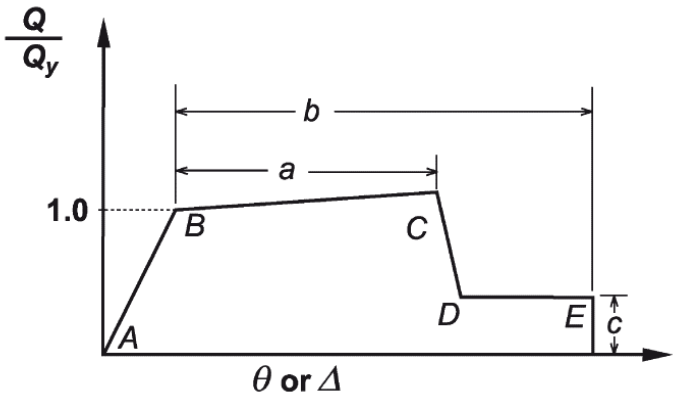

Braces in Tension	Modeling Parameters			Acceptance Criteria		
	Plastic Deformation		Residual Strength Ratio	Plastic Deformation		
	a	*b*	*c*	IO	LS	CP
Rod Bracing	$8\Delta_t$	$9\Delta_t$	0.6	$0.25\Delta_t$	$3.5\Delta_t$	$4.5\Delta_t$
Single Angle	$10\Delta_t$	$11\Delta_t$	0.6	$0.25\Delta_t$	$4\Delta_t$	$5\Delta_t$

Figure 4-60. Generalized Force-Deformation Relation for Axial Link Element (ASCE 2013)

The cyclic behavior of tension-only braces exhibits a ratcheting effect. Without any compression capacity, the cumulative inelastic energy capacity is limited to one-cycle of plastic deformation in the tensile range. The hysteresis model necessary to capture this effect in SAP2000 is the Takeda hysteresis method. A one link-element model was constructed of Brace 1.125 from Model 41 and cyclically tested at increments of 0.5 inch up to a peak amplitude of 7.0 inches to validate the modeling procedure. The resulting hysteresis loop shown in Figure 4-61 indicates that the modeling procedure is capturing the correctly capturing the ratcheting effect that would be observed in tension-only braces.

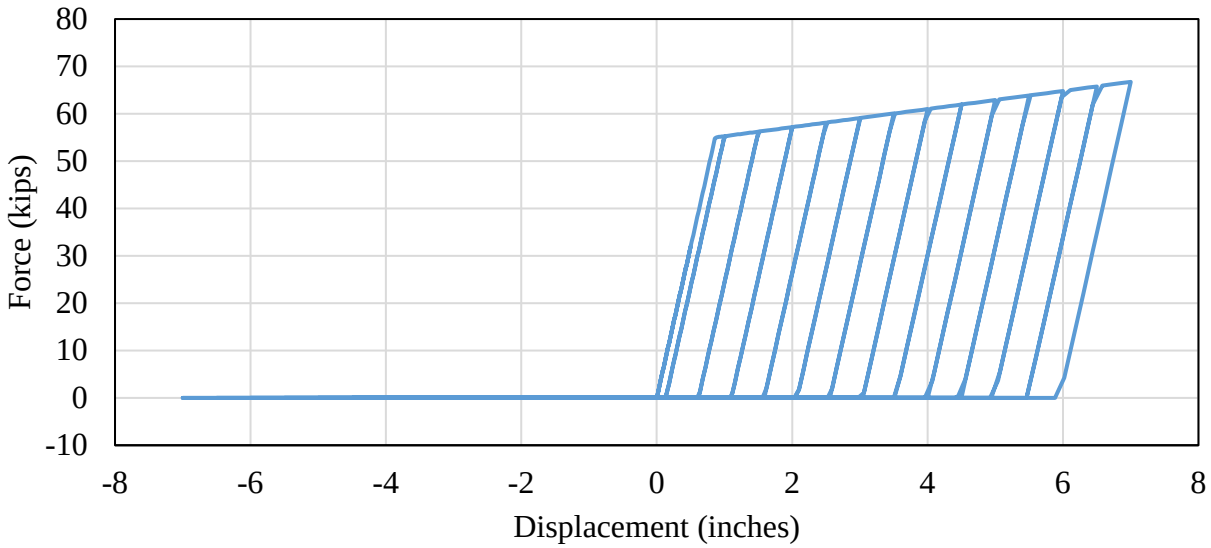

Figure 4-61. Hysteresis Verification for Brace Link Element

4.10 Hard Wall Connection Configurations

The location of the new resilient connections must be constructible, practical, and effective. To provide relief for the stiffness incompatibility between the hard wall and metal building frame, the following connection configuration was used in the SAP2000 models.

The connection configuration places the rotational friction connection at the interface between the walls and the spandrel beam (Figure 4-62). For all models, three rotational friction connections were placed in each tilt-up panel. These connections are designed to slip at a prescribed longitudinal load (See Figure 4-62 for slip direction). The metal building framing system will be able to move as one unit in the longitudinal direction, allowing all the energy dissipating connections to participate. The spandrel beam serves three structural functions in this configuration. First, it transfers the out-of-plane seismic load from the walls into the metal building moment frame. Second, the beam acts as a strut for the sidewall brace and the outermost roof diaphragm brace. Lastly, the spandrel beam acts a collector element by transferring load from the roof diaphragm to the rotational friction connections in adjacent bays.

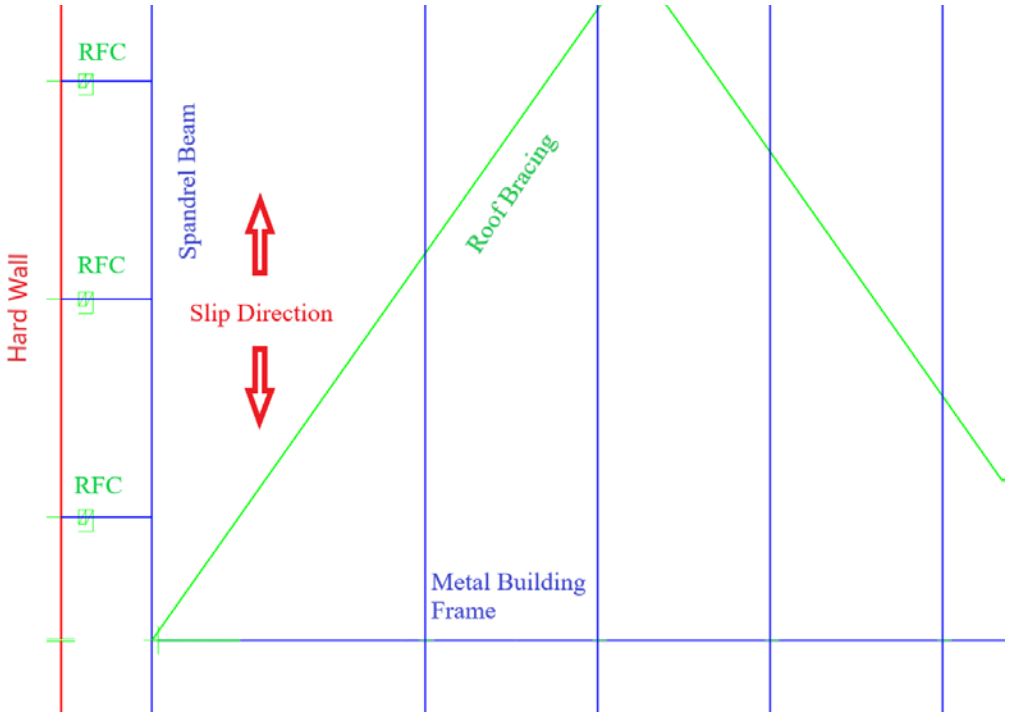

Figure 4-62. Plan View of Rotational Friction Connection Configuration and Slip Direction

Initially, the rotational friction connections are the stiffer components in the longitudinal direction versus the sidewall braces due to the total number of connections running parallel along the length of the wall. Seismic load will travel from the roof diaphragm, to the roof bracing, along the spandrel beam, and then to the friction connections. The load will initially circumvent tension-only side wall x-braces. It is only after the rotational friction connection slips, that load will enter the x-braces.

This connection configuration requires communication between the hard wall engineer and the engineer-of-record so that connection forces are accounted for. Also, this connection configuration will require changes to the typical spandrel beam bracing. The flange bracing must not be connected to the wall because it will not allow for longitudinal movement. Instead, the flange bracing will need to be tied into a purlin in the roofing system (Figure 4-63). This will be of benefit to the metal building engineers as they will have full control of the bracing design, and

the hard wall engineer will not need to be concerned with bracing details. The spandrel beams were designed using ASCE 7 (2016) and AISC 360 (2016). The 15-foot wall required a C10x15.3 and the 30-foot wall required a C12x20.7. Model 42 had an east wall height of 36 feet 8 inches and used a C12x25.

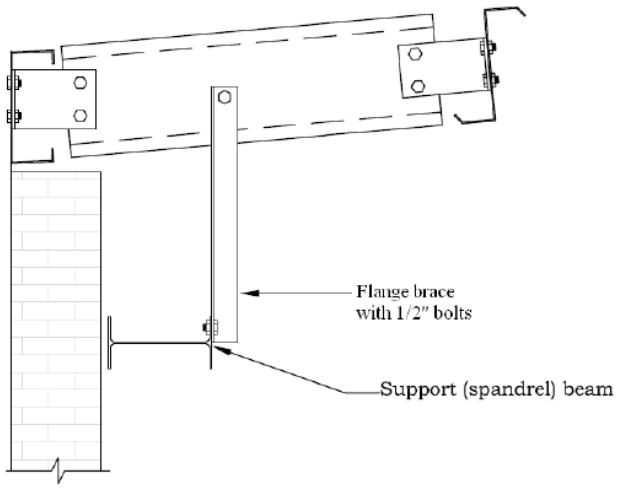

Figure 4-63. Spandrel Beam Bracing Detail (NCI Engineering 2006)

4.11 Rotational Friction Connection in SAP2000

The 3-D solid finite element model developed in Chapter 3 provided insight into the fundamental behavior of the rotational friction connection. However, the complexity of the model makes it computationally unfeasible for use in many nonlinear response history analyses. This section focuses on the development of a simplified rotational friction connection model for use in SAP2000.

4.11.1 Simplified RFC Model

The experimental setup was used to develop the simplified finite element model of the connection. The rotational friction connection was discretized into three components: the steel

strut, a rotational zero-length element, and a rigid beam element. Figure 4-64 shows the RFC configuration of the experimental setup. A 7.5 in. x 3.0 in. x 0.5 in. steel strut meshed into four frame elements attaches to a zero-length multi-linear plastic link element. The location of the link element matches the center of the angle bolt hole. Finally, a high stiffness element connects the link element to a node located at the centerline of the wall's shell elements.

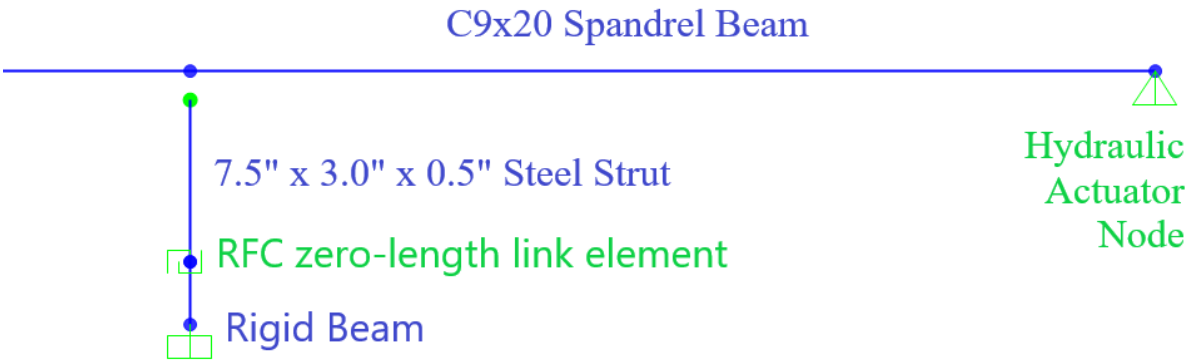

Figure 4-64. Simplified RFC finite element model of Experimental Setup

The link element was modeled using a multi-linear plastic link element. The translational degrees of freedom of the link element were defined as fixed. SAP defines the local axis U1, U2, U3, R1, R2, and R3 respectively as axial deformation, vertical deformation, horizontal deformation, torsional deformation, minor axis bending rotation, and major axis bending rotation (Figure 4-65).

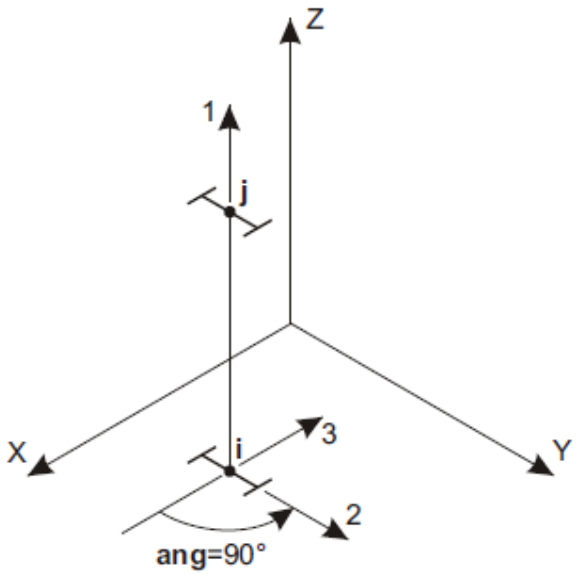

Figure 4-65. Local Axis as defined in SAP2000 (CSI 2017)

The local orientation of the frame elements along the connection and the link element are shown in plan view in Figure 4-66. The red axis refers to the local U1 direction is used for the out-of-plane action. The green axis corresponds to the local U2 direction and handles the in-plane horizontal action. Following the right-hand rule, the local U3 direction is captures the in-plane vertical action. The horizontal translation degrees of freedom were assigned as fixed. The rotational degree of freedom in the R1 and R2 rotations were also assigned as fixed. The axial stiffness (U1) was calibrated from a linear fit of the experimental out-of-plane tests with a value of 66 kips/in (Sellers 2017).

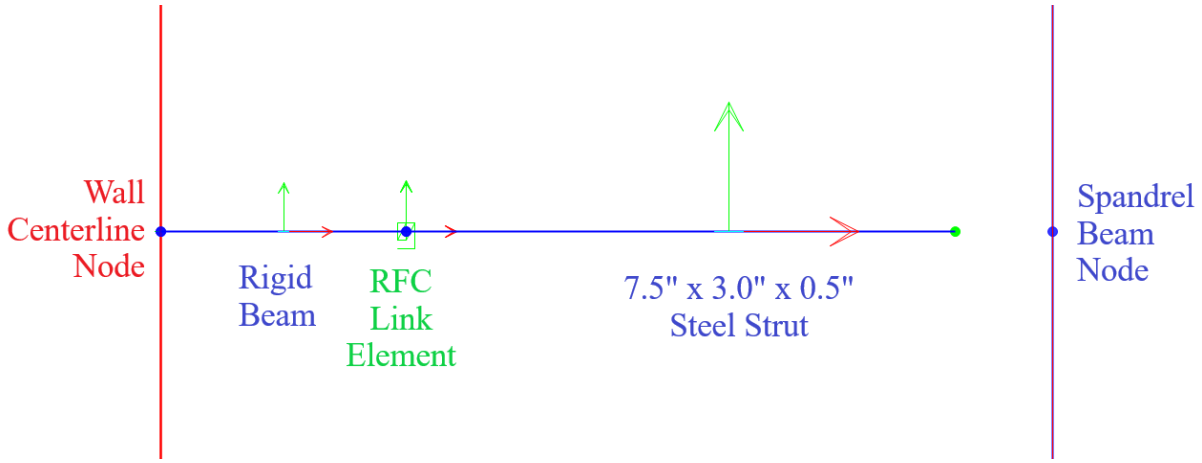

Figure 4-66. Plan View of Local Axes of RFC model

An iterative process was used to calibrate the rotational stiffness in the R3 direction of the link element. An R3 moment release was applied to the far node of the steel strut because the experiment showed that the low tensile force in the spandrel bolt provided little to no rotational friction resistance (shown by a green dot in Figure 4-64). A monotonic pushover analysis was performed by imposing a longitudinal displacement at the fixed boundary attached to the spandrel beam to mimic the hydraulic actuator. Moment arm lengths of 7.5 inches, 14.5 inches, and 18.0 inches were calibrated and the corresponding stiffnesses are shown in Table 4-5.

Table 4-5. Rotational Stiffness Values for RFC

RFC Model	Free Rotation Force (kips)	Free Rotation Moment (kip-in)	Initial Slip Rotation (rad)	Rotational Stiffness (k-in/rad)
RFC1000_SL18.0	0.604	10.87	0.00713	1525
RFC1000_SL14.5	0.760	11.02	0.00732	1503
RFC0875_SL14.5	0.520	7.54	0.00602	1253
RFC0750_SL14.5	0.320	4.64	0.00488	950
RFC0625_SL14.5	0.200	2.90	0.00440	658
RFC1000_SL07.5	1.440	10.80	0.00857	1225
RFC0875_SL07.5	0.990	7.43	0.00710	1046
RFC0750_SL07.5	0.620	4.65	0.00577	806
RFC0625_SL07.5	0.380	2.85	0.00520	547

4.11.2 Idealized RFC Cyclic Behavior

The cyclic behavior of the idealized finite element model was validated using the same FEMA 461 cyclic protocol that was used for the experimental testing. The link element was assigned with zero damping values and is therefore velocity independent.

SAP2000 has three options for analysis to include the effects of geometric nonlinearity. They are to ignore geometric effects, consider P-Delta effects, and P-Delta effects plus large displacement. P-Delta effects consider the change in elements lateral stiffness due to the presence of an axial load while solving the equations of equilibrium in the undeformed displacement condition. The large displacement analysis solves for equilibrium of the structure in the deformed configuration. Using large displacements provides the most realistic results for the rotational friction connection. However, these analyses are substantially more computationally expensive as additional iterations are required for the solution to convergence within the defined tolerance. Figure 4-67 displays the hysteresis loops of the same connection for the two analyses.

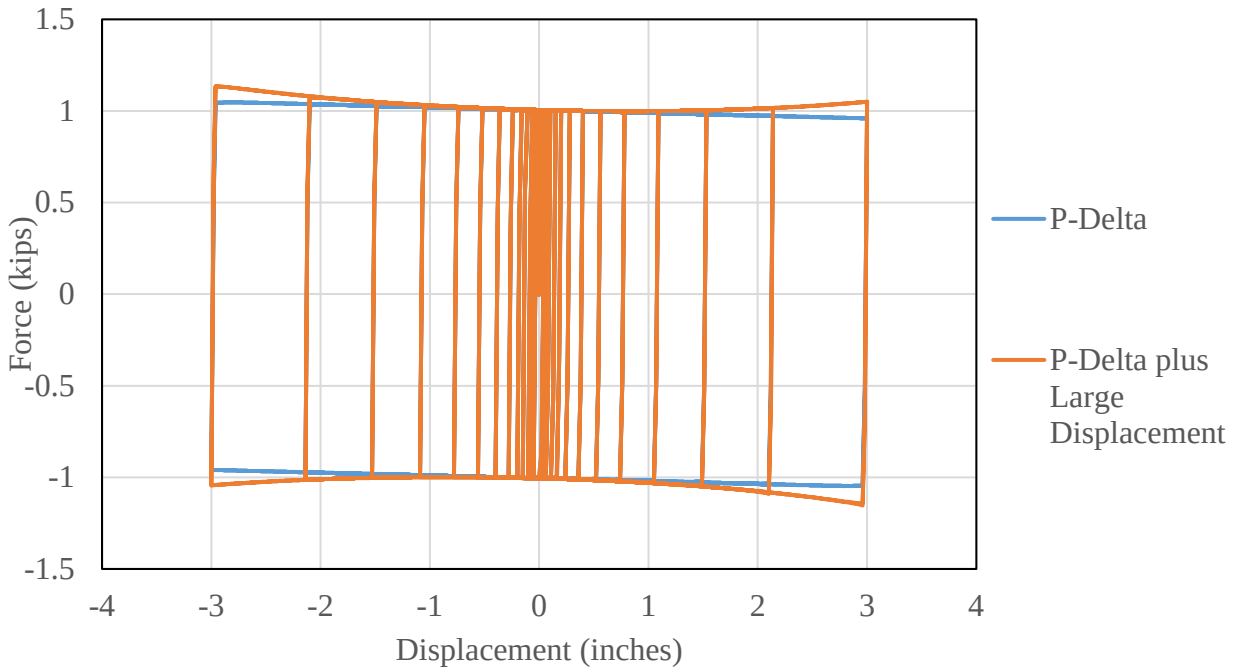

Figure 4-67. RFC Hysteresis Comparison for P-Delta and Large-Displacement

The P-Delta analysis has linear post-slip stiffness while the large-displacement analysis causes a positive slope with curvature in the hysteresis loops at the top and bottom as the rotation increases. The percent difference in the peak force generated is 1.05 kips for the P-Delta analysis and 1.13 kips for the large displacement analysis. The percent difference of the two analyses is 7.3%. The total hysteretic energy dissipated is 48.4 versus 49.0 kip-inches or a percent difference of 1.2%.

For the nonlinear dynamic analyses that will be presented in Chapter 5, the RFC will exhibit a lower peak force and dissipated slightly less hysteretic energy for the P-Delta. One of the performance goals of the rotational friction connection is limit the peak displacement so that the large-displacement effects do not become significant. Also, the energy dissipation between the two analyses is nearly the same. Based on these results, it is acceptable to use P-Delta analysis and ignore large-displacement effects.

4.11.3 Cyclic Hardening Behavior

In addition to the stiffness and slip force of the link-element, the cyclic behavior must also be considered. Cyclic hardening refers to the increase in strength with plastic deformation that causes the backbone curve, and the hysteresis loop, to progressively increase in size (CSI 2017). One of the important observations from the experiment came from the 100 cycle tests. For this test, the hydraulic actuator imposed a triangular displacement protocol with 100 cycles at an amplitude of 0.56” and then an additional 10 cycles with an amplitude of 1.12”.

During this test run, the tension in the ¾” diameter angle bolt decreased from 32.5 kips to 26.9 kips. Despite this 17.2% drop in initial bolt tension, the resisting force of the rotational friction connection continued to grow with each subsequent cycle as shown in Figure 4-68. The

roughening of the rotating surfaces caused the effective coefficient to rise from approximately 0.13 to 0.35 by the end of the test.

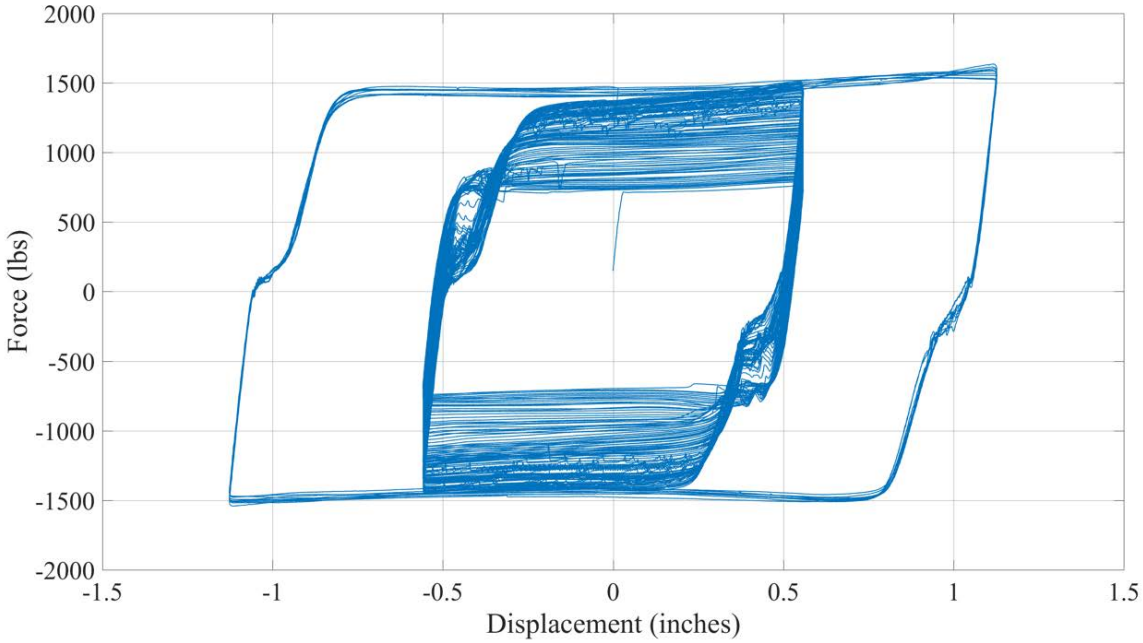

Figure 4-68. Hysteresis Loop of 100 cycle test

One way to account for this hardening behavior in SAP2000 is by utilizing the buckling-restrained brace hardening hysteresis model. Though the buckling-restrained braced hysteretic model is intended for use with axial behavior, this model can be used in any degree of freedom. For the rotational friction connection link element, the corresponding degree of freedom is the rotation about the local z-axis (R3). The plastic deformation is measured in two ways: maximum plastic deformation in both the positive and negative directions, and the accumulated plastic deformation. The parameter of interest is the accumulated plastic deformation as it allows for hardening to occur under cyclic loading of constant amplitude, which is precisely what occurred in the 100-cycle experimental testing. The net hardening factor is calculated in Equation 4-1where h_{pos} is the net hardening factor due to positive deformation, a is the accumulated deformation weighting factor that must be greater than or equal to 0 and less than or equal to 1.0. For an a

value of 1.0, the buckling restrained brace hardening model degenerates to the kinematic hysteresis model (CSI 2017). The maximum positive plastic deformation is defined as $h_{max\ pos}$. A separate hardening factor is computed for negative excursions.

$$h_{pos} = a\ h_{acc\ pos} + (1\text{-}a)h_{\max\ pos} \qquad \textbf{Equation 4-1.}$$

A calibration process was undertaken to fit the hysteresis loops of the numerical model to the experimental results. The stiffness of the rotational link element is 806 kip-inches per radian. The free-rotation moment is 5.41 kip-inches with a corresponding slip-rotation of 6.71e-03 radians. The hardening factor was set to 2.05 and the accumulated deformation weighting factor was set to 1. The accumulated plastic deformation at full hardening as a ratio of yield was set to 4000, which corresponds to an accumulated plastic rotation of 26.8 radians. The comparison of the hysteresis loops is shown in Figure 4-69. The results show a reasonable match in the resisting force of the rotational friction connection between the experiment and the model using the hardening model. The experimental hysteresis loops were not perfectly rectangular due to the 1/16” gap between the bolt and the bolt hole. Every time the load reversed, the bolt had to translate laterally until it came into bearing with the other side of the bolt hole.

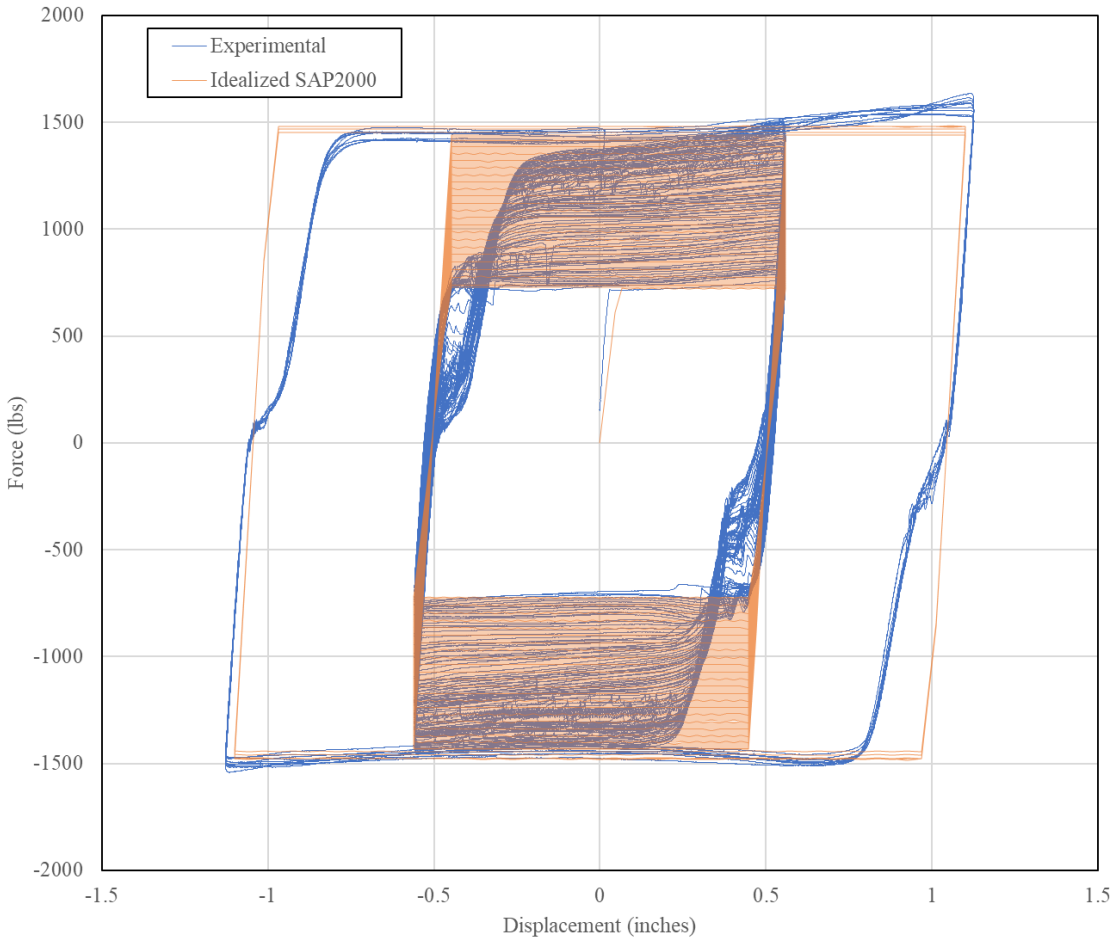

Figure 4-69. Hysteresis Comparison of 100 Cycle Medium Displacement Test

The inclusion of the hardening behavior is computationally expensive. However, excluding it may be acceptable in the nonlinear dynamic analyses if the total accumulated plastic rotation remains small. The results seismic analyses in Chapter 5 will determine if a rerun of the analysis including the hardening behavior will be necessary.

4.12 Conclusions

A 3-D finite element model of a metal building system with hard walls was developed using the commercial finite element program SAP2000. The metal building moment frame, wall elements, sidewall and roof diaphragm bracing, and wall connections were identified as critical to

the structural behavior of the global system during seismic events. Each component was modeled and underwent a verification and validation process and was found to be in acceptable agreement with experimental data or previous seismic research in metal building systems. The focus of this model was to accurately capture the behavior in the longitudinal direction of metal building systems. The metal building moment frame model spanning the transverse direction successfully captures the peak frame capacity. Though 2-D shake table tests currently do not exist to validate the analytical model on a global level, the model developed in this research was validated on a component level and provides a powerful analytical tool to evaluate the performance enhancement that rotational friction connections provide to metal building systems with hard walls.

Chapter 5 Analytical Evaluation of Metal Building Systems utilizing Rotational Friction Connections

5.1 Introduction

This chapter presents the results of the predicted seismic response of metal building systems utilizing rotational friction connections as passive energy dissipating elements between the hard walls and steel frame. A baseline model that did not have energy dissipating connections was analyzed and used as a means of comparison of the global seismic response of metal building systems equipped with the rotational friction connections. In the baseline model, the rotational stiffness of the RFCs was set to nearly zero so that they would not dissipate any inelastic energy. The 3-D SAP2000 models developed in the previous chapter were used to perform the analytical tests, which included nonlinear static pushover analyses, modal analyses, and nonlinear response history analyses. The results of these analyses will quantify the improvement that the rotational friction connections have on the seismic performance of metal building systems with hard walls.

5.2 Design Rationale of RFC for the Analytical Study

When the rotational friction connection was experimentally tested in the laboratory, as described in Chapter 3, it exhibited large displacement capacity while maintaining a consistent free-rotation force and a stable hysteretic behavior that was capable of dissipating energy through frictional heat. The design parameters of the connection require a displacement target along with a desired slip-force. Therefore, the proposed design of the rotational friction connection utilizes a combination of a displacement-based approach and a forced-based approach.

One of the performance objectives of the rotational friction connection was to limit the peak rotation to 30 degrees in the in-plane horizontal direction. This is primarily due to the significant P-Delta effects that occur when out-of-plane forces act on the connection at large displacements. When the connection reaches large rotations over 30 degrees the P-Delta effect increases at an exponential rate. The first step in designing the rotational friction connection was the selection of the moment-arm length. This length plays a role in determining the free-rotation moment and the connection's displacement capacity.

According to ASCE 7 (2016), the allowable seismic drift of an ordinary steel concentrically braced frame is 2% of the story height. Because the rotational friction connections are working in parallel with the braced frame system, the displacement target for the rotational friction connection in the in-plane horizontal direction was set to 2% of the story height. The allowed seismic displacement drift of the metal building system in the longitudinal direction is calculated using Equation 5-1:

$$\Delta_a = 0.02h \qquad \textbf{Equation 5-1.}$$

Where,

Δ_a = allowable story drift

h = story height

Using trigonometry, the moment-arm length of the rotational friction connection shown in Figure 5-1 leads to Equation 5-2:

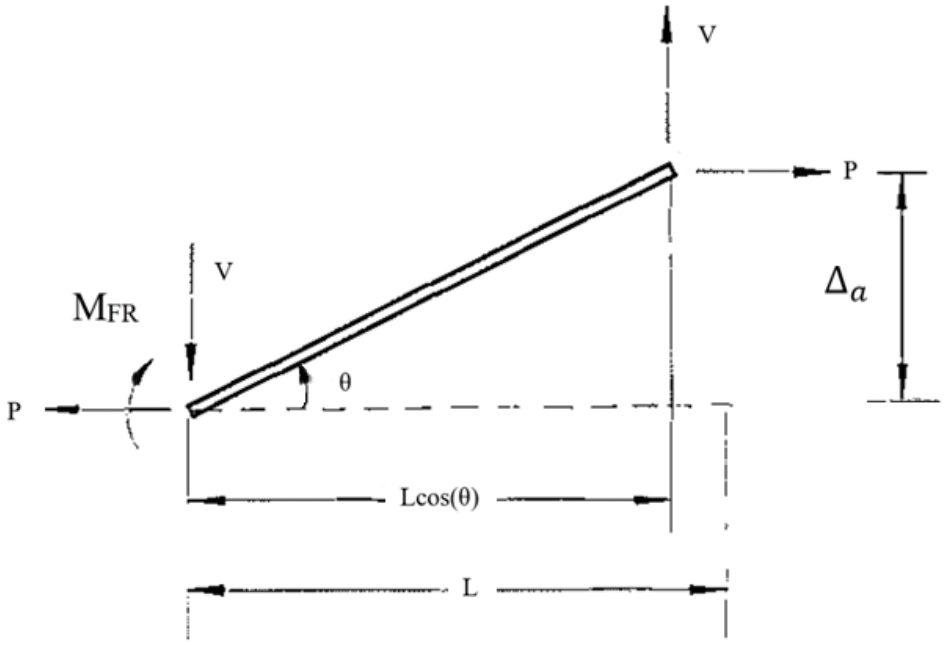

Figure 5-1. Geometry of Rotational Friction Connection in the Deformed Configuration

$$L = \Delta_a / \sin(30) \qquad \textbf{Equation 5-2.}$$

Where,

L = moment-arm length

Δ_a = allowable story drift

The peak displacement target is expected to be reached only during extreme ground motions. At this point, the ordinary concentrically braced frame would be near its fracture and no longer be providing lateral resistance. If the bracing system fractured, the rotational friction connections would have additional rotational capacity and provide lateral resistance, reducing the possibility of structural collapse.

The second step in designing the rotational friction connection is the selection of the slip-force capacity. The experimental results from the laboratory testing showed that the force capacity of the rotational friction connections was not as high as anticipated due to the low coefficient of

friction of 0.13. For this analytical study, the coefficient of friction of 0.13 was used so that the structural properties of the rotational friction connections in the models matched the ones that were experimentally tested. One significant advantage of the low coefficient of friction is that the forces transferred into the wall panel are so low that the risk of damage to the panel is essentially eliminated. Once the moment-arm length has been selected, the magnitude of the free-rotation force can be determined by selecting the diameter of the angle bolt. It was determined that a one-inch diameter bolt was the largest size that was practical for use in the rotational friction connection.

The final step was to decide the number of rotational friction connections per wall panel should be used. The metal building system transverse moment frames were designed with a 25-foot spacing between the frame lines (Smith 2013). Two precast concrete panels per bay were used to clad the metal building system. Each panel requires an absolute minimum of two connections near the top of the panel. Due to the height of these panels, the out-of-plane force demands on these connections could be significant. If one connection ever failed due to fracture, the likelihood of the failure of the other connection would be high. To reduce the out-of-plane load per connection and to improve the system's redundancy, three rotational friction connections were used in each panel.

The geometry and the design parameters of the five metal building systems selected from Smith's Approximate Fundamental Period Study (2013d) are shown in Table 5-1. The rotational friction connections for each model were designed using the procedure laid out in the preceding section. Table 5-2 lists the geometric and structural properties of the rotational friction connection that was resulted. The free-rotation force and rotational stiffness values were calibrated using the 3-D solid finite element analysis models from Chapter 3.

Table 5-1. Metal Building Design Parameters

Model Number	Building Type	Eave Height (ft)	Transverse Length (ft)	Snow Load (psf)	Wind Speed ASCE 7-05 (mph)
16	Clear Span Symmetrical Gable	30	40	0	120
41	Clear Span Symmetrical Gable	30	100	0	85
42	Clear Span Monoslope	30	160	42	85
85	Clear Span Symmetrical Gable	15	40	0	120
138	Modular Symmetrical Gable	30	120	0	85

Table 5-2. Rotational Friction Connection Geometric and Structural Properties

Model	Total Number of RFC	Angle Bolt Diameter (in)	Moment Arm Length (in)	Free-Rotation Force (kips)	Rotational Stiffness (kip-in/rad)
16	32	1.000	14.5	0.760	1503
41	60	1.000	14.5	0.760	1503
42 West Wall	42	1.000	14.5	0.760	1503
42 East Wall	42	1.000	18.0	0.604	1525
85	32	0.625	7.5	0.380	547
138	60	1.000	14.5	0.760	1503

5.3 Nonlinear Static Analyses

Nonlinear static pushover analyses were performed to compare the force-displacement behavior of the baseline models with the models that include the contribution of the rotational friction connections. In a pushover analysis, a series of static analyses are performed in which the frames of the structures are subjected to an increasing lateral load. Prior to each pushover analysis case, a static analysis was performed on each structure with the anticipated gravity load of 1.0 dead and 1.0 collateral load, as per ASCE 7 (2016).

5.3.1 Pushover Results for Model 16

The pushover curves for Model 16 are shown in Figure 5-2, comparing the baseline model with the model containing the rotational friction connections. The pushover curve for the baseline

model is bilinear with an initial stiffness of 53.7 kips/inch. When the base shear of the structure reaches 74.0 kips, the tension-only braces yield, and the secondary stiffness becomes 2.5 kips/inch. When the RFCs are added, the initial stiffness increases to 283 kips/inch which is a 282% increase in stiffness over the baseline model. This significant increase in the initial stiffness is due to the precast concrete cladding panels behaving like a shear wall. Because the connections are stiffer than the sidewall braces, the connections attract the lateral load first and then slip. The base shear continues increasing and reaches 109 kips at which the tension-only braces reach the yield point. The thirty-two rotational connections have added 35.0 kips to the lateral capacity of the structure, which is a 47% increase over the baseline model. After the connections slip, no more additional force is resisted by the connections. As a result, the force resisted by the wall panels is capped. This results in a pushover curve that parallels the baseline model.

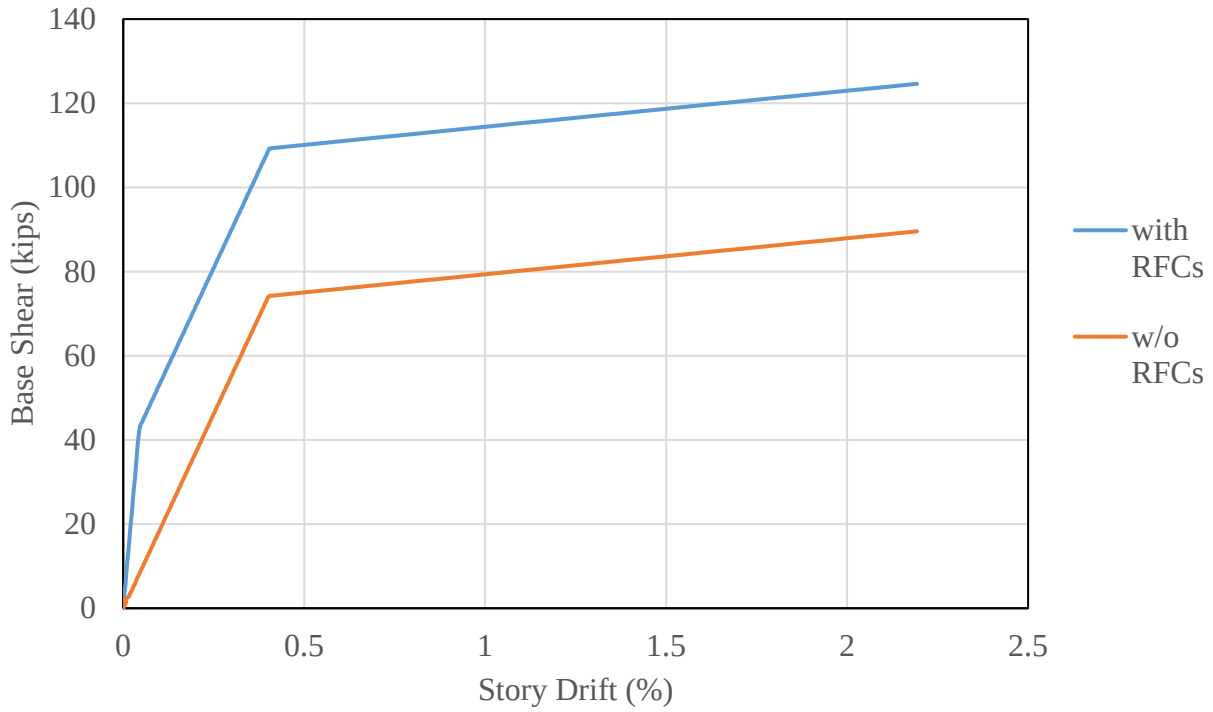

Figure 5-2. Longitudinal Pushover Curve for Model 16

5.3.2 Pushover Results for Model 41

The general shape of the pushover curves for Model 41, shown in Figure 5-3, is identical to that of Model 16. However, the added capacity from the energy dissipating connections is less than the previous model. For the baseline model, the initial stiffness is 134 kips/inch. When the base shear of the structure reaches 170 kips, the tension-only braces yield, and the secondary stiffness becomes 9.2 kips/inch. When the RFCs are added, the initial stiffness increases to 502 kips/inch which is a 275% increase in stiffness over the baseline model. As the lateral force increases, the rotational friction connections slip first. The base shear continues increasing and reaches 227 kips, which is when the tension-only braces begin yielding. The sixty energy dissipating connections have added 57.0 kips to the lateral capacity of the structure, which is a 34% increase over the baseline model

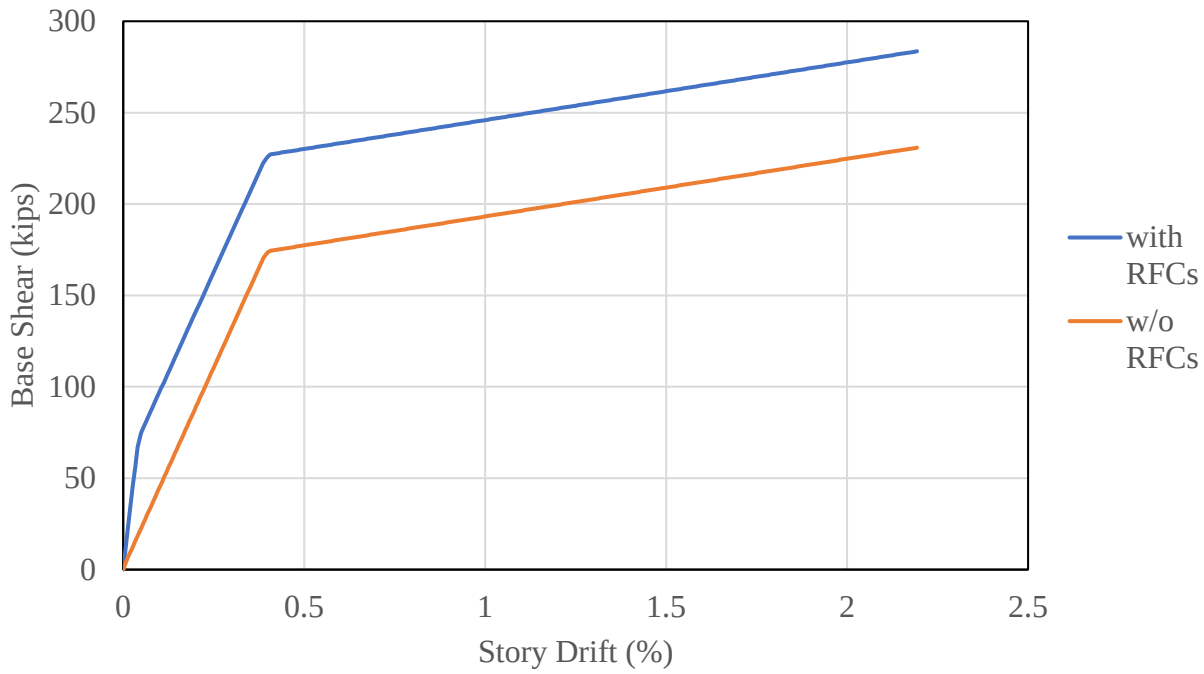

Figure 5-3. Longitudinal Pushover Curve for Model 41

5.3.3 Pushover Results for Model 42

The two pushover curves for Model 42 are shown in Figure 5-4. This model had the smallest difference between the two pushover curves because the 160-foot span length of the transverse moment frame added significant seismic demand to the structure. The increased demand required higher capacity sidewall braces composed of L4x4x3/8 members instead of rod braces found in the other models. For the baseline model, the initial stiffness is 408 kips/inch. When the base shear of the structure reaches 703 kips, the tension-only braces yield, and the secondary stiffness becomes 16.5 kips/inch. When the RFCs are added, the initial stiffness increases to 785 kips/inch which is a 72% increase in stiffness over the baseline model. As lateral force increase, the RFCs slip first. Then braces yield when the base shear reaches 761 kips. The eighty-four rotational friction connections added 58.0 kips to the lateral force capacity, which is only an 8% increase in the base shear capacity.

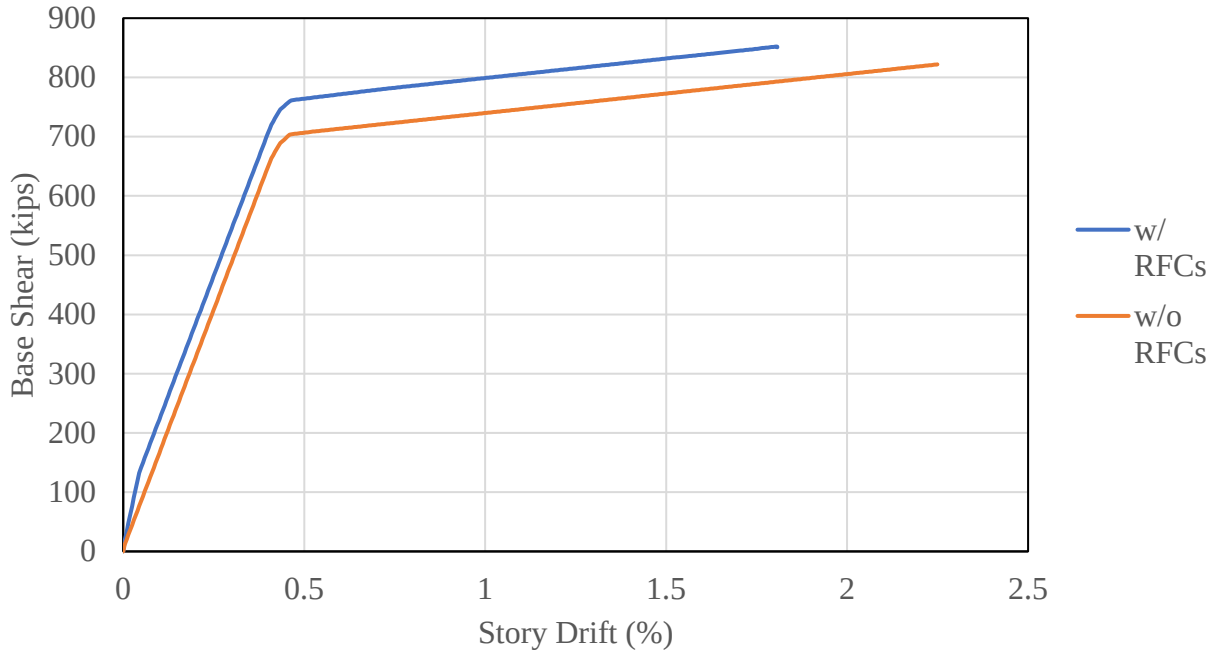

Figure 5-4. Pushover Analysis of Model 42

5.3.4 Pushover Results for Model 85

The pushover curves for Model 85 are shown in Figure 5-5. For the baseline model, the initial stiffness is 44.6 kips/inch. When the base shear of the structure reaches 34.1 kips, the tension-only braces yield, and the secondary stiffness becomes 2.5 kips/inch. When the RFCs are added, the initial stiffness increases to 369 kips/inch which is a 727% increase in stiffness over the baseline model. The RFCs attract the lateral load and slip first. The tension-only braces yield when the base shear reaches 49.5 kips. The thirty-six energy dissipating connections have added 15.4 kips to the lateral capacity of the structure, which is a 45% increase over the baseline model

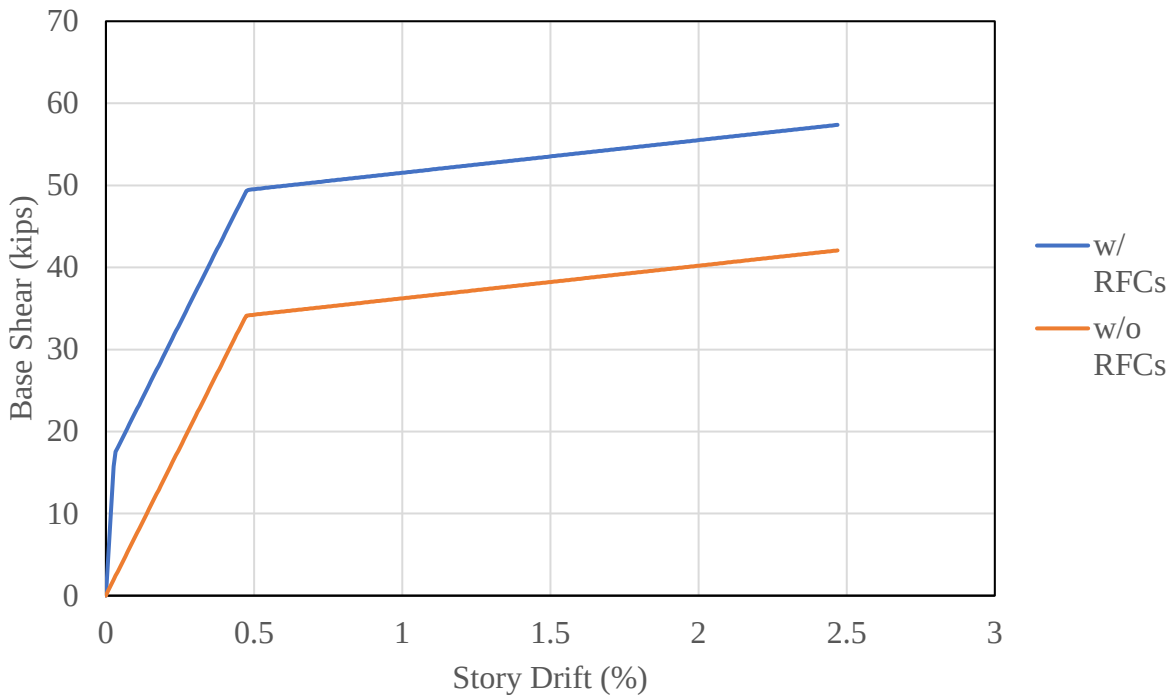

Figure 5-5. Pushover Analysis of Model 85

5.3.5 Pushover Results for Model 138

The pushover curves for Model 138 are shown in Figure 5-6. For the baseline model, the initial stiffness is 137 kips/inch. When the base shear of the structure reaches 193 kips, the tension-only braces yield, and the secondary stiffness becomes 4.3 kips/inch. When the RFCs are added,

the initial stiffness increases to 467 kips/inch which is a 241% increase in stiffness over the baseline model. The RFCs slip and the base shear continues to increase. The braces yield when the base shear reaches 242 kips. The sixty energy dissipating connections have added 49.0 kips to the lateral capacity of the structure, which is a 25% increase over the baseline model

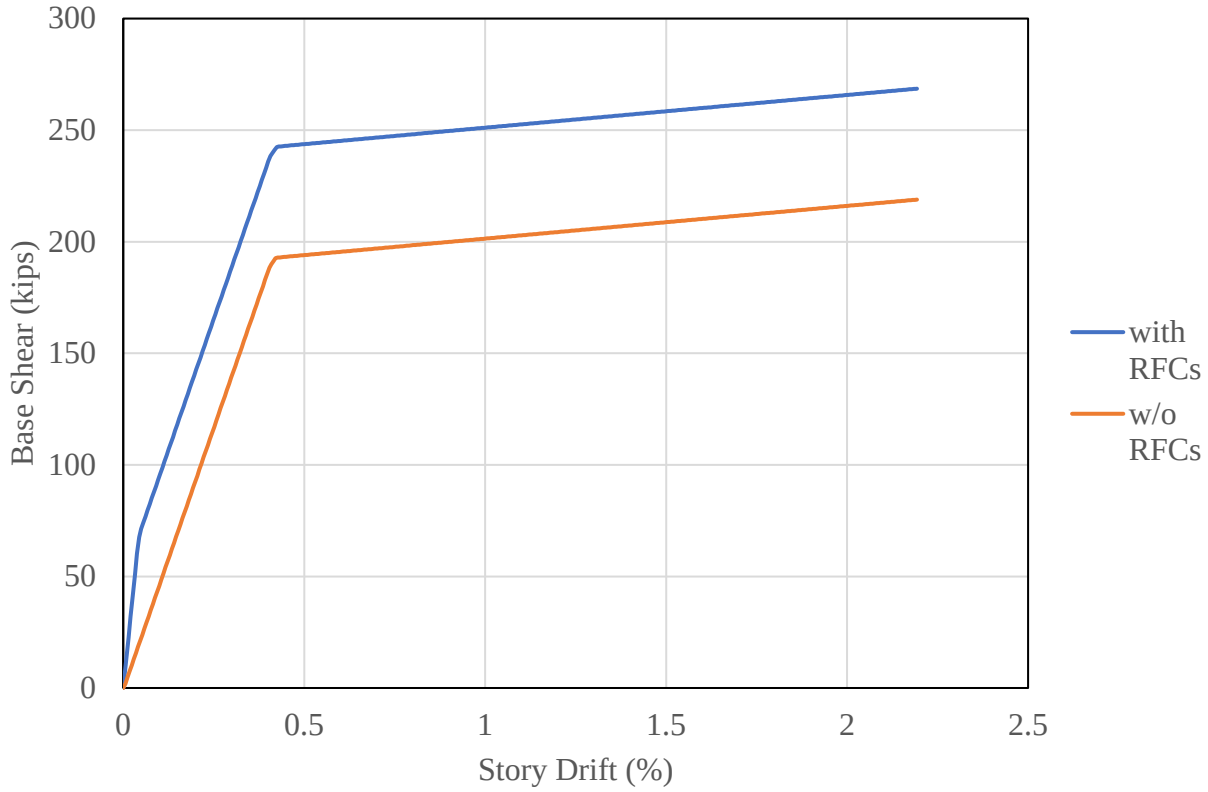

Figure 5-6. Pushover Analysis of Model 138

The pushover curves for each of these models shows that the rotational friction connections increase the lateral force capacity of the structures. Because the decision was made to utilize a maximum of three rotational friction connections per panel, and the largest bolt size used was 1-inch in diameter, there was ceiling on the lateral capacity that the rotational friction connections could add to the structure. Models 16, 41, 42, and 138 use the rotational friction connection configuration that achieves this maximum additional capacity. Model 85 was small enough that a 5/8-inch diameter bolt could be used for the rotational friction connection.

5.4 Modal Response

A modal analysis was performed on each of the models to assess the impact the rotational friction connections have on the natural periods and corresponding modes of vibration of the metal building system. These modes and corresponding periods are structural properties that play a central role in the dynamics and response of structures to earthquakes. The calculation of the natural frequencies of vibration of a structure is a matrix eigenvalue problem as shown in Equation 5-3, where k is the global stiffness matrix, m is the mass matrix, ω_n is a scalar that represents the natural frequencies of vibration, and φ_n is the corresponding mode shape.

$$[k - {\omega_n}^2 m]\varphi_n = 0 \qquad \textbf{Equation 5-3. (Chopra 2009)}$$

SAP2000 uses the subspace iteration method to solve for the natural periods and mode shapes (CSI 2017). The two significant modes of vibration for a metal building system are the first mode in the longitudinal direction, as shown in Figure 5-7, and the first mode in the transverse moment frame direction, shown in Figure 5-8. The periods of vibration and cumulative mass participation ratios for each model are listed in Table 5-3. For all the models, the longitudinal mode period of vibration is shorter than the period in the transverse direction. This is not surprising due to the fact that moment frames are more flexible than the braced frame system. When the rotational friction connections are added to the structure, the period of the first longitudinal mode decreases varied from 5% to 32%, which is indicative of a structure that has stiffened. The mass participation ratio of the first mode in the longitudinal direction decreases roughly 1% to 16%. In the transverse direction, the periods of vibration and mass participation ratios appear unchanged by the presence of rotational friction connections.

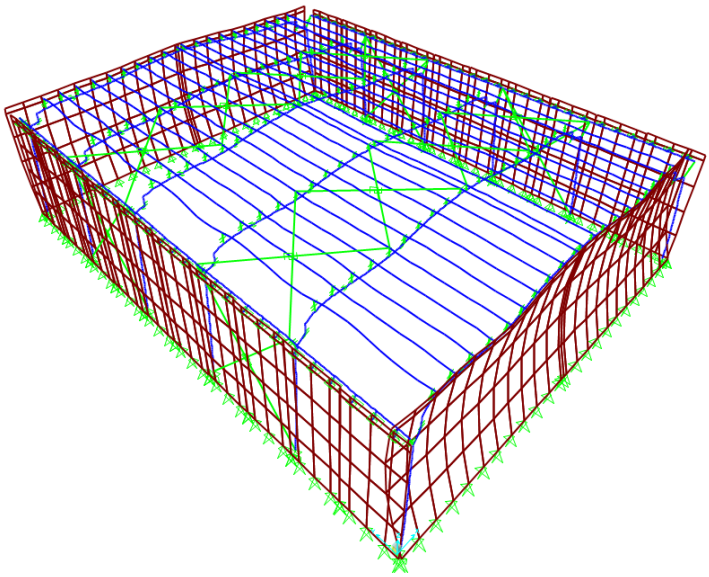

Figure 5-7. First Longitudinal Mode Shape for Model 41

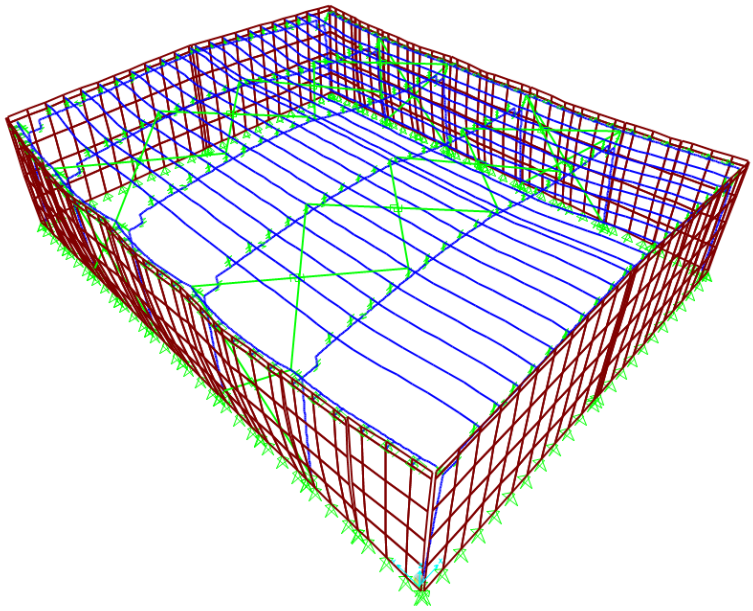

Figure 5-8. First Transverse Mode Shape for Model 41

Table 5-3. Period of Vibration and Mass Participation Ratios for Models

Model	Mode	Period (sec)			Cumulative MPR		
		Baseline	With RFC	Percent Difference	Baseline	With RFC	Percent Difference
16	Longitudinal Mode 1	0.64	0.54	-18.1	0.92	0.86	-6.6
	Longitudinal Mode 2	0.22	0.22	-0.4	0.93	0.91	-2.6
	Transverse Mode 1	0.74	0.73	-0.9	0.75	0.75	0.3
	Transverse Mode 2	0.53	0.53	-0.9	0.84	0.84	0.2
41	Longitudinal Mode 1	0.73	0.63	-15.1	0.92	0.92	-0.6
	Longitudinal Mode 2	0.48	0.48	-0.1	0.92	0.92	-0.6
	Transverse Mode 1	0.85	0.84	-0.6	0.76	0.76	0.1
	Transverse Mode 2	0.54	0.53	-0.9	0.80	0.80	0.2
42	Longitudinal Mode 1	0.72	0.68	-4.7	0.77	0.66	-16.4
	Longitudinal Mode 2	0.61	0.60	-1.8	0.84	0.79	-6.7
	Transverse Mode 1	0.87	0.87	-0.4	0.69	0.69	0.1
	Transverse Mode 2	0.81	0.81	-0.6	0.71	0.71	0.1
85	Longitudinal Mode 1	0.48	0.34	-32.4	0.85	0.84	-1.2
	Longitudinal Mode 2	0.10	0.10	-0.7	0.94	0.93	-1.6
	Transverse Mode 1	0.48	0.48	-0.5	0.68	0.68	0.1
	Transverse Mode 2	0.29	0.29	-1.2	0.76	0.76	0.1
138	Longitudinal Mode 1	0.74	0.63	-15.9	0.90	0.85	-5.7
	Longitudinal Mode 2	0.45	0.44	-1.1	0.94	0.93	-0.9
	Transverse Mode 1	0.85	0.84	-0.6	0.75	0.75	0.1
	Transverse Mode 2	0.52	0.51	-0.8	0.81	0.81	0.0

5.5 Nonlinear Response History Analyses

5.5.1 Ground Motion Suite

The earthquake ground motions that were used in the nonlinear dynamic analyses for the 3-D models are listed in Table 5-2. The suite of ground motions was downloaded from the PEER NGA database (PEER 2015). The earthquake records were scaled, as highlighted in Table 5-4, so that the spectra of the ground motion pairs matched the MCE spectra for Riverside, California at three frequencies of importance to the analysis. The design peak ground acceleration for a short period structure, less than 0.2 seconds, happens to be 1.0 g in Riverside, California. The earthquake records were selected due to the fact that the shape of the record's spectrum was consistent with the MCE spectrum. The response spectrum of the ground motion suite is shown in Figure 5-9.

Table 5-4. Earthquake Suite for Nonlinear Dynamic Analyses

	NGA#	Event	Year	Station	Timestep (seconds)	Scale Factor	Duration (seconds)	Frame Direction	Long. Direction
1	57	San Fernando	1971	Castaic Old Ridge Route	0.01	3.1	30	ORR021	ORR291
2	125	Friuli, Italy	1976	Tolmezzo	0.005	3.028	36.345	TMZ270	TMZ000
3	126	Gazli, USSR	1976	Karakyr	0.005	1.073	16.265	GAZ000	GAZ090
4	184	Imperial Valley-06	1979	El Centro Differential Array	0.005	1.456	38.96	EDA360	EDA270
5	725	Superstition Hills	1987	POE	0.01	2.366	22.3	POE270	POE360
6	752	Loma Prieta	1989	Capitola	0.005	1.697	39.955	CAP090	CAP000
7	960	Northridge	1994	Canyon Country - W Lost Canyon	0.01	1.272	19.99	LOS000	LOS270
8	1084	Northridge	1994	Sylmar Converter Station	0.005	0.876	40	SCS142	SCS052
9	1107	Kobe, Japan	1995	Kakogawa	0.01	2.147	40.96	KAK000	KAK090
10	1158	Kocaeli	1999	Duzce	0.005	1.872	27.185	DZC270	DZC180
11	1513	Chi-Chi, Taiwan	1999	TCU079	0.005	1.434	90	TCU079-N	TCU079-E

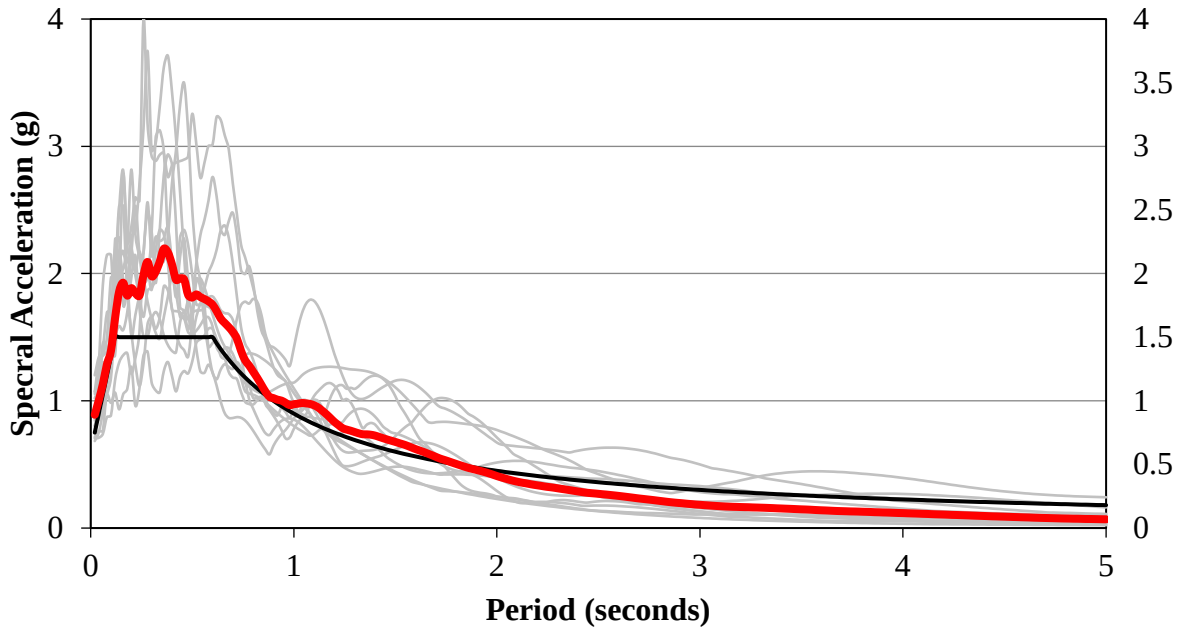

Figure 5-9. Response Spectra of Scaled Earthquake Ground Motions with MCE Spectrum

The seismic provisions in the building code provide prescriptive means in achieving life-safety at the design basis event and a 10% probability of collapse during a maximum considered event. The performance of a structure during more frequent events is not considered unless a rigorous analysis investigates these load cases. Considering recent earthquake events, the public has demanded more of structural engineers in providing structures that are not only providing life safety, but have resiliency so that life and business can return as quickly to normal operations following a seismic event. The analyses performed in this research considers the impact that rotational friction connections have on improving the seismic performance of metal building systems during less intense, more frequent seismic events. Table 5-5 lists the four earthquake hazards that were considered for the nonlinear dynamic analyses. The MCE suite of ground motions were scaled accordingly to match the seismic hazard of the more frequent events.

Table 5-5. Performance-Based Design Earthquake Hazard Levels

Earthquake Hazard	Probability of Exceedance	Return Period	Scaling Factor
Service Level Earthquake 1 (SLE1)	50%/50 years	75	25%
Service Level Earthquake 2 (SLE2)	20%/50 years	225	50%
Design Basis Earthquake (DBE)	10%/50 years	500	66.7%
Maximum Considered Earthquake (MCE)	2%/50 years	2500	100%

5.5.2 Expected Gravity Loads

The analyses assumed an expected gravity load of 1.0D, where D is the expected gravity load. ASCE 7 (2016) calls for an additional analysis that 1.0D + 0.5L, where D is the expected dead load and L is 40% of the unreduced live load. The additional load case that adds a portion of the live load component would be significant in multi-story structures. However, metal building systems are one or two-story structures. The metal building frames included in this study have only one-story, where the only live load component is a roof live load. Due to the low probability that a live load of this magnitude would be present during the event of an earthquake, the case involving the addition of live load was not performed.

One frame (Frame 42) in this study was designed with a snow load of 42 psf on the roof. The expected dead load does not include the contribution due to snow. In the design of the frame, the seismic mass of the snow was considered. However, for the nonlinear dynamic analyses, the snow load and its contribution to seismic mass were eliminated.

5.5.3 Rayleigh Damping

The inherent damping used in all analyses was represented using Rayleigh Damping (Figure 5-10). Metal building systems have been shown experimentally to have lower inherent damping than conventional moment frames due to fewer connections (Smith 2013d). The damping

ratios were set to 2% critical damping at periods that corresponded to the natural period of vibration and 10% of the natural period ($0.1T_n$).

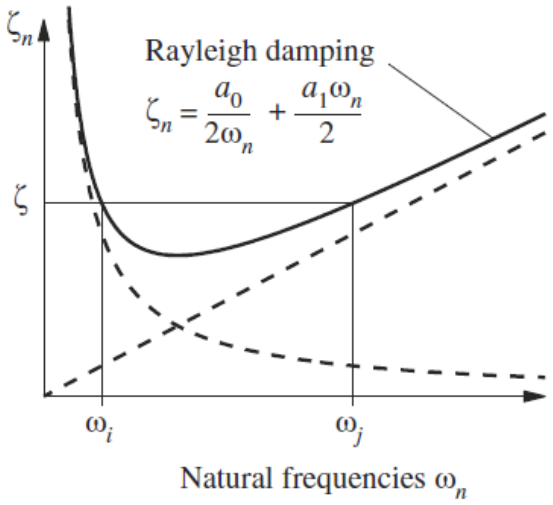

Figure 5-10. Rayleigh Damping (Chopra 2009)

Before each nonlinear dynamic analysis, a nonlinear static analysis with the full dead load and collateral load was applied to ensure the structure had the necessary vertical loads to properly represent the P-Delta effects on the structural response. The nonlinear dynamic analyses started from the last step of that nonlinear static analysis. The time-integration method used was the Hilber-Hughes-Taylor alpha method (Hilber et al. 1977). This method was selected because excess vibrations that have a frequency less than the time step can be damped out. A nonlinear solution is more likely to converge when small amounts of numerical damping are used (CSI 2017). The alpha value used in the all analyses was -1/96.

5.5.4 Structural Response

This section presents the peak story drifts and peak accelerations for the baseline model and the model utilizing the rotational friction connections. Due to the nature of nonlinear analyses, convergence to a solution may not be achieved for every load case. Several of the baseline

structures under the MCE level ground motions did not converge. Upon inspection, in the time leading up to the convergence failure, many of the structures exhibited large story drifts that would have resulted in fracture of the side wall braces. For Model 42, the axial force demands coupled with the flexural demand from the out-of-plane forces from the wall panel overstressed the spandrel beam. Failure of this element would have led to the possibility of a wall panel falling away from the structure. For these reasons, these structures were defined as having collapsed. Table 5-6 lists the analytical models that did not converge and collapsed. To provide a meaningful comparison in structural performance, the DBE level results for the models utilizing the RFCs were compared with the DBE level results for the baseline models for those cases.

Table 5-6. Analysis Models with Convergence Error indicating Collapse Mechanisms

Analytical Model	EQ Case	Collapse Justification
41P3_RFC0000_SL14.5_MCE	CAP	Fracture of Sidewall Braces
	SCS	
42P3_RFC0000_SL14.5_MCE	CAP	Spandrel Beam Failure
	SCS	
	TMZ	
85P3_RFC0000_SL07.5_MCE	CAP	Fracture of Sidewall Braces
138P3_RFC0000_SL14.5_MCE	CAP	Fracture of Sidewall Braces
	SCS	
	TCU	
42P3_RFC1000_SL14.5_MCE	CAP	Spandrel Beam Failure
	LOS	
	TCU	

The results are divided into the longitudinal and transverse direction. The results show a significant improvement in the seismic response in the longitudinal direction of the structure. The seismic response in the transverse direction did not appear to be negatively or positively impacted in terms of the peak story drifts.

Due to the variable nature of earthquake ground motions, the peak displacement demands experienced by the structure are not identical. Figure 5-12 shows a box-and-whiskers plot of the peak transverse story drift for Model 16P3_RFC1000_SL14.5 under the maximum-considered event level. These joints are located on the frameline where the spandrel beam connects to the metal building moment frame, as seen in Figure 5-11. This shows the distribution of the peak transverse displacements. There is an improvement in the peak story drift in the nodes along the connection line when the rotational friction connections are added. This reduction in the peak story drift was true in every model. Table 5-7 shows that adding the rotational friction connections reduced the mean peak story drift in to longitudinal direction by 28% for Model 42 and 63% for Model 16.

The effect of the rotational friction connections is much lower in the transverse direction of the metal building system. As seen in Table 5-6, the rotational friction connections reduced the mean peak transverse story drift by up to 7% and in Model 85. The RFCs had no impact in the reduction in the transverse story drift for Model 42. The energy dissipation of the rotational friction connection was geared in the longitudinal direction, so the decrease in mean peak story drift in the longitudinal direction is not surprising. The effect of the rotational friction connections on the seismic response in the transverse behavior is minimal.

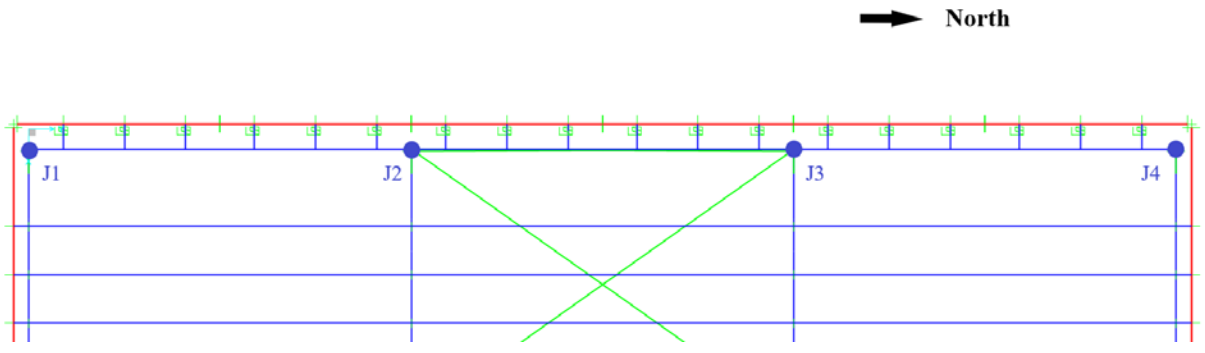

Figure 5-11. Joint along the West Wall Spandrel Beam for 16P3_RFC1000_SL14.5 (Plan View)

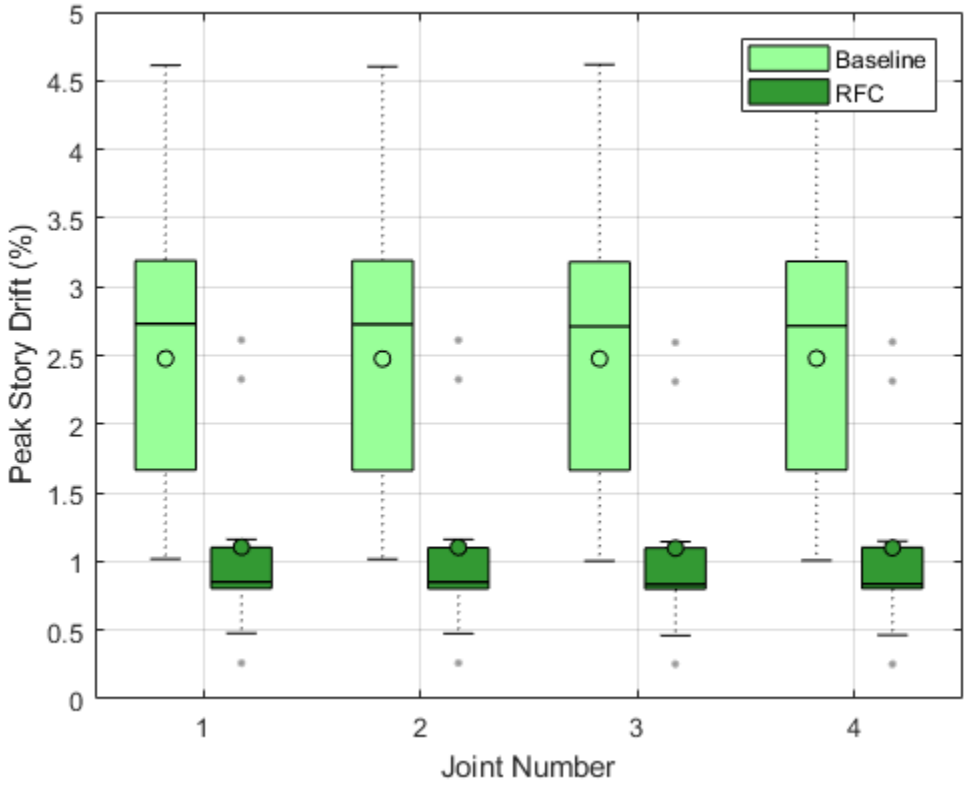

Figure 5-12. Box and Whisker Plot of Peak Longitudinal Story Drifts for 16P3_RFC1000_SL14.5 at MCE Level

Table 5-7. Mean Longitudinal Story Drifts for DBE and MCE Level (Joint 3)

Model	Mean Peak Longitudinal Story Drift (%)			Percent Reduction of DBE Demand
	Baseline, DBE	RFC, DBE	RFC, MCE	
16	1.32	0.49	1.10	63%
41	1.17	0.69	1.37	41%
42	0.32	0.23	0.38	28%
85	2.78	0.74	1.47	73%
138	1.40	0.74	1.91	47%

Table 5-8. Mean Transverse Story Drifts for DBE and MCE Level (Joint 3)

Model	Mean Peak Transverse Story Drift (%)			Percent Reduction of DBE Demand
	Baseline, DBE	RFC, DBE	RFC, MCE	
16	1.60	1.54	2.67	4%
41	1.67	1.64	2.46	2%
42	1.03	1.03	1.44	0%
85	2.00	1.86	2.92	7%
138	1.69	1.66	2.49	2%

5.5.5 Energy Response Histories

A useful way to analyze the seismic performance of a structure is through energy response histories. During seismic events, the earthquake energy is imparted into structures. The energy in the structure can take to form of elastic strain energy, kinetic energy, inherent damping, and hysteretic energy from plastic strain energy. In metal building systems, the plastic strain energy is due to permanent damage from yielding of the tension-only bracing elements and the lateral torsional buckling of the metal building moment frame. Figure 5-13 show the comparison of the energy response history of the baseline model of Model 42 (left) with the model equipped with the rotational friction connections (right) under the MCE level ground motions. There is a significant decrease in the total input energy, inelastic frame energy, and inelastic brace energy for the structure clad with RFCs. However, the reduction in total input energy was not observed for every earthquake. In Figure 5-14, there was not a signification decrease in the total input energy. This can be explained by the increase in the stiffness of the structure due to the RFCs. A change in stiffness can affect how a structure responds to the ground motion. The magnitude of the change depends upon the characteristics of the earthquake's ground motion (Baird 2014).

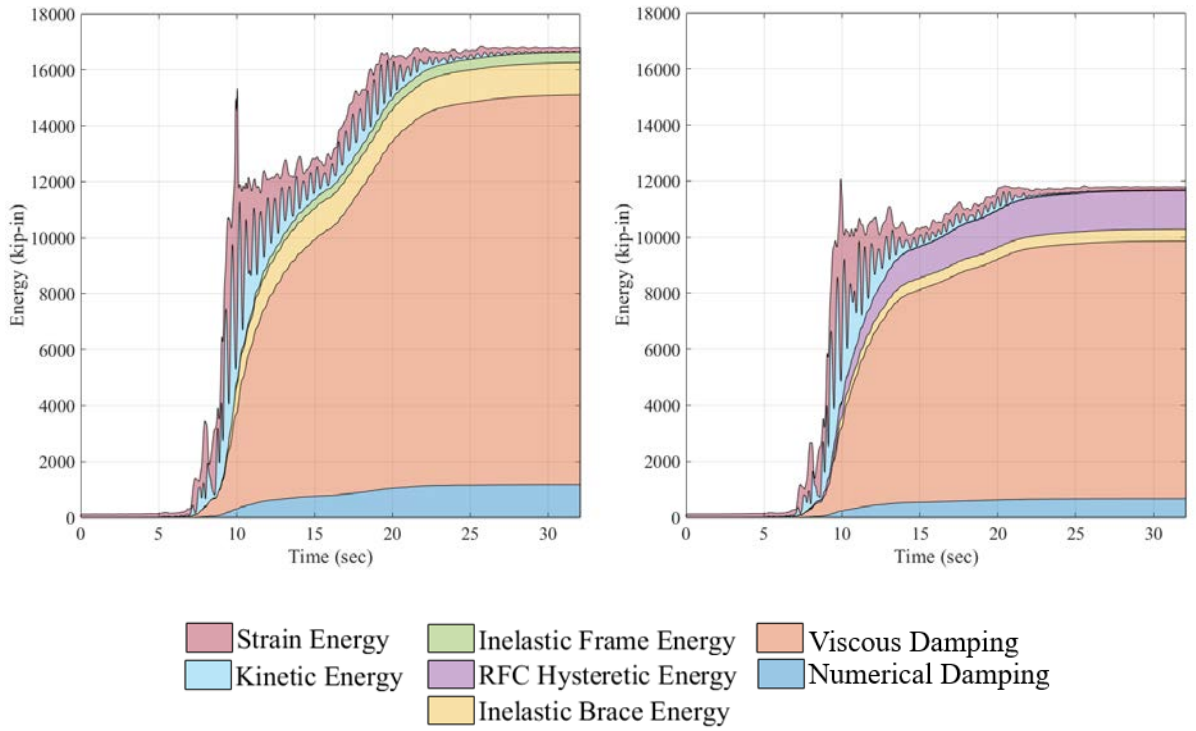

Figure 5-13. Energy Response History for Baseline Structure (left) and Metal Building System clad with RFC (right) for Kocaeli, Turkey (1999) earthquake ground motion scaled to MCE Level

It can be seen in Figure 5-14 that the addition of the RFCs significantly reduces the hysteretic energy absorbed by the tension-only steel braces and the metal building frame. Energy that would have been absorbed by the braces is instead being transferred to the RFCs. The reduction in hysteretic energy of the metal building system components in equivalent to a reduction in structural damage. These energy results confirm that the rotational friction connections are performing their intended function of reducing damage to surrounding components.

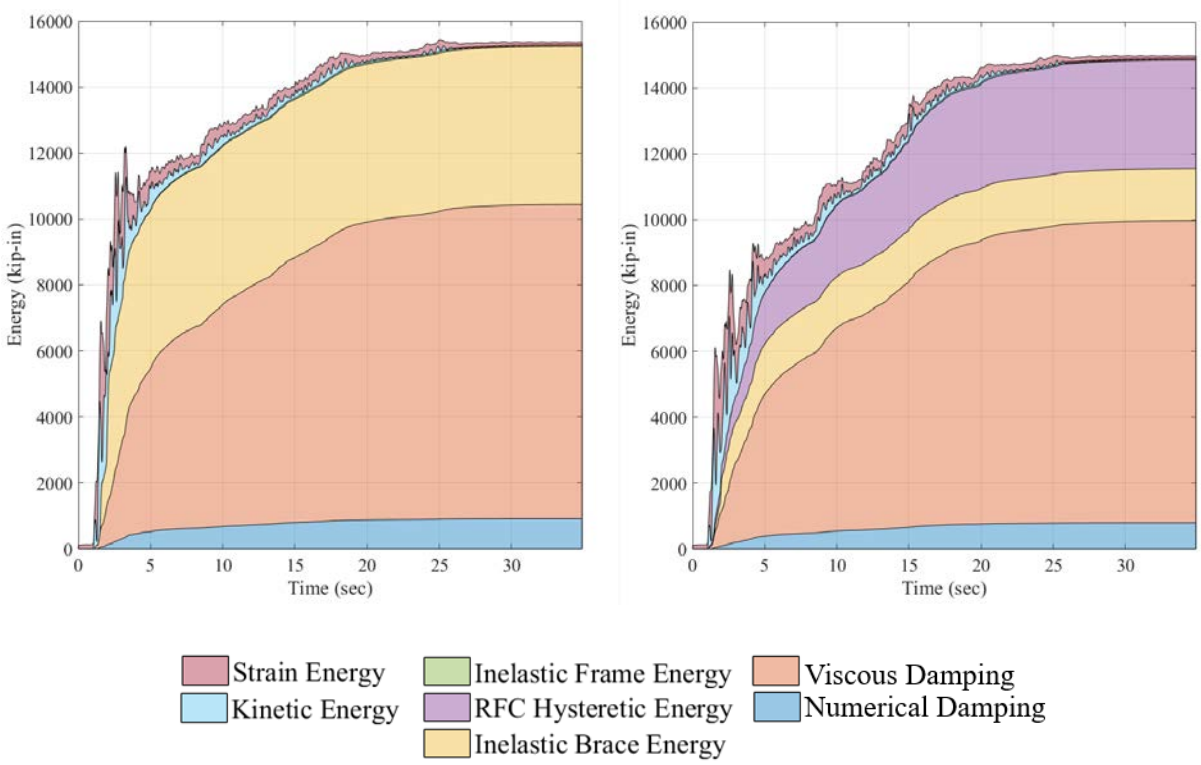

Figure 5-14. Energy Response History for Baseline Structure (left) and Metal Building System clad with RFC (right) for San Fernando (1971) earthquake ground motion scaled to MCE Level

5.5.6 Tension-Only Brace Performance

The energy response history diagrams have shown that the rotational friction connections are absorbing seismic energy that would have otherwise been absorbed as inelastic strain energy in the tension-only braces. By using the peak expected axial displacement, the performance of each brace was assigned one of four performance categories: Fully Operation, Immediate Occupancy, Life-Safety, or Collapse Prevention. As discussed in Chapter 4, ASCE 41 (ASCE/SEI 2013) performance categories for a tension-only brace was utilized.

The brace numbers are identified for Model 85 in Figure 5-15. Table 5-9 illustrates the structural performance level achieved for all the tension-only braces in the baseline Model 85 for the DBE suite of 11 earthquakes. The peak axial displacements in the braces were normalized to

the expected axial yield displacement. The cells are color-coded as follows: Fully Operation (blue), Immediate Occupancy (green), Life-Safety (yellow), or Collapse Prevention (red). For the baseline model subjected to the DBE level suite, five earthquake analyses strained the braces beyond the collapse prevention acceptance criteria shown in red. The mean value of the sidewall braces ranged between 4.64 and 5.00, which is close to the collapse prevention performance level.

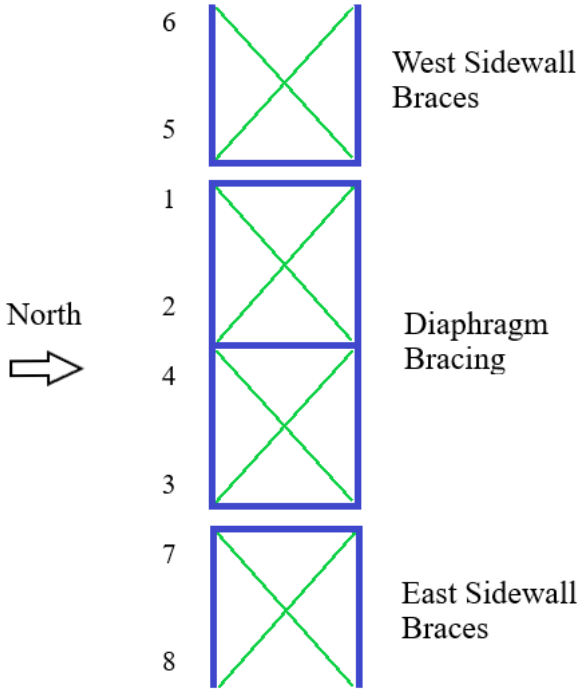

Figure 5-. Brace Identification for Model 85

Table 5-9. Brace Performance and Ductility Demand for Model 85P3_RFC0000_SL07.5_DBE

Brace Number	CAP	DZC	EDA	GAZ	KAK	LOS	ORR	POE	SCS	TCU	TMZ	Mean	Median
6	9.61	4.79	1.39	1.57	5.76	4.67	7.62	4.43	1.26	9.28	4.56	5.00	4.67
5	8.06	4.45	2.41	2.79	4.15	12.95	4.38	4.65	2.53	3.48	3.65	4.86	4.15
1	0.98	1.37	0.68	0.73	0.89	2.21	1.10	0.81	0.75	0.80	0.90	1.02	0.89
2	1.18	0.81	0.70	0.65	1.15	2.02	0.73	0.86	0.60	0.97	0.98	0.97	0.86
4	1.20	0.99	0.81	0.75	0.60	2.14	0.97	0.83	0.68	0.76	1.75	1.04	0.83
3	0.92	0.71	0.60	0.74	0.76	1.94	1.40	0.75	0.61	0.96	0.98	0.94	0.76
7	6.67	4.94	2.09	2.66	6.13	9.87	4.01	4.79	1.90	5.16	2.80	4.64	4.79
8	10.54	5.16	0.95	2.21	4.70	4.33	7.24	4.57	2.50	8.54	3.66	4.95	4.57

Legend	FO	IO	LS	CP

By adding the rotational friction connections, Table 5-10 illustrates a significant improvement in the performance level of the braces. For the DBE level event, all braces achieved either an immediate occupancy or fully operational performance level. In some cases, the structural performance of the braces improved by two performance categories. The mean normalized yield displacement values for the braces improved to a range of 1.17 to 1.32.

Table 5-10. Brace Performance and Ductility Demand for Model 85P3_RFC0625_SL07.5_DBE

Brace Number	CAP	DZC	EDA	GAZ	KAK	LOS	ORR	POE	SCS	TCU	TMZ	Mean	Median
6	1.27	1.01	0.30	0.67	0.96	0.66	2.04	1.21	0.50	3.69	2.31	1.33	1.01
5	1.74	1.53	0.53	1.32	1.41	1.29	0.85	0.89	0.56	1.71	1.01	1.17	1.29
1	0.95	0.84	0.43	0.69	0.76	0.70	0.83	0.88	0.52	0.95	1.14	0.79	0.83
2	0.89	0.98	0.66	0.81	0.88	0.80	0.72	0.71	0.55	0.83	1.09	0.81	0.81
4	0.95	0.75	0.58	0.91	0.84	0.88	0.65	0.84	0.59	0.95	0.85	0.80	0.84
3	0.85	0.89	0.50	0.58	0.83	0.73	0.92	0.78	0.56	1.03	0.93	0.78	0.83
7	1.69	1.68	0.54	1.23	1.44	1.03	0.84	0.94	0.56	1.82	1.18	1.18	1.18
8	1.63	1.08	0.34	0.69	0.95	0.67	1.68	1.30	0.51	3.54	2.17	1.32	1.08

Legend	FO	IO	LS	CP

The structure equipped with RFCs was analyzed using the MCE level ground motions to further investigate the performance, as shown in Table 5-11. Two of the earthquake analyses produced collapse level performance in the sidewall braces. The contribution of the RFCs reduced the mean ductility demand in the wall braces at the MCE level so much that it is less than those experienced at the DBE demands of the baseline model.

Table 5-11. Brace Performance and Ductility Demand for Model 85P3_RFC0625_SL07.5_MCE

Brace Number	CAP	DZC	EDA	GAZ	KAK	LOS	ORR	POE	SCS	TCU	TMZ	Mean	Median
6	3.65	2.00	0.65	1.06	0.97	2.30	6.62	2.58	0.94	5.78	2.82	2.67	2.30
5	2.22	1.84	0.90	4.51	1.68	3.42	2.09	2.18	1.31	5.43	1.68	2.48	2.09
1	1.00	0.96	0.72	0.87	0.83	0.95	0.95	0.94	0.80	4.08	1.38	1.23	0.95
2	1.56	1.10	0.78	0.81	1.61	0.80	0.99	0.81	0.85	0.86	1.74	1.08	0.86
4	0.94	0.89	0.91	1.26	0.90	1.54	1.74	1.02	0.84	2.28	1.63	1.27	1.02
3	1.01	0.88	0.60	0.81	0.93	0.96	1.86	0.92	0.79	0.99	0.85	0.96	0.92
7	4.05	2.95	1.59	3.23	2.94	1.85	2.63	1.54	1.04	4.48	2.24	2.59	2.63
8	3.87	2.23	0.49	1.09	1.00	1.14	3.19	1.88	0.92	12.50	3.37	2.88	1.88

Legend	FO	IO	LS	CP

It is evident that metal building system clad with rotational friction connections perform superior to the baseline model in terms of reducing the inelastic demand in the metal building longitudinal seismic force resisting system. The improvement was visible for every model tested, whose results are displayed in Appendix C.

5.6 Rotational Friction Connection Response

5.6.1 Peak Rotation

The rotational friction connections in the metal building system between the hard walls and steel frame were connected to a spandrel beam that served as a collector element. The spandrel beam transferred seismic load from the tension-only rod braces through axial behavior. Due to the axial rigidity of the spandrel beam, the rotation in the energy dissipating connections was expected to be identical for all the connections along the side wall. Figure 5-16 displays a box-and-whisker's plot of the peak rotation of the west wall RFCs in Model 41P3_RFC1000_SL14.5 at the MCE level, which confirms a uniformity in the rotation in all the connections. This trend was repeated in all analysis models.

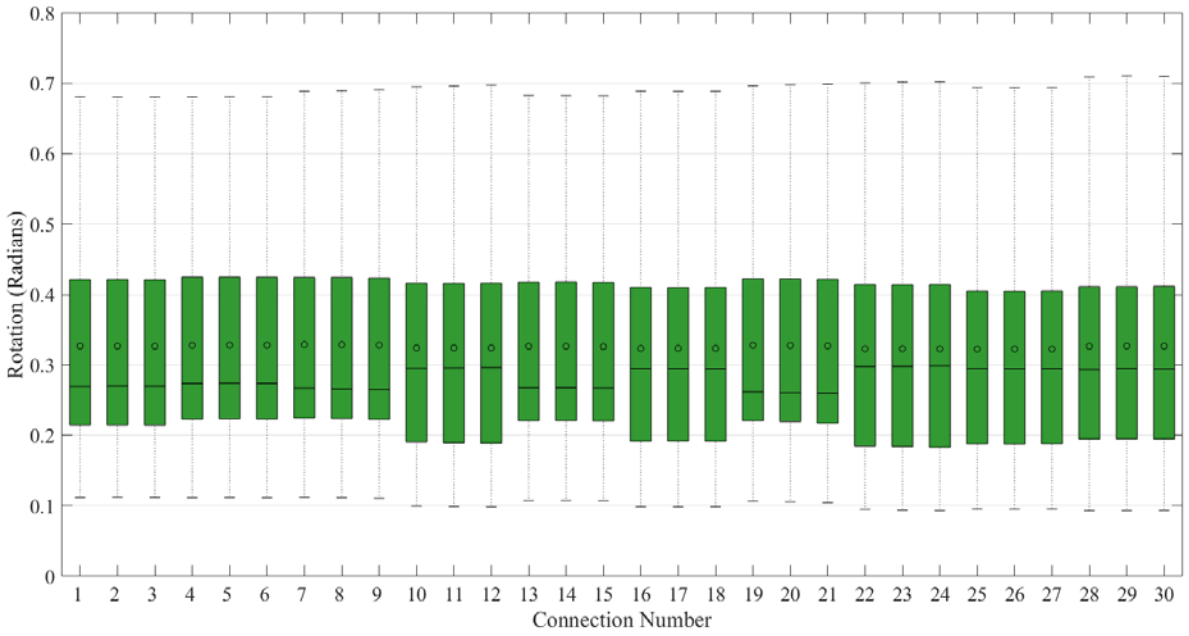

Figure 5-16. Peak Rotation along West Wall RFCs for Model 41P3_RFC1000_SL14.5 at MCE Level

5.6.2 Peak Out-of-Plane Forces

During a seismic event, the rotational friction connection is subjected to forces in all three dimensions. The rotational friction connections along the west wall are labeled for Model 41 as shown in Figure 5-17. The connections are numbered in an increasing fashion from south to north along the wall. A box-and-whiskers plot shown in Figure 5-18 displays the out-of-plane forces for the west wall rotational friction connections from Model 41P3_RFC1000_SL14.5. The bay spacing set at 25-feet with two wall panels per bay. In stark contrast to the uniformity of the peak rotations, the force demands varied significantly from connection to connection. The connections that experienced the highest out-of-plane demand were the connections closest to the metal building moment frame line. In Model 41, those connections were 1, 6, 7, 12, 13, 18, 19, 24, 25, and 30.

This large difference in the out-of-plane demand is likely due to the flexibility of the spandrel beam in its major axis of bending that is introduced between the wall system and the

metal building frame. If the spandrel beam was infinitely rigid, the out-of-plane demand for all the connections would be uniform. Because of the flexibility of the spandrel beam, most of the inertial load from the wall panels was resisted by the outermost connections. The rotational friction connection located along center of each wall panel (2, 5 8, 11, 14, 17, 20, 23, 26, and 29) experienced the lowest out-of-plane force demand.

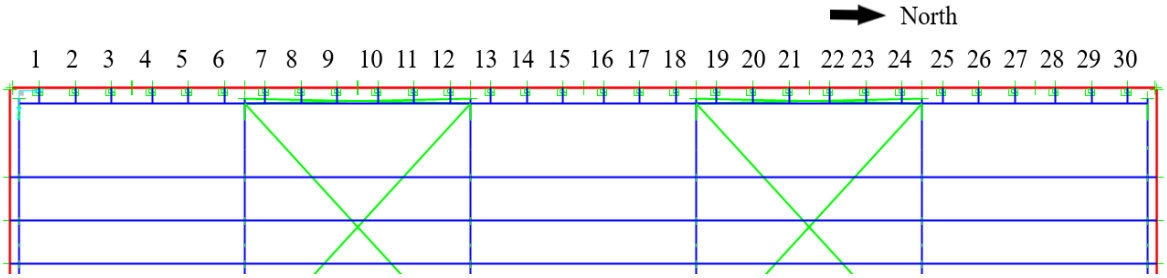

Figure 5-17. West Wall RFC Identification (Model 41 Plan View)

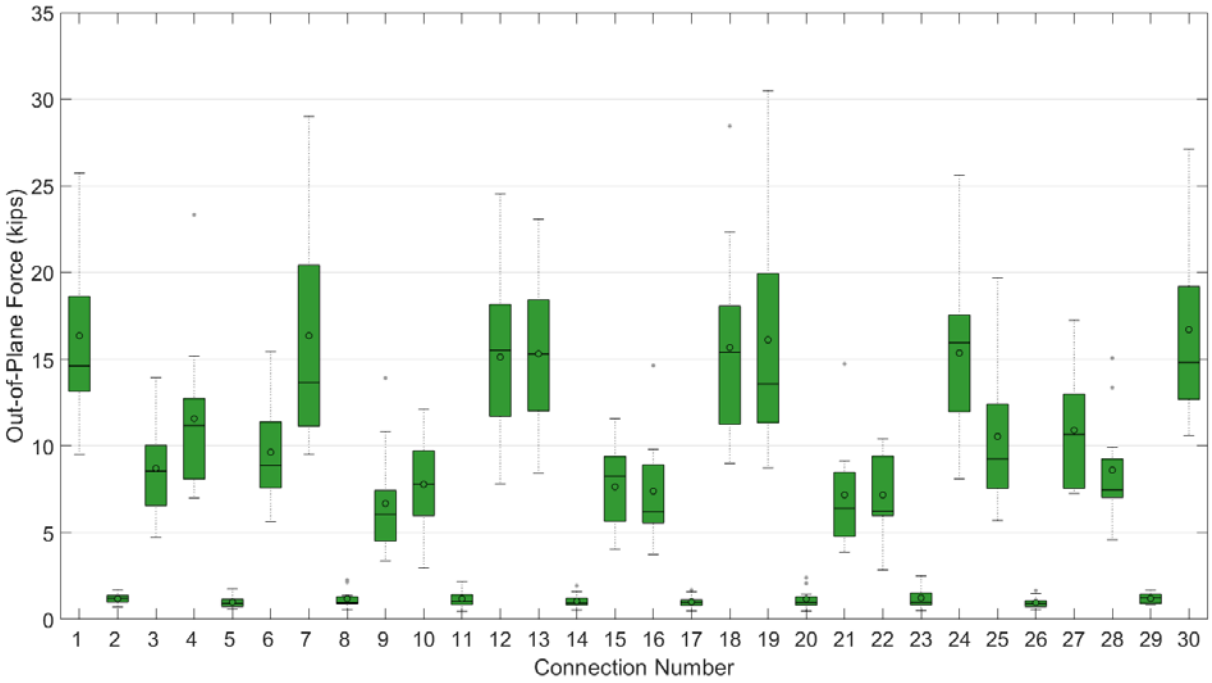

Figure 5-18. Out-of-Plane Force Demands for West Wall RFCs for Model 41P3_RFC1000_SL14.5_MCE

5.6.3 Peak In-plane Forces

A box-and-whiskers plot was generated for the in-plane vertical forces on all the connections along the west wall for Model 41P3_RFC1000_SL14.5, as shown in Figure 5-19. The in-plane vertical forces were much lower in magnitude than the out-of-plane forces. However, like the out-of-plane forces, the rotational friction connections closest to the metal building moment frame line exhibited higher in-plane vertical forces. Again, this variation in the in-plane vertical forces is due to the flexibility of the spandrel beam.

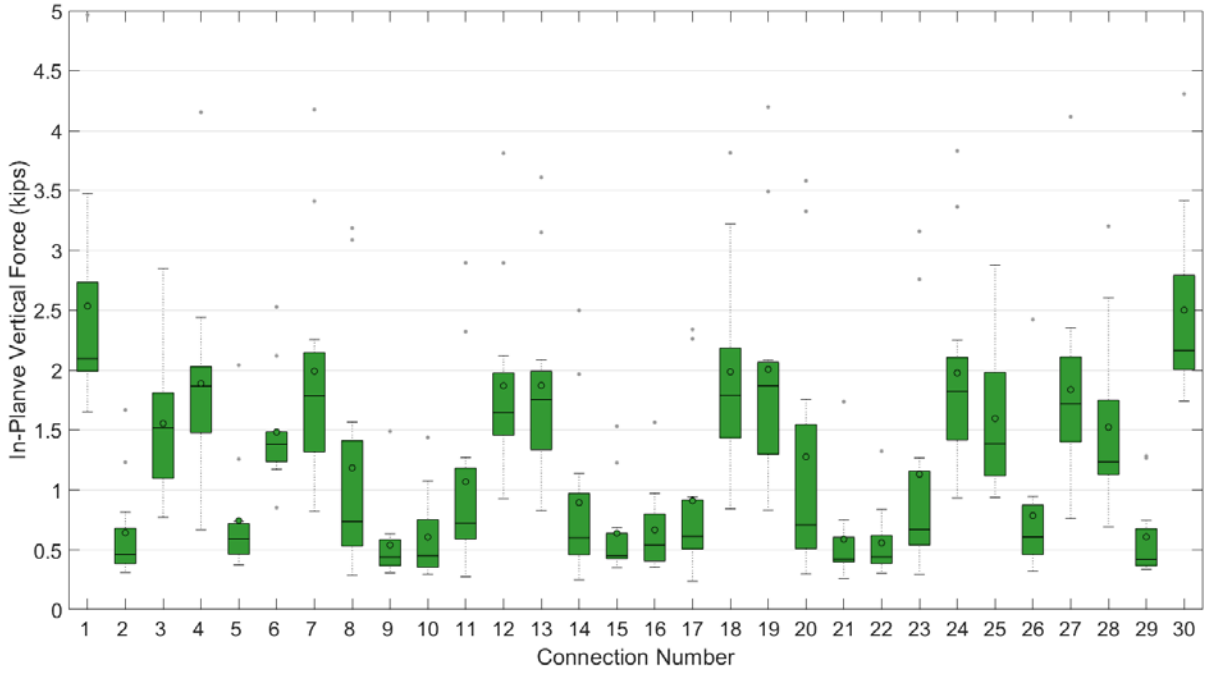

Figure 5-19. Peak In-Plane Vertical Forces on West Wall RFCs for 41P3_RFC1000_SL14.5_MCE

Finally, a box-and-whiskers plot was generated for the in-plane horizontal forces on all the connections along the west wall for Model 41P3_RFC1000_SL14.5, as shown in Figure 5-120. Due to the fundamental mechanics of the rotational friction connection, the absence of any out-of-plane load would cause the in-plane horizontal shear force to be uniform across every connection. The magnitude of the peak in-plane horizontal force would be equal to the free-rotation force of

the rotational friction connection. For Model 41, the free-rotation force of the connection was 0.76 kips. In a 3-D seismic analysis, it was expected that the out-of-plane forces played a significant role the in-plane horizontal force demand in these connections. As expected, the connections 1, 6, 7, 12, 13, 18, 19, 24, 25, and 30 experienced the highest mean in-plane horizontal shear force of all the connections along the side wall because they experienced the highest out-of-plane forces.

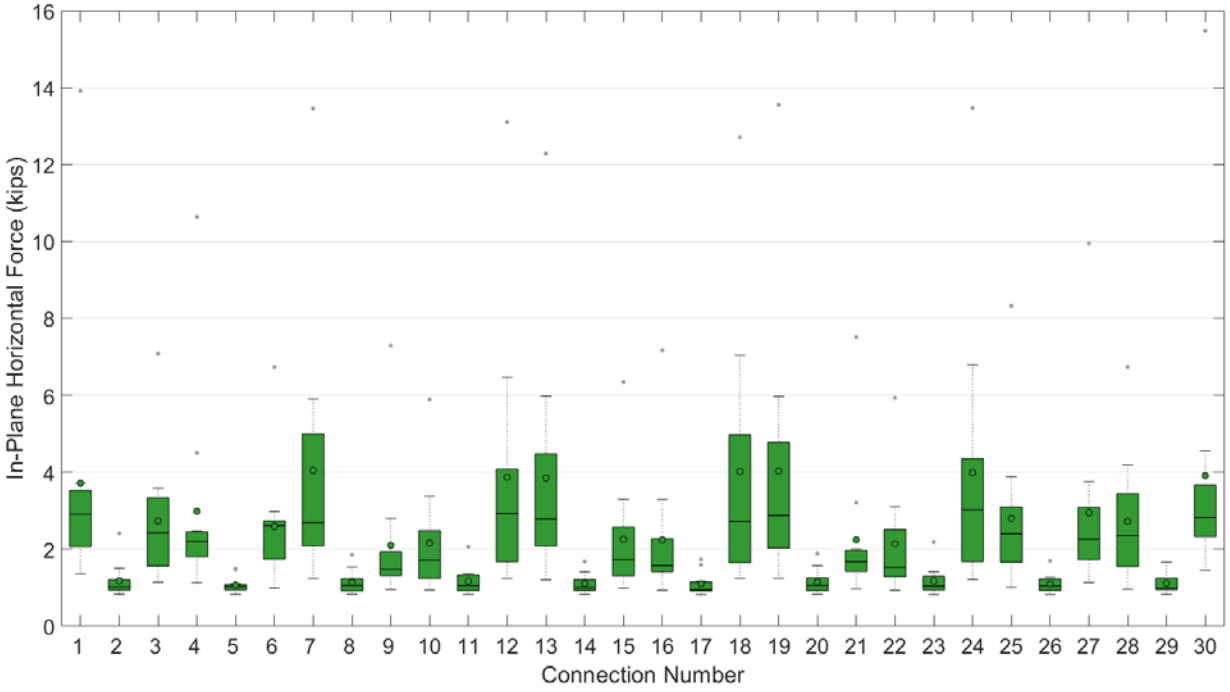

Figure 5-20. Peak In-Plane Horizontal Forces in RFCs along West Wall RFCs for 41P3_RFC1000_SL14.5_MCE

5.6.3 Hysteresis Loops for RFC

To investigate the behavior of the rotational friction connection, hysteresis loops were generated for individual connections during the MCE level earthquake analyses. Hysteresis loops are used to plot the force-displacement history of the rotational friction connection during the seismic event. Figure 5-21 displays the hysteresis loop of connection number 19 along the west wall of Model 41P3_RFC1000_SL14.5 during the Gazli, USSR ground motion. The loops are nearly rectangular in shape, which is indicative of a rotational friction connection that did not

experience much out-of-plane force demand. This connection was designed to initiate rotation after 0.76 kips of in-plane horizontal force has been developed. The peak in-plane shear force is nearly 0.76 kips which is the free-rotation force of the connection for this model.

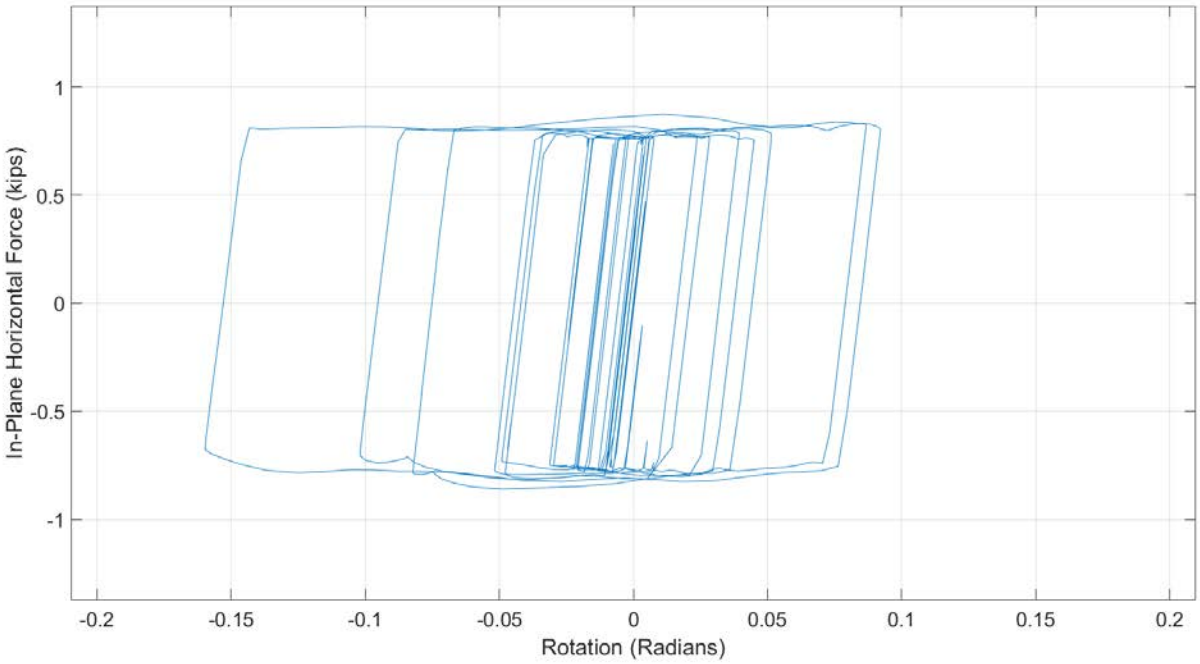

Figure 5-21. Hysteresis Loop of West Wall RFC 19 in 42P3_RFC1000_SL14.5_MCE_GAZ

The hysteresis loop of the adjacent connection, number 19, has a different shape, as seen in Figure 5-22. Though these connections experienced the same rotation history, the in-plane horizontal shear force was much higher in connection 19 due to the presence of the out-of-plane force. This behavior was predicted in the theoretical development of the rotational friction connection discussed in Chapter 3 and is due to the P-Delta effect. Three theoretical force-rotation envelopes are shown in Figure 5-23. The shape of these envelopes is reflected in the hysteresis loop of Figure 5-24. As the connection moves to higher rotations, in-plane shear forces are developed to satisfy force and moment equilibrium in the presence of an out-of-plane force.

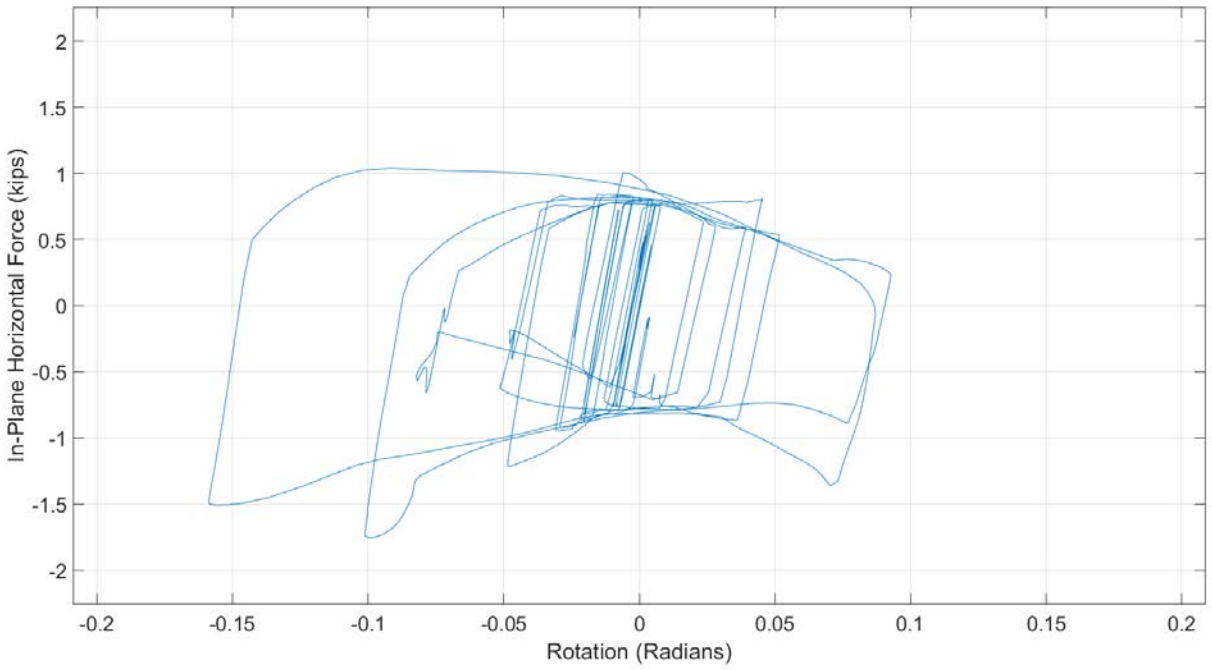

Figure 5-22. Hysteresis Loop of West Wall RFC 20 in 42P3_RFC1000_SL14.5_MCE_GAZ

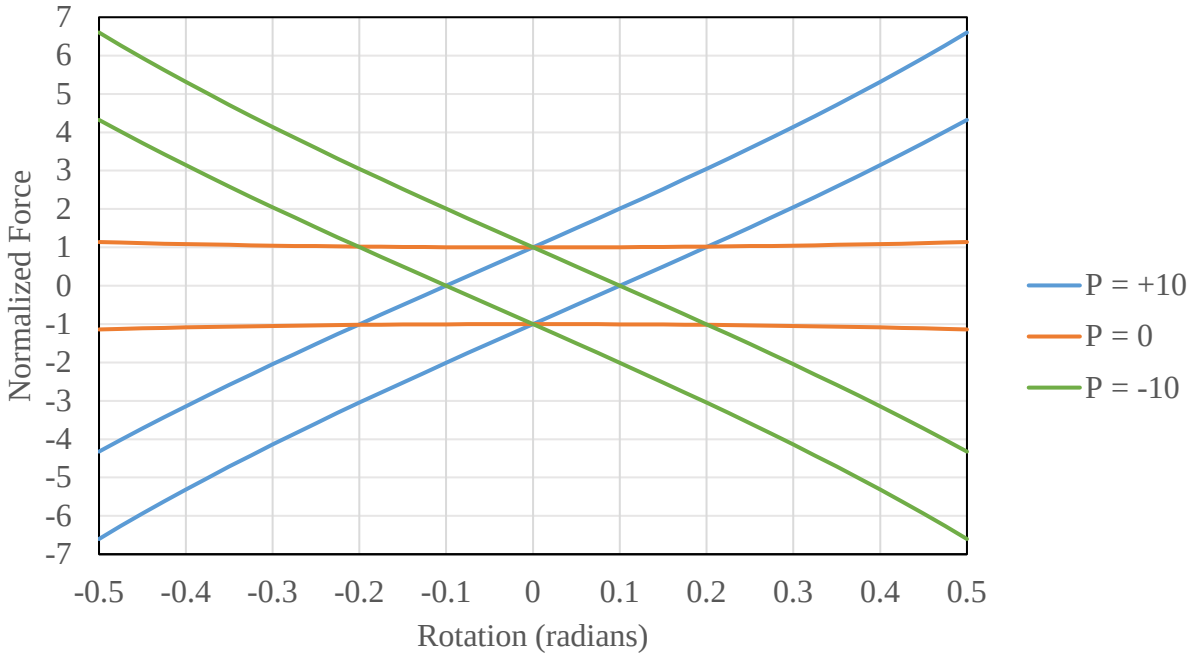

Figure 5-23. Force-Rotation Envelopes of RFCs

The ORR MCE level earthquake case generated much higher demands on the rotataion friction connections. The peak rotation achieved in the west wall connections was 0.53 radians

and for connection number 20, the peak in-plane horizontal force of 1.23 kips, as shown in Figure 5-24. The loop is nearly rectangular as expected due to the low out-of-plane force.

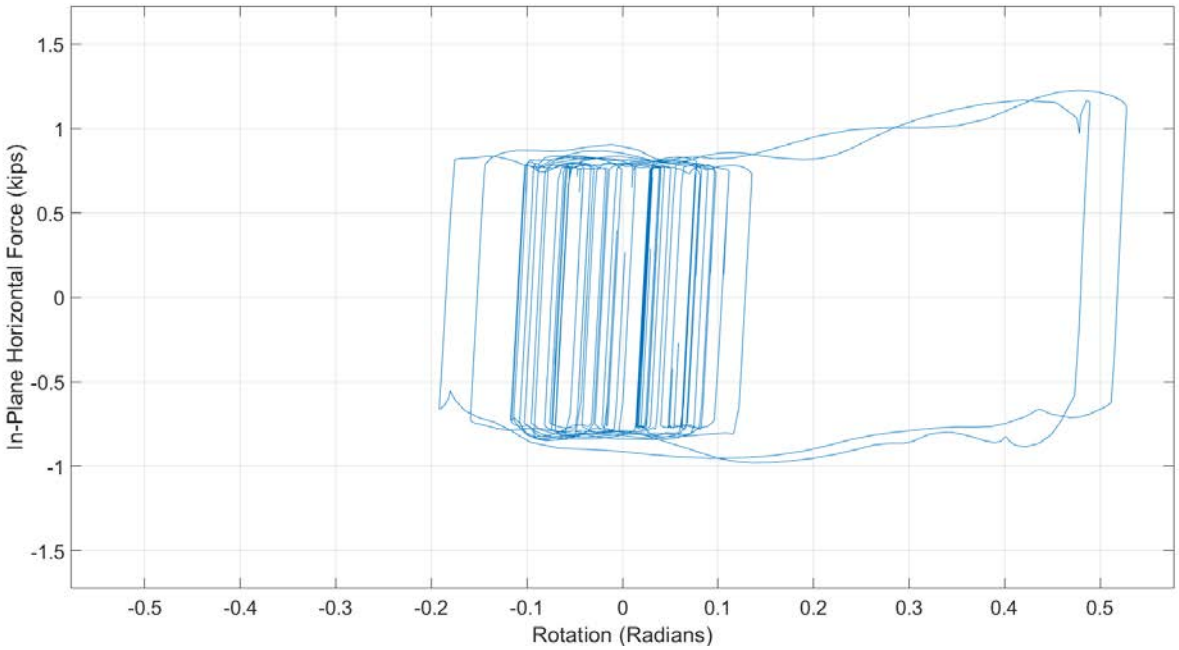

Figure 5-24. Hysteresis Loop of West Wall RFC 20 in Model 4P3_RFC1000_SL14.5_MCE_ORR

The hysteresis loop in Figure 5-25 shows that Connection 19 experienced significant P-Delta effects. While the connection was displaced at the peak rotations, the in-plane horizontal force increased significantly to -4.34 kips. This is much higher than the free-rotation force of 0.76 kips. The dynamic out-of-plane load is a critical component in determining the shape of the hysteresis loop.

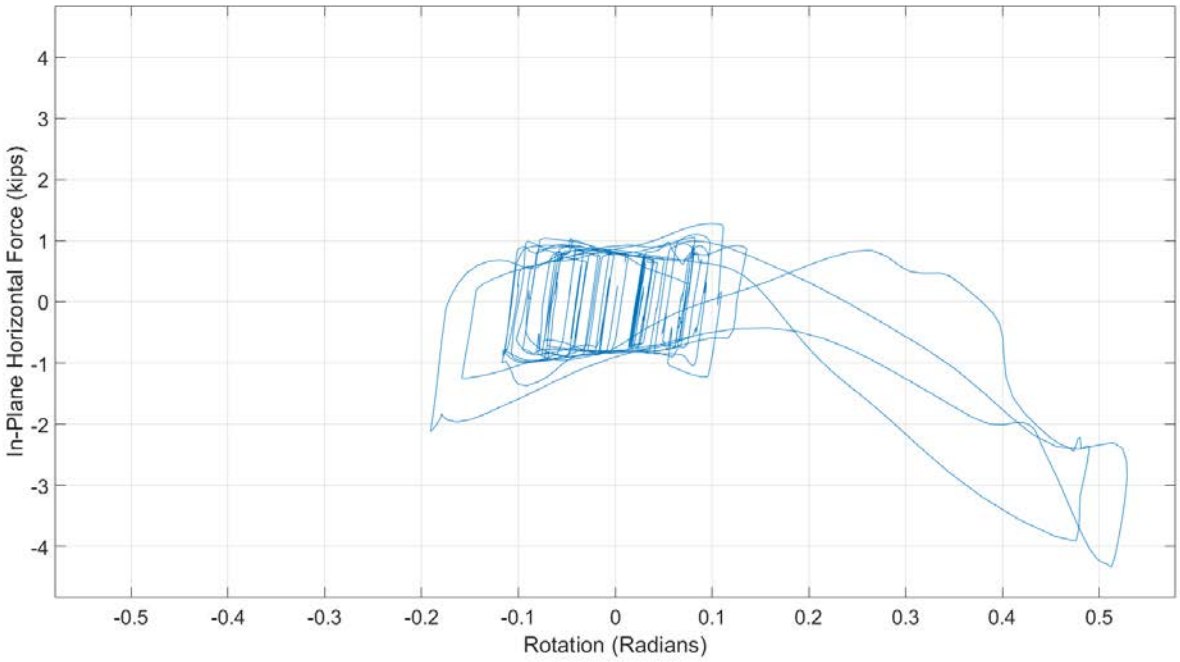

Figure 5-25. Hysteresis Loop of West Wall RFC 19 in Model 41P3_RFC1000_SL14.5_MCE_ORR

5.6.4 Implications on Design with Rotational Friction Connections

The results shown here clearly indicate that the peak out-of-plane and in-plane horizontal demands of the rotational friction connections occur simultaneously. This fact is significant when designing the elements surrounding the rotational friction connection, especially the anchorage system. Failure of the anchorage system in a brittle manner is unacceptable as it could lead to the wall panel falling away from the structure. In the design of metal building systems, a 2-D planar frame analysis is sufficient for designing the metal building moment frame, longitudinal force resisting system, and the wall connections. It is evident that if rotational friction connections are to be utilized in metal building systems, the orthogonal seismic demands must be applied simultaneously in order to accurately reflect the fundamental nature of these connections.

Based on the research results, it is recommended that a capacity design is necessary for the elements surrounding the RFC. The following steps are proposed in determining the force demands resulting from the RFC. By this point, the rotational friction connection parameters have

been determined, which includes the free-rotation force, free-rotation moment, and peak expected rotation.

1) Determine the design out-of-plane forces using ASCE 7 (ASCE/SEI 2016) for the wall elements
2) Solve for the design in-plane shear force at the expected peak rotation using the free-rotation force plus the P-Delta force.
3) Design the anchorage system using these amplified forces and moments.

5.7 Conclusions

Using the SAP2000 models developed in Chapter 4, numerical analyses were conducted to assess the seismic performance of metal building systems utilizing rotational friction connections between the hard wall and steel frame. This chapter began by presenting a proposed design of rotational friction connections for incorporation in metal building systems with precast tilt-up wall panels. A displacement target of 2% the story height was set for the design of the connections. Nonlinear static analyses were performed on a baseline metal building model and a model utilizing the rotational friction connections. The results showed that force-displacement behavior of the structure changed from bilinear curve to a trilinear curve with added base shear force capacity. Modal analyses showed that the added lateral stiffness in the longitudinal direction decreased the longitudinal mode of vibration by a range of 5% to 32%, while the transverse direction was unaffected.

Extensive nonlinear seismic response history analyses were performed to quantify the global seismic performance of the metal building system clad with the rotational friction connections. Energy analyses identified where the input seismic energy was distributed to the

metal building system. According to the energy results, there was a significant reduction in the inelastic demands of the side wall tension-only bracing elements due to the added energy dissipating capacity of the rotational friction connections. The reduction in inelastic deformation of the braces improved the response by up to two performance categories when compared to the baseline models.

Finally, the force-displacement demands of the connections were quantified. The peak rotations in the connections are uniform along the entire length of the wall. The out-of-plane and in-plane vertical force demands were highest in the connections adjacent to the metal building moment frame line. The results confirmed that the P-Delta effect in rotational friction connections is significant and cannot be ignored in the design of the surrounding elements, such as the anchorage system.

By taking advantage of the stiffness incompatibility between the flexible steel frame and rigid hard walls, the rotational friction connections have shown excellent potential to reduce inelastic damage during seismic events to structural elements in the longitudinal direction of metal building systems. The decrease in peak story drifts also reduces the damage to other nonstructural components.

Chapter 6 Conclusions

6.1. Introduction

There has been a concerted effort for over two decades, between the MBMA and researchers, to improve the seismic design and performance of metal building systems. The considerations for seismic improvement involve life safety concerns as well as the economic considerations of damaged buildings. Research and reconnaissance has exposed the vulnerability of metal building system's concrete/masonry hard wall to collapse. In order to improve life-safety and provide an enhanced level of seismic performance, the proposed solution was the development of a simple, reliable energy dissipating connection between the stiff walls and the flexible steel frame of the metal building system, to create a longitudinal lateral system capable of dissipating energy generated during a seismic event. The connection developed to address these concerns is the rotational friction connection.

The rotational friction connection's energy dissipating capacity is geared to response in the in-plane horizontal direction (parallel to the ridge) without losing out-of-plane strength for the transverse response. The research performed here included both the development, design, laboratory testing, and analytical investigation to determine the performance reliability of the rotational friction connection for use in metal buildings with hard walls.

6.2. Conclusions

The tasks involved in the development and testing (both experimental and analytical) of the rotational friction connection and the resulting conclusions drawn from those tasks are described in this section.

6.2.1 Evaluation of Current Energy Dissipating Connections

Current design techniques for connections used for precast concrete wall panels were investigated to determine their suitability to dissipate energy generated in seismic events while maintaining the integrity of the metal building system. The differential stiffness of the flexible metal building frame and the concrete/masonry hard walls creates a stiffness incompatibility and careful attention must be paid attention to the connections between these two elements. A connection is needed that takes advantage of this differential stiffness between the hard walls and the steel frame by forcing the ductile fuse element to be the connections themselves. There is a need for a continuous load path which is not provided if the connections are not ductile or have sufficient capacity for the full strength of the structure. Both the energy dissipation and the load path are critical.

The following section reviews current energy dissipating connections that were considered and ultimately rejected for use as a connection at the frame-to-wall interface in metal building systems.

Reasons for discarding yielding tapered connections:

1) Yielded tapered connections are used primarily in unidirectional displacement demand applications. The out-of-plane forces would most likely cause excessive strain in the

steel material of the tapered plates of the connection, which could lead to premature fracture.

2) The fabrication of the tapered steel for the yielding connection was judged to be challenging and costly.
3) Yielding tapered sections would have to be replaced following a seismic event.

Reasons for discarding tie-back rods:

1) Tie-back rods are susceptible to low-cycle fatigue and the treaded rods developed cracks during testing.
2) Simultaneous out-of-plane forces and in-plane horizontal displacement could potentially exceed the fracture strain in the plastic hinge and lead to ruptures of the rod.
3) Any rods that yield would require replacement following a seismic event.

Reasons for discarding slotted-bolted friction connections:

1) The slotted-bolted friction connection is designed to function in unidirectional displacement demands. The frame to wall connections in metal building systems must be able to slip predictably and reliably. The presence of a dynamic out-of-plane force changes the contact pressure acting on the sliding surfaces. This undermines the reliability of the slip force.
2) High contact pressure can cause galling in and around the slotted hole of the connection and reduce its effectiveness.
3) These connections are susceptible to lock up when the bolt encounters the end of the slotted hole.

It is evident that the bidirectional demands on the wall connections between the hard wall and steel frame of metal building systems imposed a significant challenge on energy dissipating connections that have been developed. A new energy dissipating connection was needed that could resolve the stiffness incompatibility problem while maintaining out-of-plane strength

6.2.2 Development of the Rotational Friction Connection

The rotational friction connection provided a new approach to connecting the hard walls to the steel frame of metal building systems by taking advantage of the stiffness incompatibility that exists between these two elements. The RFCs are designed to slip in the in-plane horizontal direction during an earthquake event. Seismic energy is dissipated through frictional heating. With the connections acting as the ductile fuse element, damage to the wall elements can be precluded. A primary characteristic of the RFC is that the energy dissipating mechanism is decoupled from the presence of out-of-plane forces. For a given displacement cycle, the same amount of frictional energy is dissipated no matter if there is an out-of-plane force present. This is a significant advantage over other energy dissipating connections that rely on the formation of plastic hinges to dissipate energy. However, P-Delta effects still act on the rotational friction connection and must be considered when designing the anchorage system.

In addition to satisfying the structural performance objectives, the connection needed to be economical and constructible. The rotational friction connection is an efficient option because it is composed of readily available steel components, which include two steel angle sections, bar stock, standard high strength bolts, and hardened washers. The simplicity and economy of the connection should help accelerate the adoption of the connection by the metal building industry.

6.2.3 Experimental Testing

Rotational friction connection prototypes were experimentally tested in the Structures Research Laboratory at Auburn University. Testing included monotonic, unidirectional cyclic, bidirectional, out-of-plane, and 100-cycle testing. There were several significant findings that resulted from the experimentation:

1) The connection proved itself to be highly ductile in the in-plane horizontal direction. The force required to cause slipping is predictable and reliable.
2) The hysteresis loops were rectangular and stable. Even though there was some loss in the bolt tension, hardening behavior was observed especially during the second run and 100-cycle tests. The roughening of the surfaces more than compensated for the drop in the bolt tension.
3) The coefficient of friction initially began at 0.13 and ended near 0.35. The surface preparation method polished the steel surfaces and significantly reduced the initial friction coefficient.
4) The bidirectional testing confirmed that the tensile out-of-plane load causes a substantial increase in the in-plane horizontal shear force in the rotational friction connection. Compressive out-of-plane forces have the opposite effect. The P-Delta effects are significant and cannot be ignored. The connection is still able to reliably dissipate energy in the presence of an out-of-plane force. The experimental test applied a constant tensile force, but during an earthquake, the out-of-plane force would be dynamic. The P-Delta forces would therefore be dynamic.

5) There was no damage detected in the surrounding components. The only visible damage to the connection itself was roughening of the contact surfaces. The rotational friction connection is highly resilient and would not require replacement following a seismic event, but could be easily replaced if it were needed.

6.2.4 Development of 3-D solid finite element models

The commercial finite element analysis software Abaqus was used to develop 3-D solid finite element models of the rotational friction connection to simulate the experimental testing.

1) Theoretical equations defining the free-rotation moment and force-displacement curves were derived using mechanics of materials and equilibrium principles.
2) The numerical model was verified using the theoretical equations and validated using the experimental results. The model was shown to provide good agreement with the experimental data regarding the free-rotation force.
3) The calibrated friction coefficient was determined to be 0.13. Friction coefficients higher than the tested forces would be achievable though blast cleaning the steel angles and struts.
4) The bolt pretension, coefficient of friction, and the moment arm length governs the force-displacement behavior of the connection. A parametric study expanded upon the experimental dataset to determine the force-displacement curves for rotational friction connection that utilized different bolt sizes and moment arm lengths.

6.2.5 Development of global metal building system models with hard walls

A 3-D analytical model was developed in SAP2000 for quantifying the seismic performance of metal building systems with hard walls. The components critical to the structural behavior were modeled and underwent a verification and validation process and were found to be in acceptable agreement on the component level.

1) The ratcheting effect of the tension-only braces was successfully captured using the Takeda hysteresis method.
2) Shell finite element models were developed to determine the lateral force capacity of the metal building moment frames.
3) An empirical LTB hinge was developed to capture the inelastic behavior of the metal building moment frame.
4) A simplified RFC model in SAP2000 was developed and calibrated using the Abaqus results. The model captures the initial stiffness, free-rotation force, and P-Delta effects. Hardening behavior can be included through the use of the buckling-restrained brace hysteresis method.

6.2.6 Analytical evaluation of RFC impact on global seismic performance of MBS

The analytical evaluation utilized the 3-D global metal building model that was developed to assess the improvement in structural response. Analytical testing included nonlinear static pushover, modal, and nonlinear dynamic response analyses. A baseline metal building that does not utilize the RFCs served as a comparison with a metal building system that was equipped with RFCs. The seismic performance was evaluated at four seismic levels ranging from a service-level event to a maximum-considered event. The results of the rigorous analyses are as follows:

1) The longitudinal force-displacement behavior of a hard wall metal building system utilizing rotational friction connections are trilinear. The high stiffness of the connections draws lateral force into the connections first causing them to slip early. The base shear increases until the tension-only sidewall braces yield.
2) Modal analyses showed that the added lateral stiffness in the longitudinal direction decreased the longitudinal mode period of vibration by up to 32%. The transverse mode of vibration was unaffected by the presence of the RFCs.
3) The MBS utilizing the RFCs had a significant decrease in the peak story drifts in the longitudinal direction over the baseline models.
4) The energy analyses showed that the rotational friction connections decrease the inelastic demands in the braces and moment frames. The energy dissipation of the connections is performing as intended. In some cases, the brace performance improves by two performance categories.
4) Though the rotation histories of the connections are identical during each seismic event, the out-of-plane forces are highest in the connections closest to the metal building moment frame. Out-of-plane force demands are lowest in the central connection of each panel. The flexibility in the major axis of bending of the spandrel beam is the cause of this variability in the out-of-plane demands.
5) The in-plane horizontal force demand of the connections is dependent on the out-of-plane forces. This further confirms the importance of the P-Delta effects that were first identified in the theoretical development and replicated in the experiment. The anchorage system must be designed considering the P-Delta effects of the rotational friction connection in the deformed configuration.

The goal of this research was to improve the resiliency and safety of hard wall metal buildings. Collapsing wall panels present a life safety hazard and result in economic losses. The rotational friction connection is a simple, reliable ductile connection that takes advantage of the stiffness incompatibility between the hard walls and steel frames of metal building systems. Energy dissipating capacity has been successfully added in the longitudinal direction of metal buildings. The improvement in seismic performance of these structures is apparent through reduced story drifts and inelastic demands in the surrounding elements.

6.3. Future Work

The rotational friction connection showed great potential in improving the global seismic performance of metal building systems clad with hard walls. The research presented here opens the door for further investigation on improving this connection. Some suggestions for future work in this regard are listed below:

1) The laboratory testing revealed that the mean initial friction coefficient of the rotational friction connection was 0.13. A future experimental study could investigate various surface preparation methods for achieving a higher friction coefficient at the steel-to-washer interface.
2) The experiment conducted in this research tested rotational friction connections with 5/8” diameter and 3/4” diameter A325 bolts. To further validate the 3-D solid finite element models, experimental tests need to be performed for rotational friction connection using bolts with larger diameters, such as 7/8 in., 1 in., and possibly higher.

3) Investigate the use of the new rotational friction connections for application to the end wall of hard wall metal building systems. Because the longitudinal direction of metal building systems showed significant improvement in seismic performance, the transverse direction may experience a similar improvement.
4) The out-of-plane demands were highest in the outermost connections of the wall panels. An optimization study could be undertaken by placing the higher free-rotation force connections toward the center of the panel, where the out-of-plane forces are low, while having a pin-pin connection at the edges of the panel.
5) This research focused on improving the seismic behavior of metal building systems clad with hard walls. The rotational friction connection could certainly be utilized in other structures where there exists a stiffness incompatibility. An analytical study could investigate the potential benefit of using the rotational friction connection in the connections of multistory structures using hard wall cladding.
6) Perform a proper validation of the cyclic behavior of the empirical LTB hinge. At the time this research was performed, SAP2000 did not have a degrading hysteresis other than the Takeda and Pivot hysteresis method. The new degrading hysteresis could potentially provide a better fit with the cyclic testing of tapered rafter sections performs.
7) 2-D shake table testing of a metal building system utilizing the rotational friction connection would validate the improvements the connection provides. Dynamic testing would provide a better understand of how the connection performs during earthquakes.

References

ACI. (2014). ACI 318-14, *Building Code Requirements for Structural Concrete,* American Concrete Institute, Farmington Hills, MI.

AISC. (2016a). ANSI/AISC 360-16, *Specification for Structural Steel Buildings*, American Institute of Steel Construction, Inc., Chicago, IL.

AISC. (2016b). ANSI/AISC 341-16, *Seismic Provisions for Structural Steel Buildings.* American Institute of Steel Construction, Chicago, IL.

Applied Technology Council (2007). *InterimTesting Protocols for Determining the Seismic Performance Characteristics of Structural and Nonstructural Components.* Redwood, City, CA: FEMA.

ASCE/SEI. (2010). *Minimum Design Loads for Buildings and Other Structures,* ASCE/SEI 7-10, American Society of Civil Engineers, New York, NY.

ASCE/SEI. (2013). *Seismic Evaluation and Retrofit Rehabilitation of Existing Buildings.* ASCE/SEI 41-13, American Society of Civil Engineers, New York, NY.

ASCE/SEI. (2016). *Minimum Design Loads for Buildings and Other Structures,* ASCE/SEI 7-16, American Society of Civil Engineers, New York, NY.

ASTM Standard A572 (2015). Standard Specification for High-Strength Low-Alloy Columbium-Vanadium Structural Steel. ASTM International, West Conshohocken, PA.

ASTM Standard F3125 (2015). Standard Specification for High Strength Structural Bolts, Steel and Alloy Steel, Heat Treated, 120 ksi (830 MPa) and 150 (1040 MPa) Minimum Tensile Strength, Inch and Metric Dimensions. ASTM International, West Conshohocken, PA.

ASTM Standard F436 (2016). Standard Specification for Hardened Steel Washers Inch and Metric Dimensions. ASTM International, West Conshohocken, PA.

Bajwa, M.S., Charney, F.A., and Moen, C.D. (2010). Assessment of Analytical Procedures for Designing Metal Buildings for Wind Drift Serviceability. *Report No. CE/VPI-ST 10/05*, The Charles E. Via, Jr. Department of Civil and Environmental Engineering, Virginia Polytechnic Institute and State University, Blacksburg, VA.

Baird, A.C., Palermo A., Pampanin, S. (2013). Controlling Seismic Response using Passive Energy Dissipating Cladding Connections. *2012 New Zealand Society for Earthquake Engineering Conference*, Christchurch, New Zealand.

Baird, A.C. (2014). Seismic Performance of Precast Concrete Cladding Systems. *Doctoral Dissertation*, Department of Civil and Natural Resources Engineering, University of Canterbury, Christchurch, New Zealand.

Baldridge, S.M. and Marshall, J.D. (2011). Performance of Structures in the January 2010 MW 7.0 Haiti Earthquake. ASCE/SEI 2011 Structures Congress. Las Vegas, NV, April 14-16, 2011.

Balendra, T., Yu, C., & Lee, F. L. (2001). An Economical Structural System for Wind and Earthquake Loads. *Engineering Structures, 23*(5). 491-501.

Charney, F.A. and Marshall, J. (2006). A Comparison of the Krawinkler and Scissors Models for Including Beam-Column Joint Deformations in the Analysis of Moment-Resisting Steel Frames. *Engineering Journal*, AISC, 1st Quarter, 31-48.

Chopra, A.K. (2009). *Dynamics of Structures.* 4th Edition, Pearson Prentice Hall, Upper Saddle River, NJ.

Clifton, G.C. (2005). Semi-rigid joints for Moment-Resisting Steel Framed Seismic-Resisting Systems. *Doctoral Dissertation*, Department of Civil and Environmental Engineering, University of Auckland, Auckland, New Zealand.

CSI. (2017). SAP2000. Version 19.2.2, Computers and Structures, Inc., Berkeley, CA.

CSI. (2011). Perform-3D. Version 5, Computers and Structures, Inc., Berkeley, CA.

Dowell, R.K., Seible, F.S., and Wilson, E.L. (1998). Pivot Hysteretic Model for Reinforced Concrete Members. *ACI Structural Journal*, Vol. 95, pp. 607–617.

Eberhard, M.O., Baldridge, Steven, Marshall, Justin, Mooney, Walter, and Rix, G.J., 2010, The *MW* 7.0 Haiti earthquake of January 12, 2010; USGS/EERI Advance Reconnaissance Team report: U.S. Geological Survey Open-File Report 2010–1048, 58 p. [*http://pubs.usgs.gov/of/2010/1048/*].

FEMA (2009). *Quantification of Building Seismic Performance Factors*. Prepared by the Applied Technology Council for the Federal Emergency Management Agency (Report No. FEMA-P695). Washington, D.C.

FEMA. (2012). *Seismic Performance Assessment of Buildings*. Prepared by the Applied Technology Council for the Federal Emergency Management Agency (Report No. FEMA-P-58). Washington, D.C.

Filiatrault, A., Sullivan, T. (2014). Performance-based Seismic Design of Nonstructural Building Components: The Next Frontier of Earthquake Engineering. *Earthquake Engineering and Engineering Vibration*. 13. 17-46.

Gates, C. (2012). Our disappearing city centre. *The Press*. Retrieved from http://www.stuff.co.nz/the-press/news/christchurch-earthquake 2011/7744317/Ourdisappearing-city-centre

Golondrino, J.C., MacRae, G.A., Chase, J.G., Rodgers, G.W., Clifton, C.G. (2012). Behaviour of Asymmetrical Friction Connections using different shim materials. *2012 New Zealand Society for Earthquake Engineering Conference*, Christchurch, New Zealand.

Golondrino J.C., Xie, R., MacRae, G., Chase, G., Rodgers, G., Clifton, C. (2014). Low damage braces using Asymmetrical Friction Connections (AFC). *2014 New Zealand Society for Earthquake Engineering Conference*, Christchurch, New Zealand.

Goodno, B. J. (1998). *Ductile cladding connection systems for seismic design*. National Institute of Standards and Technology, Building and Fire Research Laboratory, Gaithersburg, MD.

Hilber, H.M., Hughes, T.J.R., and Taylor, R.L. (1977). Improved Numerical Dissipation for Time Integration Algorithms in Structural Dynamics. *Earthquake Engineering and Structural Dynamics*, 5:282-292.

Hong, Y.D. (2007). Development of A Seismic Design Procedure for Metal Building Systems. *Doctoral Dissertation*, Department of Structural Engineering, University of California, San Diego, La Jolla, CA.

Hutchinson, T., Pantoli, E., McMullin, K., Hildebrand, M., and Underwood, G. (2014). Seismic Drift Compatibility of Architectural Precast Concrete Panels and Connections: A Design Guide for Engineers. *Report No. SSRP-14/16*, Department of Structural Engineering, University of California, San Diego, La Jolla, CA

Judd, J. P., & Charney, F. A. (2014). Performance-based design in the Central and Eastern United States. *Structures Congress*. 2355-2368.

Kaehler, R.C., White., D.W., and Kim, Y.D. (2011). Frame Design Using Web-Tapered Members. Steel Design Guide 25, AISC/MBMA, Chicago, IL.

Kim, Y.D. (2010). Behavior and Design of Metal Building Frames with General Prismatic and Web-Tapered Steel I-Section Members. *Doctoral Dissertation*, School of Civil and Environmental Engineering, Georgia Institute of Technology, Atlanta, GA.

MacRae, G.A., Clifton, C.G., MacKinven, H., Mago, N., Butterworth, J., Pampanin, S. (2010). The Sliding Hinge Joint Moment Connection. *Bulletin of the New Zealand Society for Earthquake Engineering*. 43(3).

Marshall, J.D. and Gould, N.C. (2012). The Performance of Low-Rise Industrial Facilities in the 2010 Haiti and 2011 Christchurch, New Zealand Earthquakes. *15th World Conference on Earthquake Engineering*, Lisbon, Portugal, September 24-28, 2012.

MBMA. (2016). Metal Building Manufacturers Association Annual Report 2016. http://www.mbma.com.

MBIE. (2004). New Zealand Building Code *B1-Structure*. Wellington, New Zealand: Ministry of Business, Innovation and Employment.

Mazzoni, S., McKenna, F., Scott, M.H., Fenves, G.L., et al. (2007). *Open System for Earthquake Engineering Simulation (OpenSEES) Command Language Manual*. Pacific Earthquake Engineering Research Center, University of California, Berkeley.

McCabe, S., Satter, S. (2018). Earthquake Risk Reduction in Buildings and Infrastructure Program, *National Institute of Standards and Technology*. https://www.nist.gov/programs-projects/earthquake-risk-reduction-buildings-and-infrastructure-program.

Montgomery, J. (2008). Boundary Condition Influences on Shank Stress in 3D Solid Bolt Simulation. *2008 International Abaqus Users' Conference*, Newport, RI.

Mualla, I.H. 2000. Experimental Evaluation of a New Friction Damper Device. *12th World Conference on Earthquake Engineering*, Auckland, New Zealand.

Mualla, I.H., Nielsen, L.O., Belev, B., Liao, W.I., Loh, C.H., Agrawal, A. (2002). Numerical Predictions of Shaking Table Tests on a Full Scale Friction-Damped Structure. *12th European Conference on Earthquake Engineering*, London, United Kingdom.

Naeim, Farzad. (2004). Impact of the 1994 Northridge earthquake on the art and practice of structural engineering. *The Structural Design of Tall and Special Buildings*. 13 (5). 373-389.

NCI Engineering. (2013). *Design Practice Manual*. NCI Engineering Building Systems.

NCMA. (2011). *Concrete Masonry Walls for Metal Buildings Systems*. National Concrete Masonry Association, Herndon, VA.

Newman, A. (2004). Metal Building Systems: Design and Specifications. 2nd Edition, McGraw-Hill, New York, NY.

Nucor. (2009). *Products and Engineering Manual*. 4.10.3, http://www.nucorbuildingsystems.com/nbsproductandengineeringmanual/.

Pantoli, E., Hutchinson T. (2015). Experimental and Analytical Study of the Dynamic Characteristics of Architectural Precast Concrete Cladding. *Proc., ACT-SEI, 2nd Conference on Improving the Seismic Performance of Existing Buildings and Other Structures*, December 10-12, San Francisco, CA.

Pantoli, E., Hutchinson, T.C., McMullin, K.M., Underwood, G.A., Hildebrand, M.J. (2016). Seismic drift-compatible design of architectural precast concrete cladding: tieback connections and corner joints. *PCI journal*, July-August, pp. 38-52.

PCI (2004). *PCI Design Handbook-Precast and Prestressed Concrete*. Precast/Prestressed Concrete Institute, Chicago, IL.

PEER. (2015). *PEER NGA Database.* Pacific Earthquake Engineering Research Center, University of California, Berkeley, California, http://peer.berkeley.edu/nga/.

PGI. (2016). A572 Steel Plate. *Precision Grinding Inc.* Birmingham, AL. http://precisiongrinding.com/a572-steel-plate/

Pinelli, J. P., Craig, J.I., & Goodno, B.J. (1995). Energy-Based Seismic Design of Ductile Cladding Systems. *Journal of Structural Engineering, 121*(3). 567-578.

Pinelli, J. P., Moor, C., Craig, J. I., & Goodno, B. J. (1996). Testing of Energy Dissipating Cladding Connections. *Earthquake Engineering & Structural Dynamics, 25*(2). 129-147.

Ramhormozian, S., Clifton, G. & MacRae, G. (2014). The Asymmetric Friction Connection with Belleville springs in the Sliding Hinge Joint. *New Zealand Society for Earthquake Engineering (NZSEE) Annual Technical Conference, Towards Integrated Seismic Design*, Auckland, New Zealand.

Ramhormozian, S., Clifton, C.G., Macrae, G.A. and Khoo, H.H. (2015). Improving the seismic behaviour of the Sliding Hinge Joint using Belleville Springs. *8th Conference on Behaviour of Steel Structures in Seismic Areas (STESSA)*. Shanghai, China.

Rihal, S.S. (1989). Earthquake Resistance and Behavior of APCC and Connections. Paper presented at the Architectural Precast Concrete Cladding - Its Contribution to Lateral Resistance of Buildings, Chicago, IL., USA.

Rogers, C.A. and Tremblay, R. (2008). Impact of diaphragm behavior on the seismic design of low-rise steel buildings. *North American Steel Construction Conference*, Nashville, USA, Paper No. 0133.

Sellers, V.A. (2016). Experimental Testing of a Rotational Friction Connection for Use with Precast Concrete Cladding Panels in Metal Building Systems. *Master's Thesis*, Department of Civil Engineering, Auburn University, Auburn, AL.

Simulia. (2016). Abaqus. Standard Version 2016. Dassault Systemes Simulia Corp. Providence, RI.

Shoemaker, W.L. (2006). Seismic Design and Performance of Metal Buildings, http://www.mbma.com/display.cfm?p=37&pp=3&i=87.

Shoemaker, W.L. (2015). Seismic Research: Metal Buildings are on Solid Ground, *Metal Construction News*. October 2015, pp 14-20.

Smith, M.D. and Uang, C.M. (2013a). Earthquake Simulator Testing of a Metal Building with Metal Panel Sidewalls. *Report No. SSRP-12/03*, Department of Structural Engineering, University of California, San Diego, La Jolla, CA

Smith, M.D. and Uang, C.M. (2013b). Earthquake Simulator Testing of a Metal Building with Concrete Sidewalls. *Report No. SSRP-12/04*, Department of Structural Engineering, University of California, San Diego, La Jolla, CA

Smith, M.D., Turner, K.T., and Uang, C.M. (2013c). Experimental Investigation of Cyclic Lateral Buckling of Web-Tapered I-Beams. *Report No. SSRP-12/06*, Department of Structural Engineering, University of California, San Diego, La Jolla, CA

Smith, M.D. (2013d). Seismic Testing and Analytical Studies for the Development of New Seismic Force Resisting Systems for Metal Buildings. *Doctoral Dissertation*, Department of Structural Engineering, University of California, San Diego, La Jolla, CA.

SSPC. (2016). SP3-Power Tool Cleaning. Society of Protective Coatings. Pittsburg, PA.

Stuart, D.M. (2013) Metal Building Systems, PDHonline Course S120. Fairfax, VA. https://www.pdhonline.com/courses/s120a/s120a.htm

Appendix A RFC Capacity Design Example

The following section steps though all the applicable limit states encountered when designing the rotational friction connection. This example will show that the capacity exceeds the demand for the MCE level in Riverside, California. Other considerations, such as constructability and practicality, help provide the connection is inherently high capacity.

The steel angles have a minimum practical thickness of 3/8" due to weldability. The smallest possible steel angle that could be used is the L4x3x3/8. A standard 1" diameter hole at the gage length of 2.5" satisfies the minimum edge distance requirements. The leg length of 4" provides sufficient offset from the wall, so that the edge of the rotating steel strut never impacts the embed plate.

The steel strut is 10.5"x3"x1/2". A minimum width of 3" and thickness of 0.5" is recommended because it provides enough rigidity for the strut to act a moment lever arm. The 3" wide dimension also satisfies the minimum edge distance requirements for standard 1" diameter holes.

The section concerning concrete breakout has been well described by Hutchinson et. al. (2014) and is used below to calculate the anchorage capacity of the rotational friction connection. The equations have been updated to reflect the ACI 318-17 (

1) Concrete Breakout

Design against concrete breakout is performed following the prescriptions found in ACI Chapter 17 and using the following quantities:

The effective embedment depth of the anchors h_{ef} = plate thickness + stud length – head thickness = (0.5" + 4.5" – 0.313" = 4.687");

The breakout surface is defined as a square whose sides are equal to the inter-anchor space s_1 plus two times $1.5h_{ef}$ (ACI Fig. R17.4.2.1);

The modification factors for eccentric load Ψ_{ec}, edge effects Ψ_{ed}, cracking Ψ_c and for post-installed anchors Ψ_{cp} are all equal to 1. Their definition can be found in (ACI sections 17.4.2.4-17.4.2.7)

The anchor is cast-in, thus the parameter kc is equal to 24 (ACI Equation 17.4.2.2a);

The concrete is normalweight, and the corresponding λ_a factor is 1.0. (ACI Section 17.2.6).

The check against concrete breakout can be performed following the procedure in ACI, Section 17.4.2. The parameter ANCO, which is the projected concrete failure area of a single anchor with an edge distance equal to or greater than 1.5hef, is defined as:

$$A_{NCO} = 9h_{ef}^2 = 9 \cdot (4.69)^2 = 198\ in^2 \qquad \text{(ACI Equation 17.4.2.1c)}$$

The parameter ANC is the projected concrete failure area of a single anchor group (ACI Section 17.4.2.1), and in this case is:

$$A_{NC} = \left(s_1 + 1.5h_{ef} + 1.5h_{ef}\right)^2 = (6 + 1.5 \cdot 4.96 + 1.5 \cdot 4.96)^2 = (20.88)^2 = 436\ in^2$$

The basic concrete breakout strength of a single anchor in tension in cracked concrete N_b is defined as:

$$N_b = k_c \lambda_a \sqrt{f_c'} h_{ef}^{1.5} = 24\sqrt{5000}\ 4.96^{1.5} = 17.2\ kips \qquad \text{(ACI Equation 17.4.2.2a)}$$

Finally, the basic concrete breakout strength of the group will be:

$N_{cbg} = \frac{A_{NC}}{A_{NCO}} \Psi_{ec} \Psi_{ed} \Psi_c \Psi_{cp} N_b = \frac{436}{198} \cdot 1 \cdot 1 \cdot 1 \cdot 1 \cdot 1 \cdot 17.2 = 37.9$ kips (ACI Equation 17.4.2.1b)

The capacity to demand relation needs to be satisfied in all cases such that:

$\varphi N_n \geq N_{ua}$ (ACI Section 17.3.1.1)

However, in Seismic Design Categories C, D, E, or F (ASCE 7), there is an additional reduction in capacity applied to concrete failures modes such that:

$0.75\varphi N_n \geq N_{ua}$ (ACI Section 17.2.3.4.4)

Applying the additional reduction factor of 0.75 yields:

$0.75\varphi N_{cbg} = 0.75 \cdot 0.75 \cdot 37.9 = 21.3\ kips$

Steel Anchors

The capacity of anchors in tension can be found through ACI Chapter 17 considering that the number of anchors per embed *n* is 4, the effective cross-sectional area on the single anchor in tension $A_{se,N}$ is 0.2 in^2 and that the ultimate strength for the anchor in tension f_{uta} is 60ksi:

$N_{sa} = n\, A_{se,N} f_{uta} = 4 \cdot 0.2 \cdot 65 = 52.0\ kips$ (ACI Equation 17.4.1.2)

Then:

$\varphi N_{sa} = 0.75 \cdot 52.0 = 39.0\ kips$ (ACI Equation 17.2.3.4.4)

2) Headed Stud Weld

The headed stud welds qualify as a fastener component and must be designed for shear through the effective throat of the fillet weld. The length of the weld is calculated based on the fracture surface of the weld, located on the mid-thickness of the weld (Figure A-1).

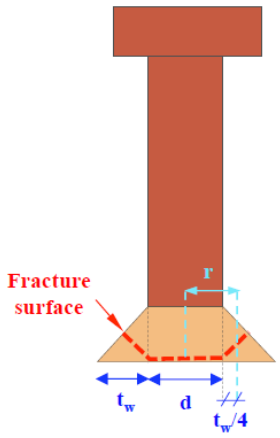

Figure A-1. Fracture surface of the stud welds (Hutchinson et al. 2014)

In this case, L = 2πr, where r is equal to the radius of the stud plus a quarter of the thickness of the weld (Figure A-1).

$$L = 2\pi\left(0.25 + \frac{0.313}{4}\right) = 2.06"$$

The weld capacity is determined as follows:

$\varphi R_n > R_u$ (AISC 360, B3-1)

$\varphi R_n/l = 6.96$ k/in (for 5/16" fillet weld) (AISC 360 Section J2)

$\varphi R_n = (6.96)(2.06) = 14.3\ kips$

3) Plate Flexure

The embed plate in the column should be checked in flexure, with load points at the 5/16" fillet welds, and support points at the headed studs. In this example, the studs and welds are nearly concentric, so the bending moment is negligible.

4) Angle Weld

The strength of weld metal R_n is defined in AISC, Section J2.4 from the nominal strength of the weld F_w and the weld area A_w as:

$$R_n = F_w A_w \qquad \text{(AISC 360-16 Equation J2-3)}$$

AISC Table J2.5 defines that F_w is $0.6F_{EXX}$, where F_{EXX} is the electrode classification number. In addition, the same table defines ϕ equal to 0.75. In this case:

$$\varphi R_n = \varphi F_{EXX} A_w = 0.75 \cdot 0.6 \cdot 70 \cdot \left(\frac{0.313}{\sqrt{2}} \cdot 3\right) \cdot 2 = 41.8\ kips$$

5) Shearing of the Angle Section

Shear Yielding

$$R_n = 0.60 F_y A_{gv} \qquad \text{(AISC 360-16 J4-3)}$$

$$R_n = 0.60 \cdot 50 \cdot (3 - 1 - 0.75) \cdot 0.375 = 14.1\ kips/in$$

$$\varphi R_n = 1.0 \cdot 14.1 = 14.1\ kips/in$$

Shear Rupture

$$R_n = 0.60 F_u A_{nv} \qquad \text{(AISC 360-16 J4-4)}$$

$$R_n = 0.60 \cdot 65 \cdot (3 - 1 - 0.75) \cdot 0.375 = 18.3\ kips/in$$

$$\varphi R_n = 0.75 \cdot 18.3 = 13.7\ kips/in$$

6) Angle Bolt Bearing into the Angle Section

Section J3 of the AISC code specifies the bearing capacity around a bolt hole. The RFC does not consider the deformation of the bolt hole at service loads as a design consideration. The edge distance is defined as l_c, the thickness of the angle leg is t, the specified minimum tensile strength is F_u, and the nominal bolt diameter is d. Lastly, the capacity is doubled because there are two angle sections in this connection that resist the load.

$R_n = 1.5 l_c t F_u \leq 3.0\ d\ t\ F_u$ (AISC 360-16 J3-6b)

$$R_n = 1.5 \cdot \left(1.5 - \left(\frac{1.0625}{2}\right)\right) \cdot 0.375 \cdot 65 \leq 3.0 \cdot 1.0625 \cdot 0.375 \cdot 65$$

$R_n = 35.4\ kips\ \leq 77.7\ kips$

$\varphi R_n = 0.75 \cdot 35.4 = 26.6\ kips\ for\ one\ angle\ section$

$\varphi R_n = 53.2\ kips\ for\ two\ angle\ section$

7) Angle Bolt Shear

The angle bolt is subjected to double shear when the connection is subjected to an out-of-plane force. This limit state is unlikely to ever control because the spandrel bolt has one shear plane. The nominal area of the bolt, A_b, in this example excludes the threads. The nominal shear stress is found in Table J3.2.

$R_n = F_{nv} A_b$ (AISC 360-16 J3-1)

$R_n = 68 \cdot (2 \cdot 0.785) = \ 106.8\ kips$

$\varphi R_n = 0.75 \cdot 106.8 = 80.1\ kips$

8) Angle Bolt Bearing into the Strut

This case follows the same procedure for the angle bolt bearing into the angle section. The applicable dimensions and material strength utilizes the properties of the steel strut.

$R_n = 1.5 l_c t F_u \leq 3.0\ d\ t\ F_u$ (AISC 360-16 J3-6b)

$$R_n = 1.5 \cdot \left(1.5 - \left(\frac{1.0625}{2}\right)\right) \cdot 0.5 \cdot 65 \leq 3.0 \cdot 1.0 \cdot 0.5 \cdot 65$$

$R_n = 47.2\ kips\ \leq 97.5\ kips$

$\varphi R_n = 0.75 \cdot 47.2 = 35.4\ kips$

9) Tensile Failure of the Strut

The steel strut that connects the angles to the spandrel beam must be checked for tension. There are two cases in AISC code: yielding of the gross section and rupture of the net section.

Yielding of the Gross Section

$R_n = F_y A_g$ (AISC 360-16 J4-1)

$R_n = 50 \cdot (3 \cdot 0.5) = 75\ kips$

$\varphi R_n = 0.9 \cdot 75 = 67.5\ kips$

Rupture of the Net Section

$R_n = F_u A_e$ (AISC 360-16 J4-2)

$R_n = 65 \cdot (3 - 1.0625) \cdot 1.0 \cdot 0.5 = 63.0\ kips$

$\varphi R_n = 0.75 \cdot 63 = 47.2\ kips$

10) Spandrel Bolt Bearing into the Strut

$R_n = 1.5 l_c t F_u \leq 3.0\ d\ t\ F_u$ (AISC 360-16 J3-6b)

$R_n = 1.5 \cdot \left(1.5 - \left(\frac{0.8125}{2}\right)\right) \cdot 0.5 \cdot 65 \leq 3.0 \cdot 0.75 \cdot 0.5 \cdot 65$

$R_n = 53.3\ kips\ \leq 73.1\ kips$

$\varphi R_n = 0.75 \cdot 53.3 = 40.0\ kips$

11) Spandrel Bolt Shear

The spandrel bolt is subjected to single shear when the connection is subjected to an out-of-plane force. The nominal area of the bolt, A_b, in this example excludes the threads. The nominal shear stress, F_{nv}, is found in Table J3.2.

$R_n = F_{nv} A_b$ (AISC 360-16 J3-1)

$R_n = 68 \cdot 0.442 = 30.1\ kips$

$\varphi R_n = 0.75 \cdot 30.1 = 22.5\ kips$

12) Spandrel Bolt Bearing into the Channel

The bearing capacity around the bolt hole in the channel is calculated using AISC Section J3. The bolt hole is in the interior of the channel's web, therefore bearing calculations based on edge distance calculations are not applicable. The nominal bolt diameter is *d*, the thickness of the channel web is *t*, and the specified minimum tensile strength of the channel is F_u.

$R_n = 3.0\ d\ t\ F_u$ (AISC 360-16 J3-6b)

$R_n = 3.0 \cdot 0.75 \cdot 0.5 \cdot 65 = 73.1\ kips$

$\varphi R_n = 0.75 \cdot 73.1 = 54.8\ kips$

Table A-1. Summary of RFC Out-of-Plane Capacities

Component	Limit State	Capacity (kips)
Embed Plate	Concrete Breakout	21.3 kips
	Steel Anchor	52.0 kips
	Headed Stud Weld	57.2 kips
	Plate Flexure	N.A.
Steel Angle	Angle Weld	41.8 kips
	Shear Yielding	84.6 kips
	Shear Rupture	82.2 kips
	Angle Bolt Bearing	53.2 kips
Angle Bolt	Bolt Shear	80.1 kips
Steel Strut	Angle Bolt Bearing	35.4 kips
	Tensile Yielding	67.5 kips
	Tensile Rupture	47.2 kips
	Spandrel Bolt Bearing	40.0 kips
Spandrel Bolt	Bolt Shear	22.5 kips
Spandrel Beam	Spandrel Bolt Bearing	54.8 kips

Appendix B. Longitudinal and Diaphragm Brace Design and Modeling

The metal building frame designs used in this research were designed for the Approximate Fundamental Period of Metal Building Frames Project (Smith 2013). The designs included only the transverse moment frame, therefore it was necessary to design the longitudinal seismic force resisting system of these structures. This section presents the wall braces and diaphragm braces of the five metal building systems. Seismic loads were determined using the Equivalent Lateral Force Method from ASCE 7 (2016). The braces were design as tension-only ordinary concentrically braced frames in accordance with AISC 360 Steel Specification (2016a) and AISC 341 Seismic Provisions for Structural Steel Buildings (2016b).

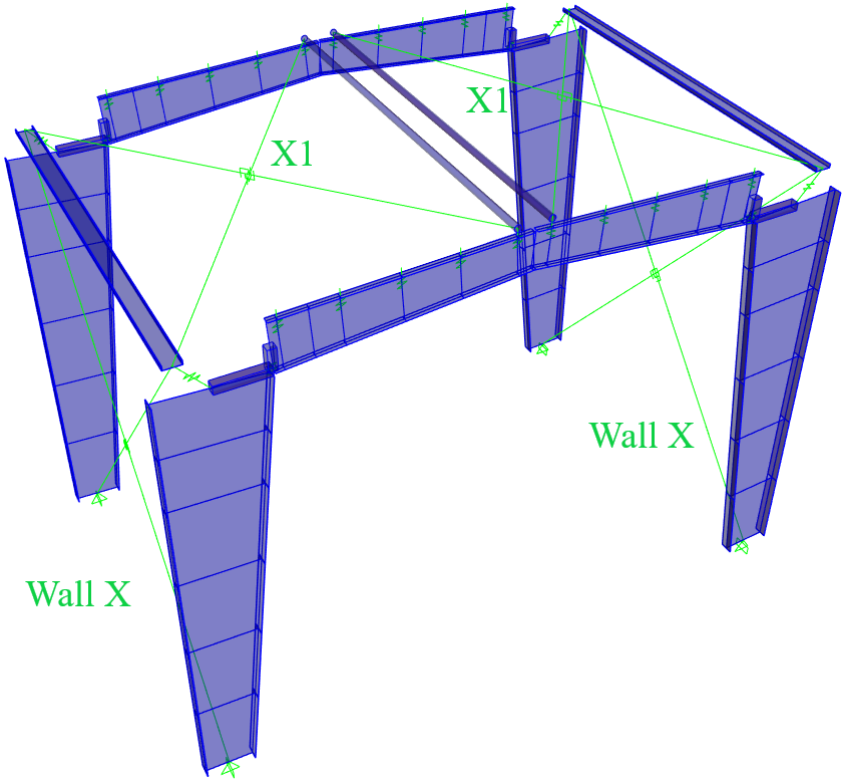

Figure B-1. Brace Identification for Model 16

Table B-1. Brace Properties and Design for Model 16

Model 16	Brace Properties			Strength Design Check		
	Element Name	Area (in^2)	Yield Stress (ksi)	Design Tensile Strength (kips)	Demand (kips)	Load Case
Wall X	Brace 1.0	0.790	50.0	35.6	29.6	1.2D+ρE+L+0.2S
X1	Brace 0.875	0.600	50.0	27.0	22.6	1.2D+ΩE+L+0.2S

Table B-2. Link Element Properties for Model 16

Model 16	Link Element Properties					
	Element Name	E (ksi)	Area (in^2)	Length (in)	Stiffness (k/in)	Expected Yield Stress (ksi)
Wall X	Brace 1.0	29000	0.79	454.9	50.4	55
X1	Brace 0.875	29000	0.6	368.1	47.3	55

Table B-3. Brace Backbone Curve Points and Acceptance Criteria for Model 16

Model 16	Backbone Curve Points				Acceptance Criteria, Plastic Deformation (inches)		
	Expected Yield Displacement (in)	Expected Yield Force (kips)	Strain Hardened Displacement (in)	Strain Hardened Force (kips)	IO	LS	CP
Wall X	0.863	43.5	7.77	53.9	0.22	3.02	3.88
X1	0.698	33.0	6.28	40.9	0.17	2.44	3.14

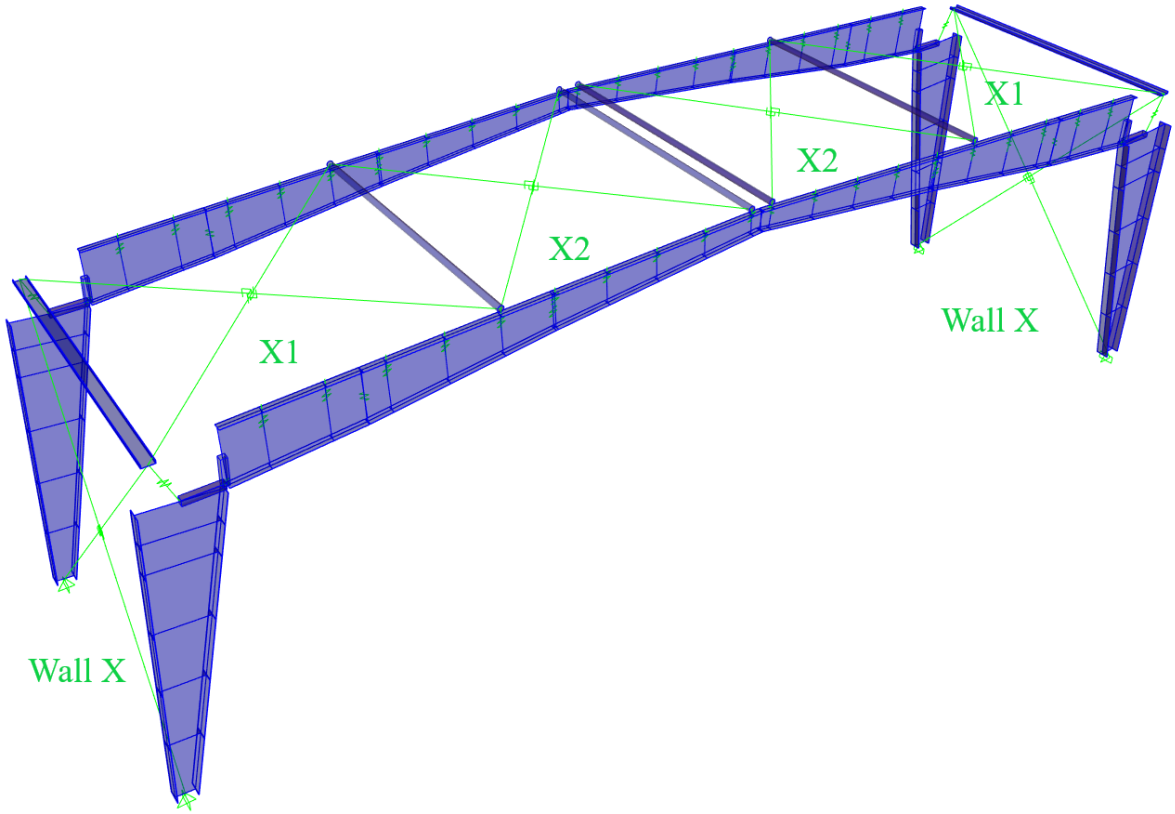

Figure B-2. Brace Identification for Model 41

Table B-4. Brace Properties and Design for Model 41

Model 41	Brace Properties			Strength Design Check		
	Element Name	Area (in^2)	Yield Stress (ksi)	Design Tensile Strength (kips)	Demand (kips)	Load Case
West X	Brace 1.125	1.000	50.0	45.0	43.2	1.2D+ρE+L+0.2S
X1	Brace 1.25	1.227	50.0	55.2	54.0	1.2D+ΩE+L+0.2S
X2	Brace 0.625	0.310	50.0	14.0	10.5	1.2D+ΩE+L+0.2S

Table B-5. Link Element Properties for Model 41

Model 41	Link Element Properties					
	Element Name	E (ksi)	Area (in^2)	Length (in)	Stiffness (k/in)	Expected Yield Stress (ksi)
Wall X	Brace 1.125	29000	1.00	455.0	63.7	55
X1	Brace 1.25	29000	1.23	428.4	83.1	55
X2	Brace 0.625	29000	0.31	402.0	22.4	55

Table B-6. Brace Backbone Curve Points and Acceptance Criteria for Model 41

Model 41	Backbone Curve Points				Acceptance Criteria, Plastic Deformation (inches)		
	Expected Yield Displacement (in)	Expected Yield Force (kips)	Strain Hardened Displacement (in)	Strain Hardened Force (kips)	IO	LS	CP
Wall X	0.863	55.0	7.77	68.2	0.22	3.02	3.88
X1	0.813	67.5	7.31	83.7	0.20	2.84	3.66
X2	0.762	17.1	6.86	21.1	0.19	2.67	3.43

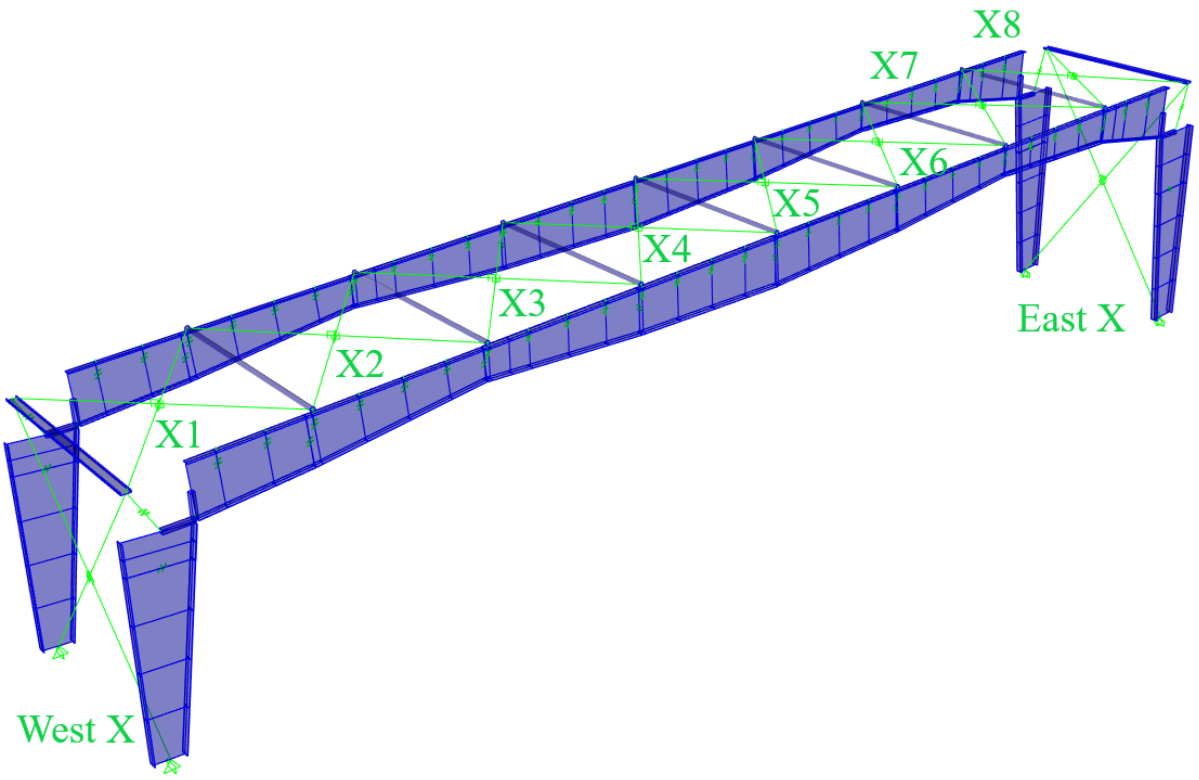

Figure B-3. Brace Identification for Model 42

Table B-7. Brace Properties and Design for Model 42

Model 42	Brace Properties			Strength Design Check		
	Element Name	Area (in^2)	Yield Stress (ksi)	Design Tensile Strength (kips)	Demand (kips)	Load Case
West X	L4x4x3/8	2.860	36.0	92.7	85.9	1.2D+ρE+L+0.2S
X1	L4x4x7/16	3.300	36.0	106.9	98.3	1.2D+ΩE+L+0.2S
X2	L4x4x5/16	2.400	36.0	77.8	66.8	1.2D+ΩE+L+0.2S
X3	Brace1.125	1.000	50.0	45.0	39.5	1.2D+ΩE+L+0.2S
X4	Brace0.75	0.440	50.0	19.8	12.5	0.9D+ΩE
X5	Brace0.75	0.440	50.0	19.8	10.3	1.2D+ΩE+L+0.2S
X6	Brace1.125	1.000	50.0	45.0	38.3	1.2D+ΩE+L+0.2S
X7	L4x4x5/16a	2.400	36.0	77.8	68.0	1.2D+ΩE+L+0.2S
X8	L4x4x7/16	3.300	36.0	106.9	101.8	1.2D+ΩE+L+0.2S
East X	L4x4x7/16a	3.300	36.0	106.9	97.8	1.2D+ρE+L+0.2S

Table B-8. Link Element Properties for Model 42

Model 42	Link Element Properties					
	Element Name	E (ksi)	Area (in^2)	Length (in)	Stiffness (k/in)	Expected Yield Stress (ksi)
West X	L4x4x3/8	29000	2.86	455.0	182.3	54
X1	L4x4x7/16	29000	3.30	378.5	252.9	54
X2	L4x4x5/16	29000	2.40	383.0	181.7	54
X3	Brace1.125	29000	1.00	383.4	75.6	55
X4	Brace0.75	29000	0.44	383.4	33.3	55
X5	Brace0.75	29000	0.44	383.4	33.3	55
X6	Brace1.125	29000	1.00	383.4	75.6	55
X7	L4x4x5/16a	29000	2.40	386.3	180.2	54
X8	L4x4x7/16	29000	3.30	376.7	254.0	54
East X	L4x4x7/16a	29000	3.30	517.8	184.8	54

Table B-9. Brace Backbone Curve Points and Acceptance Criteria for Model 42

Model 42	Backbone Curve Points				Acceptance Criteria, Plastic Deformation (inches)		
	Expected Yield Displacement (in)	Expected Yield Force (kips)	Strain Hardened Displacement (in)	Strain Hardened Force (kips)	IO	LS	CP
West X	0.847	154.4	9.32	200.8	0.21	3.39	4.24
X1	0.705	178.2	7.75	231.7	0.18	2.82	3.52
X2	0.713	129.6	7.85	168.5	0.18	2.85	3.57
X3	0.727	55.0	6.54	68.2	0.18	2.54	3.27
X4	0.727	24.2	6.54	30.0	0.18	2.54	3.27
X5	0.727	24.2	6.54	30.0	0.18	2.54	3.27
X6	0.727	55.0	6.54	68.2	0.18	2.54	3.27
X7	0.719	129.6	7.91	168.5	0.18	2.88	3.60
X8	0.701	178.2	7.72	231.7	0.18	2.81	3.51
East X	0.964	178.2	10.61	231.7	0.24	3.86	4.82

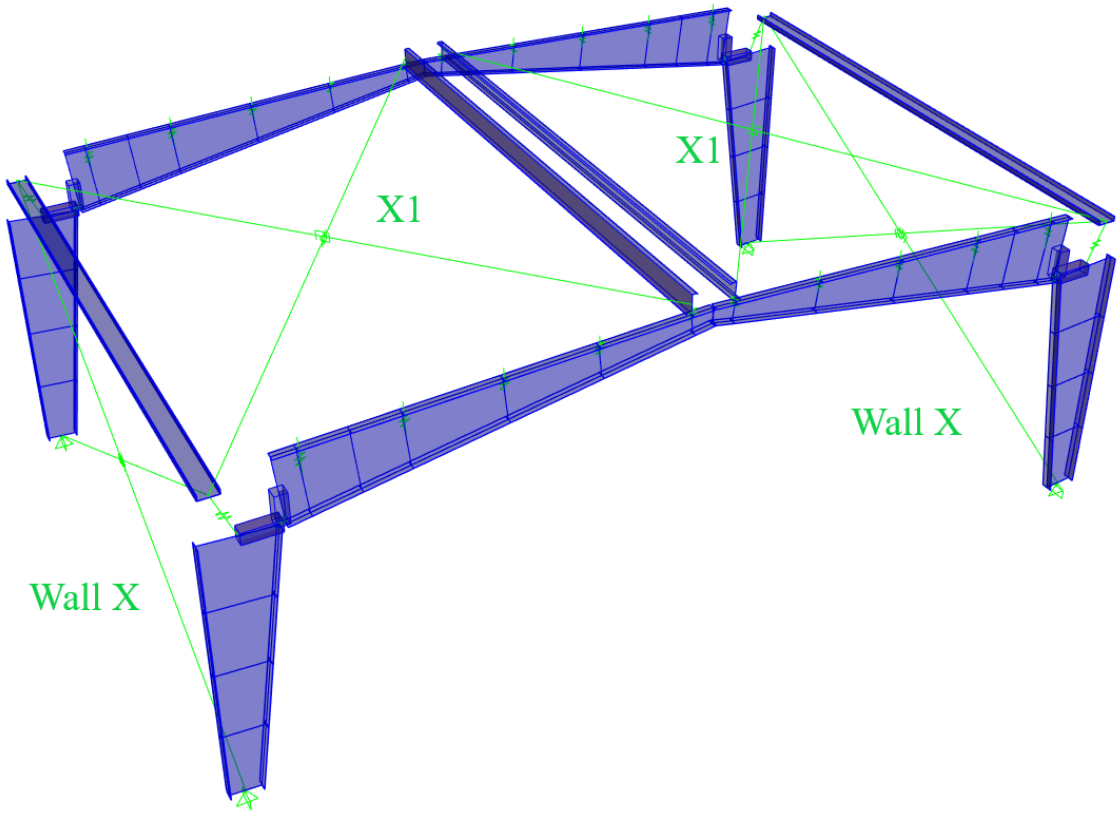

Figure B-4. Brace Identification for Model 85

Table B-10. Brace Properties and Design for Model 85

Model 85	Brace Properties			Strength Design Check		
	Element Name	Area (in^2)	Yield Stress (ksi)	Design Tensile Strength (kips)	Demand (kips)	Load Case
Wall X	Brace 0.625	0.310	50.0	14.0	13.5	1.2D+ρE+L+0.2S
X1	Brace 0.625a	0.310	50.0	14.0	11.8	1.2D+ΩE+L+0.2S

Table B-11. Link Element Properties Element for Model 85

Model 85	Link Element Properties					
	Element Name	E (ksi)	Area (in^2)	Length (in)	Stiffness (k/in)	Expected Yield Stress (ksi)
Wall X	Brace 0.625	29000	0.31	341.0	26.4	55
X1	Brace 0.625a	29000	0.31	372.3	24.1	55

Table B-12. Brace Backbone Curve Points and Acceptance Criteria for Model 85

Model 85	Backbone Curve Points				Acceptance Criteria, Plastic Deformation (inches)		
	Expected Yield Displacement (in)	Expected Yield Force (kips)	Strain Hardened Displacement (in)	Strain Hardened Force (kips)	IO	LS	CP
Wall X	0.647	17.1	5.82	21.1	0.16	2.26	2.91
X1	0.706	17.1	6.35	21.1	0.18	2.47	3.18

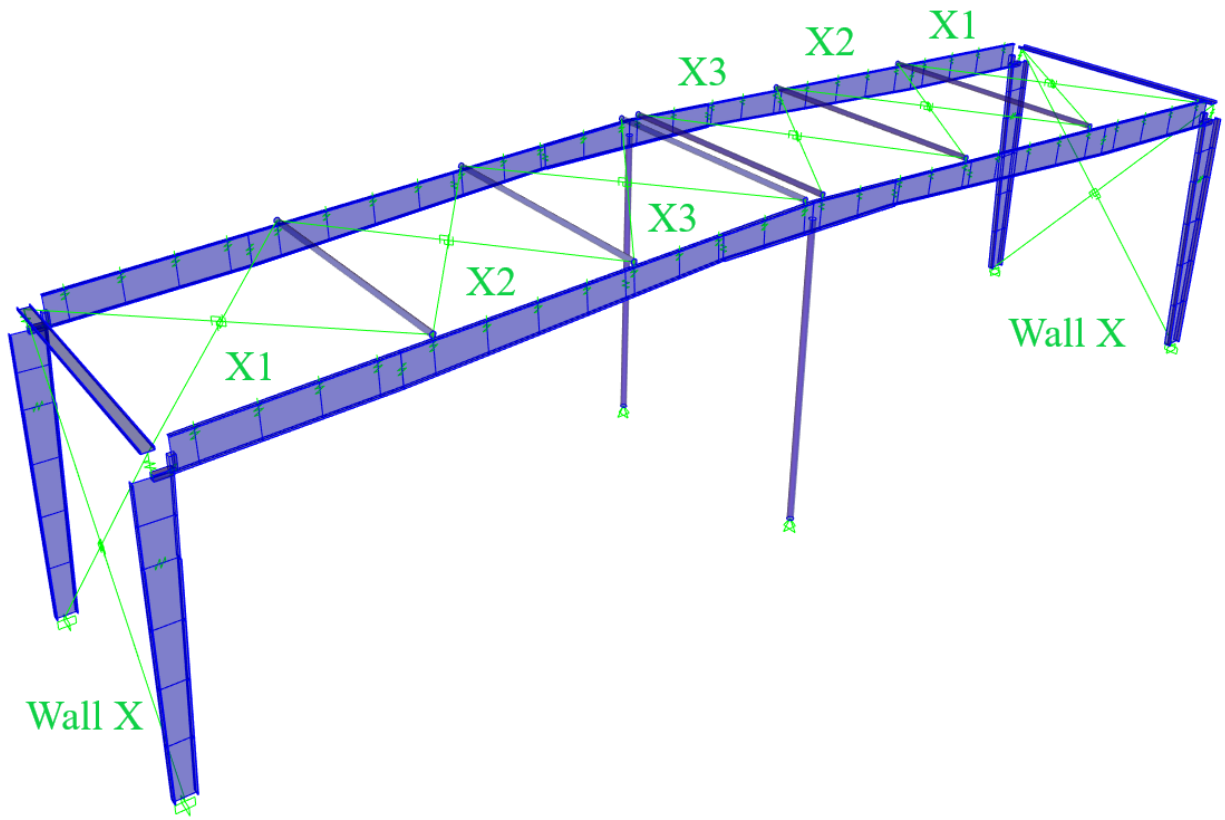

Figure B-5. Brace Identification for Model 138

Table B-13. Brace Properties and Design for Model 138

Model 138	Brace Properties			Strength Design Check		
	Element Name	Area (in^2)	Yield Stress (ksi)	Design Tensile Strength (kips)	Demand (kips)	Load Case
Wall X	Brace1.25	1.227	50.0	55.2	48.8	1.2D+ρE+L+0.2S
X1	L3-1/2x3x5/16	1.950	36.0	63.2	63.0	1.2D+ΩE+L+0.2S
X2	Brace1.0	0.790	50.0	35.6	31.6	1.2D+ΩE+L+0.2S
X3	Brace0.625	0.310	50.0	14.0	11.0	1.2D+ΩE+L+0.2S

Table B-14. Link Element Properties Element for Model 138

Model 138	Link Element Properties					
	Element Name	E (ksi)	Area (in^2)	Length (in)	Stiffness (k/in)	Expected Yield Stress (ksi)
Wall X	Brace1.25	29000	1.23	455.0	78.2	55
X1	L3-1/2x3x5/16	29000	1.95	395.2	143.1	54
X2	Brace1.0	29000	0.79	370.9	61.8	55
X3	Brace0.625	29000	0.31	370.9	24.2	55

Table B-15. Brace Backbone Curve Points and Acceptance Criteria for Model 138

Model 138	Backbone Curve Points				Acceptance Criteria, Plastic Deformation (inches)		
	Expected Yield Displacement (in)	Expected Yield Force (kips)	Strain Hardened Displacement (in)	Strain Hardened Force (kips)	IO	LS	CP
Wall X	0.863	67.5	7.77	83.7	0.22	3.02	3.88
X1	0.736	105.3	8.09	136.9	0.18	2.94	3.68
X2	0.703	43.5	6.33	53.9	0.18	2.46	3.17
X3	0.703	17.1	6.33	21.1	0.18	2.46	3.17

Appendix C. Performance of Tension-Only Braces

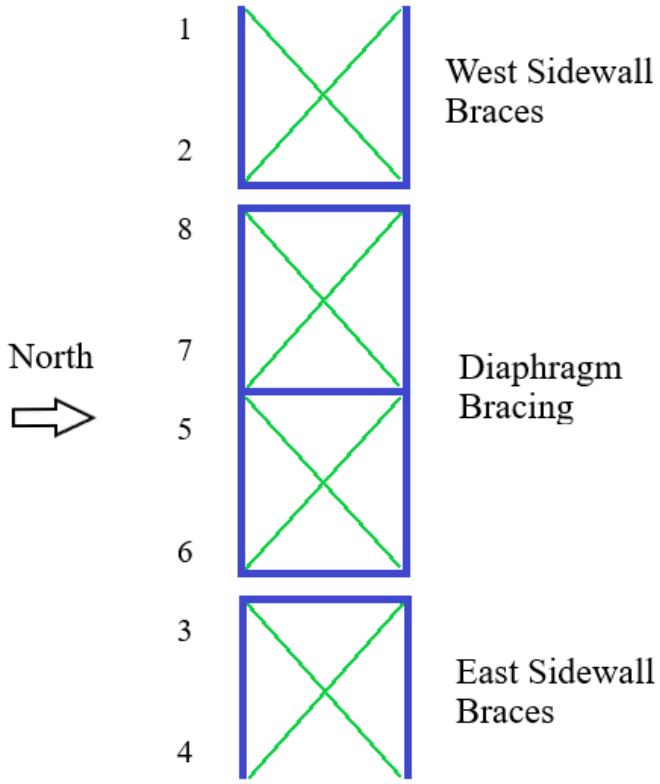

Figure C-1. Brace Identification for Model 16

Table C-1. Brace Performance for Model 16P3_RFC0000_SL14.5_MCE

Brace Number	CAP	DZC	EDA	GAZ	KAK	LOS	ORR	POE	SCS	TCU	TMZ	Mean	Median
1	7.46	4.15	3.09	1.64	2.61	4.57	9.09	7.05	6.59	7.47	2.89	5.14	4.57
2	9.11	2.59	4.72	2.88	2.01	7.11	4.94	4.82	12.00	7.08	4.47	5.61	4.82
8	1.04	0.64	0.80	0.66	0.79	0.91	0.73	0.78	1.11	1.01	0.70	0.83	0.79
7	1.30	0.87	0.75	0.72	0.62	0.74	1.50	0.94	0.95	0.99	0.95	0.94	0.94
5	1.28	0.76	0.76	0.75	0.69	1.39	0.71	0.98	1.67	0.84	0.75	0.96	0.76
6	0.93	0.75	0.73	0.77	0.76	0.78	1.79	1.08	0.94	0.99	0.65	0.92	0.78
3	7.71	2.95	4.03	2.29	1.61	5.44	4.62	3.18	8.54	8.01	5.09	4.86	4.62
4	8.44	3.48	2.75	1.60	2.32	3.46	4.26	5.43	10.59	8.59	1.54	4.77	3.48

Legend	FO	IO	LS	CP

Table C-2. Brace Performance for Model 16P3_RFC0000_SL14.5_DBE

Brace Number	CAP	DZC	EDA	GAZ	KAK	LOS	ORR	POE	SCS	TCU	TMZ	Mean	Median
1	5.16	2.96	1.34	1.58	0.97	1.79	5.79	3.85	3.19	5.52	1.76	3.08	2.96
2	4.23	2.57	2.14	1.49	1.23	3.34	3.92	1.14	4.13	2.17	1.88	2.57	2.17
8	0.82	0.72	0.69	0.66	0.52	0.71	0.61	0.66	0.97	0.80	0.61	0.71	0.69
7	0.81	0.80	0.70	0.64	0.58	0.67	0.69	0.73	0.75	0.74	0.71	0.71	0.71
5	0.78	0.69	0.64	0.62	0.62	0.73	0.86	0.65	0.87	0.79	0.67	0.72	0.69
6	0.80	0.72	0.62	0.63	0.58	0.68	0.89	0.73	0.64	0.87	0.76	0.72	0.72
3	4.94	2.62	1.99	1.11	1.08	1.66	2.24	0.93	3.07	3.23	1.79	2.24	1.99
4	5.87	2.92	1.33	1.44	0.93	2.35	3.19	3.54	2.94	6.26	1.72	2.95	2.92

Legend	FO	IO	LS	CP

Table C-3. Brace Performance for Model 16P3_RFC0000_SL14.5_SLE2

Brace Number	CAP	DZC	EDA	GAZ	KAK	LOS	ORR	POE	SCS	TCU	TMZ	Mean	Median
1	3.11	2.27	0.98	0.99	0.72	2.71	3.26	1.68	2.56	3.40	0.93	2.05	2.27
2	2.79	1.41	1.01	0.90	0.83	3.59	1.37	1.99	4.47	2.40	0.82	1.96	1.41
8	0.82	0.64	0.55	0.64	0.39	0.75	0.64	0.74	0.71	0.81	0.53	0.66	0.64
7	0.84	0.74	0.60	0.56	0.48	0.68	0.66	0.78	0.61	0.68	0.54	0.65	0.66
5	0.68	0.66	0.59	0.51	0.46	0.76	0.65	0.70	0.80	0.73	0.50	0.64	0.66
6	0.71	0.64	0.56	0.52	0.43	0.75	0.74	0.67	0.67	0.67	0.55	0.63	0.67
3	3.89	1.60	1.09	0.86	0.79	2.86	1.31	2.31	2.24	2.26	0.88	1.83	1.60
4	3.51	1.44	1.03	0.95	0.70	2.53	2.74	2.01	1.92	4.36	0.85	2.00	1.92

Legend	FO	IO	LS	CP

Table C-4. Brace Performance for Model 16P3_RFC0000_SL14.5_SLE1

Brace Number	CAP	DZC	EDA	GAZ	KAK	LOS	ORR	POE	SCS	TCU	TMZ	Mean	Median
1	0.99	0.87	0.34	0.63	0.68	0.77	1.19	0.74	0.46	1.90	0.69	0.84	0.74
2	1.02	0.91	0.33	0.69	0.67	0.69	1.31	0.77	0.61	1.53	0.66	0.83	0.69
8	0.55	0.51	0.20	0.42	0.43	0.52	0.65	0.47	0.30	0.79	0.43	0.48	0.47
7	0.69	0.60	0.23	0.39	0.43	0.39	0.67	0.46	0.38	0.65	0.40	0.48	0.43
5	0.56	0.54	0.19	0.45	0.41	0.45	0.65	0.50	0.39	0.79	0.43	0.49	0.45
6	0.67	0.57	0.23	0.37	0.44	0.46	0.70	0.47	0.28	0.62	0.42	0.47	0.46
3	1.18	0.93	0.33	0.65	0.67	0.67	1.38	0.77	0.62	1.70	0.65	0.87	0.67
4	0.95	0.84	0.35	0.64	0.69	0.81	1.23	0.76	0.46	2.38	0.70	0.89	0.76

Legend	FO	IO	LS	CP

Table C-5. Brace Performance for Model 16P3_RFC1000_SL14.5_MCE

Brace Number	CAP	DZC	EDA	GAZ	KAK	LOS	ORR	POE	SCS	TCU	TMZ	Mean	Median
1	2.97	2.15	0.64	0.88	1.18	1.63	5.99	2.11	1.14	6.76	2.02	2.50	2.02
2	2.89	1.85	0.62	2.69	0.86	2.54	1.12	0.73	2.09	2.21	1.15	1.70	1.85
8	0.94	1.32	0.71	0.87	0.88	0.96	0.97	0.95	0.93	1.95	0.95	1.04	0.95
7	1.13	1.21	0.70	0.93	0.84	0.96	0.95	0.76	0.96	0.97	1.19	0.96	0.96
5	1.04	0.91	0.66	1.05	0.78	1.04	0.83	0.82	1.00	1.09	0.94	0.92	0.94
6	1.13	0.98	0.70	0.82	0.95	1.09	2.63	0.94	0.86	1.60	1.16	1.17	0.98
3	3.06	2.09	0.62	2.10	0.97	2.08	1.32	0.75	1.83	1.97	1.48	1.66	1.83
4	2.16	1.94	0.64	0.91	1.08	1.87	3.05	2.18	1.11	7.30	1.71	2.18	1.87

Legend	FO	IO	LS	CP

Table C-6. Brace Performance for Model 16P3_RFC1000_SL14.5_DBE

Brace Number	CAP	DZC	EDA	GAZ	KAK	LOS	ORR	POE	SCS	TCU	TMZ	Mean	Median
1	0.89	1.52	0.37	0.62	0.55	0.89	1.78	0.85	0.49	3.21	0.93	1.10	0.89
2	1.61	0.91	0.24	1.20	0.51	0.85	0.55	0.82	0.79	2.59	0.89	1.00	0.85
8	0.81	0.87	0.55	0.68	0.60	0.81	0.90	0.78	0.60	0.98	0.78	0.76	0.78
7	0.99	0.88	0.46	0.92	0.58	0.82	0.69	0.79	0.73	1.12	0.94	0.81	0.82
5	0.90	0.86	0.46	0.90	0.59	0.76	0.65	0.76	0.73	1.09	0.69	0.76	0.76
6	0.82	0.92	0.52	0.70	0.62	0.84	0.99	0.77	0.55	0.99	0.87	0.78	0.82
3	1.84	1.08	0.24	1.03	0.53	0.72	0.60	0.77	0.72	2.55	0.84	0.99	0.77
4	0.79	1.03	0.36	0.64	0.57	0.97	1.49	0.85	0.50	3.15	0.91	1.02	0.85

Legend	FO	IO	LS	CP

Table C-7. Brace Performance for Model 16P3_RFC1000_SL14.5_SLE2

Brace Number	CAP	DZC	EDA	GAZ	KAK	LOS	ORR	POE	SCS	TCU	TMZ	Mean	Median
1	0.57	0.84	0.26	0.47	0.28	0.62	0.87	0.55	0.33	1.21	0.68	0.61	0.57
2	0.78	0.59	0.12	0.78	0.33	0.51	0.64	0.53	0.48	2.04	0.62	0.68	0.59
8	0.64	0.78	0.48	0.55	0.44	0.64	0.76	0.59	0.52	0.90	0.65	0.63	0.64
7	0.79	0.65	0.35	0.75	0.47	0.57	0.69	0.60	0.56	0.95	0.74	0.65	0.65
5	0.74	0.65	0.36	0.76	0.47	0.58	0.65	0.58	0.53	0.95	0.56	0.62	0.58
6	0.60	0.68	0.43	0.59	0.44	0.64	0.80	0.59	0.48	0.92	0.74	0.63	0.60
3	0.84	0.65	0.10	0.76	0.34	0.47	0.60	0.51	0.40	2.08	0.57	0.67	0.57
4	0.50	0.66	0.25	0.45	0.30	0.67	0.83	0.54	0.41	1.37	0.72	0.61	0.54

Legend	FO	IO	LS	CP

Table C-8. Brace Performance for Model 16P3_RFC1000_SL14.5_SLE1

Brace Number	CAP	DZC	EDA	GAZ	KAK	LOS	ORR	POE	SCS	TCU	TMZ	Mean	Median
1	0.27	0.10	0.06	0.12	0.18	0.23	0.26	0.34	0.06	0.47	0.27	0.22	0.23
2	0.31	0.26	0.09	0.16	0.27	0.16	0.27	0.28	0.08	0.32	0.28	0.22	0.27
8	0.48	0.32	0.21	0.34	0.42	0.45	0.46	0.54	0.21	0.61	0.43	0.41	0.43
7	0.47	0.45	0.29	0.40	0.46	0.37	0.49	0.46	0.25	0.49	0.45	0.42	0.45
5	0.48	0.48	0.26	0.39	0.47	0.41	0.46	0.50	0.29	0.51	0.48	0.43	0.47
6	0.48	0.36	0.21	0.40	0.43	0.43	0.46	0.50	0.27	0.59	0.53	0.42	0.43
3	0.30	0.28	0.08	0.15	0.28	0.18	0.27	0.30	0.09	0.32	0.26	0.23	0.27
4	0.27	0.12	0.06	0.13	0.19	0.24	0.27	0.34	0.07	0.51	0.31	0.23	0.24

Legend	FO	IO	LS	CP

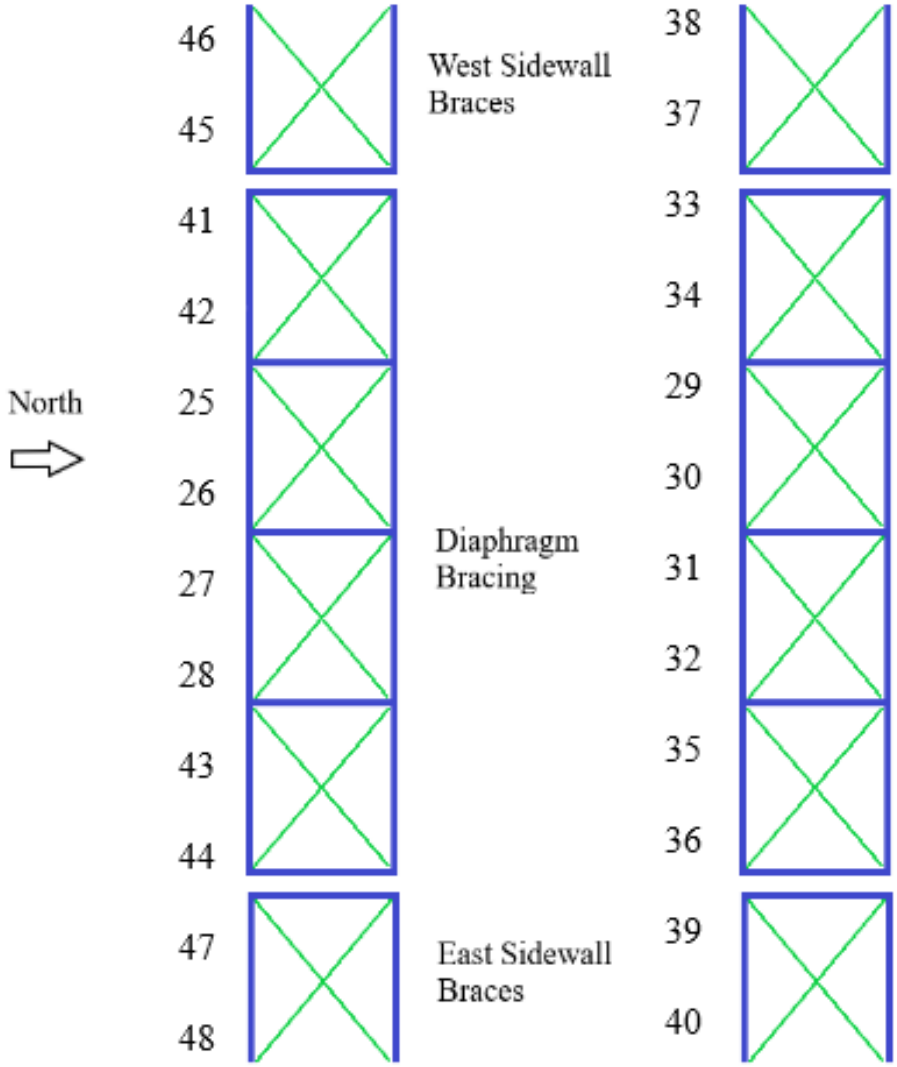

Figure C-2. Brace Identification for Model 41

Table C-9. Brace Performance for Model 41P3_RFC0000_SL14.5_DBE

Brace Number	CAP	DZC	EDA	GAZ	KAK	LOS	ORR	POE	SCS	TCU	TMZ	Mean	Median
46	3.40	1.88	1.13	0.91	1.19	1.17	4.10	2.11	3.81	3.74	1.02	2.22	1.88
45	1.52	1.46	3.57	1.14	0.88	2.60	2.54	2.33	6.06	2.60	3.19	2.54	2.54
41	0.81	0.78	0.74	0.65	0.70	0.67	0.76	0.82	1.03	0.79	0.70	0.77	0.76
42	0.79	0.79	0.73	0.71	0.65	0.74	0.91	0.72	0.83	0.76	0.77	0.76	0.76
25	1.31	1.01	0.70	0.58	0.62	0.66	0.94	0.97	6.84	2.97	0.99	1.60	0.97
26	1.50	0.99	0.76	0.71	0.64	0.81	1.63	1.08	4.25	3.94	0.91	1.57	0.99
27	0.84	0.66	0.81	0.59	0.48	0.76	0.93	0.71	4.80	2.69	1.24	1.32	0.81
28	0.98	0.66	0.78	0.54	0.63	0.72	0.94	0.77	5.04	2.74	0.84	1.33	0.78
43	0.82	0.69	0.82	0.66	0.57	0.79	0.72	0.82	0.91	0.84	0.95	0.78	0.82
44	0.80	0.72	0.67	0.59	0.66	0.79	0.84	0.73	0.86	0.79	0.77	0.75	0.77
47	3.36	2.74	2.73	1.47	0.88	1.70	4.79	2.82	13.34	3.03	1.80	3.51	2.74
48	4.94	2.28	1.81	1.00	1.33	1.85	2.95	2.55	6.72	6.90	1.96	3.12	2.28
38	3.34	1.82	1.07	0.86	1.13	1.11	4.04	2.04	3.75	3.69	0.97	2.17	1.82
37	1.56	1.49	3.61	1.18	0.91	2.63	2.57	2.38	6.11	2.64	3.22	2.57	2.57
33	0.81	0.78	0.76	0.59	0.75	0.86	0.84	0.85	1.54	0.91	0.76	0.86	0.81
34	0.64	0.69	0.69	0.61	0.54	0.72	0.75	0.78	0.79	0.70	0.73	0.69	0.70
29	1.52	1.02	0.85	0.62	0.64	0.87	1.00	0.85	7.06	3.04	0.97	1.68	0.97
30	1.63	0.94	0.68	0.61	0.53	0.81	1.59	1.05	4.26	3.76	0.88	1.52	0.94
31	0.82	0.71	0.80	0.62	0.50	0.81	1.08	0.75	5.12	2.67	1.00	1.35	0.81
32	1.07	0.95	0.76	0.66	0.61	0.72	0.96	0.94	5.21	2.90	0.73	1.41	0.94
35	0.80	0.71	0.81	0.68	0.59	0.75	0.83	0.65	0.95	0.75	0.80	0.76	0.75
36	0.89	0.88	0.75	0.72	0.72	0.70	0.89	0.86	0.98	0.75	0.79	0.81	0.79
39	3.40	2.78	2.78	1.51	0.91	1.75	4.84	2.86	13.37	3.07	1.84	3.55	2.78
40	4.90	2.24	1.77	0.96	1.29	1.81	2.91	2.52	6.67	6.85	1.91	3.07	2.24

Legend	FO	IO	LS	CP

Table C-10. Brace Performance for Model 41P3_RFC0000_SL14.5_SLE2

Brace Number	CAP	DZC	EDA	GAZ	KAK	LOS	ORR	POE	SCS	TCU	TMZ	Mean	Median
46	1.82	1.00	0.94	0.67	0.80	1.10	2.22	1.09	1.53	3.12	1.29	1.42	1.10
45	1.11	0.91	2.02	0.78	0.69	2.20	2.07	0.97	3.59	2.07	2.31	1.70	2.02
41	0.85	0.74	0.67	0.47	0.56	0.73	0.74	0.67	0.75	0.76	0.78	0.70	0.74
42	0.77	0.77	0.71	0.55	0.51	0.78	0.83	0.66	0.65	0.73	0.76	0.70	0.73
25	0.80	0.72	0.69	0.45	0.48	0.73	0.67	0.63	0.92	0.96	0.61	0.70	0.69
26	1.06	0.73	0.64	0.52	0.44	0.88	0.80	0.66	1.16	0.75	0.67	0.76	0.73
27	0.85	0.52	0.64	0.46	0.37	0.74	0.66	0.58	0.93	1.01	0.79	0.69	0.66
28	0.66	0.54	0.54	0.42	0.44	0.82	0.94	0.57	0.92	0.80	0.84	0.68	0.66
43	0.71	0.63	0.72	0.57	0.43	0.76	0.68	0.71	0.82	0.78	0.75	0.69	0.71
44	0.68	0.61	0.65	0.51	0.53	0.70	0.72	0.66	0.68	0.79	0.76	0.66	0.68
47	1.56	1.65	1.78	0.81	0.67	2.41	3.00	1.15	3.24	2.37	1.69	1.85	1.69
48	4.19	1.05	1.35	0.85	0.83	1.95	2.20	1.31	2.83	4.19	1.30	2.01	1.35
38	1.76	0.94	0.88	0.63	0.75	1.05	2.16	1.03	1.48	3.06	1.23	1.36	1.05
37	1.14	0.94	2.06	0.81	0.72	2.24	2.11	1.01	3.63	2.11	2.36	1.74	2.06
33	0.79	0.59	0.69	0.54	0.58	0.81	0.79	0.74	0.85	0.88	0.80	0.73	0.79
34	0.67	0.61	0.66	0.50	0.43	0.71	0.66	0.61	0.69	0.71	0.76	0.64	0.66
29	0.84	0.75	0.67	0.49	0.49	0.75	0.66	0.62	0.76	0.99	0.82	0.71	0.75
30	1.23	0.63	0.58	0.48	0.37	0.74	0.72	0.59	1.11	0.71	0.67	0.71	0.67
31	0.95	0.56	0.56	0.45	0.39	0.77	0.72	0.45	0.82	0.95	0.76	0.67	0.72
32	0.75	0.77	0.61	0.51	0.44	0.89	0.99	0.56	1.12	0.80	0.80	0.75	0.77
35	0.78	0.68	0.70	0.52	0.45	0.72	0.75	0.66	0.70	0.73	0.69	0.67	0.70
36	0.85	0.81	0.69	0.51	0.56	0.73	0.76	0.67	0.68	0.83	0.74	0.71	0.73
39	1.61	1.69	1.82	0.84	0.70	2.44	3.05	1.19	3.27	2.41	1.73	1.89	1.73
40	4.15	1.02	1.31	0.82	0.80	1.91	2.15	1.27	2.79	4.14	1.26	1.97	1.31

Legend	FO	IO	LS	CP

Table C-11. Brace Performance for Model 41P3_RFC0000_SL14.5_SLE1

Brace Number	CAP	DZC	EDA	GAZ	KAK	LOS	ORR	POE	SCS	TCU	TMZ	Mean	Median
46	0.88	0.66	0.60	0.44	0.37	1.02	0.77	0.67	0.69	0.98	0.53	0.69	0.67
45	0.96	0.67	0.65	0.52	0.36	1.12	0.70	0.80	0.78	1.79	0.52	0.81	0.70
41	0.62	0.52	0.42	0.30	0.26	0.72	0.52	0.53	0.46	0.71	0.44	0.50	0.52
42	0.69	0.47	0.47	0.33	0.24	0.71	0.51	0.52	0.50	0.78	0.41	0.51	0.50
25	0.54	0.45	0.37	0.31	0.18	0.65	0.42	0.48	0.48	0.64	0.47	0.45	0.47
26	0.58	0.47	0.41	0.35	0.17	0.62	0.40	0.46	0.48	0.60	0.39	0.45	0.46
27	0.47	0.37	0.35	0.34	0.23	0.48	0.39	0.43	0.43	0.67	0.41	0.42	0.41
28	0.46	0.37	0.32	0.37	0.19	0.51	0.36	0.41	0.48	0.51	0.41	0.40	0.41
43	0.67	0.48	0.43	0.35	0.28	0.67	0.50	0.52	0.58	0.69	0.42	0.51	0.50
44	0.60	0.41	0.41	0.39	0.24	0.65	0.52	0.50	0.53	0.66	0.45	0.49	0.50
47	1.10	0.69	0.64	0.53	0.41	1.44	0.73	0.72	0.78	1.75	0.55	0.85	0.72
48	0.97	0.72	0.66	0.60	0.40	1.22	0.83	0.78	0.82	1.36	0.65	0.82	0.78
38	0.83	0.62	0.57	0.42	0.34	0.96	0.72	0.63	0.65	0.92	0.50	0.65	0.63
37	1.00	0.70	0.67	0.54	0.38	1.16	0.72	0.83	0.82	1.83	0.54	0.84	0.72
33	0.62	0.43	0.46	0.37	0.28	0.75	0.60	0.53	0.58	0.67	0.44	0.52	0.53
34	0.65	0.48	0.39	0.37	0.24	0.63	0.49	0.55	0.52	0.65	0.39	0.49	0.49
29	0.47	0.37	0.34	0.35	0.20	0.65	0.50	0.48	0.51	0.66	0.32	0.44	0.47
30	0.53	0.40	0.32	0.38	0.20	0.58	0.42	0.51	0.50	0.55	0.31	0.43	0.42
31	0.47	0.41	0.32	0.32	0.20	0.53	0.40	0.53	0.46	0.76	0.33	0.43	0.41
32	0.49	0.40	0.33	0.31	0.19	0.59	0.40	0.44	0.40	0.65	0.33	0.41	0.40
35	0.64	0.48	0.42	0.36	0.24	0.68	0.50	0.51	0.49	0.76	0.39	0.50	0.49
36	0.69	0.56	0.43	0.34	0.26	0.71	0.53	0.54	0.50	0.75	0.42	0.52	0.53
39	1.14	0.72	0.66	0.56	0.42	1.48	0.76	0.75	0.81	1.79	0.57	0.88	0.75
40	0.93	0.69	0.63	0.58	0.39	1.18	0.80	0.75	0.79	1.32	0.63	0.79	0.75

Legend	FO	IO	LS	CP

Table C-12. Brace Performance for Model 41P3_RFC1000_SL14.5_MCE

Brace Number	CAP	DZC	EDA	GAZ	KAK	LOS	ORR	POE	SCS	TCU	TMZ	Mean	Median
46	2.92	1.98	0.98	0.92	1.14	1.29	5.61	2.51	6.38	6.07	0.83	2.78	1.98
45	1.43	1.46	3.47	1.64	0.64	3.35	1.99	0.98	7.54	2.52	2.73	2.52	1.99
41	1.18	0.97	0.81	0.84	0.88	0.93	1.01	0.92	1.37	1.96	0.89	1.07	0.93
42	1.16	0.96	0.92	0.97	0.61	1.65	1.88	0.76	1.07	0.88	0.96	1.08	0.96
25	0.97	0.84	0.85	0.77	0.67	0.96	0.98	0.76	2.74	1.44	0.90	1.08	0.90
26	0.98	0.84	0.86	0.89	0.73	1.29	2.20	0.92	1.50	1.18	0.87	1.11	0.92
27	1.43	1.38	0.83	0.77	0.56	1.22	0.85	0.90	4.22	2.81	1.45	1.49	1.22
28	2.19	1.55	0.64	0.66	0.71	1.02	1.20	0.90	4.33	2.48	0.88	1.50	1.02
43	0.83	0.90	0.96	0.87	0.65	1.09	0.89	0.89	1.63	1.38	1.38	1.04	0.90
44	0.95	0.95	0.87	0.81	0.85	1.06	1.84	0.98	1.00	3.63	0.77	1.25	0.95
47	1.66	1.51	2.66	1.71	0.66	2.64	3.21	0.88	3.78	1.64	1.55	1.99	1.66
48	4.28	2.52	1.07	0.98	1.17	1.73	3.34	2.49	3.35	5.69	1.19	2.53	2.49
38	2.85	1.90	0.92	0.85	1.07	1.23	5.53	2.45	6.29	5.99	0.78	2.71	1.90
37	1.47	1.50	3.52	1.68	0.67	3.39	2.03	1.02	7.60	2.58	2.81	2.57	2.03
33	1.17	1.08	0.89	0.76	0.93	1.17	1.19	1.07	1.83	2.95	1.13	1.29	1.13
34	0.81	0.80	0.89	0.85	0.62	1.06	1.34	0.80	1.33	0.98	0.93	0.95	0.89
29	1.21	0.84	0.89	0.62	0.69	1.24	0.92	0.92	2.22	2.11	1.16	1.17	0.92
30	0.79	0.69	0.81	0.74	0.64	1.02	1.83	1.03	1.68	1.28	1.16	1.06	1.02
31	1.41	1.50	0.78	0.81	0.63	1.30	1.14	0.63	4.39	2.34	1.29	1.47	1.29
32	2.29	2.13	0.78	0.85	0.65	1.09	1.11	0.82	4.92	2.47	0.91	1.64	1.09
35	0.99	1.01	0.97	0.91	0.58	1.33	0.97	0.70	1.16	1.03	0.92	0.96	0.97
36	1.18	1.11	0.88	0.97	0.89	0.92	1.87	0.94	1.28	3.18	0.78	1.27	0.97
39	1.72	1.55	2.72	1.76	0.69	2.70	3.26	0.91	3.83	1.67	1.59	2.04	1.72
40	4.22	2.47	1.02	0.94	1.12	1.68	3.29	2.44	3.29	5.63	1.14	2.48	2.44

Legend	FO	IO	LS	CP

Table C-13. Brace Performance for Model 41P3_RFC1000_SL14.5_DBE

Brace Number	CAP	DZC	EDA	GAZ	KAK	LOS	ORR	POE	SCS	TCU	TMZ	Mean	Median
46	0.83	1.09	0.61	0.52	0.58	1.26	2.08	0.83	0.80	3.76	0.75	1.19	0.83
45	2.01	0.89	0.78	0.62	0.41	1.61	1.09	0.65	2.50	1.57	0.74	1.17	0.89
41	0.77	0.78	0.59	0.53	0.53	0.77	0.74	0.65	0.66	0.87	0.58	0.68	0.66
42	0.86	0.76	0.64	0.59	0.46	0.83	0.79	0.53	0.65	0.83	0.57	0.68	0.65
25	0.65	0.60	0.42	0.42	0.36	0.68	0.58	0.51	0.61	0.86	0.51	0.56	0.58
26	0.68	0.64	0.48	0.52	0.44	0.78	0.70	0.45	0.51	0.62	0.48	0.57	0.52
27	0.64	0.59	0.51	0.44	0.35	0.65	0.54	0.55	0.68	1.25	0.60	0.62	0.59
28	0.48	0.55	0.38	0.43	0.35	0.65	0.67	0.62	0.55	0.81	0.53	0.55	0.55
43	0.73	0.66	0.67	0.50	0.40	0.72	0.68	0.63	0.82	0.81	0.69	0.67	0.68
44	0.65	0.66	0.56	0.46	0.50	0.73	0.77	0.72	0.70	1.03	0.66	0.68	0.66
47	2.70	1.04	0.80	0.61	0.39	2.21	1.23	0.61	1.40	2.22	0.73	1.27	1.04
48	1.04	0.92	0.77	0.58	0.61	1.66	1.93	0.96	1.03	3.11	0.81	1.22	0.96
38	0.77	1.02	0.57	0.48	0.54	1.20	2.02	0.78	0.75	3.70	0.71	1.14	0.77
37	2.05	0.93	0.81	0.65	0.43	1.65	1.13	0.68	2.54	1.61	0.78	1.21	0.93
33	0.69	0.68	0.56	0.47	0.55	0.78	0.81	0.73	0.80	1.09	0.69	0.71	0.69
34	0.73	0.66	0.61	0.51	0.39	0.69	0.67	0.60	0.73	0.79	0.66	0.64	0.66
29	0.53	0.51	0.42	0.43	0.38	0.63	0.62	0.64	0.71	0.76	0.58	0.56	0.58
30	0.60	0.47	0.45	0.44	0.39	0.65	0.59	0.54	0.60	0.61	0.49	0.53	0.54
31	0.64	0.63	0.49	0.37	0.38	0.72	0.59	0.43	0.58	1.19	0.55	0.60	0.58
32	0.71	0.74	0.46	0.53	0.35	0.71	0.67	0.56	0.57	0.82	0.48	0.60	0.57
35	0.76	0.69	0.65	0.54	0.43	0.78	0.73	0.55	0.68	0.78	0.55	0.65	0.68
36	0.83	0.94	0.64	0.56	0.54	0.79	0.79	0.70	0.62	1.00	0.63	0.73	0.70
39	2.75	1.08	0.84	0.64	0.41	2.26	1.27	0.64	1.43	2.26	0.75	1.30	1.08
40	1.00	0.88	0.74	0.56	0.58	1.63	1.89	0.92	0.99	3.06	0.77	1.18	0.92

Legend	FO	IO	LS	CP

Table C-14. Brace Performance for Model 41P3_RFC1000_SL14.5_SLE2

Brace Number	CAP	DZC	EDA	GAZ	KAK	LOS	ORR	POE	SCS	TCU	TMZ	Mean	Median
46	0.83	0.81	0.40	0.38	0.51	0.99	1.04	0.70	0.64	1.75	0.55	0.78	0.70
45	1.26	0.73	0.53	0.47	0.40	1.02	0.85	0.55	0.96	1.79	0.58	0.83	0.73
41	0.82	0.79	0.48	0.49	0.53	0.93	0.87	0.62	0.60	0.92	0.52	0.69	0.62
42	0.93	0.73	0.54	0.54	0.52	0.90	0.79	0.53	0.74	0.99	0.54	0.71	0.73
25	0.70	0.60	0.40	0.39	0.40	0.87	0.79	0.49	0.56	0.81	0.42	0.58	0.56
26	0.79	0.65	0.46	0.47	0.49	0.68	0.67	0.49	0.58	0.81	0.47	0.60	0.58
27	0.68	0.54	0.49	0.49	0.41	0.67	0.60	0.56	0.79	1.06	0.55	0.62	0.56
28	0.63	0.52	0.36	0.43	0.38	0.66	0.67	0.58	0.57	0.88	0.53	0.57	0.57
43	0.85	0.64	0.58	0.51	0.45	0.84	0.77	0.62	0.87	0.89	0.66	0.70	0.66
44	0.69	0.64	0.47	0.43	0.52	0.81	0.85	0.69	0.72	0.90	0.57	0.66	0.69
47	1.55	0.75	0.56	0.46	0.38	1.24	0.87	0.55	0.90	2.54	0.60	0.94	0.75
48	0.86	0.81	0.51	0.44	0.53	1.43	1.11	0.78	0.81	1.92	0.60	0.89	0.81
38	0.77	0.75	0.37	0.35	0.47	0.92	0.98	0.65	0.60	1.68	0.52	0.73	0.65
37	1.30	0.76	0.55	0.49	0.42	1.06	0.89	0.58	1.01	1.84	0.61	0.87	0.76
33	0.69	0.64	0.47	0.45	0.56	0.89	0.92	0.71	0.75	0.96	0.60	0.69	0.69
34	0.84	0.63	0.53	0.47	0.45	0.76	0.71	0.62	0.82	0.90	0.63	0.67	0.63
29	0.64	0.50	0.39	0.41	0.43	0.82	0.77	0.59	0.66	0.75	0.48	0.59	0.59
30	0.71	0.50	0.45	0.39	0.43	0.63	0.56	0.56	0.66	0.77	0.43	0.55	0.56
31	0.70	0.57	0.46	0.39	0.45	0.75	0.60	0.45	0.64	1.05	0.50	0.60	0.57
32	0.80	0.75	0.43	0.53	0.40	0.79	0.71	0.56	0.60	0.95	0.47	0.64	0.60
35	0.85	0.68	0.56	0.50	0.48	0.88	0.77	0.55	0.74	0.90	0.48	0.67	0.68
36	0.88	0.85	0.54	0.51	0.54	0.92	0.89	0.68	0.64	1.00	0.55	0.73	0.68
39	1.59	0.79	0.59	0.48	0.41	1.29	0.91	0.57	0.93	2.58	0.62	0.98	0.79
40	0.83	0.78	0.48	0.42	0.51	1.39	1.07	0.74	0.77	1.87	0.57	0.86	0.77

Legend	FO	IO	LS	CP

Table C-15. Brace Performance for Model 41P3_RFC1000_SL14.5_SLE1

Brace Number	CAP	DZC	EDA	GAZ	KAK	LOS	ORR	POE	SCS	TCU	TMZ	Mean	Median
46	0.33	0.35	0.11	0.23	0.21	0.30	0.43	0.28	0.16	0.61	0.32	0.30	0.30
45	0.40	0.36	0.16	0.39	0.23	0.30	0.32	0.26	0.24	0.80	0.27	0.34	0.30
41	0.40	0.45	0.31	0.36	0.33	0.40	0.49	0.42	0.30	0.62	0.45	0.41	0.40
42	0.47	0.46	0.32	0.49	0.35	0.36	0.44	0.38	0.32	0.76	0.38	0.43	0.38
25	0.28	0.34	0.24	0.30	0.23	0.29	0.35	0.33	0.22	0.50	0.33	0.31	0.30
26	0.38	0.42	0.26	0.39	0.27	0.28	0.38	0.31	0.29	0.53	0.36	0.35	0.36
27	0.35	0.32	0.25	0.29	0.24	0.35	0.39	0.33	0.30	0.54	0.34	0.34	0.33
28	0.39	0.33	0.18	0.29	0.24	0.28	0.34	0.29	0.28	0.44	0.37	0.31	0.29
43	0.48	0.46	0.30	0.41	0.36	0.44	0.47	0.37	0.41	0.69	0.42	0.44	0.42
44	0.43	0.40	0.26	0.33	0.32	0.42	0.48	0.39	0.32	0.61	0.48	0.40	0.40
47	0.42	0.37	0.15	0.34	0.22	0.29	0.32	0.24	0.25	0.75	0.28	0.33	0.29
48	0.34	0.37	0.15	0.24	0.21	0.36	0.46	0.33	0.17	0.69	0.39	0.34	0.34
38	0.30	0.32	0.10	0.21	0.19	0.28	0.40	0.26	0.15	0.57	0.30	0.28	0.28
37	0.42	0.38	0.17	0.41	0.24	0.32	0.34	0.28	0.26	0.84	0.29	0.36	0.32
33	0.46	0.44	0.28	0.34	0.34	0.44	0.51	0.40	0.38	0.63	0.49	0.43	0.44
34	0.44	0.45	0.29	0.43	0.35	0.43	0.43	0.37	0.39	0.71	0.40	0.42	0.43
29	0.32	0.30	0.20	0.28	0.26	0.31	0.37	0.31	0.25	0.45	0.38	0.31	0.31
30	0.34	0.30	0.23	0.30	0.27	0.30	0.36	0.29	0.24	0.50	0.26	0.31	0.30
31	0.35	0.40	0.23	0.34	0.23	0.29	0.34	0.30	0.22	0.60	0.26	0.32	0.30
32	0.33	0.35	0.24	0.31	0.26	0.27	0.41	0.35	0.28	0.49	0.32	0.33	0.32
35	0.47	0.48	0.30	0.45	0.34	0.36	0.43	0.36	0.32	0.68	0.34	0.41	0.36
36	0.40	0.50	0.34	0.38	0.34	0.42	0.51	0.45	0.31	0.66	0.43	0.43	0.42
39	0.44	0.39	0.16	0.36	0.23	0.30	0.34	0.26	0.26	0.78	0.29	0.35	0.30
40	0.32	0.36	0.14	0.23	0.19	0.34	0.44	0.31	0.15	0.66	0.37	0.32	0.32

Legend	FO	IO	LS	CP

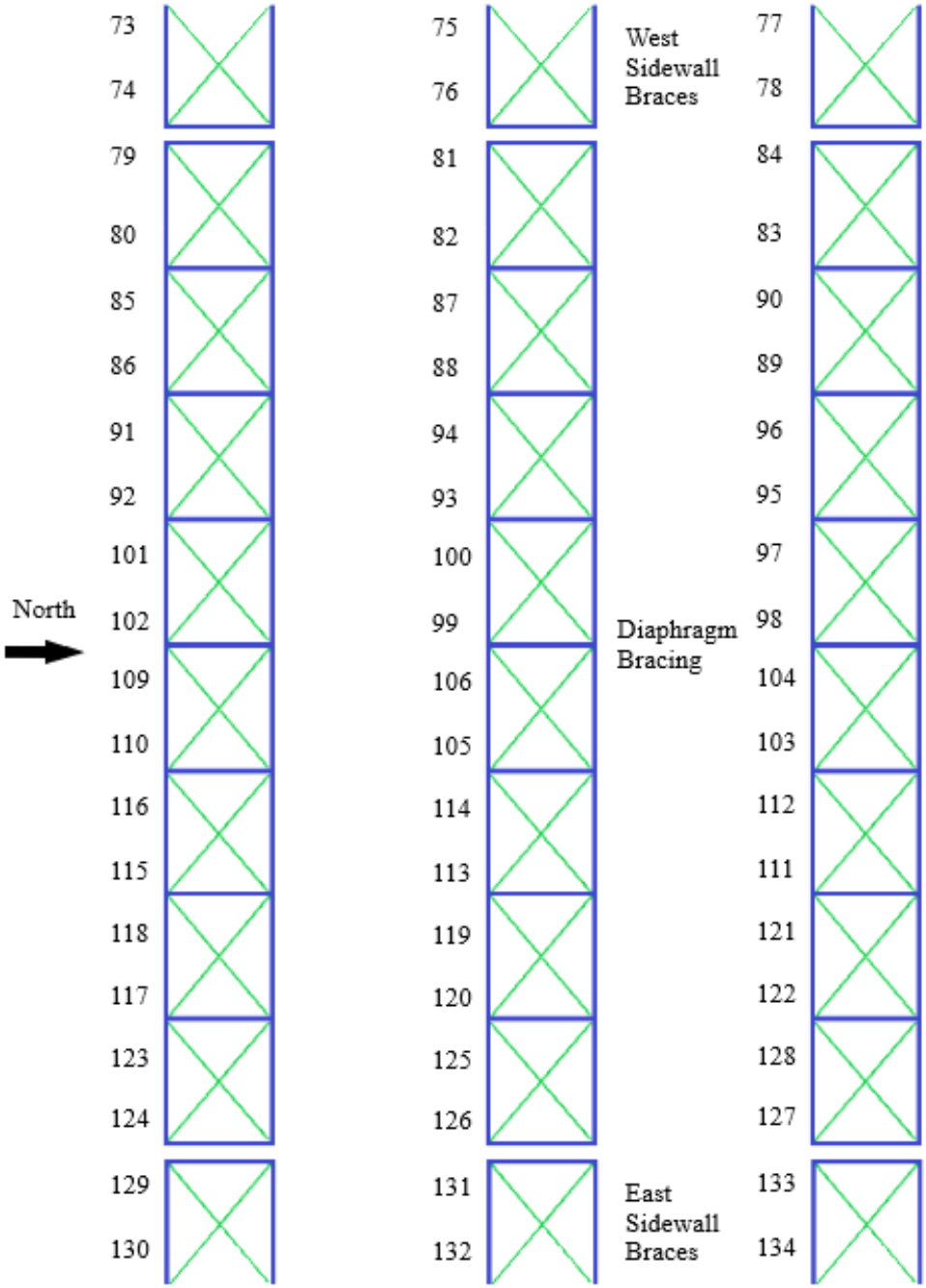

Figure C-3. Brace Identification for Model 42

Table C-16. Brace Performance for Model 42P3_RFC0000_SL14.5_DBE

Brace Number	CAP	DZC	EDA	GAZ	KAK	LOS	ORR	POE	SCS	TCU	TMZ	Mean	Median
73	0.84	0.66	0.53	0.40	0.58	0.70	0.87	0.56	0.74	2.27	0.62	0.80	0.66
74	0.74	0.45	0.51	0.50	0.35	0.56	0.71	0.43	0.64	1.37	0.52	0.62	0.52
79	0.50	0.41	0.33	0.26	0.32	0.39	0.51	0.32	0.46	0.67	0.36	0.41	0.39
80	0.60	0.39	0.39	0.38	0.28	0.44	0.55	0.32	0.50	0.76	0.44	0.46	0.44
85	0.56	0.51	0.37	0.35	0.39	0.49	0.55	0.37	0.52	0.77	0.42	0.48	0.49
86	0.67	0.50	0.38	0.37	0.38	0.52	0.61	0.33	0.56	0.94	0.52	0.53	0.52
91	1.97	0.84	0.62	0.59	0.60	0.99	0.89	0.63	0.86	4.72	0.78	1.23	0.84
92	2.77	0.88	0.62	0.66	0.67	0.98	1.04	0.60	1.00	5.70	0.99	1.45	0.98
101	4.01	0.86	0.74	0.66	0.60	2.55	0.90	0.70	0.95	5.60	1.48	1.73	0.90
102	4.89	0.90	0.79	0.83	0.63	2.02	1.03	0.80	1.18	5.18	2.34	1.87	1.03
109	0.80	0.63	0.45	0.61	0.62	0.79	0.75	0.63	0.50	1.76	0.92	0.77	0.63
110	0.94	0.48	0.31	0.69	0.57	0.73	0.70	0.62	0.35	1.85	0.95	0.74	0.69
116	1.08	0.75	0.56	0.58	0.65	0.76	0.95	0.60	0.80	4.24	0.80	1.07	0.76
115	0.84	0.74	0.52	0.49	0.59	0.66	0.84	0.61	0.66	3.37	0.68	0.91	0.66
118	0.73	0.50	0.39	0.43	0.37	0.58	0.64	0.37	0.59	0.88	0.56	0.55	0.56
117	0.59	0.50	0.36	0.38	0.40	0.55	0.59	0.42	0.54	0.83	0.43	0.51	0.50
123	0.69	0.43	0.47	0.37	0.29	0.68	0.65	0.44	0.65	0.74	0.50	0.54	0.50
124	0.67	0.48	0.44	0.37	0.36	0.61	0.54	0.37	0.61	0.68	0.40	0.50	0.48
129	1.03	0.61	0.66	0.44	0.36	1.17	0.88	0.57	0.92	2.69	0.64	0.91	0.66
130	1.24	0.73	0.76	0.53	0.59	1.47	0.89	0.59	1.10	1.22	0.67	0.89	0.76
75	0.77	0.60	0.48	0.36	0.53	0.64	0.80	0.51	0.68	2.15	0.57	0.74	0.60
76	0.81	0.50	0.55	0.55	0.39	0.61	0.78	0.47	0.71	1.50	0.57	0.68	0.57
81	0.50	0.40	0.33	0.26	0.34	0.40	0.53	0.34	0.48	0.68	0.36	0.42	0.40
82	0.55	0.36	0.36	0.36	0.26	0.40	0.52	0.29	0.47	0.71	0.39	0.42	0.39
87	0.57	0.50	0.38	0.36	0.39	0.50	0.57	0.39	0.55	0.79	0.42	0.49	0.50
88	0.64	0.47	0.36	0.37	0.35	0.47	0.58	0.32	0.54	0.88	0.49	0.50	0.47
94	1.95	0.85	0.64	0.61	0.62	1.01	0.92	0.65	0.91	4.68	0.78	1.24	0.85
93	2.67	0.82	0.59	0.64	0.63	0.92	0.97	0.58	0.95	5.58	0.94	1.39	0.92
100	4.06	0.88	0.75	0.67	0.59	2.61	0.93	0.72	0.99	5.60	1.48	1.75	0.93
99	4.84	0.84	0.74	0.77	0.58	1.96	0.98	0.75	1.09	5.07	2.28	1.81	0.98
106	0.76	0.63	0.45	0.59	0.58	0.72	0.72	0.62	0.47	1.73	0.84	0.74	0.63
105	0.82	0.51	0.34	0.68	0.58	0.74	0.72	0.64	0.37	1.92	0.87	0.74	0.68
114	1.04	0.73	0.53	0.53	0.62	0.72	0.90	0.57	0.75	4.21	0.76	1.03	0.73
113	0.88	0.80	0.55	0.50	0.61	0.68	0.88	0.64	0.70	3.49	0.70	0.95	0.70
119	0.71	0.49	0.38	0.40	0.36	0.55	0.61	0.34	0.58	0.85	0.55	0.53	0.55
120	0.63	0.55	0.40	0.40	0.40	0.57	0.60	0.43	0.59	0.86	0.46	0.54	0.55
125	0.65	0.41	0.43	0.32	0.27	0.62	0.60	0.39	0.61	0.72	0.48	0.50	0.48

126	0.67	0.50	0.44	0.37	0.36	0.61	0.54	0.38	0.61	0.71	0.42	0.51	0.50
131	1.10	0.65	0.70	0.47	0.38	1.23	0.94	0.60	0.98	2.76	0.69	0.95	0.70
132	1.17	0.69	0.71	0.50	0.56	1.40	0.84	0.55	1.03	1.15	0.63	0.84	0.71
77	0.70	0.54	0.44	0.33	0.48	0.58	0.73	0.46	0.62	2.04	0.51	0.68	0.54
78	0.88	0.54	0.60	0.61	0.42	0.67	0.85	0.51	0.77	1.61	0.63	0.74	0.63
84	0.53	0.41	0.35	0.26	0.36	0.44	0.56	0.35	0.52	0.72	0.38	0.44	0.41
83	0.53	0.34	0.35	0.37	0.25	0.39	0.51	0.29	0.46	0.67	0.38	0.41	0.38
90	0.58	0.50	0.40	0.37	0.41	0.53	0.59	0.40	0.58	0.82	0.42	0.51	0.50
89	0.61	0.44	0.35	0.38	0.35	0.46	0.57	0.32	0.50	0.86	0.49	0.48	0.46
96	2.04	0.85	0.68	0.63	0.64	1.10	0.96	0.68	0.96	4.68	0.81	1.28	0.85
95	2.66	0.78	0.58	0.63	0.61	0.92	0.95	0.59	0.91	5.51	0.92	1.37	0.91
97	4.11	0.88	0.78	0.70	0.63	2.68	0.99	0.73	1.10	5.61	1.55	1.80	0.99
98	4.81	0.80	0.71	0.75	0.57	1.95	0.93	0.74	1.04	5.06	2.26	1.78	0.93
104	0.83	0.68	0.48	0.63	0.56	0.72	0.67	0.68	0.44	1.70	0.90	0.75	0.68
103	0.84	0.57	0.39	0.72	0.62	0.79	0.76	0.68	0.37	2.05	0.87	0.79	0.72
112	0.99	0.71	0.51	0.50	0.63	0.69	0.88	0.56	0.71	4.15	0.74	1.01	0.71
111	0.93	0.87	0.58	0.53	0.63	0.71	0.92	0.68	0.72	3.63	0.76	1.00	0.72
121	0.69	0.50	0.35	0.40	0.39	0.53	0.59	0.33	0.55	0.86	0.54	0.52	0.53
122	0.65	0.59	0.40	0.43	0.41	0.58	0.63	0.45	0.60	0.93	0.49	0.56	0.58
128	0.64	0.42	0.42	0.30	0.28	0.62	0.60	0.38	0.62	0.73	0.50	0.50	0.50
127	0.74	0.54	0.47	0.39	0.39	0.68	0.58	0.40	0.67	0.77	0.46	0.55	0.54
133	1.17	0.69	0.74	0.50	0.40	1.31	1.00	0.64	1.05	2.84	0.74	1.01	0.74
134	1.09	0.64	0.67	0.46	0.52	1.33	0.79	0.52	0.96	1.07	0.60	0.79	0.67

Legend	FO	IO	LS	CP

Table C-17. Brace Performance for Model 42P3_RFC0000_SL14.5_SLE2

Brace Number	CAP	DZC	EDA	GAZ	KAK	LOS	ORR	POE	SCS	TCU	TMZ	Mean	Median
73	0.63	0.49	0.40	0.30	0.43	0.52	0.64	0.41	0.56	1.11	0.45	0.54	0.49
74	0.56	0.34	0.38	0.38	0.26	0.43	0.53	0.31	0.47	0.92	0.40	0.45	0.40
79	0.37	0.30	0.24	0.20	0.24	0.29	0.38	0.24	0.34	0.64	0.27	0.32	0.29
80	0.44	0.29	0.29	0.28	0.21	0.33	0.41	0.23	0.37	0.72	0.32	0.35	0.32
85	0.42	0.38	0.27	0.27	0.30	0.37	0.42	0.28	0.39	0.70	0.32	0.37	0.37
86	0.51	0.38	0.28	0.28	0.28	0.39	0.45	0.25	0.41	0.84	0.38	0.41	0.38
91	0.68	0.62	0.45	0.45	0.46	0.72	0.68	0.48	0.64	3.01	0.59	0.80	0.62
92	0.95	0.67	0.46	0.51	0.52	0.68	0.78	0.45	0.73	3.07	0.74	0.87	0.68
101	0.86	0.65	0.54	0.52	0.45	0.91	0.66	0.54	0.70	3.62	0.72	0.92	0.66
102	1.14	0.69	0.59	0.62	0.48	0.88	0.76	0.63	0.79	3.51	1.22	1.03	0.76
109	0.55	0.49	0.34	0.47	0.48	0.60	0.56	0.48	0.39	0.98	0.69	0.55	0.49
110	0.53	0.36	0.24	0.54	0.44	0.56	0.54	0.47	0.27	1.02	0.67	0.51	0.53
116	0.80	0.57	0.42	0.44	0.49	0.57	0.72	0.45	0.60	2.41	0.59	0.73	0.57
115	0.61	0.55	0.39	0.37	0.45	0.51	0.64	0.46	0.49	1.57	0.52	0.60	0.51
118	0.56	0.38	0.29	0.33	0.28	0.39	0.48	0.27	0.43	0.80	0.41	0.42	0.39
117	0.45	0.38	0.27	0.30	0.31	0.38	0.45	0.31	0.40	0.71	0.32	0.39	0.38
123	0.53	0.32	0.35	0.28	0.23	0.53	0.49	0.32	0.48	0.72	0.37	0.42	0.37
124	0.48	0.36	0.33	0.28	0.27	0.50	0.40	0.28	0.46	0.67	0.30	0.39	0.36
129	0.72	0.45	0.49	0.34	0.28	0.77	0.66	0.42	0.66	1.47	0.48	0.61	0.49
130	0.80	0.55	0.56	0.41	0.44	0.88	0.66	0.45	0.79	1.40	0.50	0.68	0.56
75	0.58	0.44	0.36	0.27	0.40	0.48	0.59	0.38	0.51	1.00	0.42	0.49	0.44
76	0.62	0.38	0.42	0.41	0.29	0.48	0.58	0.34	0.52	1.01	0.43	0.50	0.43
81	0.37	0.30	0.25	0.20	0.25	0.30	0.39	0.25	0.36	0.65	0.27	0.33	0.30
82	0.41	0.27	0.27	0.27	0.20	0.31	0.39	0.21	0.34	0.66	0.29	0.33	0.29
87	0.43	0.37	0.28	0.27	0.30	0.38	0.43	0.29	0.41	0.72	0.32	0.38	0.37
88	0.49	0.35	0.27	0.28	0.27	0.35	0.44	0.24	0.40	0.79	0.36	0.38	0.35
94	0.70	0.63	0.47	0.46	0.48	0.72	0.70	0.49	0.68	3.05	0.58	0.81	0.63
93	0.91	0.62	0.45	0.50	0.48	0.63	0.74	0.43	0.70	2.98	0.70	0.83	0.63
100	0.88	0.66	0.54	0.52	0.44	0.92	0.68	0.55	0.74	3.64	0.73	0.94	0.68
99	1.07	0.65	0.55	0.59	0.45	0.83	0.72	0.59	0.74	3.45	1.17	0.98	0.72
106	0.50	0.48	0.34	0.45	0.45	0.56	0.55	0.48	0.38	0.94	0.63	0.52	0.48
105	0.55	0.38	0.26	0.53	0.44	0.57	0.55	0.48	0.28	0.91	0.62	0.51	0.53
114	0.77	0.55	0.40	0.40	0.47	0.54	0.68	0.43	0.56	2.38	0.56	0.71	0.55
113	0.64	0.59	0.41	0.38	0.46	0.52	0.66	0.48	0.52	1.67	0.53	0.62	0.52
119	0.55	0.37	0.29	0.31	0.28	0.38	0.45	0.26	0.43	0.78	0.41	0.41	0.38
120	0.47	0.41	0.29	0.31	0.30	0.42	0.46	0.32	0.44	0.76	0.34	0.41	0.41
125	0.50	0.31	0.32	0.25	0.21	0.48	0.45	0.28	0.45	0.68	0.36	0.39	0.36

126	0.48	0.37	0.32	0.28	0.27	0.50	0.40	0.29	0.46	0.69	0.31	0.40	0.37
131	0.76	0.47	0.52	0.37	0.30	0.81	0.70	0.45	0.71	1.54	0.51	0.65	0.52
132	0.76	0.52	0.53	0.38	0.42	0.83	0.62	0.42	0.75	1.32	0.47	0.64	0.53
77	0.53	0.40	0.33	0.25	0.36	0.43	0.53	0.34	0.47	0.91	0.38	0.45	0.40
78	0.67	0.41	0.45	0.46	0.32	0.52	0.63	0.37	0.57	1.11	0.48	0.54	0.48
84	0.40	0.30	0.26	0.20	0.27	0.33	0.41	0.26	0.39	0.68	0.28	0.34	0.30
83	0.40	0.26	0.26	0.28	0.19	0.30	0.38	0.21	0.34	0.64	0.28	0.32	0.28
90	0.44	0.37	0.29	0.28	0.31	0.40	0.44	0.30	0.43	0.75	0.32	0.39	0.37
89	0.46	0.34	0.26	0.29	0.26	0.34	0.42	0.24	0.37	0.76	0.36	0.37	0.34
96	0.72	0.63	0.50	0.48	0.49	0.75	0.73	0.51	0.71	3.10	0.61	0.84	0.63
95	0.89	0.60	0.43	0.49	0.47	0.60	0.73	0.44	0.67	2.90	0.69	0.81	0.60
97	0.93	0.66	0.56	0.55	0.47	0.97	0.72	0.57	0.77	3.66	0.79	0.97	0.72
98	1.02	0.61	0.54	0.57	0.44	0.81	0.69	0.58	0.72	3.44	1.14	0.96	0.69
104	0.49	0.52	0.36	0.47	0.44	0.55	0.52	0.52	0.35	0.91	0.64	0.53	0.52
103	0.58	0.42	0.30	0.57	0.47	0.61	0.59	0.51	0.29	0.96	0.61	0.54	0.57
112	0.73	0.54	0.38	0.38	0.48	0.52	0.67	0.42	0.52	2.32	0.55	0.68	0.52
111	0.68	0.64	0.43	0.40	0.48	0.54	0.70	0.51	0.54	1.77	0.58	0.66	0.54
121	0.53	0.38	0.26	0.31	0.29	0.36	0.44	0.25	0.41	0.77	0.40	0.40	0.38
122	0.50	0.44	0.30	0.33	0.31	0.43	0.48	0.34	0.45	0.81	0.37	0.43	0.43
128	0.50	0.32	0.32	0.23	0.21	0.49	0.45	0.28	0.46	0.68	0.37	0.39	0.37
127	0.54	0.40	0.35	0.30	0.29	0.55	0.43	0.30	0.50	0.76	0.34	0.43	0.40
133	0.81	0.51	0.55	0.38	0.32	0.86	0.75	0.47	0.75	1.62	0.55	0.69	0.55
134	0.71	0.49	0.50	0.36	0.39	0.78	0.59	0.39	0.70	1.25	0.44	0.60	0.50

Legend	FO	IO	LS	CP

Table C-18. Brace Performance for Model 42P3_RFC0000_SL14.5_SLE1

Brace Number	CAP	DZC	EDA	GAZ	KAK	LOS	ORR	POE	SCS	TCU	TMZ	Mean	Median
73	0.56	0.37	0.25	0.28	0.25	0.49	0.41	0.47	0.29	0.44	0.24	0.37	0.37
74	0.45	0.33	0.23	0.23	0.23	0.45	0.32	0.33	0.30	0.42	0.19	0.32	0.32
79	0.32	0.23	0.14	0.17	0.15	0.30	0.24	0.29	0.17	0.27	0.16	0.22	0.23
80	0.35	0.28	0.18	0.16	0.18	0.35	0.25	0.27	0.22	0.33	0.15	0.25	0.25
85	0.39	0.28	0.20	0.20	0.18	0.37	0.29	0.31	0.18	0.34	0.20	0.27	0.28
86	0.44	0.34	0.19	0.19	0.21	0.36	0.26	0.33	0.25	0.38	0.19	0.29	0.26
91	0.66	0.54	0.35	0.31	0.28	0.61	0.49	0.53	0.29	0.55	0.37	0.45	0.49
92	0.68	0.56	0.35	0.33	0.42	0.58	0.47	0.55	0.43	0.67	0.38	0.49	0.47
101	0.69	0.69	0.34	0.39	0.31	0.60	0.53	0.64	0.29	0.60	0.36	0.49	0.53
102	0.70	0.54	0.37	0.43	0.42	0.60	0.50	0.58	0.41	0.71	0.50	0.52	0.50
109	0.54	0.45	0.26	0.30	0.29	0.33	0.35	0.43	0.27	0.45	0.32	0.36	0.33
110	0.44	0.36	0.24	0.26	0.33	0.33	0.37	0.36	0.21	0.34	0.32	0.32	0.33
116	0.60	0.46	0.30	0.28	0.42	0.54	0.40	0.47	0.44	0.59	0.29	0.43	0.44
115	0.57	0.42	0.32	0.32	0.25	0.54	0.42	0.48	0.29	0.48	0.35	0.40	0.42
118	0.40	0.30	0.20	0.23	0.23	0.39	0.29	0.34	0.30	0.41	0.22	0.30	0.30
117	0.40	0.33	0.20	0.21	0.18	0.38	0.31	0.32	0.20	0.34	0.20	0.28	0.31
123	0.39	0.30	0.18	0.20	0.19	0.38	0.26	0.31	0.28	0.36	0.21	0.28	0.28
124	0.36	0.30	0.17	0.18	0.17	0.36	0.29	0.31	0.20	0.33	0.18	0.26	0.29
129	0.52	0.42	0.24	0.24	0.24	0.50	0.34	0.39	0.35	0.46	0.28	0.36	0.35
130	0.57	0.46	0.26	0.29	0.28	0.56	0.46	0.50	0.31	0.53	0.27	0.41	0.46
75	0.51	0.34	0.23	0.26	0.23	0.45	0.37	0.43	0.27	0.39	0.22	0.34	0.34
76	0.50	0.36	0.26	0.25	0.25	0.50	0.35	0.36	0.33	0.47	0.21	0.35	0.35
81	0.32	0.23	0.14	0.18	0.15	0.31	0.25	0.29	0.18	0.28	0.14	0.22	0.23
82	0.32	0.26	0.17	0.16	0.17	0.33	0.22	0.25	0.22	0.31	0.14	0.23	0.22
87	0.39	0.28	0.19	0.22	0.17	0.38	0.30	0.32	0.20	0.33	0.19	0.27	0.28
88	0.41	0.31	0.18	0.19	0.21	0.35	0.25	0.31	0.26	0.37	0.20	0.28	0.26
94	0.67	0.53	0.35	0.33	0.28	0.63	0.50	0.54	0.31	0.56	0.36	0.46	0.50
93	0.65	0.52	0.34	0.32	0.41	0.56	0.45	0.52	0.43	0.65	0.37	0.48	0.45
100	0.69	0.69	0.34	0.39	0.32	0.63	0.54	0.65	0.29	0.63	0.39	0.51	0.54
99	0.66	0.51	0.36	0.44	0.40	0.56	0.49	0.56	0.41	0.68	0.46	0.50	0.49
106	0.52	0.43	0.23	0.33	0.27	0.31	0.35	0.42	0.24	0.43	0.35	0.35	0.35
105	0.47	0.37	0.25	0.28	0.33	0.35	0.39	0.37	0.21	0.35	0.33	0.34	0.35
114	0.58	0.46	0.29	0.27	0.40	0.52	0.39	0.46	0.40	0.57	0.30	0.42	0.40
113	0.60	0.45	0.32	0.32	0.26	0.56	0.44	0.50	0.28	0.50	0.34	0.42	0.44
119	0.41	0.32	0.21	0.21	0.22	0.38	0.28	0.33	0.28	0.38	0.20	0.29	0.28
120	0.42	0.35	0.20	0.20	0.18	0.40	0.32	0.34	0.19	0.37	0.23	0.29	0.32
125	0.38	0.30	0.17	0.18	0.18	0.36	0.24	0.30	0.26	0.34	0.20	0.26	0.26

126	0.37	0.31	0.17	0.18	0.17	0.36	0.30	0.32	0.19	0.34	0.18	0.26	0.30
131	0.56	0.45	0.25	0.26	0.25	0.53	0.36	0.42	0.37	0.49	0.29	0.38	0.37
132	0.54	0.43	0.24	0.27	0.26	0.53	0.43	0.47	0.29	0.50	0.26	0.38	0.43
77	0.47	0.31	0.21	0.24	0.21	0.41	0.34	0.39	0.24	0.36	0.21	0.31	0.31
78	0.54	0.39	0.28	0.27	0.28	0.54	0.38	0.39	0.37	0.51	0.23	0.38	0.38
84	0.34	0.24	0.16	0.20	0.16	0.33	0.26	0.31	0.20	0.28	0.15	0.24	0.24
83	0.31	0.24	0.16	0.16	0.17	0.31	0.22	0.24	0.23	0.31	0.13	0.23	0.23
90	0.39	0.27	0.19	0.23	0.18	0.39	0.31	0.33	0.21	0.35	0.20	0.28	0.27
89	0.41	0.30	0.19	0.18	0.22	0.34	0.25	0.30	0.26	0.36	0.17	0.27	0.26
96	0.68	0.54	0.36	0.36	0.30	0.66	0.52	0.56	0.33	0.57	0.36	0.48	0.52
95	0.62	0.50	0.34	0.33	0.41	0.55	0.44	0.51	0.43	0.65	0.35	0.47	0.44
97	0.73	0.71	0.36	0.38	0.33	0.66	0.57	0.67	0.32	0.63	0.36	0.52	0.57
98	0.65	0.50	0.34	0.44	0.39	0.56	0.48	0.56	0.40	0.68	0.45	0.49	0.48
104	0.53	0.42	0.23	0.31	0.25	0.29	0.34	0.40	0.22	0.43	0.30	0.34	0.31
103	0.49	0.38	0.27	0.27	0.36	0.38	0.40	0.38	0.21	0.38	0.34	0.35	0.38
112	0.56	0.45	0.28	0.27	0.39	0.50	0.38	0.45	0.37	0.55	0.29	0.41	0.39
111	0.64	0.48	0.35	0.32	0.27	0.57	0.45	0.51	0.28	0.53	0.36	0.43	0.45
121	0.38	0.31	0.20	0.19	0.22	0.36	0.27	0.32	0.26	0.37	0.22	0.28	0.27
122	0.44	0.38	0.21	0.20	0.19	0.40	0.33	0.34	0.19	0.38	0.24	0.30	0.33
128	0.37	0.30	0.17	0.18	0.18	0.35	0.24	0.29	0.24	0.33	0.21	0.26	0.24
127	0.40	0.33	0.18	0.18	0.18	0.38	0.32	0.33	0.19	0.37	0.21	0.28	0.32
133	0.60	0.48	0.27	0.27	0.27	0.56	0.38	0.45	0.39	0.52	0.32	0.41	0.39
134	0.50	0.40	0.23	0.25	0.24	0.49	0.40	0.43	0.27	0.46	0.24	0.36	0.40

Legend	FO	IO	LS	CP

Table C-19. Brace Performance for Model 42P3_RFC1000_SL14.5_DBE

Brace Number	CAP	DZC	EDA	GAZ	KAK	LOS	ORR	POE	SCS	TCU	TMZ	Mean	Median
73	0.68	0.55	0.35	0.27	0.44	0.53	0.70	0.41	0.54	1.19	0.48	0.56	0.53
74	0.56	0.34	0.33	0.39	0.28	0.41	0.55	0.25	0.48	0.93	0.43	0.45	0.41
79	0.47	0.40	0.28	0.26	0.32	0.36	0.47	0.30	0.40	0.71	0.33	0.39	0.36
80	0.51	0.36	0.32	0.36	0.30	0.38	0.52	0.26	0.44	0.81	0.42	0.42	0.38
85	0.53	0.49	0.32	0.35	0.36	0.43	0.50	0.33	0.45	0.77	0.36	0.44	0.43
86	0.58	0.46	0.31	0.33	0.34	0.46	0.56	0.33	0.47	0.95	0.43	0.48	0.46
91	0.87	0.82	0.57	0.63	0.56	0.85	0.78	0.55	0.76	4.10	0.64	1.01	0.76
92	1.24	0.79	0.51	0.65	0.59	0.83	0.86	0.63	0.81	4.63	0.85	1.13	0.81
101	1.04	0.87	0.66	0.73	0.58	1.32	0.79	0.74	0.79	5.03	0.98	1.23	0.79
102	1.57	0.78	0.67	0.83	0.55	1.15	1.00	0.83	0.87	4.22	1.88	1.30	0.87
109	0.73	0.67	0.38	0.53	0.67	0.69	0.71	0.61	0.42	1.44	0.85	0.70	0.67

110	0.71	0.46	0.27	0.72	0.62	0.67	0.69	0.53	0.30	1.61	0.81	0.67	0.67
116	0.92	0.71	0.45	0.55	0.54	0.68	0.86	0.60	0.71	3.86	0.66	0.96	0.68
115	0.75	0.72	0.43	0.50	0.56	0.61	0.73	0.52	0.59	2.52	0.59	0.77	0.59
118	0.63	0.46	0.32	0.40	0.33	0.47	0.58	0.35	0.51	0.86	0.48	0.49	0.47
117	0.58	0.49	0.32	0.39	0.38	0.43	0.53	0.37	0.47	0.76	0.36	0.46	0.43
123	0.60	0.39	0.39	0.35	0.29	0.64	0.61	0.37	0.54	0.77	0.44	0.49	0.44
124	0.63	0.48	0.39	0.39	0.34	0.59	0.50	0.36	0.53	0.72	0.35	0.48	0.48
129	0.76	0.48	0.48	0.35	0.31	0.84	0.76	0.44	0.66	1.80	0.48	0.67	0.48
130	0.95	0.65	0.58	0.50	0.46	0.95	0.69	0.49	0.82	1.18	0.51	0.71	0.65
75	0.62	0.49	0.32	0.25	0.40	0.48	0.64	0.38	0.49	1.07	0.45	0.51	0.48
76	0.62	0.38	0.37	0.43	0.32	0.46	0.61	0.28	0.54	1.04	0.48	0.50	0.46
81	0.46	0.40	0.28	0.26	0.33	0.36	0.48	0.31	0.41	0.71	0.32	0.39	0.36
82	0.48	0.34	0.30	0.34	0.28	0.35	0.48	0.26	0.42	0.73	0.37	0.40	0.35
87	0.54	0.48	0.32	0.35	0.37	0.43	0.52	0.35	0.47	0.79	0.36	0.45	0.43
88	0.56	0.43	0.30	0.33	0.32	0.41	0.54	0.33	0.46	0.87	0.41	0.45	0.41
94	0.89	0.83	0.58	0.64	0.58	0.85	0.80	0.57	0.80	4.13	0.63	1.03	0.80
93	1.15	0.74	0.50	0.63	0.56	0.76	0.82	0.60	0.78	4.53	0.81	1.08	0.76
100	1.07	0.88	0.69	0.74	0.56	1.35	0.81	0.73	0.84	5.02	1.00	1.25	0.84
99	1.49	0.72	0.62	0.77	0.52	1.08	0.95	0.78	0.80	4.12	1.83	1.24	0.80
106	0.68	0.64	0.38	0.51	0.63	0.64	0.69	0.61	0.40	1.38	0.82	0.67	0.64
105	0.73	0.47	0.29	0.71	0.65	0.68	0.72	0.56	0.32	1.59	0.74	0.68	0.68
114	0.89	0.68	0.43	0.53	0.53	0.64	0.83	0.56	0.66	3.85	0.63	0.93	0.64
113	0.78	0.78	0.46	0.52	0.56	0.62	0.77	0.54	0.62	2.63	0.61	0.81	0.62
119	0.62	0.45	0.31	0.38	0.33	0.45	0.56	0.33	0.48	0.83	0.47	0.48	0.45
120	0.60	0.53	0.35	0.40	0.39	0.48	0.54	0.39	0.51	0.82	0.39	0.49	0.48
125	0.58	0.38	0.36	0.31	0.27	0.58	0.56	0.34	0.50	0.74	0.43	0.46	0.43
126	0.62	0.49	0.39	0.38	0.33	0.59	0.50	0.36	0.53	0.75	0.35	0.48	0.49
131	0.81	0.51	0.52	0.37	0.33	0.90	0.81	0.47	0.71	1.88	0.52	0.71	0.52
132	0.90	0.61	0.55	0.47	0.43	0.89	0.64	0.45	0.77	1.11	0.48	0.66	0.61
77	0.56	0.44	0.28	0.21	0.36	0.43	0.58	0.34	0.44	0.96	0.40	0.45	0.43
78	0.68	0.42	0.41	0.48	0.35	0.50	0.67	0.31	0.59	1.14	0.52	0.55	0.50
84	0.49	0.40	0.30	0.26	0.34	0.40	0.51	0.33	0.45	0.75	0.35	0.42	0.40
83	0.47	0.33	0.29	0.36	0.27	0.35	0.48	0.26	0.42	0.71	0.36	0.39	0.36
90	0.55	0.48	0.34	0.36	0.38	0.45	0.54	0.36	0.51	0.82	0.38	0.47	0.45
89	0.52	0.41	0.29	0.34	0.31	0.40	0.52	0.33	0.46	0.85	0.41	0.44	0.41
96	0.91	0.83	0.62	0.66	0.60	0.89	0.83	0.59	0.84	4.19	0.65	1.06	0.83
95	1.08	0.71	0.48	0.63	0.53	0.74	0.80	0.60	0.77	4.46	0.79	1.05	0.74
97	1.13	0.89	0.73	0.78	0.60	1.41	0.85	0.77	0.88	4.99	1.08	1.28	0.88
98	1.44	0.70	0.62	0.75	0.52	1.03	0.91	0.76	0.78	4.07	1.80	1.22	0.78

104	0.68	0.62	0.40	0.55	0.64	0.63	0.69	0.66	0.38	1.35	0.83	0.68	0.64
103	0.77	0.49	0.33	0.77	0.67	0.73	0.74	0.59	0.32	1.65	0.77	0.71	0.73
112	0.86	0.66	0.41	0.51	0.52	0.61	0.79	0.54	0.62	3.79	0.61	0.90	0.61
111	0.83	0.84	0.48	0.55	0.58	0.65	0.81	0.58	0.64	2.71	0.66	0.85	0.65
121	0.60	0.45	0.28	0.37	0.34	0.43	0.54	0.33	0.45	0.83	0.46	0.46	0.45
122	0.63	0.57	0.36	0.43	0.40	0.49	0.57	0.41	0.52	0.89	0.42	0.52	0.49
128	0.58	0.39	0.36	0.29	0.27	0.59	0.57	0.34	0.51	0.74	0.44	0.46	0.44
127	0.70	0.54	0.42	0.41	0.35	0.65	0.53	0.39	0.57	0.82	0.38	0.52	0.53
133	0.86	0.55	0.55	0.39	0.35	0.96	0.87	0.51	0.76	1.96	0.56	0.76	0.56
134	0.84	0.57	0.51	0.43	0.40	0.84	0.60	0.42	0.72	1.03	0.45	0.62	0.57

Legend	FO	IO	LS	CP

Table C-20. Brace Performance for Model 42P3_RFC1000_SL14.5_SLE2

Brace Number	CAP	DZC	EDA	GAZ	KAK	LOS	ORR	POE	SCS	TCU	TMZ	Mean	Median
73	0.47	0.37	0.23	0.18	0.31	0.35	0.49	0.28	0.36	0.84	0.32	0.38	0.35
74	0.39	0.23	0.22	0.26	0.20	0.27	0.38	0.17	0.33	0.77	0.30	0.32	0.27
79	0.34	0.30	0.21	0.19	0.24	0.26	0.35	0.23	0.29	0.58	0.24	0.29	0.26
80	0.37	0.27	0.24	0.27	0.23	0.28	0.38	0.20	0.32	0.70	0.31	0.32	0.28
85	0.40	0.36	0.23	0.26	0.27	0.30	0.38	0.25	0.31	0.63	0.26	0.33	0.30
86	0.41	0.35	0.23	0.25	0.26	0.33	0.42	0.26	0.34	0.78	0.31	0.36	0.33
91	0.67	0.61	0.41	0.49	0.44	0.62	0.62	0.43	0.52	1.02	0.46	0.57	0.52
92	0.80	0.61	0.39	0.51	0.47	0.58	0.63	0.50	0.58	1.79	0.61	0.68	0.58
101	0.80	0.67	0.48	0.61	0.44	0.80	0.60	0.61	0.57	1.26	0.62	0.68	0.61
102	0.92	0.60	0.53	0.62	0.42	0.80	0.74	0.65	0.59	1.18	1.01	0.73	0.65
109	0.53	0.52	0.28	0.43	0.55	0.55	0.59	0.49	0.35	0.89	0.67	0.53	0.53
110	0.54	0.37	0.21	0.58	0.49	0.53	0.54	0.41	0.25	0.93	0.61	0.50	0.53
116	0.67	0.56	0.34	0.43	0.43	0.51	0.66	0.46	0.51	1.49	0.48	0.59	0.51
115	0.56	0.54	0.31	0.40	0.45	0.47	0.56	0.40	0.41	0.98	0.44	0.50	0.45
118	0.46	0.36	0.24	0.30	0.26	0.35	0.44	0.28	0.37	0.76	0.35	0.38	0.35
117	0.44	0.37	0.24	0.30	0.29	0.31	0.42	0.28	0.33	0.63	0.28	0.35	0.31
123	0.44	0.29	0.28	0.27	0.22	0.47	0.45	0.27	0.40	0.71	0.32	0.37	0.32
124	0.46	0.36	0.29	0.29	0.25	0.43	0.36	0.28	0.38	0.63	0.26	0.36	0.36
129	0.53	0.34	0.33	0.24	0.22	0.60	0.55	0.31	0.46	0.89	0.33	0.44	0.34
130	0.68	0.48	0.41	0.36	0.32	0.67	0.48	0.35	0.56	0.96	0.35	0.51	0.48
75	0.42	0.33	0.20	0.16	0.28	0.32	0.45	0.25	0.33	0.76	0.30	0.35	0.32
76	0.43	0.26	0.24	0.29	0.23	0.31	0.42	0.19	0.37	0.86	0.34	0.36	0.31
81	0.34	0.29	0.21	0.19	0.25	0.26	0.35	0.23	0.29	0.58	0.24	0.29	0.26
82	0.35	0.25	0.22	0.26	0.22	0.26	0.36	0.20	0.31	0.65	0.27	0.30	0.26
87	0.40	0.36	0.24	0.26	0.27	0.30	0.39	0.26	0.33	0.64	0.25	0.34	0.30
88	0.41	0.33	0.23	0.25	0.25	0.30	0.40	0.25	0.34	0.73	0.30	0.34	0.30
94	0.69	0.61	0.41	0.50	0.45	0.61	0.63	0.43	0.55	1.07	0.45	0.58	0.55
93	0.77	0.57	0.37	0.50	0.44	0.55	0.60	0.48	0.56	1.71	0.59	0.65	0.56
100	0.82	0.68	0.50	0.61	0.42	0.81	0.61	0.61	0.61	1.30	0.62	0.69	0.61
99	0.86	0.57	0.49	0.60	0.40	0.76	0.71	0.60	0.57	1.08	0.97	0.69	0.60
106	0.49	0.51	0.30	0.42	0.52	0.51	0.57	0.49	0.33	0.85	0.65	0.51	0.51
105	0.56	0.37	0.23	0.58	0.51	0.54	0.56	0.43	0.26	0.96	0.55	0.50	0.54
114	0.65	0.54	0.33	0.40	0.40	0.48	0.63	0.44	0.48	1.45	0.46	0.57	0.48
113	0.60	0.58	0.33	0.41	0.45	0.48	0.59	0.41	0.43	1.04	0.45	0.52	0.45
119	0.45	0.35	0.23	0.29	0.26	0.34	0.42	0.27	0.35	0.74	0.35	0.37	0.35
120	0.46	0.40	0.26	0.31	0.29	0.34	0.42	0.29	0.36	0.66	0.27	0.37	0.34
125	0.42	0.28	0.26	0.24	0.20	0.42	0.42	0.25	0.37	0.68	0.31	0.35	0.31

126	0.45	0.37	0.28	0.29	0.24	0.43	0.36	0.27	0.38	0.64	0.25	0.36	0.36
131	0.56	0.36	0.35	0.26	0.24	0.64	0.58	0.33	0.49	0.96	0.36	0.47	0.36
132	0.64	0.45	0.39	0.34	0.29	0.63	0.45	0.33	0.52	0.90	0.33	0.48	0.45
77	0.38	0.29	0.18	0.14	0.25	0.29	0.40	0.22	0.29	0.69	0.27	0.31	0.29
78	0.47	0.29	0.27	0.33	0.25	0.34	0.47	0.22	0.41	0.93	0.37	0.40	0.34
84	0.36	0.29	0.22	0.19	0.26	0.29	0.37	0.24	0.32	0.60	0.25	0.31	0.29
83	0.34	0.25	0.22	0.27	0.22	0.26	0.36	0.21	0.31	0.63	0.26	0.30	0.26
90	0.41	0.35	0.25	0.26	0.28	0.31	0.40	0.27	0.35	0.65	0.28	0.35	0.31
89	0.38	0.31	0.22	0.25	0.24	0.29	0.39	0.26	0.33	0.69	0.30	0.33	0.30
96	0.71	0.61	0.44	0.51	0.47	0.64	0.65	0.45	0.58	1.14	0.48	0.61	0.58
95	0.74	0.55	0.36	0.50	0.43	0.54	0.59	0.48	0.56	1.64	0.58	0.63	0.55
97	0.85	0.69	0.53	0.65	0.45	0.85	0.63	0.64	0.63	1.34	0.68	0.72	0.65
98	0.83	0.53	0.48	0.58	0.39	0.72	0.68	0.59	0.56	1.05	0.96	0.67	0.59
104	0.49	0.49	0.30	0.46	0.53	0.51	0.56	0.51	0.32	0.81	0.65	0.51	0.51
103	0.59	0.38	0.26	0.62	0.53	0.58	0.58	0.45	0.26	1.00	0.60	0.53	0.58
112	0.62	0.52	0.32	0.39	0.39	0.46	0.60	0.42	0.44	1.38	0.45	0.55	0.45
111	0.63	0.63	0.35	0.44	0.47	0.50	0.62	0.44	0.44	1.14	0.48	0.56	0.48
121	0.44	0.35	0.22	0.29	0.27	0.33	0.41	0.26	0.32	0.72	0.34	0.36	0.33
122	0.48	0.43	0.26	0.32	0.31	0.35	0.45	0.31	0.36	0.70	0.29	0.39	0.35
128	0.42	0.30	0.26	0.23	0.21	0.43	0.42	0.26	0.36	0.68	0.32	0.35	0.32
127	0.51	0.40	0.31	0.31	0.26	0.47	0.39	0.29	0.41	0.70	0.27	0.39	0.39
133	0.60	0.39	0.38	0.28	0.25	0.68	0.62	0.36	0.52	1.03	0.38	0.50	0.39
134	0.60	0.42	0.36	0.31	0.27	0.59	0.42	0.30	0.49	0.84	0.31	0.45	0.42

Legend	FO	IO	LS	CP

Table C-21. Brace Performance for Model 42P3_RFC1000_SL14.5_SLE1

Link Number	CAP	DZC	EDA	GAZ	KAK	LOS	ORR	POE	SCS	TCU	TMZ	Mean	Median
73	0.25	0.20	0.07	0.18	0.12	0.16	0.25	0.21	0.15	0.37	0.17	0.19	0.18
74	0.16	0.17	0.06	0.16	0.12	0.12	0.18	0.13	0.12	0.38	0.13	0.16	0.13
79	0.20	0.18	0.10	0.18	0.14	0.17	0.21	0.17	0.13	0.29	0.18	0.18	0.18
80	0.21	0.22	0.09	0.20	0.16	0.18	0.22	0.18	0.15	0.38	0.17	0.20	0.18
85	0.20	0.22	0.15	0.22	0.19	0.21	0.25	0.22	0.14	0.31	0.24	0.21	0.22
86	0.29	0.24	0.12	0.27	0.20	0.19	0.26	0.23	0.17	0.38	0.26	0.24	0.24
91	0.34	0.38	0.23	0.42	0.29	0.37	0.44	0.42	0.25	0.55	0.40	0.37	0.38
92	0.47	0.40	0.24	0.50	0.32	0.35	0.43	0.44	0.27	0.58	0.50	0.41	0.43
101	0.53	0.48	0.19	0.49	0.38	0.37	0.51	0.46	0.26	0.64	0.43	0.43	0.46
102	0.43	0.58	0.27	0.51	0.30	0.48	0.51	0.55	0.30	0.63	0.57	0.47	0.51
109	0.59	0.32	0.19	0.28	0.29	0.21	0.35	0.38	0.21	0.39	0.28	0.32	0.29
110	0.49	0.30	0.13	0.26	0.22	0.19	0.34	0.35	0.14	0.32	0.32	0.28	0.30
116	0.40	0.35	0.20	0.37	0.32	0.30	0.39	0.33	0.29	0.48	0.35	0.34	0.35
115	0.34	0.34	0.20	0.30	0.27	0.33	0.38	0.31	0.24	0.41	0.37	0.32	0.33
118	0.24	0.25	0.13	0.30	0.18	0.22	0.29	0.25	0.20	0.37	0.27	0.25	0.25
117	0.21	0.25	0.13	0.23	0.16	0.22	0.27	0.24	0.17	0.33	0.23	0.22	0.23
123	0.26	0.24	0.11	0.30	0.18	0.22	0.27	0.24	0.20	0.42	0.26	0.25	0.24
124	0.24	0.26	0.13	0.22	0.18	0.22	0.27	0.23	0.18	0.36	0.24	0.23	0.23
129	0.28	0.25	0.09	0.30	0.14	0.21	0.28	0.24	0.17	0.48	0.25	0.25	0.25
130	0.29	0.32	0.13	0.27	0.20	0.25	0.34	0.25	0.19	0.49	0.29	0.27	0.27
75	0.23	0.18	0.07	0.15	0.10	0.14	0.22	0.18	0.14	0.33	0.14	0.17	0.15
76	0.18	0.20	0.07	0.18	0.14	0.15	0.21	0.15	0.13	0.43	0.15	0.18	0.15
81	0.20	0.18	0.10	0.17	0.14	0.17	0.21	0.17	0.15	0.28	0.17	0.18	0.17
82	0.20	0.20	0.08	0.20	0.15	0.16	0.21	0.17	0.15	0.35	0.17	0.19	0.17
87	0.21	0.23	0.15	0.21	0.19	0.21	0.26	0.22	0.16	0.31	0.24	0.22	0.21
88	0.27	0.23	0.11	0.27	0.19	0.18	0.25	0.22	0.17	0.37	0.24	0.23	0.23
94	0.35	0.40	0.23	0.42	0.30	0.38	0.45	0.43	0.27	0.56	0.40	0.38	0.40
93	0.44	0.38	0.23	0.48	0.31	0.33	0.41	0.42	0.28	0.54	0.45	0.39	0.41
100	0.51	0.50	0.19	0.51	0.37	0.39	0.52	0.47	0.28	0.65	0.46	0.44	0.47
99	0.41	0.56	0.27	0.50	0.29	0.44	0.51	0.54	0.29	0.58	0.56	0.45	0.50
106	0.55	0.31	0.18	0.26	0.29	0.20	0.34	0.33	0.21	0.40	0.26	0.30	0.29
105	0.50	0.32	0.14	0.26	0.22	0.19	0.34	0.36	0.15	0.33	0.31	0.28	0.31
114	0.39	0.34	0.19	0.36	0.31	0.29	0.38	0.32	0.27	0.47	0.36	0.33	0.34
113	0.34	0.35	0.21	0.31	0.27	0.34	0.39	0.31	0.23	0.44	0.36	0.32	0.34
119	0.24	0.25	0.13	0.28	0.18	0.21	0.28	0.24	0.19	0.36	0.25	0.24	0.24
120	0.22	0.26	0.13	0.25	0.17	0.23	0.27	0.24	0.15	0.36	0.27	0.23	0.24
125	0.24	0.23	0.11	0.27	0.16	0.21	0.25	0.23	0.18	0.38	0.24	0.23	0.23

126	0.23	0.26	0.13	0.23	0.17	0.21	0.26	0.21	0.15	0.36	0.25	0.22	0.23
131	0.30	0.28	0.10	0.32	0.16	0.23	0.30	0.26	0.19	0.52	0.27	0.27	0.27
132	0.26	0.30	0.11	0.25	0.19	0.23	0.32	0.23	0.17	0.46	0.28	0.26	0.25
77	0.20	0.16	0.06	0.13	0.09	0.12	0.19	0.16	0.11	0.30	0.12	0.15	0.13
78	0.21	0.22	0.08	0.20	0.15	0.16	0.23	0.18	0.15	0.47	0.17	0.20	0.18
84	0.23	0.19	0.10	0.18	0.14	0.18	0.23	0.18	0.17	0.31	0.18	0.19	0.18
83	0.20	0.21	0.08	0.19	0.16	0.16	0.21	0.19	0.16	0.34	0.18	0.19	0.19
90	0.23	0.24	0.15	0.21	0.20	0.22	0.28	0.24	0.17	0.32	0.27	0.23	0.23
89	0.28	0.22	0.12	0.26	0.19	0.17	0.25	0.22	0.18	0.34	0.21	0.22	0.22
96	0.39	0.41	0.24	0.42	0.31	0.39	0.48	0.46	0.29	0.58	0.43	0.40	0.41
95	0.43	0.37	0.23	0.47	0.30	0.32	0.41	0.42	0.28	0.52	0.46	0.38	0.41
97	0.54	0.52	0.21	0.52	0.39	0.41	0.57	0.50	0.31	0.67	0.47	0.46	0.50
98	0.41	0.55	0.26	0.48	0.28	0.45	0.50	0.53	0.28	0.57	0.55	0.44	0.48
104	0.55	0.30	0.18	0.25	0.27	0.18	0.33	0.34	0.20	0.38	0.24	0.29	0.27
103	0.52	0.32	0.14	0.26	0.23	0.21	0.34	0.38	0.14	0.35	0.31	0.29	0.31
112	0.38	0.34	0.19	0.35	0.31	0.30	0.38	0.31	0.24	0.46	0.37	0.33	0.34
111	0.33	0.36	0.21	0.33	0.27	0.36	0.40	0.32	0.23	0.48	0.34	0.33	0.33
121	0.22	0.24	0.13	0.27	0.18	0.21	0.25	0.23	0.16	0.34	0.24	0.22	0.23
122	0.23	0.28	0.14	0.26	0.17	0.23	0.28	0.24	0.15	0.38	0.28	0.24	0.24
128	0.24	0.24	0.11	0.28	0.16	0.22	0.26	0.23	0.17	0.39	0.24	0.23	0.24
127	0.24	0.28	0.13	0.24	0.18	0.22	0.28	0.22	0.16	0.39	0.27	0.24	0.24
133	0.32	0.30	0.11	0.35	0.17	0.25	0.33	0.28	0.20	0.56	0.28	0.29	0.28
134	0.24	0.28	0.10	0.23	0.17	0.21	0.29	0.21	0.16	0.42	0.25	0.24	0.23

Legend	FO	IO	LS	CP

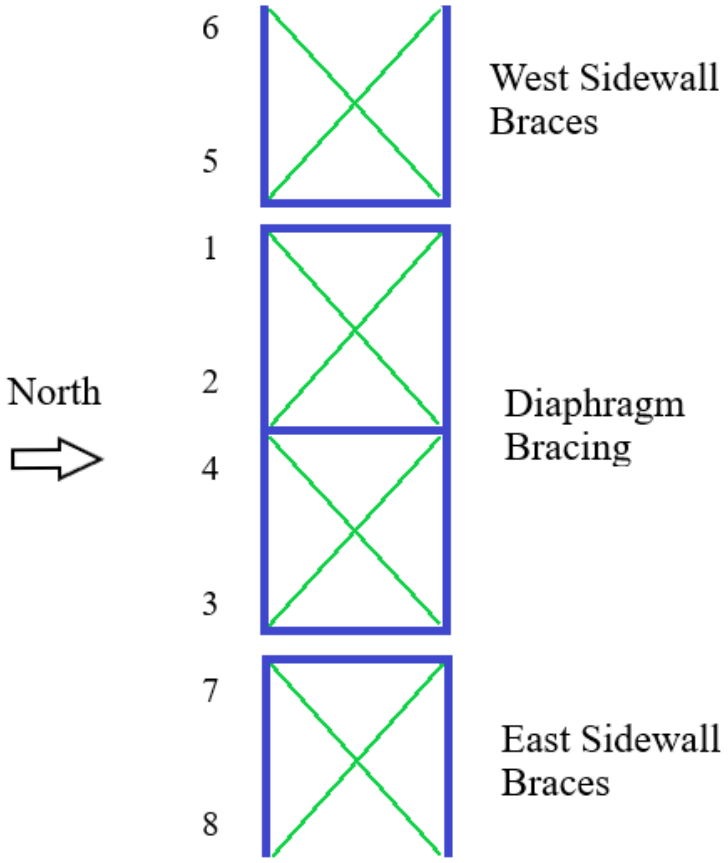

Figure C-4. Brace Identification for Model 85

Table C-22. Brace Performance for Model 85P3_RFC0000_SL14.5_MCE

Brace Number	CAP	DZC	EDA	GAZ	KAK	LOS	ORR	POE	SCS	TCU	TMZ	Mean	Median
1	7.46	4.15	3.09	1.64	2.61	4.57	9.09	7.05	6.59	7.47	2.89	5.14	4.57
2	9.11	2.59	4.72	2.88	2.01	7.11	4.94	4.82	12.00	7.08	4.47	5.61	4.82
8	1.04	0.64	0.80	0.66	0.79	0.91	0.73	0.78	1.11	1.01	0.70	0.83	0.79
7	1.30	0.87	0.75	0.72	0.62	0.74	1.50	0.94	0.95	0.99	0.95	0.94	0.94
5	1.28	0.76	0.76	0.75	0.69	1.39	0.71	0.98	1.67	0.84	0.75	0.96	0.76
6	0.93	0.75	0.73	0.77	0.76	0.78	1.79	1.08	0.94	0.99	0.65	0.92	0.78
3	7.71	2.95	4.03	2.29	1.61	5.44	4.62	3.18	8.54	8.01	5.09	4.86	4.62
4	8.44	3.48	2.75	1.60	2.32	3.46	4.26	5.43	10.59	8.59	1.54	4.77	3.48

Legend	FO	IO	LS	CP

Table C-23. Brace Performance for Model 85P3_RFC0000_SL07.5_DBE

Brace Number	CAP	DZC	EDA	GAZ	KAK	LOS	ORR	POE	SCS	TCU	TMZ	Mean	Median
6	9.61	4.79	1.39	1.57	5.76	4.67	7.62	4.43	1.26	9.28	4.56	5.00	4.67
5	8.06	4.45	2.41	2.79	4.15	12.95	4.38	4.65	2.53	3.48	3.65	4.86	4.15
1	0.98	1.37	0.68	0.73	0.89	2.21	1.10	0.81	0.75	0.80	0.90	1.02	0.89
2	1.18	0.81	0.70	0.65	1.15	2.02	0.73	0.86	0.60	0.97	0.98	0.97	0.86
4	1.20	0.99	0.81	0.75	0.60	2.14	0.97	0.83	0.68	0.76	1.75	1.04	0.83
3	0.92	0.71	0.60	0.74	0.76	1.94	1.40	0.75	0.61	0.96	0.98	0.94	0.76
7	6.67	4.94	2.09	2.66	6.13	9.87	4.01	4.79	1.90	5.16	2.80	4.64	4.79
8	10.54	5.16	0.95	2.21	4.70	4.33	7.24	4.57	2.50	8.54	3.66	4.95	4.57

Legend	FO	IO	LS	CP

Table C-24. Brace Performance for Model 85P3_RFC0000_SL07.5_SLE2

Brace Number	CAP	DZC	EDA	GAZ	KAK	LOS	ORR	POE	SCS	TCU	TMZ	Mean	Median
6	5.91	3.14	0.76	2.71	2.22	2.98	3.93	2.77	0.83	6.76	3.07	3.19	2.98
5	5.52	3.40	1.13	2.01	2.42	2.84	1.79	3.87	1.02	4.50	2.59	2.83	2.59
1	0.89	0.68	0.53	0.73	0.86	1.44	0.74	0.82	0.47	0.86	0.95	0.82	0.82
2	0.75	0.72	0.60	0.70	0.89	0.77	0.61	0.85	0.58	0.76	0.86	0.74	0.75
4	1.04	0.77	0.58	0.69	0.54	0.76	0.70	0.79	0.53	0.78	1.04	0.75	0.76
3	0.91	0.70	0.45	0.57	0.64	0.73	0.76	0.72	0.43	0.85	0.79	0.69	0.72
7	4.28	3.52	1.25	2.13	3.91	3.60	2.04	2.95	0.99	4.69	2.35	2.88	2.95
8	4.91	2.75	0.86	2.72	1.28	5.26	3.56	3.80	0.83	6.85	2.03	3.17	2.75

Legend	FO	IO	LS	CP

Table C-25. Brace Performance for Model 85P3_RFC0000_SL07.5_SLE1

Brace Number	CAP	DZC	EDA	GAZ	KAK	LOS	ORR	POE	SCS	TCU	TMZ	Mean	Median
6	0.96	0.62	0.39	0.63	1.06	0.98	1.23	1.20	0.41	1.43	2.36	1.02	0.98
5	0.85	0.89	0.54	0.72	1.09	0.84	1.23	1.05	0.50	1.59	1.61	0.99	0.89
1	0.55	0.30	0.25	0.39	0.52	0.55	0.61	0.50	0.23	0.59	0.61	0.47	0.52
2	0.47	0.53	0.30	0.39	0.61	0.48	0.55	0.58	0.29	0.61	0.78	0.51	0.53
4	0.51	0.46	0.32	0.43	0.55	0.49	0.63	0.55	0.26	0.61	0.55	0.49	0.51
3	0.54	0.38	0.22	0.34	0.60	0.54	0.60	0.65	0.22	0.59	0.77	0.50	0.54
7	0.86	0.90	0.55	0.72	1.20	0.81	1.25	1.17	0.49	1.58	2.10	1.06	0.90
8	0.97	0.60	0.42	0.66	0.99	0.98	1.26	1.21	0.41	1.36	1.88	0.98	0.98

Legend	FO	IO	LS	CP

Table C-26. Brace Performance for Model 85P3_RFC0625_SL07.5_MCE

Brace Number	CAP	DZC	EDA	GAZ	KAK	LOS	ORR	POE	SCS	TCU	TMZ	Mean	Median
6	3.65	2.00	0.65	1.06	0.97	2.30	6.62	2.58	0.94	5.78	2.82	2.67	2.30
5	2.22	1.84	0.90	4.51	1.68	3.42	2.09	2.18	1.31	5.43	1.68	2.48	2.09
1	1.00	0.96	0.72	0.87	0.83	0.95	0.95	0.94	0.80	4.08	1.38	1.23	0.95
2	1.56	1.10	0.78	0.81	1.61	0.80	0.99	0.81	0.85	0.86	1.74	1.08	0.86
4	0.94	0.89	0.91	1.26	0.90	1.54	1.74	1.02	0.84	2.28	1.63	1.27	1.02
3	1.01	0.88	0.60	0.81	0.93	0.96	1.86	0.92	0.79	0.99	0.85	0.96	0.92
7	4.05	2.95	1.59	3.23	2.94	1.85	2.63	1.54	1.04	4.48	2.24	2.59	2.63
8	3.87	2.23	0.49	1.09	1.00	1.14	3.19	1.88	0.92	12.50	3.37	2.88	1.88

Legend	FO	IO	LS	CP

Table C-27. Brace Performance for Model 85P3_RFC0625_SL07.5_DBE

Brace Number	CAP	DZC	EDA	GAZ	KAK	LOS	ORR	POE	SCS	TCU	TMZ	Mean	Median
6	1.27	1.01	0.30	0.67	0.96	0.66	2.04	1.21	0.50	3.69	2.31	1.33	1.01
5	1.74	1.53	0.53	1.32	1.41	1.29	0.85	0.89	0.56	1.71	1.01	1.17	1.29
1	0.95	0.84	0.43	0.69	0.76	0.70	0.83	0.88	0.52	0.95	1.14	0.79	0.83
2	0.89	0.98	0.66	0.81	0.88	0.80	0.72	0.71	0.55	0.83	1.09	0.81	0.81
4	0.95	0.75	0.58	0.91	0.84	0.88	0.65	0.84	0.59	0.95	0.85	0.80	0.84
3	0.85	0.89	0.50	0.58	0.83	0.73	0.92	0.78	0.56	1.03	0.93	0.78	0.83
7	1.69	1.68	0.54	1.23	1.44	1.03	0.84	0.94	0.56	1.82	1.18	1.18	1.18
8	1.63	1.08	0.34	0.69	0.95	0.67	1.68	1.30	0.51	3.54	2.17	1.32	1.08

Legend	FO	IO	LS	CP

Table C-28. Brace Performance for Model 85P3_RFC0625_SL07.5_SLE2

Brace Number	CAP	DZC	EDA	GAZ	KAK	LOS	ORR	POE	SCS	TCU	TMZ	Mean	Median
6	1.23	0.79	0.21	0.35	0.63	0.37	0.86	0.64	0.28	1.25	1.43	0.73	0.64
5	1.02	0.94	0.35	0.59	0.78	0.79	0.86	0.68	0.30	0.99	0.79	0.74	0.79
1	0.93	0.75	0.39	0.47	0.59	0.54	0.70	0.60	0.41	0.79	1.02	0.65	0.60
2	0.78	0.72	0.56	0.57	0.72	0.64	0.71	0.63	0.42	0.81	0.86	0.68	0.71
4	0.92	0.87	0.47	0.62	0.65	0.70	0.67	0.64	0.44	0.84	0.68	0.68	0.67
3	0.79	0.73	0.43	0.45	0.62	0.50	0.76	0.63	0.41	0.87	0.91	0.65	0.63
7	1.00	1.00	0.29	0.58	0.75	0.74	0.73	0.67	0.30	0.99	0.84	0.72	0.74
8	1.50	0.82	0.24	0.34	0.64	0.41	0.83	0.58	0.28	1.19	1.36	0.75	0.64

Legend	FO	IO	LS	CP

Table C-29. Brace Performance for Model 85P3_RFC0625_SL07.5_SLE1

Brace Number	CAP	DZC	EDA	GAZ	KAK	LOS	ORR	POE	SCS	TCU	TMZ	Mean	Median
6	0.52	0.22	0.09	0.10	0.25	0.06	0.22	0.35	0.06	0.53	0.46	0.26	0.22
5	0.39	0.25	0.05	0.17	0.22	0.34	0.23	0.22	0.11	0.27	0.28	0.23	0.23
1	0.55	0.41	0.31	0.33	0.41	0.28	0.38	0.46	0.30	0.53	0.53	0.41	0.41
2	0.44	0.40	0.26	0.34	0.38	0.44	0.38	0.41	0.32	0.36	0.46	0.38	0.38
4	0.49	0.41	0.30	0.36	0.39	0.46	0.39	0.47	0.32	0.42	0.42	0.40	0.41
3	0.52	0.36	0.32	0.33	0.42	0.34	0.39	0.48	0.31	0.56	0.51	0.41	0.39
7	0.41	0.27	0.06	0.20	0.24	0.32	0.23	0.20	0.11	0.29	0.29	0.24	0.24
8	0.52	0.21	0.09	0.10	0.24	0.11	0.23	0.24	0.07	0.54	0.48	0.26	0.23

Legend	FO	IO	LS	CP

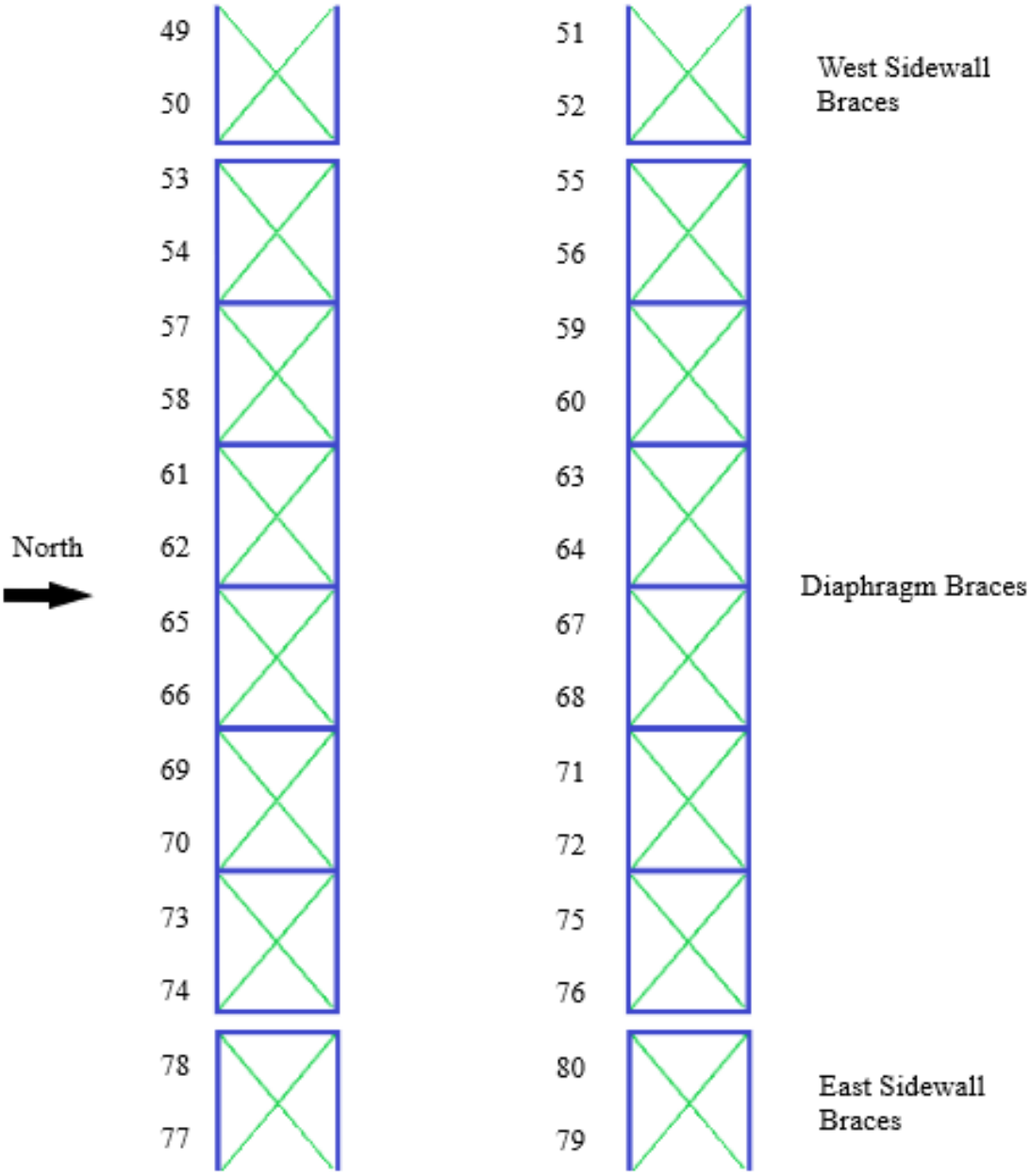

Figure C-5. Brace Identification for Model 138

Table C-30. Brace Performance for Model 138P3_RFC0000_SL14.5_DBE

Brace Number	CAP	DZC	EDA	GAZ	KAK	LOS	ORR	POE	SCS	TCU	TMZ	Mean	Median
49	5.74	1.88	1.71	1.21	1.47	1.23	5.06	2.15	4.11	5.71	1.80	2.92	1.88
50	2.98	1.55	3.81	1.59	0.94	2.44	3.11	2.36	6.74	2.35	2.63	2.77	2.44
53	0.59	0.54	0.53	0.47	0.47	0.48	0.53	0.55	0.51	0.60	0.50	0.52	0.53
54	0.55	0.56	0.53	0.56	0.47	0.49	0.58	0.53	0.58	0.49	0.53	0.53	0.53
57	1.01	0.81	0.76	0.72	0.75	0.76	0.99	0.98	0.71	0.97	0.75	0.84	0.76
58	0.85	0.81	0.88	0.85	0.71	0.85	0.73	0.73	0.68	0.81	0.95	0.80	0.81
61	1.35	0.99	0.82	0.73	0.76	0.70	1.07	1.61	0.91	1.32	0.86	1.01	0.91
62	1.76	0.89	0.80	0.89	0.67	0.93	0.84	0.87	0.77	2.10	1.30	1.07	0.89
65	1.58	1.00	1.00	0.72	0.87	0.99	1.05	1.10	1.37	5.49	1.41	1.51	1.05
66	2.96	1.36	0.75	0.73	0.72	1.13	0.86	1.10	1.85	5.43	0.79	1.61	1.10
69	0.81	0.73	0.90	0.77	0.73	0.97	0.72	0.81	0.82	0.85	1.02	0.83	0.81
70	0.97	0.84	0.75	0.67	0.75	0.84	0.94	0.78	0.81	1.09	0.78	0.84	0.81
73	0.52	0.49	0.56	0.50	0.49	0.61	0.47	0.59	0.58	0.53	0.69	0.55	0.53
74	0.55	0.50	0.47	0.44	0.48	0.56	0.61	0.56	0.50	0.59	0.55	0.53	0.55
78	2.41	2.41	2.19	1.95	0.92	1.46	3.05	2.83	3.28	1.16	1.92	2.14	2.19
77	6.50	1.53	1.24	1.20	1.39	1.35	2.98	2.62	2.74	6.89	2.11	2.78	2.11
51	5.70	1.83	1.66	1.16	1.42	1.19	5.01	2.10	4.07	5.67	1.76	2.87	1.83
52	3.03	1.59	3.86	1.64	0.98	2.48	3.16	2.41	6.80	2.39	2.68	2.82	2.48
55	0.59	0.54	0.52	0.46	0.51	0.59	0.52	0.56	0.60	0.71	0.57	0.56	0.56
56	0.48	0.47	0.50	0.49	0.46	0.56	0.53	0.53	0.53	0.48	0.57	0.51	0.50
59	1.05	0.80	0.76	0.64	0.81	0.88	1.01	0.93	0.82	1.09	0.91	0.88	0.88
60	0.77	0.69	0.82	0.76	0.67	0.90	0.68	0.82	0.74	0.78	1.12	0.80	0.77
63	1.37	1.01	0.83	0.68	0.81	0.82	1.13	1.64	0.97	1.42	1.02	1.06	1.01
64	1.68	0.91	0.76	0.80	0.67	0.96	0.81	0.81	0.78	2.03	1.28	1.04	0.81
67	1.50	0.95	0.97	0.72	0.83	0.93	0.91	1.03	1.25	5.45	1.39	1.45	0.97
68	2.96	1.39	0.83	0.83	0.76	1.16	0.88	1.08	1.88	5.42	0.77	1.63	1.08
71	0.82	0.77	0.88	0.79	0.70	0.83	0.67	0.72	0.72	0.83	0.98	0.79	0.79
72	1.03	0.90	0.81	0.81	0.76	0.84	1.00	0.87	0.76	1.00	0.77	0.87	0.84
75	0.51	0.54	0.55	0.53	0.45	0.51	0.47	0.48	0.50	0.47	0.54	0.51	0.51
76	0.60	0.63	0.55	0.52	0.52	0.50	0.64	0.60	0.51	0.57	0.46	0.55	0.55
80	2.46	2.45	2.24	2.01	0.96	1.51	3.10	2.88	3.34	1.20	1.98	2.19	2.24
79	6.45	1.49	1.19	1.16	1.34	1.30	2.94	2.56	2.69	6.85	2.05	2.73	2.05

Legend	FO	IO	LS	CP

Table C-31. Brace Performance for Model 138P3_RFC0000_SL14.5_SLE2

Brace Number	CAP	DZC	EDA	GAZ	KAK	LOS	ORR	POE	SCS	TCU	TMZ	Mean	Median
49	2.23	1.21	0.99	0.95	0.90	1.45	2.60	0.99	2.27	5.63	1.63	1.89	1.45
50	0.99	0.97	1.95	0.96	0.68	2.46	2.79	0.95	3.18	1.56	2.17	1.70	1.56
53	0.56	0.53	0.46	0.44	0.40	0.48	0.52	0.47	0.50	0.58	0.54	0.50	0.50
54	0.49	0.58	0.52	0.52	0.33	0.54	0.56	0.47	0.48	0.49	0.51	0.50	0.51
57	0.92	0.78	0.66	0.62	0.55	0.72	0.88	0.65	0.75	1.05	0.87	0.77	0.75
58	0.73	0.84	0.79	0.78	0.50	0.76	0.70	0.72	0.80	0.74	0.73	0.74	0.74
61	0.92	0.72	0.68	0.59	0.62	0.80	0.88	0.60	1.31	1.45	0.92	0.86	0.80
62	0.97	0.94	0.77	0.82	0.50	0.76	0.78	0.63	1.09	1.30	0.89	0.86	0.82
65	0.73	0.66	0.84	0.70	0.53	0.84	0.85	0.81	0.82	1.53	1.10	0.86	0.82
66	0.87	0.74	0.60	0.60	0.54	0.85	1.24	0.63	0.97	1.05	1.02	0.83	0.85
69	0.70	0.66	0.82	0.70	0.52	0.85	0.59	0.81	0.84	0.74	0.93	0.74	0.74
70	0.89	0.71	0.65	0.59	0.56	0.79	0.83	0.63	0.75	0.95	0.97	0.76	0.75
73	0.52	0.47	0.53	0.48	0.30	0.54	0.49	0.53	0.59	0.53	0.62	0.51	0.53
74	0.54	0.44	0.46	0.42	0.38	0.51	0.54	0.44	0.50	0.59	0.58	0.49	0.50
78	1.32	1.54	1.63	1.01	0.71	2.15	2.57	0.97	2.70	1.27	1.22	1.55	1.32
77	3.11	1.05	1.08	0.93	0.88	1.27	1.78	0.98	2.31	5.36	1.24	1.82	1.24
51	2.18	1.15	0.95	0.91	0.86	1.40	2.55	0.95	2.22	5.58	1.58	1.85	1.40
52	1.03	1.01	2.00	1.00	0.71	2.50	2.84	1.00	3.23	1.60	2.23	1.74	1.60
55	0.56	0.44	0.48	0.44	0.40	0.53	0.51	0.47	0.57	0.67	0.61	0.52	0.51
56	0.43	0.46	0.49	0.46	0.29	0.50	0.47	0.52	0.51	0.48	0.57	0.47	0.48
59	0.94	0.70	0.67	0.62	0.59	0.83	0.89	0.67	0.79	1.16	0.90	0.80	0.79
60	0.69	0.72	0.75	0.70	0.50	0.78	0.63	0.75	0.83	0.71	0.91	0.72	0.72
63	0.96	0.69	0.68	0.61	0.66	0.86	0.93	0.68	1.33	1.56	0.95	0.90	0.86
64	0.96	0.84	0.72	0.75	0.50	0.77	0.64	0.68	1.00	1.29	0.97	0.83	0.77
67	0.73	0.68	0.82	0.65	0.48	0.76	0.93	0.72	0.74	1.53	0.96	0.82	0.74
68	0.91	0.88	0.63	0.64	0.55	0.86	1.22	0.68	1.01	1.02	1.09	0.86	0.88
71	0.70	0.71	0.78	0.71	0.48	0.74	0.65	0.71	0.73	0.70	0.77	0.70	0.71
72	0.94	0.87	0.69	0.66	0.57	0.76	0.89	0.68	0.78	0.93	1.06	0.80	0.78
75	0.46	0.49	0.52	0.50	0.31	0.50	0.49	0.45	0.50	0.48	0.48	0.47	0.49
76	0.58	0.58	0.47	0.46	0.43	0.51	0.58	0.48	0.48	0.61	0.56	0.52	0.51
80	1.36	1.59	1.68	1.06	0.74	2.19	2.62	1.01	2.75	1.31	1.27	1.60	1.36
79	3.05	1.01	1.03	0.89	0.85	1.22	1.73	0.94	2.26	5.32	1.19	1.77	1.19

Legend	FO	IO	LS	CP

Table C-32. Brace Performance for Model 138P3_RFC0000_SL14.5_SLE1

Brace Number	CAP	DZC	EDA	GAZ	KAK	LOS	ORR	POE	SCS	TCU	TMZ	Mean	Median
49	1.18	0.67	0.73	0.41	0.45	1.16	0.84	0.61	0.99	1.41	0.79	0.84	0.79
50	1.18	0.54	0.66	0.44	0.35	1.08	0.86	0.57	0.89	1.52	0.64	0.79	0.66
53	0.49	0.33	0.34	0.21	0.20	0.49	0.40	0.29	0.43	0.50	0.36	0.37	0.36
54	0.53	0.30	0.34	0.22	0.19	0.52	0.44	0.26	0.44	0.55	0.36	0.38	0.36
57	0.67	0.41	0.44	0.35	0.23	0.69	0.64	0.47	0.55	0.72	0.51	0.51	0.51
58	0.80	0.45	0.49	0.35	0.25	0.66	0.59	0.41	0.66	0.81	0.49	0.54	0.49
61	0.65	0.41	0.43	0.32	0.23	0.68	0.59	0.46	0.55	0.63	0.46	0.49	0.46
62	0.78	0.44	0.49	0.37	0.24	0.63	0.58	0.42	0.64	0.79	0.48	0.53	0.49
65	0.71	0.45	0.45	0.27	0.25	0.61	0.57	0.35	0.63	0.75	0.48	0.50	0.48
66	0.68	0.39	0.43	0.33	0.25	0.72	0.60	0.44	0.52	0.67	0.57	0.51	0.52
69	0.75	0.45	0.47	0.32	0.26	0.62	0.63	0.34	0.70	0.80	0.47	0.53	0.47
70	0.68	0.42	0.44	0.35	0.24	0.71	0.62	0.47	0.56	0.69	0.55	0.52	0.55
73	0.52	0.28	0.35	0.21	0.17	0.47	0.44	0.27	0.51	0.54	0.33	0.37	0.35
74	0.48	0.29	0.34	0.23	0.20	0.49	0.41	0.31	0.45	0.48	0.38	0.37	0.38
78	1.14	0.56	0.67	0.45	0.36	1.09	0.86	0.52	0.90	1.59	0.61	0.80	0.67
77	1.14	0.67	0.75	0.40	0.46	1.14	0.85	0.61	1.06	1.50	0.78	0.85	0.78
51	1.13	0.64	0.70	0.39	0.44	1.11	0.81	0.58	0.95	1.36	0.76	0.81	0.76
52	1.23	0.57	0.69	0.46	0.36	1.13	0.90	0.59	0.94	1.57	0.67	0.83	0.69
55	0.53	0.30	0.36	0.24	0.20	0.51	0.45	0.33	0.51	0.54	0.41	0.40	0.41
56	0.49	0.28	0.33	0.21	0.16	0.45	0.41	0.26	0.46	0.51	0.31	0.35	0.33
59	0.74	0.45	0.46	0.37	0.25	0.73	0.70	0.53	0.64	0.78	0.57	0.57	0.57
60	0.73	0.44	0.47	0.32	0.24	0.59	0.57	0.36	0.68	0.77	0.46	0.51	0.47
63	0.68	0.45	0.45	0.37	0.25	0.71	0.66	0.51	0.59	0.67	0.52	0.53	0.52
64	0.72	0.41	0.47	0.36	0.24	0.58	0.54	0.35	0.65	0.75	0.43	0.50	0.47
67	0.70	0.40	0.41	0.31	0.24	0.60	0.55	0.38	0.56	0.72	0.44	0.48	0.44
68	0.69	0.40	0.45	0.33	0.26	0.75	0.58	0.46	0.54	0.69	0.56	0.52	0.54
71	0.75	0.41	0.44	0.33	0.25	0.61	0.59	0.39	0.61	0.76	0.45	0.51	0.45
72	0.70	0.47	0.47	0.35	0.25	0.75	0.62	0.47	0.58	0.71	0.53	0.54	0.53
75	0.50	0.28	0.33	0.21	0.18	0.48	0.42	0.25	0.44	0.52	0.34	0.36	0.34
76	0.52	0.37	0.36	0.21	0.22	0.52	0.42	0.30	0.43	0.50	0.37	0.38	0.37
80	1.19	0.58	0.70	0.46	0.37	1.14	0.90	0.54	0.94	1.64	0.64	0.83	0.70
79	1.09	0.65	0.72	0.38	0.44	1.09	0.81	0.58	1.01	1.45	0.74	0.81	0.74

Legend	FO	IO	LS	CP

Table C-33. Brace Performance for Model 138P3_RFC1000_SL14.5_MCE

Brace Number	CAP	DZC	EDA	GAZ	KAK	LOS	ORR	POE	SCS	TCU	TMZ	Mean	Median
49	3.27	1.97	1.16	1.00	1.39	1.32	6.11	2.86	8.18	6.71	0.94	3.17	1.97
50	2.12	1.54	4.22	1.29	0.79	3.30	2.28	1.02	20.42	2.82	2.76	3.87	2.28
53	0.75	0.67	0.60	0.55	0.59	0.59	0.65	0.63	0.64	0.71	0.49	0.62	0.63
54	0.73	0.70	0.66	0.72	0.47	0.63	0.74	0.58	0.88	0.63	0.70	0.68	0.70
57	2.71	1.14	0.83	0.87	0.90	0.87	2.07	0.88	0.84	1.40	0.92	1.22	0.90
58	2.00	0.92	1.05	1.14	0.90	1.27	0.95	0.78	1.31	0.82	1.25	1.13	1.05
61	2.21	0.96	0.90	0.95	0.92	0.90	1.87	1.03	2.76	2.61	1.15	1.48	1.03
62	2.87	0.97	1.02	1.16	0.94	1.32	0.86	0.84	2.28	1.01	1.13	1.31	1.02
65	3.36	0.87	1.49	0.91	0.91	1.22	2.69	1.30	15.57	2.84	2.82	3.09	1.49
66	2.71	1.19	0.83	0.73	0.86	1.31	1.07	1.17	9.78	3.53	1.13	2.21	1.17
69	1.73	0.89	1.33	1.02	0.94	1.53	0.96	0.98	4.26	0.90	1.54	1.46	1.02
70	2.69	1.30	0.81	0.74	0.90	0.91	1.84	0.96	1.49	1.46	0.92	1.27	0.96
73	0.61	0.57	0.70	0.61	0.47	0.80	0.60	0.67	0.74	0.60	0.88	0.66	0.61
74	0.67	0.68	0.59	0.54	0.63	0.64	0.78	0.65	0.64	0.70	0.58	0.65	0.64
78	2.38	1.54	2.56	1.78	0.84	2.79	2.66	0.98	4.82	1.00	1.62	2.09	1.78
77	3.88	2.09	1.04	1.00	1.29	1.73	3.31	2.27	2.61	5.67	1.62	2.41	2.09
51	3.23	1.90	1.10	0.95	1.34	1.27	6.04	2.80	8.13	6.66	0.90	3.12	1.90
52	2.17	1.59	4.27	1.34	0.82	3.35	2.33	1.08	20.38	2.88	2.84	3.92	2.33
55	0.71	0.72	0.61	0.53	0.65	0.68	0.68	0.64	0.77	0.84	0.70	0.68	0.68
56	0.61	0.56	0.64	0.62	0.48	0.71	0.66	0.64	0.82	0.57	0.74	0.64	0.64
59	2.75	1.29	0.86	0.75	1.01	0.96	1.99	0.97	1.05	1.41	1.09	1.28	1.05
60	1.71	0.75	1.00	0.96	0.91	1.50	0.87	0.85	1.18	0.75	1.84	1.12	0.96
63	2.22	1.02	0.92	0.89	0.99	0.96	1.84	1.12	2.81	2.55	1.36	1.52	1.12
64	2.65	0.83	0.94	1.00	0.94	1.48	0.85	0.96	2.33	0.97	1.66	1.33	0.97
67	3.28	0.88	1.48	0.96	0.82	0.95	2.62	1.22	15.52	2.80	2.62	3.01	1.48
68	2.75	1.30	0.87	0.85	0.89	1.33	1.09	1.14	9.85	3.52	0.96	2.23	1.14
71	1.91	0.96	1.28	1.07	0.87	1.20	0.95	0.82	4.33	0.83	1.09	1.39	1.07
72	2.78	1.28	0.90	0.93	0.91	0.89	1.99	0.95	1.58	1.32	0.90	1.31	0.95
75	0.70	0.66	0.69	0.67	0.44	0.67	0.61	0.48	0.63	0.60	0.65	0.62	0.65
76	0.76	0.67	0.65	0.62	0.63	0.55	0.82	0.64	0.57	0.79	0.48	0.65	0.64
80	2.45	1.60	2.62	1.85	0.88	2.84	2.71	1.03	4.88	1.05	1.68	2.14	1.85
79	3.82	2.04	0.98	0.95	1.24	1.67	3.24	2.22	2.55	5.61	1.56	2.35	2.04

Legend	FO	IO	LS	CP

Table C-34. Brace Performance for Model 138P3_RFC1000_SL14.5_DBE

Brace Number	CAP	DZC	EDA	GAZ	KAK	LOS	ORR	POE	SCS	TCU	TMZ	Mean	Median
49	1.68	1.11	0.88	0.67	0.66	1.41	2.74	1.22	1.17	4.68	0.87	1.55	1.17
50	1.15	0.96	1.06	0.69	0.32	2.69	1.59	0.78	3.07	1.23	0.93	1.32	1.06
53	0.70	0.66	0.56	0.43	0.41	0.68	0.64	0.57	0.58	0.72	0.49	0.58	0.58
54	0.73	0.64	0.63	0.54	0.31	0.68	0.64	0.46	0.58	0.60	0.53	0.58	0.60
57	1.56	0.91	0.78	0.62	0.63	1.16	1.28	0.76	0.79	1.66	0.98	1.01	0.91
58	1.90	0.93	0.89	0.82	0.64	0.98	0.77	0.66	0.91	0.98	0.83	0.94	0.89
61	1.15	0.89	0.78	0.63	0.63	1.08	1.16	0.75	1.01	1.55	1.05	0.97	1.01
62	1.69	0.95	0.81	0.85	0.66	0.95	0.76	0.84	0.87	1.81	1.00	1.02	0.87
65	1.45	0.64	0.91	0.72	0.67	1.00	0.77	0.73	1.05	1.00	1.32	0.93	0.91
66	1.21	0.95	0.77	0.60	0.60	1.09	1.70	0.76	1.01	1.32	1.09	1.01	1.01
69	1.56	0.74	0.92	0.76	0.67	1.11	0.74	0.83	1.13	0.97	1.12	0.96	0.92
70	1.52	0.84	0.77	0.58	0.64	1.08	1.23	0.76	0.83	1.92	1.10	1.02	0.84
73	0.60	0.56	0.63	0.49	0.32	0.70	0.57	0.51	0.74	0.68	0.64	0.59	0.60
74	0.65	0.54	0.53	0.41	0.42	0.66	0.70	0.59	0.62	0.73	0.65	0.59	0.62
78	1.47	1.08	0.98	0.74	0.35	2.42	1.40	0.68	1.96	1.40	0.81	1.21	1.08
77	1.52	0.98	0.91	0.66	0.66	1.15	2.06	1.07	1.45	4.09	0.85	1.40	1.07
51	1.63	1.05	0.84	0.64	0.63	1.36	2.67	1.16	1.12	4.62	0.84	1.50	1.12
52	1.21	1.01	1.12	0.73	0.33	2.74	1.63	0.82	3.13	1.27	0.98	1.36	1.12
55	0.67	0.58	0.55	0.41	0.43	0.68	0.66	0.61	0.69	0.80	0.64	0.61	0.64
56	0.60	0.54	0.60	0.47	0.32	0.64	0.56	0.50	0.65	0.59	0.61	0.55	0.59
59	1.57	0.80	0.78	0.59	0.71	1.12	1.29	0.81	0.92	1.87	1.23	1.06	0.92
60	1.56	0.77	0.85	0.73	0.65	0.97	0.71	0.76	0.96	0.94	1.00	0.90	0.85
63	1.20	0.89	0.78	0.59	0.69	1.09	1.23	0.87	0.89	1.65	1.11	1.00	0.89
64	1.41	0.78	0.76	0.77	0.67	0.98	0.77	0.91	0.91	1.72	1.06	0.98	0.91
67	1.63	0.73	0.89	0.73	0.61	0.98	0.77	0.70	0.91	1.01	0.96	0.90	0.89
68	1.36	1.18	0.86	0.63	0.62	1.26	1.70	0.80	1.04	1.32	0.98	1.07	1.04
71	1.79	0.78	0.87	0.77	0.62	0.99	0.72	0.69	0.95	0.92	0.80	0.90	0.80
72	1.61	1.09	0.85	0.68	0.63	1.31	1.32	0.79	0.80	1.80	0.97	1.08	0.97
75	0.69	0.61	0.60	0.52	0.32	0.66	0.58	0.44	0.63	0.60	0.50	0.56	0.60
76	0.74	0.71	0.58	0.46	0.43	0.70	0.71	0.59	0.57	0.73	0.50	0.61	0.59
80	1.53	1.14	1.03	0.79	0.36	2.47	1.45	0.71	2.01	1.45	0.85	1.25	1.14
79	1.47	0.94	0.87	0.63	0.62	1.10	2.00	1.02	1.39	4.02	0.80	1.35	1.02

Legend	FO	IO	LS	CP

Table C-35. Brace Performance for Model 138P3_RFC1000_SL14.5_SLE2

Brace Number	CAP	DZC	EDA	GAZ	KAK	LOS	ORR	POE	SCS	TCU	TMZ	Mean	Median
49	0.92	0.77	0.59	0.40	0.42	1.26	1.32	0.83	0.96	2.42	0.58	0.95	0.83
50	1.06	0.68	0.67	0.45	0.24	1.27	1.00	0.58	1.11	1.56	0.56	0.83	0.68
53	0.61	0.52	0.42	0.33	0.31	0.59	0.61	0.47	0.55	0.66	0.38	0.50	0.52
54	0.68	0.49	0.47	0.40	0.28	0.64	0.61	0.38	0.58	0.75	0.38	0.52	0.49
57	0.96	0.71	0.60	0.47	0.50	0.88	0.95	0.63	0.74	1.30	0.73	0.77	0.73
58	1.18	0.73	0.68	0.62	0.50	0.80	0.76	0.59	0.80	1.76	0.60	0.82	0.73
61	0.93	0.67	0.61	0.47	0.52	0.89	0.95	0.61	0.70	0.94	0.69	0.73	0.69
62	1.20	0.75	0.60	0.63	0.56	0.76	0.67	0.70	0.83	1.38	0.72	0.80	0.72
65	1.05	0.52	0.66	0.55	0.52	0.78	0.70	0.60	0.90	1.08	0.88	0.75	0.70
66	0.92	0.71	0.58	0.44	0.50	0.81	0.90	0.60	0.80	1.09	0.77	0.74	0.77
69	0.98	0.59	0.68	0.58	0.51	0.82	0.74	0.70	0.92	1.44	0.76	0.79	0.74
70	0.89	0.66	0.59	0.44	0.51	0.82	0.95	0.60	0.80	1.51	0.79	0.78	0.79
73	0.60	0.45	0.46	0.36	0.26	0.59	0.55	0.42	0.67	0.65	0.47	0.50	0.47
74	0.53	0.43	0.39	0.30	0.33	0.59	0.64	0.47	0.59	0.68	0.47	0.49	0.47
78	1.26	0.71	0.65	0.48	0.24	1.32	0.94	0.55	0.97	1.48	0.57	0.83	0.71
77	0.95	0.73	0.60	0.40	0.41	1.31	1.10	0.79	1.03	1.95	0.58	0.90	0.79
51	0.87	0.73	0.55	0.38	0.39	1.20	1.27	0.79	0.92	2.36	0.55	0.91	0.79
52	1.11	0.71	0.70	0.48	0.26	1.32	1.05	0.61	1.17	1.62	0.60	0.88	0.71
55	0.55	0.44	0.40	0.30	0.33	0.60	0.64	0.51	0.66	0.70	0.47	0.51	0.51
56	0.59	0.42	0.46	0.35	0.24	0.57	0.55	0.39	0.61	0.69	0.45	0.48	0.46
59	0.89	0.63	0.60	0.46	0.56	0.86	0.99	0.68	0.88	1.41	0.83	0.80	0.83
60	0.97	0.60	0.65	0.55	0.51	0.76	0.68	0.67	0.81	1.65	0.72	0.78	0.68
63	0.91	0.72	0.60	0.47	0.56	0.87	0.99	0.63	0.81	1.01	0.77	0.76	0.77
64	1.04	0.61	0.56	0.57	0.51	0.75	0.61	0.76	0.82	1.28	0.77	0.75	0.75
67	1.08	0.59	0.64	0.55	0.54	0.77	0.69	0.56	0.80	1.07	0.67	0.72	0.67
68	0.96	0.86	0.64	0.46	0.51	0.90	0.95	0.66	0.77	1.11	0.75	0.78	0.77
71	1.04	0.61	0.65	0.59	0.48	0.76	0.73	0.58	0.81	1.44	0.56	0.75	0.65
72	1.05	0.82	0.65	0.52	0.50	0.91	0.99	0.63	0.75	1.51	0.74	0.83	0.75
75	0.65	0.48	0.45	0.39	0.28	0.61	0.56	0.38	0.58	0.67	0.38	0.49	0.48
76	0.64	0.56	0.43	0.34	0.32	0.62	0.66	0.48	0.53	0.68	0.39	0.51	0.53
80	1.32	0.75	0.68	0.51	0.26	1.37	0.98	0.57	1.02	1.54	0.60	0.87	0.75
79	0.91	0.70	0.57	0.38	0.39	1.26	1.05	0.75	0.98	1.89	0.55	0.86	0.75

Legend	FO	IO	LS	CP

Table C-36. Brace Performance for Model 138P3_RFC1000_SL14.5_SLE1

Brace Number	CAP	DZC	EDA	GAZ	KAK	LOS	ORR	POE	SCS	TCU	TMZ	Mean	Median
49	0.43	0.41	0.11	0.20	0.28	0.33	0.44	0.30	0.22	0.77	0.28	0.34	0.30
50	0.50	0.34	0.12	0.23	0.23	0.27	0.36	0.25	0.27	0.81	0.19	0.33	0.27
53	0.34	0.34	0.19	0.21	0.24	0.29	0.35	0.29	0.21	0.50	0.27	0.29	0.29
54	0.40	0.31	0.19	0.28	0.22	0.26	0.28	0.26	0.25	0.58	0.24	0.30	0.26
57	0.56	0.50	0.30	0.37	0.33	0.41	0.53	0.46	0.29	0.67	0.43	0.44	0.43
58	0.64	0.53	0.26	0.51	0.44	0.39	0.44	0.42	0.39	0.85	0.40	0.48	0.44
61	0.53	0.50	0.31	0.44	0.32	0.42	0.50	0.43	0.27	0.63	0.51	0.44	0.44
62	0.62	0.49	0.27	0.53	0.45	0.40	0.48	0.45	0.37	0.75	0.41	0.47	0.45
65	0.58	0.50	0.28	0.40	0.39	0.40	0.51	0.42	0.40	0.73	0.37	0.45	0.40
66	0.51	0.47	0.30	0.36	0.30	0.45	0.48	0.42	0.32	0.61	0.48	0.43	0.45
69	0.61	0.54	0.24	0.50	0.41	0.43	0.47	0.42	0.46	0.80	0.41	0.48	0.46
70	0.55	0.46	0.26	0.35	0.33	0.44	0.52	0.46	0.33	0.64	0.42	0.43	0.44
73	0.40	0.32	0.17	0.26	0.23	0.30	0.29	0.25	0.31	0.58	0.25	0.31	0.29
74	0.31	0.28	0.18	0.21	0.23	0.29	0.35	0.28	0.24	0.46	0.28	0.28	0.28
78	0.52	0.34	0.10	0.22	0.24	0.27	0.36	0.25	0.28	0.85	0.19	0.33	0.27
77	0.44	0.40	0.13	0.21	0.29	0.32	0.44	0.29	0.21	0.76	0.31	0.34	0.31
51	0.41	0.39	0.10	0.18	0.26	0.31	0.42	0.28	0.21	0.73	0.26	0.32	0.28
52	0.53	0.36	0.13	0.25	0.25	0.29	0.39	0.27	0.30	0.86	0.20	0.35	0.29
55	0.31	0.30	0.18	0.22	0.24	0.30	0.36	0.29	0.25	0.51	0.30	0.30	0.30
56	0.39	0.32	0.17	0.27	0.22	0.29	0.29	0.24	0.29	0.55	0.24	0.30	0.29
59	0.57	0.48	0.27	0.37	0.34	0.44	0.55	0.48	0.35	0.71	0.48	0.46	0.48
60	0.61	0.53	0.25	0.48	0.40	0.41	0.46	0.41	0.42	0.81	0.41	0.47	0.42
63	0.56	0.52	0.28	0.44	0.33	0.44	0.51	0.45	0.32	0.67	0.48	0.46	0.45
64	0.59	0.49	0.26	0.51	0.41	0.39	0.49	0.43	0.40	0.69	0.37	0.46	0.43
67	0.55	0.45	0.30	0.40	0.38	0.35	0.46	0.40	0.34	0.70	0.37	0.43	0.40
68	0.55	0.49	0.34	0.39	0.32	0.47	0.51	0.45	0.29	0.64	0.46	0.45	0.46
71	0.59	0.50	0.24	0.49	0.43	0.36	0.42	0.40	0.39	0.76	0.37	0.45	0.42
72	0.59	0.52	0.32	0.37	0.35	0.45	0.55	0.49	0.31	0.66	0.43	0.46	0.45
75	0.37	0.30	0.18	0.28	0.22	0.25	0.27	0.25	0.26	0.56	0.25	0.29	0.26
76	0.35	0.36	0.21	0.22	0.25	0.29	0.37	0.29	0.21	0.49	0.29	0.30	0.29
80	0.55	0.36	0.11	0.24	0.26	0.29	0.38	0.27	0.30	0.89	0.21	0.35	0.29
79	0.42	0.38	0.11	0.19	0.27	0.30	0.41	0.27	0.20	0.72	0.29	0.32	0.29

Legend	FO	IO	LS	CP

Appendix D. Global Story Drift Demands

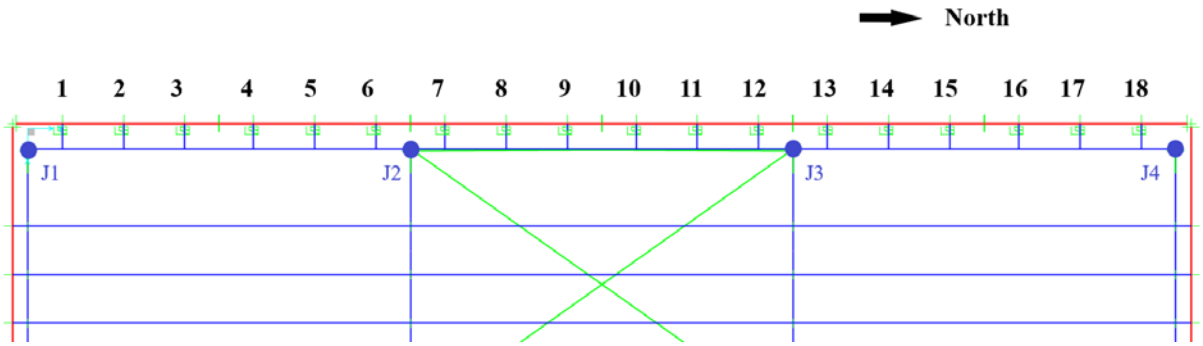

Figure D-1. Joint and RFC Identification along West Wall for Models 16 and 85 (Plan View)

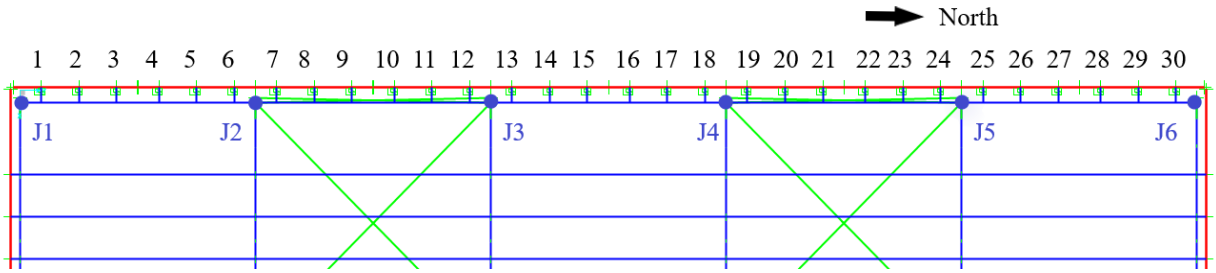

Figure D-2. Joint and RFC Identification along West Wall for Models 41 and 138 (Plan View)

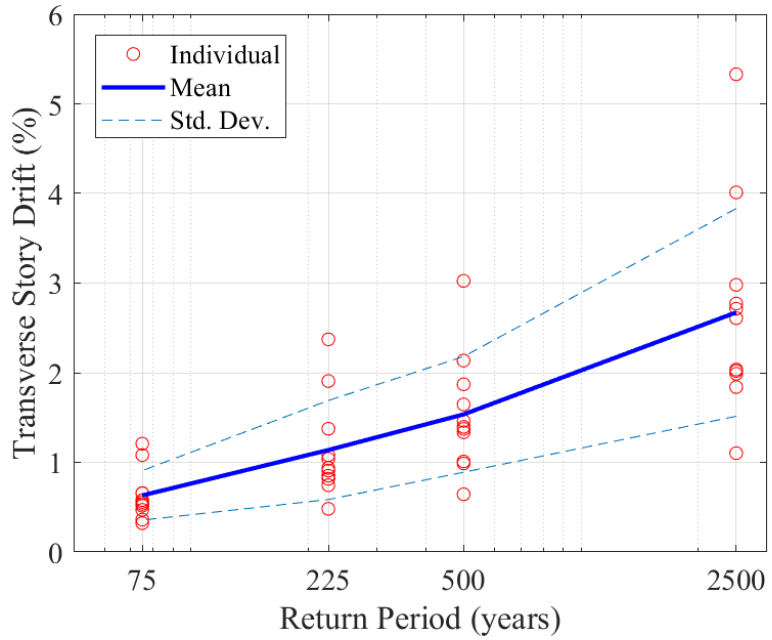

Figure D-3. Peak Transverse Story Drift for 16P3_RFC1000_SL14.5 (Joint 3)

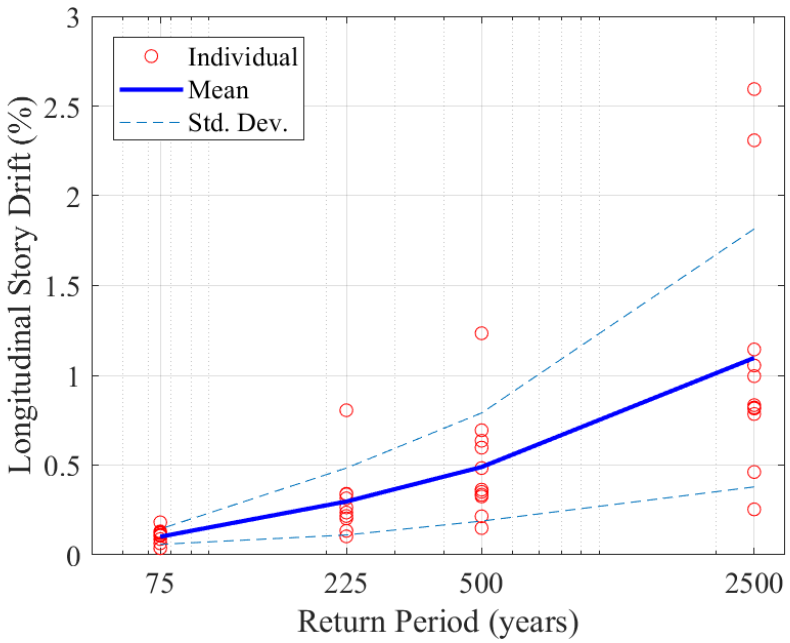

Figure D-4. Peak Longitudinal Story Drift for 16P3_RFC1000_SL14.5 (Joint 3)

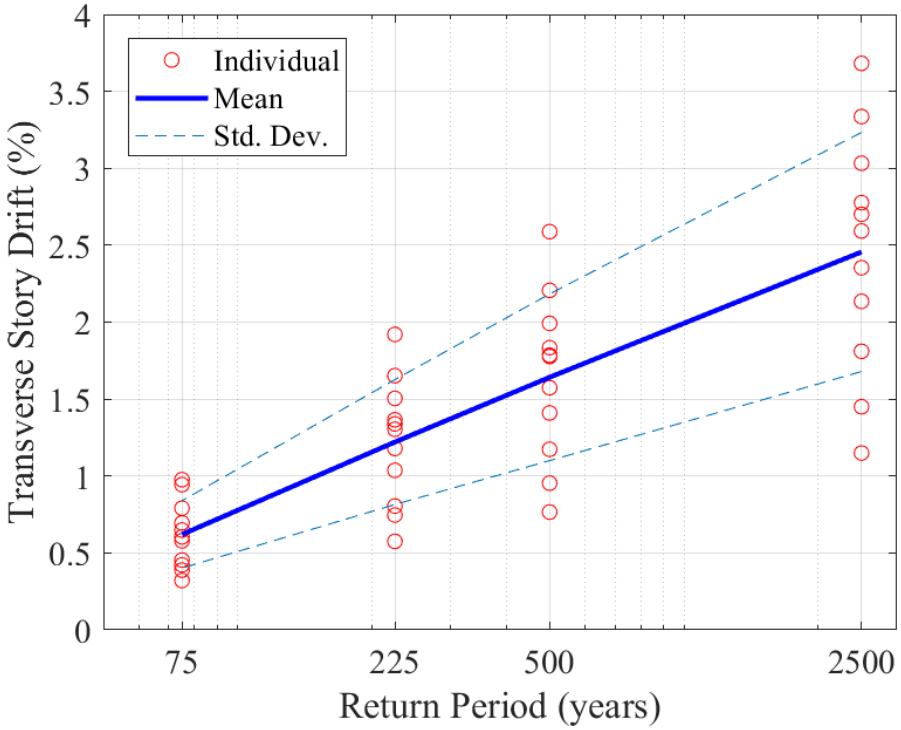

Figure D-5. Peak Transverse Story Drift for 41P3_RFC1000_SL14.5 (Joint 3)

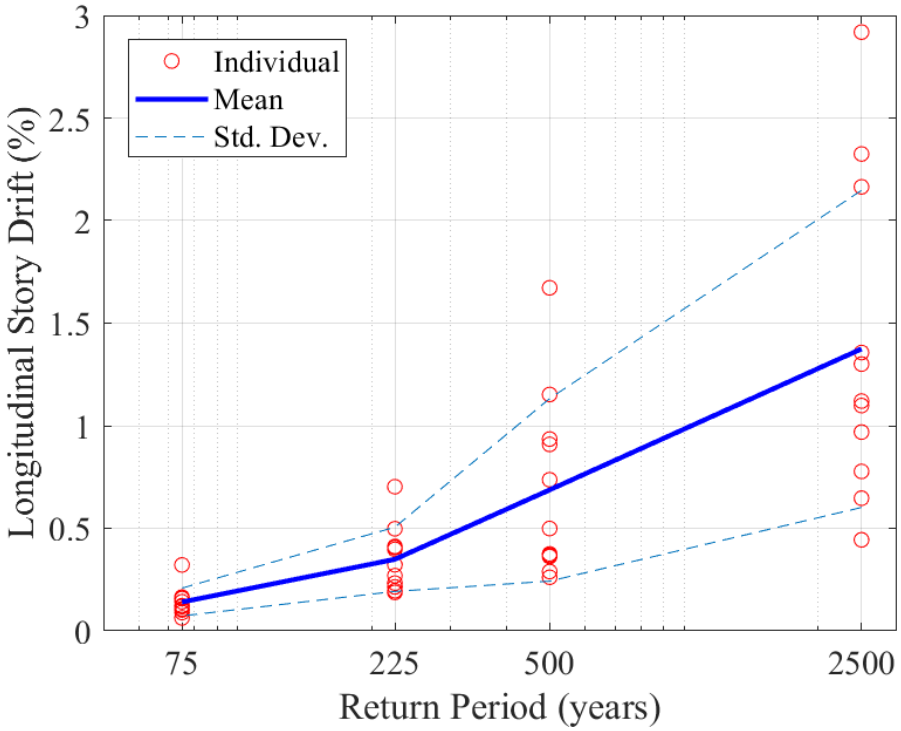

Figure D-6. Peak Longitudinal Story Drift for 41P3_RFC1000_SL14.5 (Joint 3)

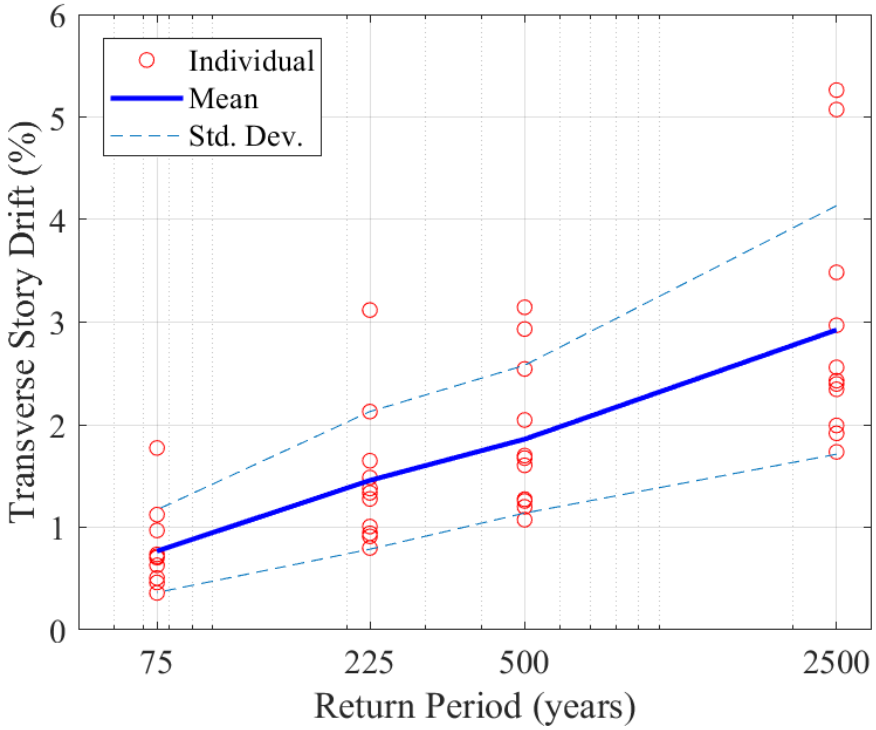

Figure D-7. Peak Transverse Story Drift for 85P3_RFC0625_SL07.5 (Joint 3)

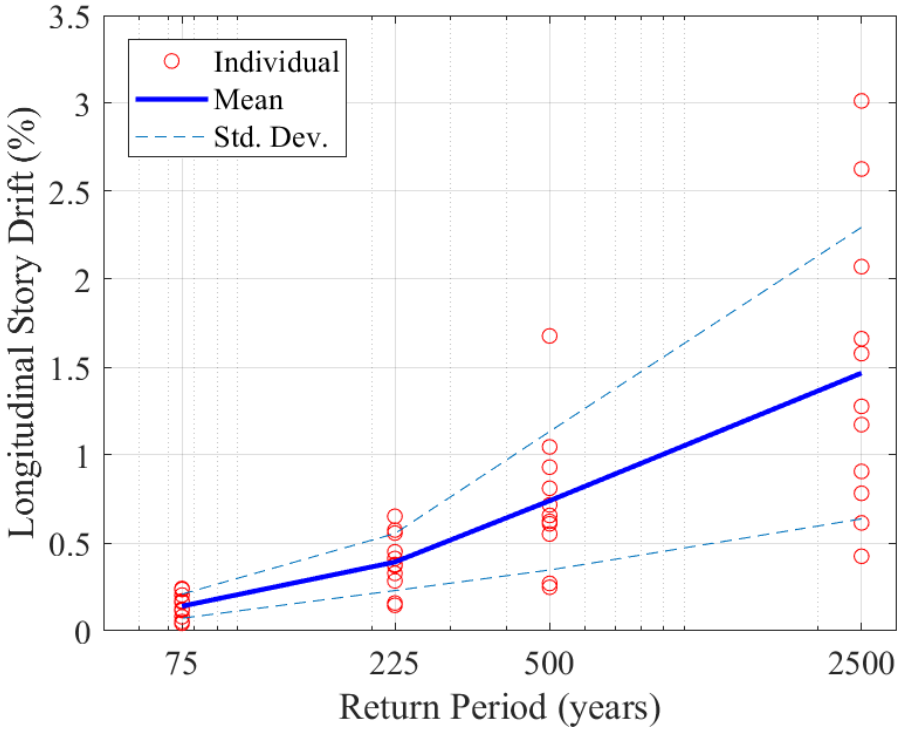

Figure D-8. Peak Longitudinal Story Drift for 85P3_RFC0625_SL07.5 (Joint 3)

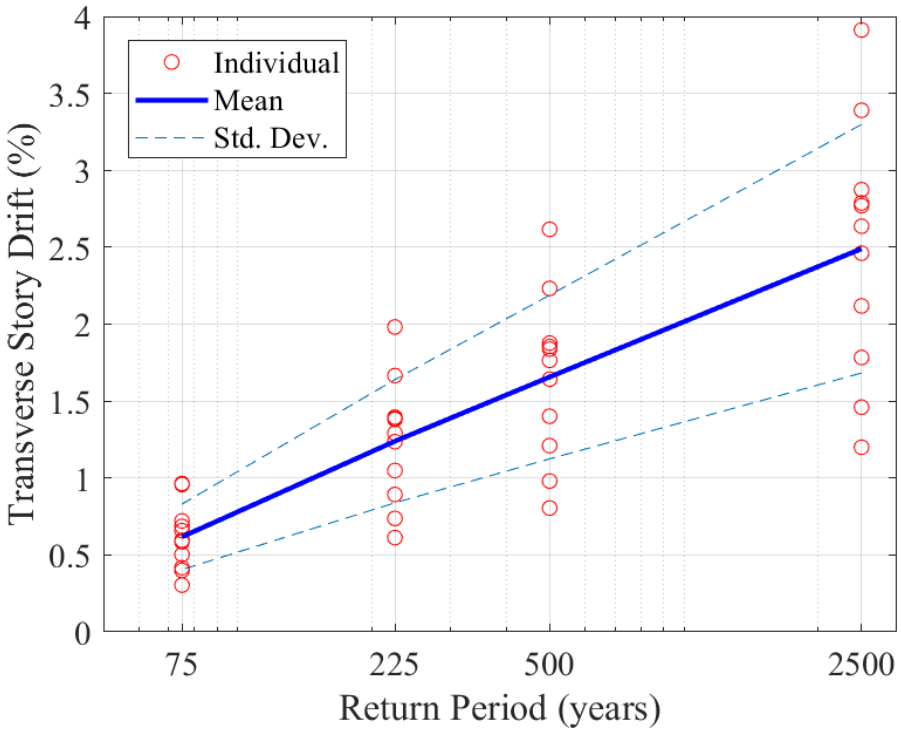

Figure D-9. Peak Transverse Story Drift for 138P3_RFC1000_SL14.5 (Joint 3)

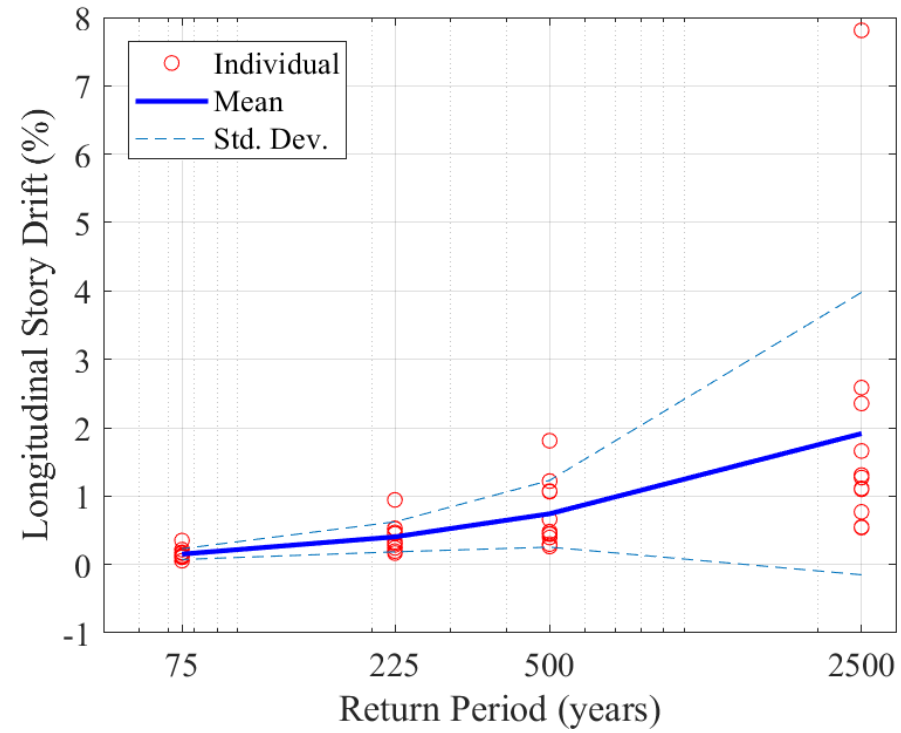

Figure D-10. Peak Longitudinal Story Drift for 138P3_RFC1000_SL14.5 (Joint 3)

Appendix E. RFC Demands for MCE Level Analysis

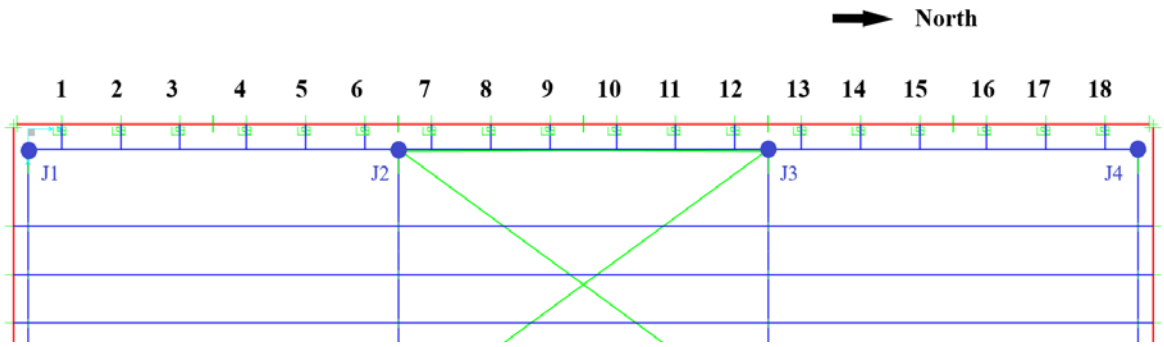

Figure E-1. West Wall RFC Identification (Model 16 Plan View)

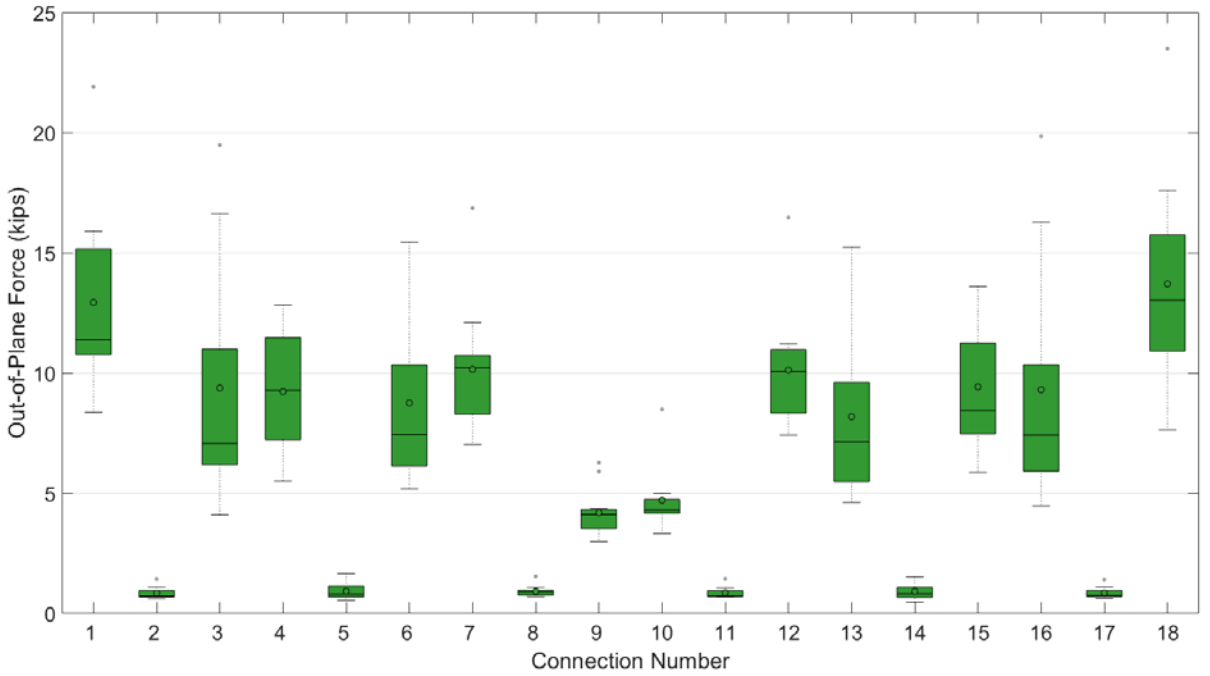

Figure E-2. Out-of-Plane Tensile Force for 16P3_RFC1000_SL14.5 at MCE Level

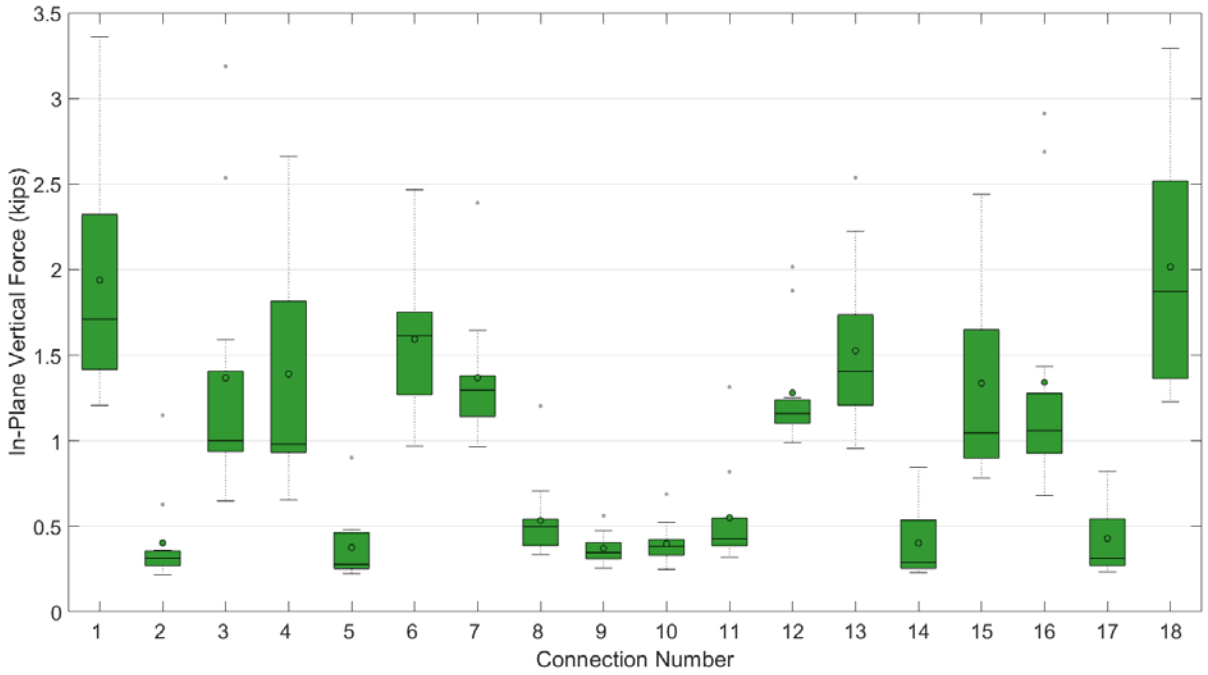

Figure E-3. In-Plane Vertical Shear Force for 16P3_RFC1000_SL14.5 at MCE Level

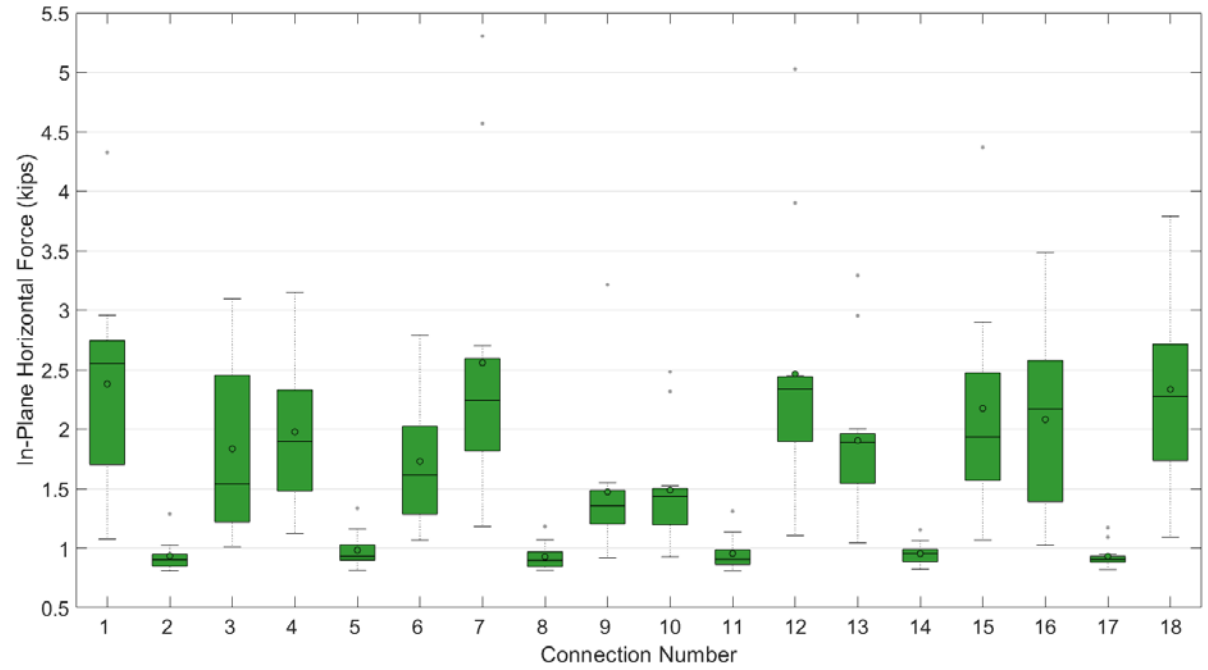

Figure E-4. In-Plane Horizontal Shear Force for 16P3_RFC1000_SL14.5 at MCE Level

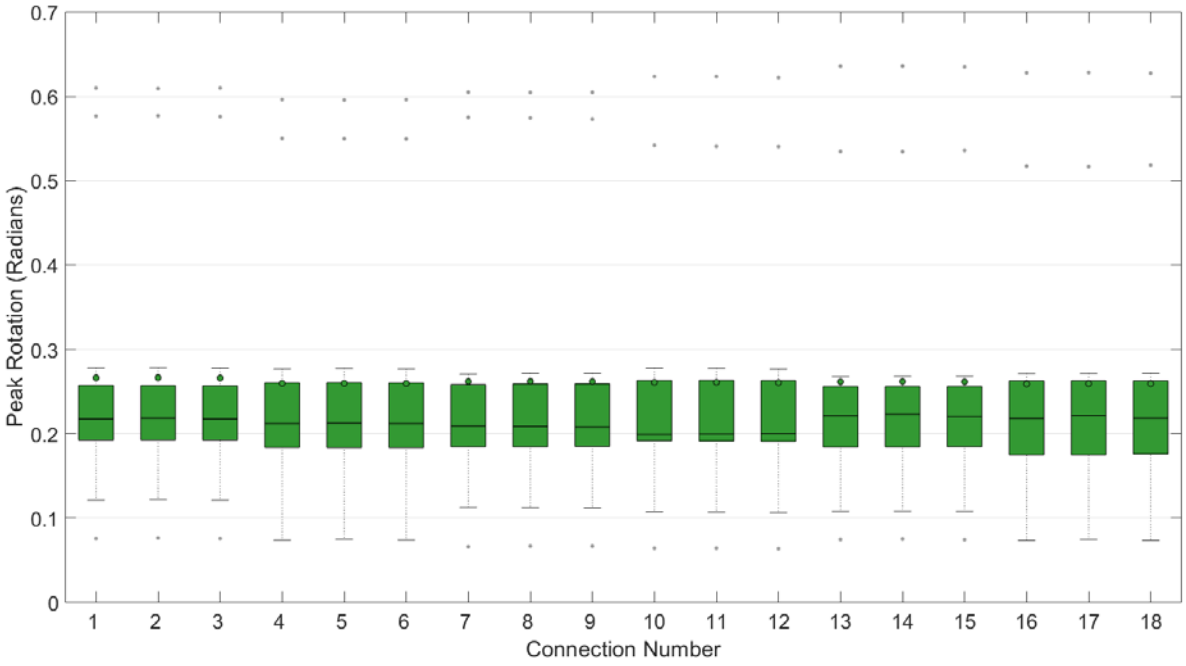

Figure E-5. Peak Rotation for 16P3_RFC1000_SL14.5 at MCE Level

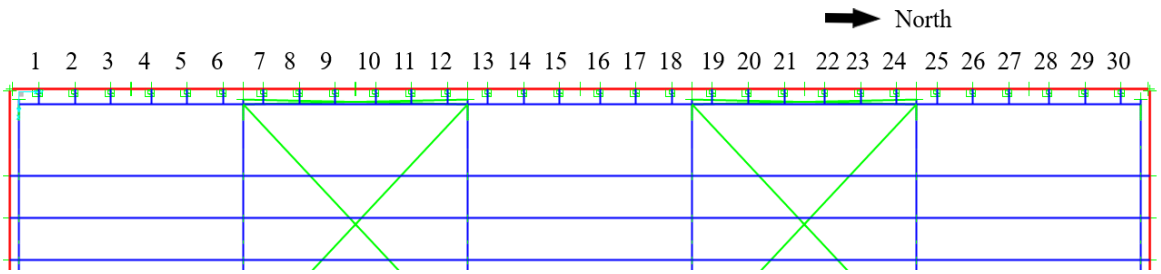

Figure E-6. West Wall RFC Identification (Model 41 Plan View)

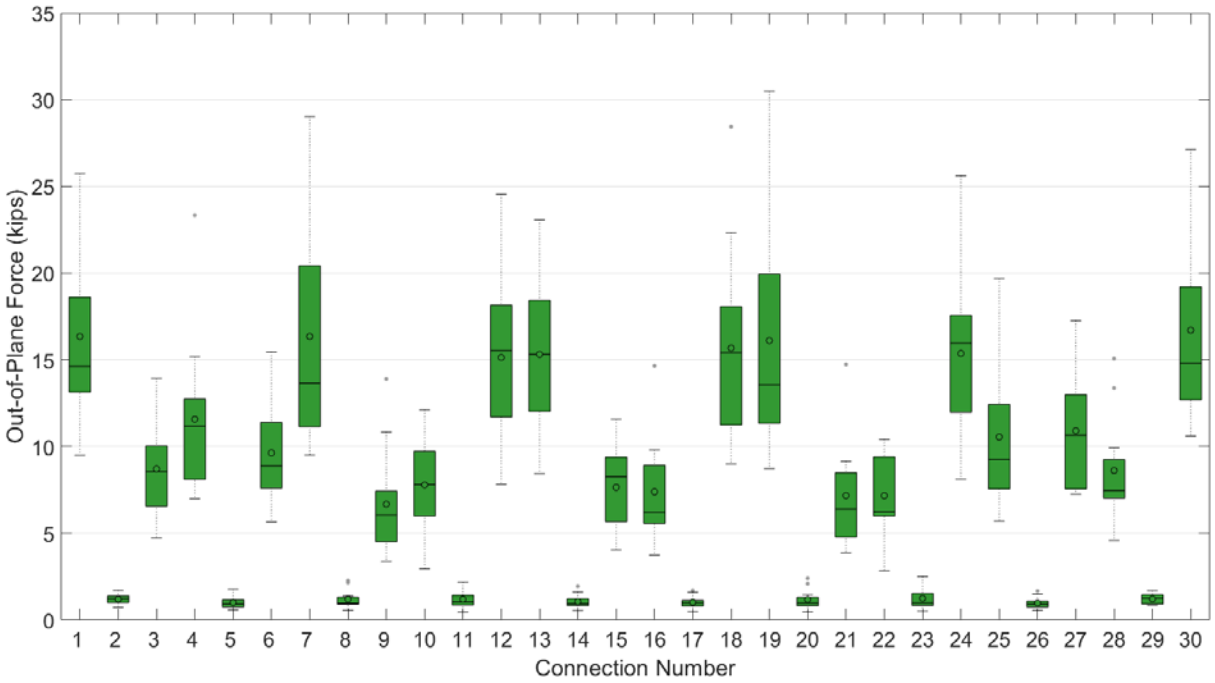

Figure E-7. Out-of-Plane Tensile Force for 41P3_RFC1000_SL14.5 at MCE Level

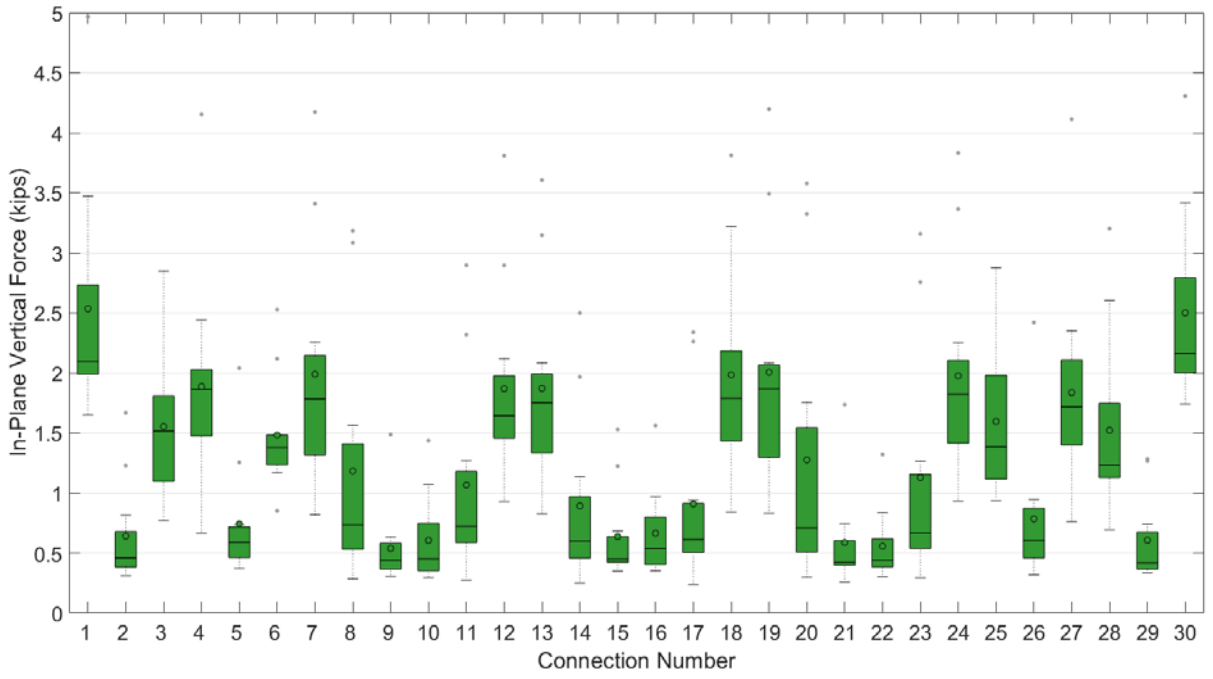

Figure E-8. In-Plane Vertical Shear Force for 41P3_RFC1000_SL14.5 at MCE Level

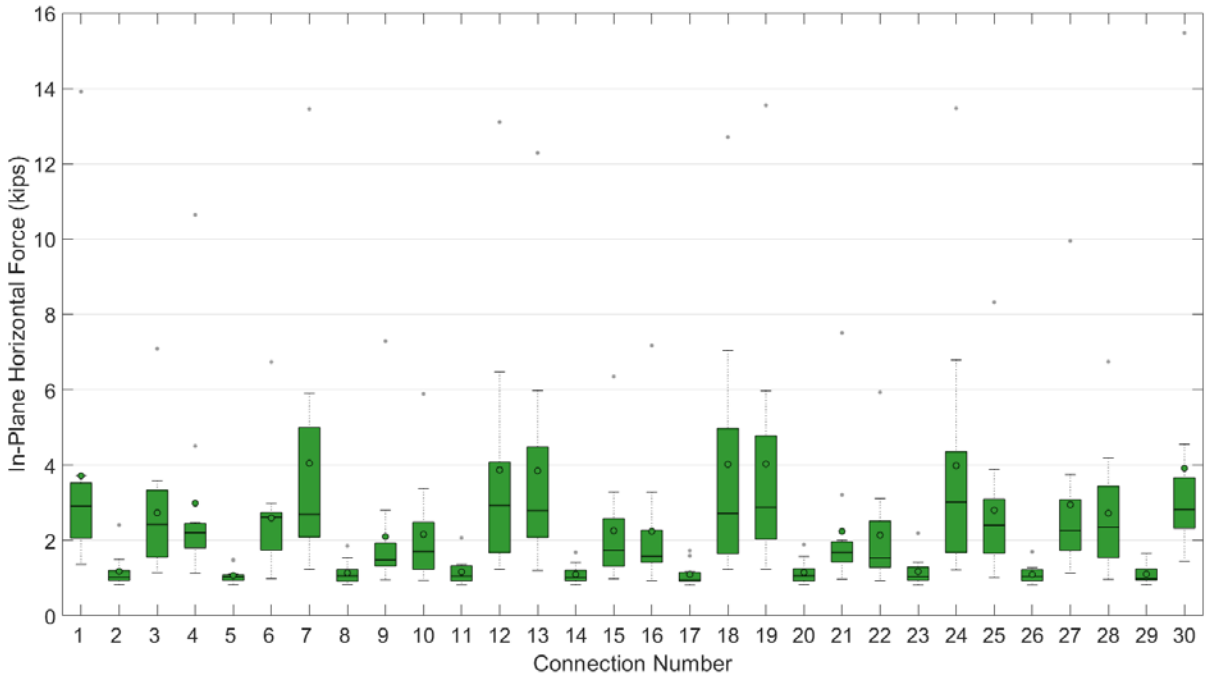

Figure E-9. In-Plane Horizontal Shear Force for 41P3_RFC1000_SL14.5 at MCE Level

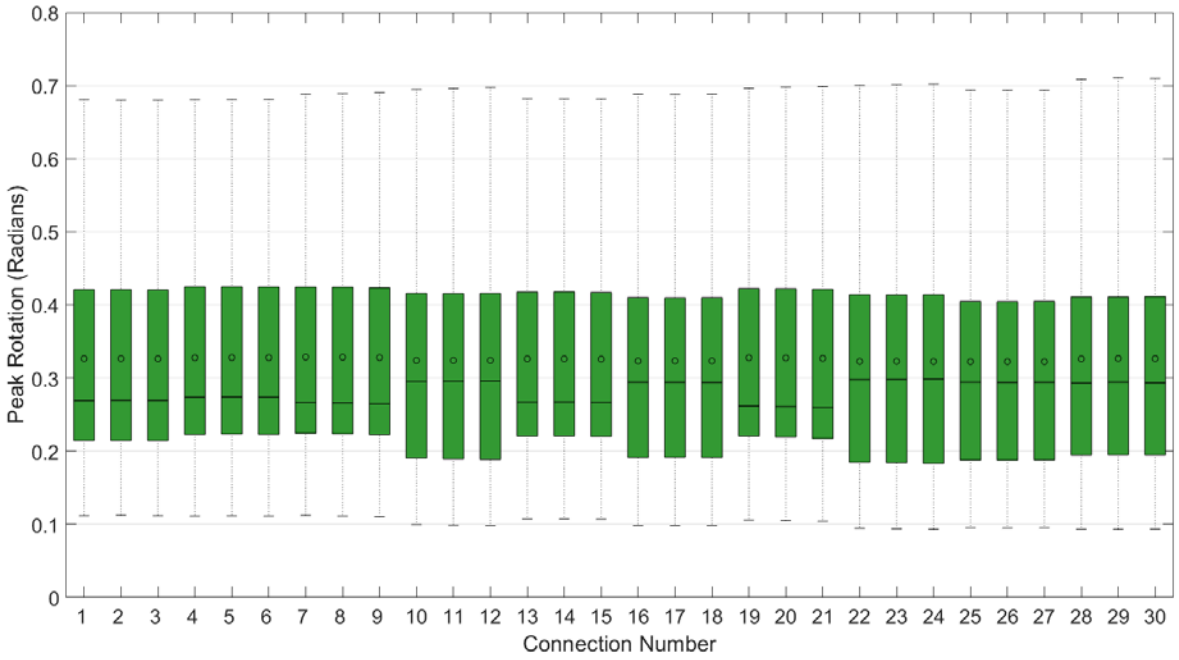

Figure E-10. Peak Rotation for 41P3_RFC1000_SL14.5 at MCE Level

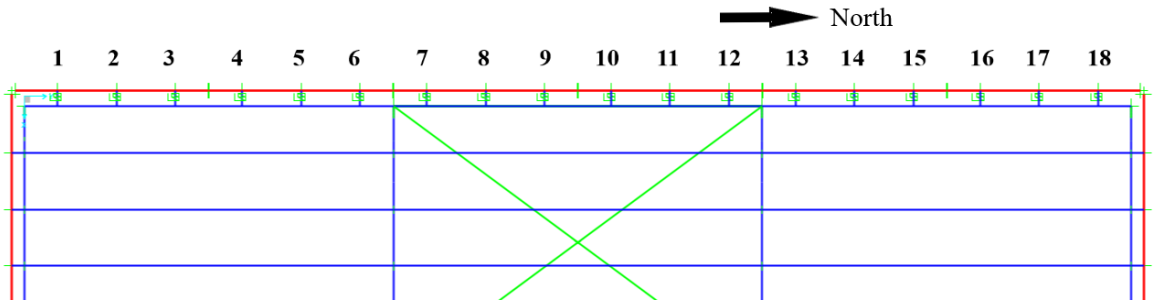

Figure E-11. West Wall RFC Identification (Model 85 Plan View)

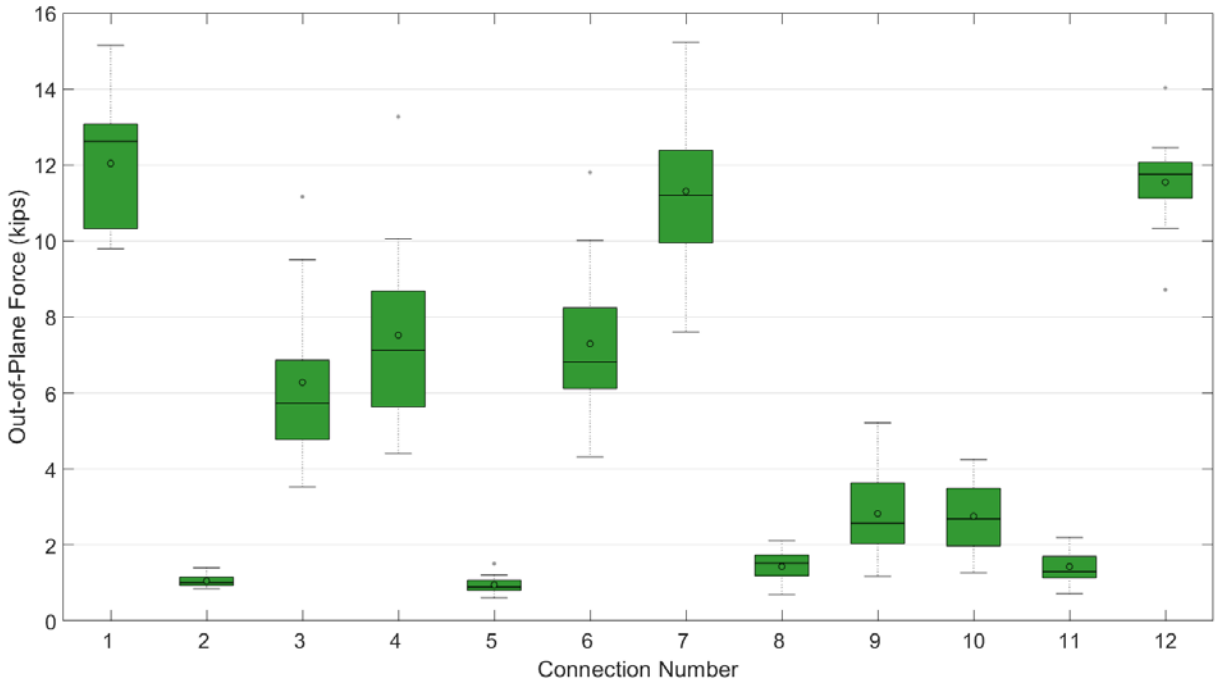

Figure E-12. Out-of-Plane Tensile Force for 85P3_RFC0625_SL07.5 at MCE Level

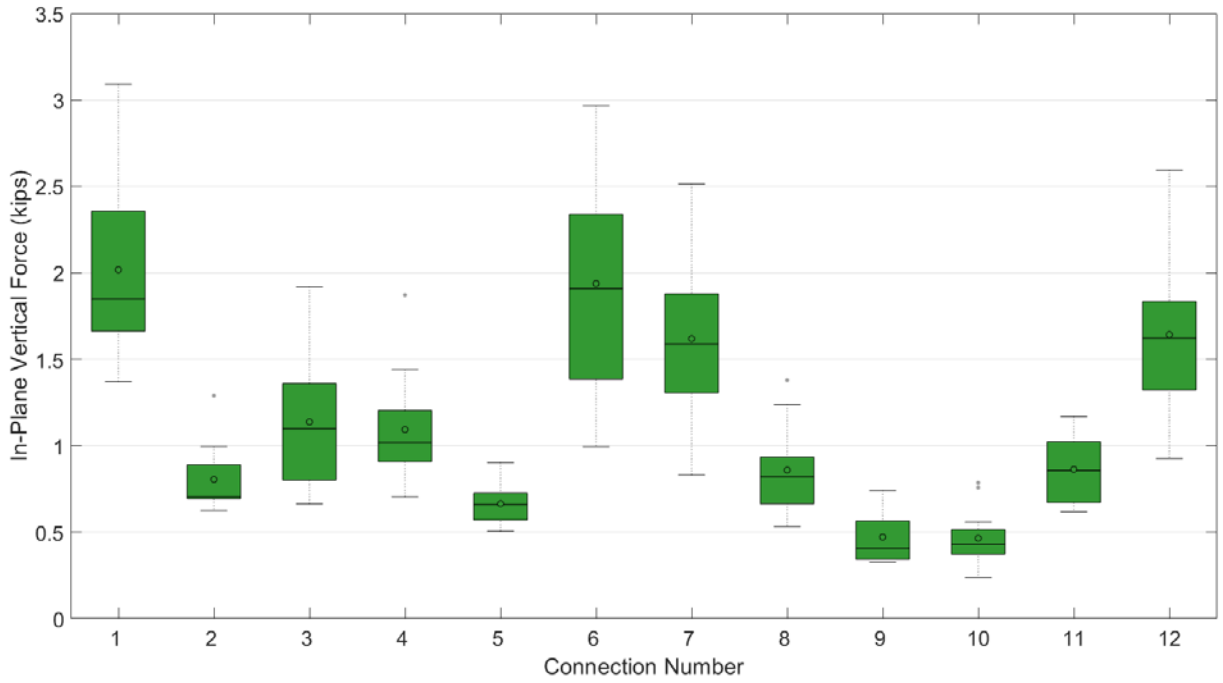

Figure E-13. In-Plane Vertical Shear Force for 85P3_RFC0625_SL07.5 at MCE Level

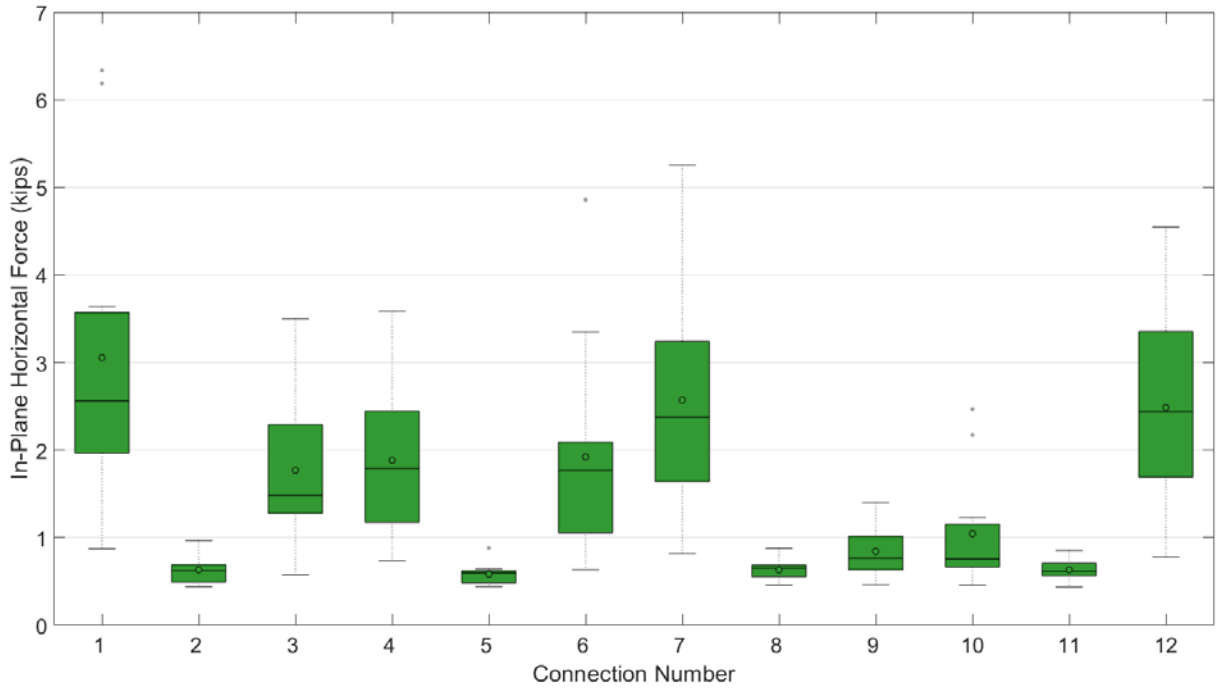

Figure E-14. In-Plane Horizontal Shear Force for 85P3_RFC0625_SL07.5 at MCE Level

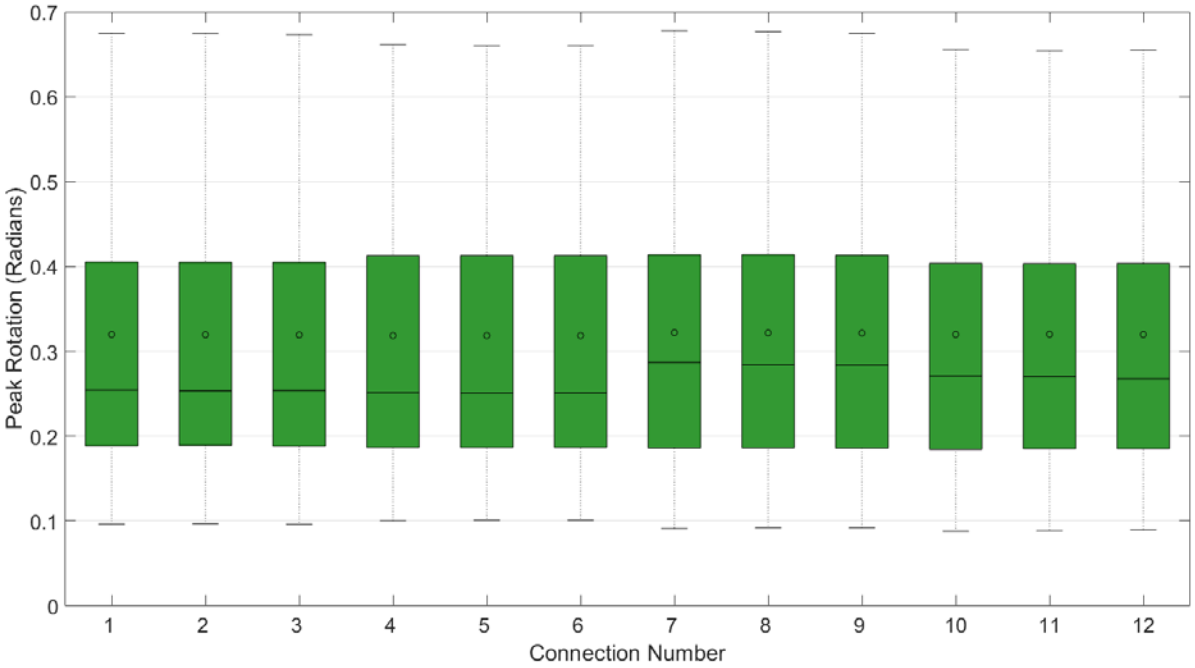

Figure E-15. Peak Rotation for 85P3_RFC0625_SL07.5 at MCE Level

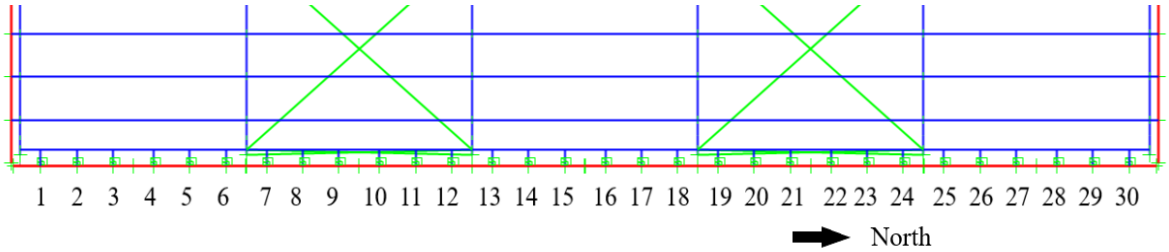

Figure E-16. East Wall RFC Identification (Model 138 Plan View)

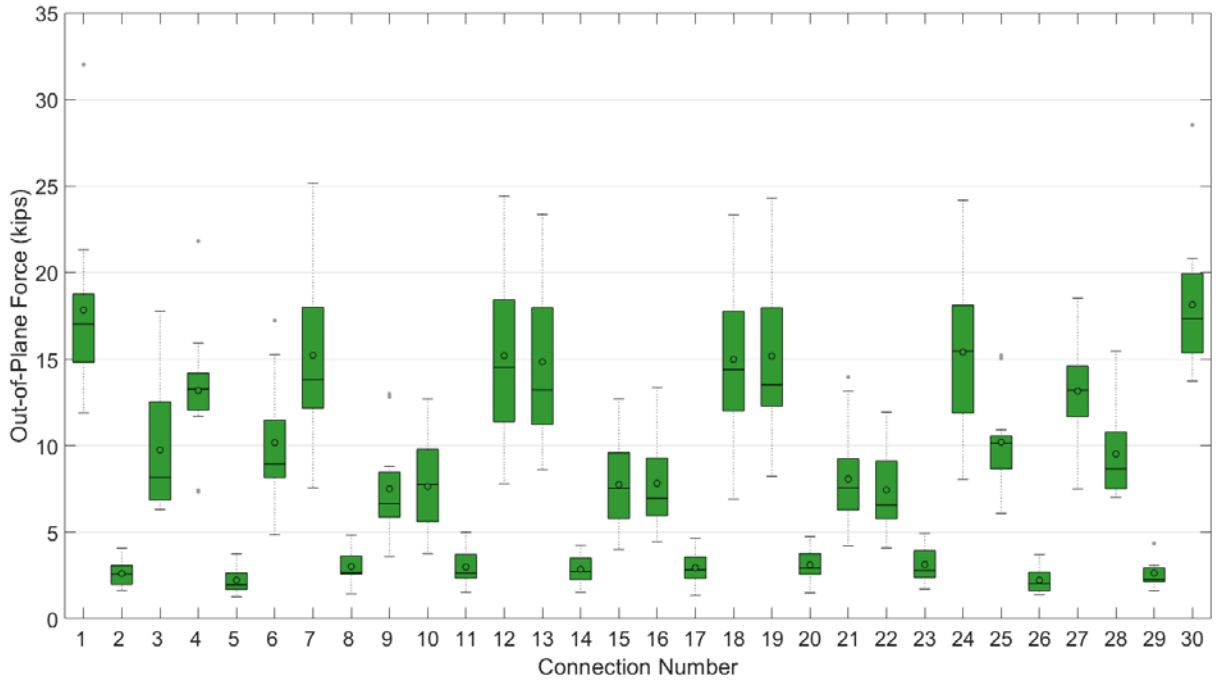

Figure E-17. Out-of-Plane Tensile Force for 138P3_RFC1000_SL14.5 at MCE Level

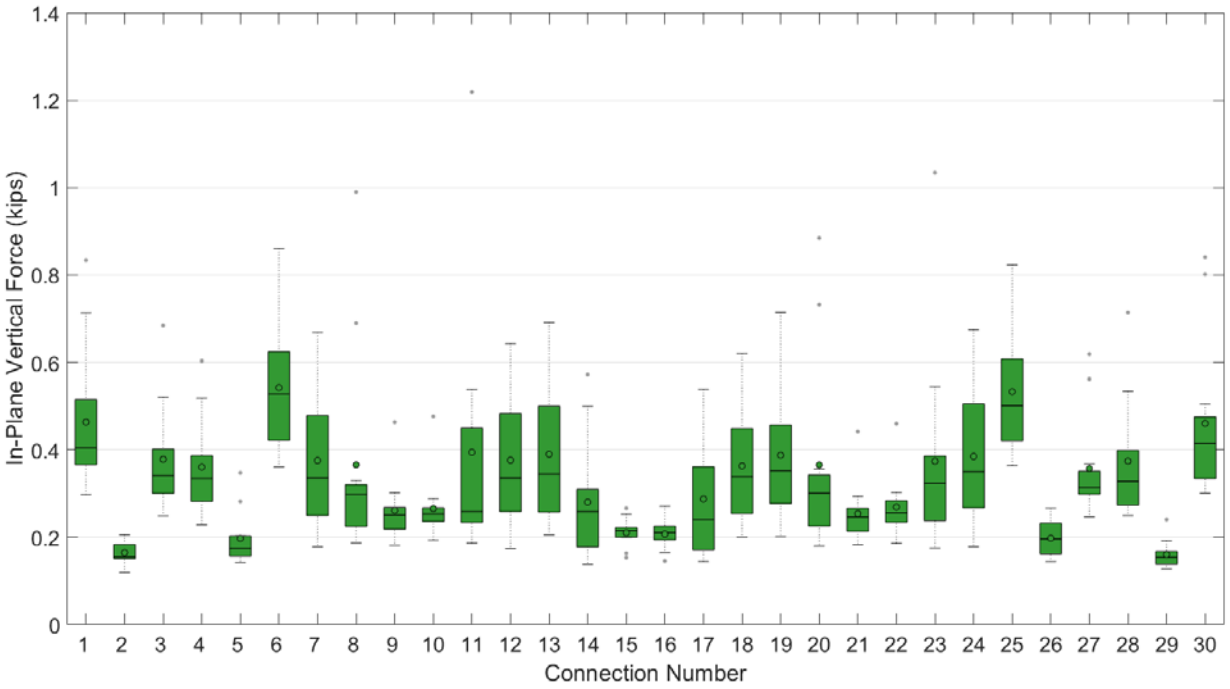

Figure E-18. In-Plane Vertical Shear Force for 138P3_ RFC1000_ SL14.5 at MCE Level

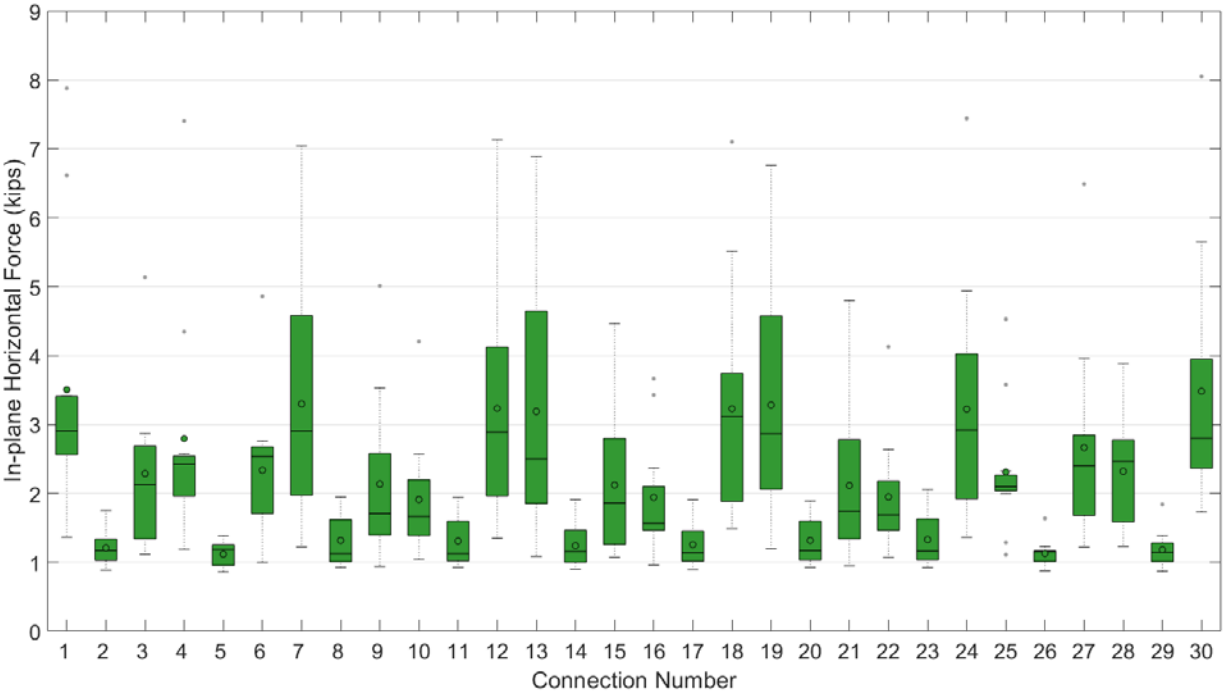

Figure E-19. In-Plane Horizontal Shear Force for 138P3_ RFC1000_ SL14.5 at MCE Level

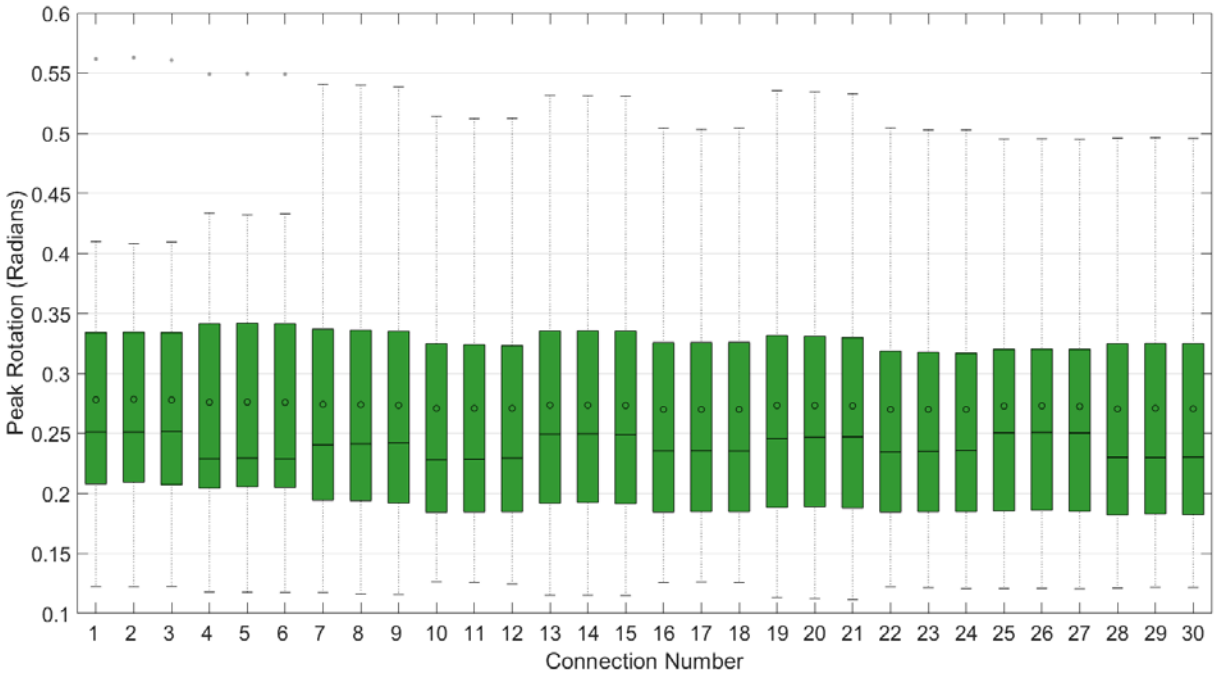

Figure E-20. Peak Rotation for 138P3_ RFC1000_ SL14.5 at MCE Level